REMAINING LIFE ASSESSMENT OF
IN-SERVICE LUMINAIRE SUPPORT STRUCTURES

by

Mark C. Frymoyer   Jeffrey W. Berman
Graduate Research Assistant   Assistant Professor

Department of Civil and Environmental Engineering
University of Washington, Box 352700
Seattle, Washington 98195

A Report Prepared for

TECHNICAL REPORT STANDARD TITLE PAGE

1. REPORT NO. TNW2010-01	2. GOVERNMENT ACCESSION NO.	3. RECIPIENT'S CATALOG NO.
4. TITLE AND SUBTITLE REMAINING LIFE ASSESSMENT OF IN-SERVICE LUMINAIRE SUPPORT STRUCTURES		5. REPORT DATE January 2010
		6. PERFORMING ORGANIZATION CODE
7. AUTHOR(S) Mark Frymoyer and Jeffrey Berman		8. PERFORMING ORGANIZATION REPORT NO. TNW2010-01
9. PERFORMING ORGANIZATION NAME AND ADDRESS Transportation Northwest Regional Center X (TransNow) Box 352700, 129 More Hall University of Washington Seattle, WA 98195-2700		10. WORK UNIT NO.
		11. CONTRACT OR GRANT NO. DTRT07-G-0010
12. SPONSORING AGENCY NAME AND ADDRESS United States Department of Transportation Office of the Secretary of Transportation 1200 New Jersey Ave, SE Washington, D.C. 20590		13. TYPE OF REPORT AND PERIOD COVERED Final Research Report
		14. SPONSORING AGENCY CODE
15. SUPPLEMENTARY NOTES This study was conducted in cooperation with the University of Washington and the US Department of Transportation		

16. ABSTRACT

   Recent fatigue failures of in-service luminaire support structures in Washington and around the country have prompted concern about their fatigue resistance. Most luminaire support structures in Washington were designed without attention to fatigue or with vague and incomplete fatigue design provisions. Furthermore, most luminaire support structures were installed during the construction of the Interstate system in the 1960s, and as many as half are estimated to have exceeded their 25-year design life. This research was initiated to help the Washington State Department of Transportation (WSDOT) prioritize the inspection and replacement of luminaire support structures throughout the state and to develop rational inspection procedures.

   The research had four primary components: a literature review, experimental fatigue testing of two in-service luminaire poles, a finite element analysis of the pole base, and development of a framework for estimating remaining life. The extensive literature review found previous experimental studies, which were used to identify details in older WSDOT luminaire support structures that may be critical and to help inform the selection of test specimens. Quasi-static and high cycle fatigue testing were performed on two previously in-service luminaire poles to determine the stress concentration factors (SCF) in critical details and determine fatigue resistance. The results were then compared to the finite element analysis and the fatigue classifications used in design. The finite element model was also used to determine the impact of parameters including base plate thickness, hand hole stiffener thickness, and location of anchor bolts. The individual components of a framework for estimating the remaining life of luminaire support structures in Washington were developed on the basis of a procedure established by Foley et al. (2004) in their study of the remaining life of sign bridge structures.

   The remaining fatigue life of the critical details in the previously in-service luminaire support structures were found to exceed their design life. Cracking at the stiffened hand hole detail was found to be the ultimate limit state for both specimens but was observed at cycle counts that were well beyond the design life. High SCFs were measured in both compression and tension at the CJP weld toe, indicating the importance of base plate flexibility, anchor bolt layout, and a uniform bearing surface. While it was not possible to know the load history for the selected specimens, it is clear that the number of damaging cycles was low and that the fatigue design life for these details is conservative. Recommendations for luminaire inspection are provided.

17. KEY WORDS Luminaires, fatigue, wind loading	18. DISTRIBUTION STATEMENT No restrictions. This document is available to the public through the National Technical Information Service, Springfield, VA 22616	
19. SECURITY CLASSIF. (of this report) None	20. SECURITY CLASSIF. (of this page) None	21. NO. OF PAGES 198	22. PRICE

DISCLAIMER

TECHNICAL REPORT STANDARD TITLE PAGE

TABLE OF CONTENTS

TECHNICAL REPORT STANDARD TITLE PAGE

List of Figures

List of Tables

TECHNICAL REPORT STANDARD TITLE PAGE

Chapter 1 Introduction

1.1 Statement of the Problem and Objectives

Thousands of luminaires are used on roadways throughout the state of Washington to provide visibility to motorists. Luminaires are supported by tall, flexible, cantilevered support structures with fixed bases and can be classified as vertical or horizontal cantilevered. Vertical cantilevered support structures have a single pole with the lighting fixture mounted on top and horizontal cantilevered support structures have a single pole with a cantilevered mast arm and the lighting fixture on the end. Most luminaire support structures in Washington were designed without attention to fatigue or with vague and incomplete fatigue design provisions. Furthermore, most luminaire support structures were installed during the construction of the interstate system in the 1960s and as many as half are estimated to have exceeded their 25-year design life.

Recent fatigue failures of luminaire support structures in Washington and around the country have prompted concern about their fatigue resistance. Wind and wind induced phenomena can cause excessive vibration and damaging stress cycles at details that are sensitive to fatigue. Such details include welded pole-to-base plate connections, stiffened hand holes, anchor bolts, and mast arm-to-pole connections. Concerns regarding the fatigue life of luminaire, highway sign, and traffic signal support structures prompted the development of fatigue provisions and an update of non-fatigue related provision to load and resistance factor design in the American Association of State Highway and Transportation Officials (AASHTO) *2001 Standard Specifications for Structural Supports for Highway Signs, Luminaires, and Traffic Signals*. The update and new fatigue design provisions are based on research initiated by the National Cooperative Highway Research Project (NCHRP). While the revised design code improved the fatigue resistance of newly designed luminaire support structures, concerns remain about structures designed prior to the revised provisions.

The primary objectives of this research are to investigate the remaining fatigue life of in-service luminaire support structures in Washington and develop recommendations for their inspection and replacement. An extensive literature review and survey of luminaire pole details is used to identify potentially vulnerable details, select high impact specimens for laboratory fatigue testing, and develop recommendations for field inspection. Laboratory fatigue testing of

previously in-service poles with common details is performed to assess their likely remaining life and develop specific replacement recommendations. Finite element analysis of the luminaire pole base is also performed to verify the test data and perform a parametric study. Finally, the components of a reliability based framework for estimating the remaining life of support structures are described and necessary additional research is identified. The results of this research should inform and assist the luminaire support structure replacement decision process.

1.2 Scope of Work

There are five primary tasks that are included in this research:

1. Perform an extensive review of the literature pertaining to the fatigue life of luminaire support structures. The review focuses on research regarding: development of code provisions for fatigue design of luminaire support structures; aerodynamic phenomena that induce large stress cycles; fatigue testing of critical details resulting in a database summarizing test results; analytical models developed to assess dynamic characteristics of luminaire support structures; and flow of stresses through critical luminaire details.

2. Experimental fatigue testing of two characteristic, previously in-service luminaire support structures with a focus on the fatigue resistance of the CJP welded pole-to-base plate connections, stiffened hand hole connections, and anchor bolts.

3. Development of a finite element model to determine the dynamic characteristics of the specific luminaire pole and mast arm combination typically used by WSDOT and model the base of the pole to verify test data and perform a parametric study.

4. Summary of the future development and additional research efforts necessary to develop a probabilistic methodology for estimating the remaining life of luminaire support structures.

5. Development of recommendations for luminaire inspection and replacement.

1.3 Outline of Report

Chapter 2 consists of an extensive review of past research focused on fatigue resistance of luminaire support structures. Specific topics include the historical development of code provisions, fatigue testing of critical details including retrofit techniques, and finite element modeling of support structures to determine dynamic characteristics and stress concentration factors.

Chapter 3 describes the setup and objectives of the experimental program to assess the remaining life of selected previously in-service luminaire poles. This chapter presents the purpose of the testing program, selection of test specimens, a procedure to identify support structures in the WSDOT inventory susceptible to high fatigue stress ranges, test specimen dimensions, critical components of the testing setup, and the instrumentation scheme.

Chapter 4 discusses the experimental program and observations. Included are discussions of the initial quasi-static testing procedure, data acquisition system, experimental challenges, and experimental observations.

Chapter 5 is an analysis of the results of quasi-static and fatigue testing of the selected luminaire poles. The quasi-static test results are described through a summary of important strain gage readings, graphical presentation of the physical behavior described by the strain gages, and analysis of strain gage readings. The results of the fatigue testing include comparison of the fatigue data to AASHTO fatigue categories.

Chapter 6 describes the development of a finite element model of one of the test specimens. The quasi-static results are then compared to the finite element analysis and the parametric study is summarized. Dynamic characteristics of a typical WSDOT luminaire pole and mast arm combinations are also presented.

Chapter 7 describes the components of a framework for estimating the remaining life of luminaire support structures. Aspects of the framework including the development of representative 5-second turbulent wind time histories, application of time histories to a structural model to determine the number and magnitude of stress cycles, and development of remaining life predictions using the stress life equation and a linear damage accumulation law are discussed and research necessary to implement the framework is identified.

Chapter 8 presents a summary of experimental results, possible inspection procedures, retrofit and replacement prioritization, conclusions, and recommendations for additional research efforts.

Chapter 2 Literature Review

2.1 General

The following chapter presents a detailed review of the literature related to wind induced fatigue loading of support structures for highway signs, luminaires, and traffic signals. The literature review includes research related to the development of design code provisions for vibration and fatigue of support structures, development of fatigue loading models, experimental fatigue testing of specific details, and retrofit procedures for damaged structures. An emphasis will be placed on cantilevered luminaire support structures.

2.2 Background

The support structures considered in the literature review can be grouped into three broad categories; horizontal cantilevered, vertical cantilevered, and bridge-type structures. Horizontal cantilevered structures consist of a pole and a mast arm. The pole is the vertical element which is attached to a fixed base and the mast arm is the horizontal element cantilevered off of the pole as shown in Figure 2.1. Vertical cantilevered support structures consist of a single vertical element attached to a fixed base with the supported mass at the top. This type of support structure is generally used for high mast luminaire (HML) structures as shown in Figure 2.2. Bridge-type structures are typically used to support signs or signals and consist of two vertical elements attached to fixed bases with a horizontal element spanning between the two vertical elements. An example of a bridge-type sign support structure is shown in Figure 2.3.

In the 1980s and 1990s, an increasing number of problems with support structures were observed. The primary problems included excessive vibration and fatigue cracking at connections. Even more concerning was a survey of state transportation departments conducted in 1990 which indicated that incidences of sign and signal support structure failures was increasing (Federal Highway Administration, 1990). Another major concern was that many of the problematic structures were only in-service for a few years.

Figure 2.1: Horizontally cantilevered sign support structure (Dexter et al., 2006)

Figure 2.2: Vertical cantilevered HML support structure (Rios, 2007)

Figure 2.3: Bridge type sign support structure (DelGrego et al., 2003)

Problems were observed in newer structures for three reasons. The first reason was that the geometry of the newer structures was changing. Cantilevered structures with longer mast arms replaced bridge structures because they were more economical and safer to motorists. The longer mast arms resulted in structures that were highly flexible and lightly damped. The second reason was that new technologies were being utilized. One of these technologies was variable or changeable message signs (VMSs or CMSs). The VMSs used cantilevered structures to support heavy signs with large frontal areas. The large mass and frontal area of the VMSs made these structures susceptible to various wind induced phenomena. The third reason was that prior to 1994, the American Association of State Highway and Transportation Officials (AASHTO) *Standard Specifications for Structural Supports for Highway Signs, Luminaires, and Traffic Signals* (hereafter referred to as the *Specifications)* provided minimal guidance on design of support structures for vibration or fatigue.

2.3 NCHRP Research

Due to the number of problems observed in support structures for highway signs, luminaires, and traffic signals, AASHTO determined that the existing *Specifications* had to be revised.

Specifically, the existing chapters of the *1994 Specifications* (AASHTO, 1994) had to be updated and a new chapter had to be developed that pertained to design of support structures for vibration and fatigue. The National Cooperative Highway Research Program (NCHRP) initiated two extensive research projects aimed at improving the *1994 Specifications*; Project 17-10 and Project 10-38. Project 17-10 took place at the University of Alabama in Birmingham and was directed at improving the existing chapters of the *1994 Specifications*. The findings of Project 17-10 were presented in *NCHRP Report 411* (Calvert *et al.*, 1998) and the revisions to the *1994 Specifications* appear in the strength design provisions found in chapters 1-10 and 12-14 of the *2001 Specifications* (AASHTO, 2001). Since Project 17-10 is not directly related to vibration or fatigue of support structures, it will not be discussed in further detail.

Project 10-38 was initiated to develop a new chapter in the *Specifications* that would provide guidance for the design of support structures for vibration and fatigue. The findings of Project 10-38 were published in *NCHRP Report 412* (Dexter *et al.*, 1996) and the recommendations were incorporated into Chapter 11 of the *2001 Specifications*. However, Project 10-38 could not address all issues related to vibration and fatigue of support structures. To develop comprehensive *Specifications*, code provisions had to be developed based on limited experimental and analytical data. A second phase was initiated called Project 10-38 (2) to address these shortcomings. Project 10-38 (2) also looked at the impact of the *2001 Specifications* on the design of support structures when compared to previous *Specifications* and considered specific issues found by designers using the *2001 Specifications*. The findings of Project 10-38 (2) were published in *NCHRP Report 469* (Dexter and Ricker, 2002) and the recommended code provisions appeared in interim *Specifications* after 2001. The findings of the NCHRP projects are presented in the following section.

2.3.1 *NCHRP Report 412* (**Dexter *et al*., 1998**)

The NCHRP initiated Project 10-38 because the *1994 Specifications* and commentary were incomplete and unclear with regard to vibration and fatigue of cantilevered support structures. Prior to Project 10-38, there had been few studies investigating the response of cantilevered support structures to cyclic wind loads and the fatigue resistance of commonly used details in cantilevered support structures. Project 10-38 included a review of the existing literature, a survey of standard practice, wind tunnel testing, anchor bolt fatigue testing, and fatigue categorization of commonly used details. The findings and recommendations of Project 10-38

were published in *NCHRP Report 412: Fatigue-Resistant Design of Cantilevered Signal, Sign and Light Supports* (Dexter *et al.*, 1996).

Project 10-38 identified four wind induced phenomena that cause fatigue damage to cantilevered support structures; galloping, vortex shedding, natural wind gusts, and truck induced wind gusts. The susceptibility of different cantilevered support structures to each phenomenon was studied using static and dynamic finite element analysis and wind tunnel testing. Equations for equivalent static load ranges were then developed to approximate the dynamic response.

Galloping occurs when wind strikes a structure vibrating in the plane normal to the direction of wind flow causing the angle of attack of the wind to vary. When the angle of attack of the wind is aligned with the vibration of the structure, the vibration amplitude of the structure will increase. Galloping occurs in flexible and lightly damped structures with non-symmetric cross-sections subjected to steady, uniform wind flow. Galloping induced vibrations were observed in the wind tunnel in signal structures with mounted attachments but not in luminaires. Project 10-38 estimated the equivalent static vertical wind pressure range due to galloping to be:

$$P_G = 1000 * I_F \quad (Pa) \tag{2.1a}$$

$$P_G = 21 * I_F \qquad (psf) \tag{2.1b}$$

where P_G is the equivalent vertical shear pressure range due to galloping and I_F is the fatigue importance factor. These equations were adopted in the *2001 Specifications*.

Vortex shedding occurs when a steady uniform wind flow strikes a bluff body and vortices are shed in the wake of the structure on alternating sides. This is called the von Karman vortex street and an illustration is shown in Figure 2.4. Areas of low pressure follow each vortex causing a pressure differential in the plane normal to the wind direction. The pressure differential results in a force similar to a sinusoidal forcing function on the structure. If vortices are shed at a frequency that approaches the natural frequency of the structure, lock-in occurs. When lock-in occurs, the structure vibrates in resonance resulting in high amplitude vibrations and significant stress ranges at fatigue sensitive details. The equation for the critical wind velocity at which vortex shedding lock-in occurs is:

$$V_c = \frac{f_n d}{S_n} \qquad (for\ circular\ sections) \tag{2.2}$$

$$V_c = \frac{f_n b}{S_n} \qquad (for\ multisided\ sections) \qquad (2.3)$$

where f_n is the first natural frequency of the structure, d and b are the diameter or flat-to-flat width for circular and multisided sections respectively, and S_n is the Strouhal number. The Strouhal number for different cross-sections is shown in Table 2.1.
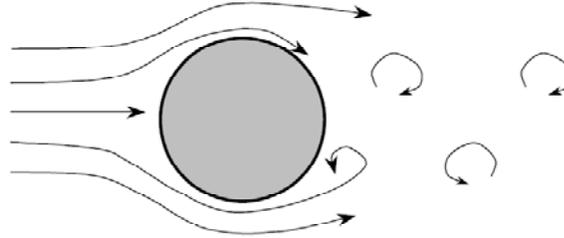
Figure 2.4: von Karman vortex street (Dexter et al., 1998)
Table 2.1: Strouhal number for different cross-sections (Adapted from Dexter et al., 1998)

Type of Section	Strouhal Number
Circular	0.18
Multisided	0.15
Square or Rectangular	0.11

Luminaires are the type of cantilevered structure most susceptible to vortex shedding because they are tall structures with symmetric cross-sections. Over the range of critical velocities at which lock-in will occur, the corresponding natural frequency is closest to that of luminaire structures. However, vortex shedding was not observed in luminaire structures with tapered poles. Vortex shedding only occurs at a given critical velocity and natural frequency for a specific diameter (for a circular section). Therefore, vortex shedding would only occur over a small part of the structure in a tapered section and would not cause the entire structure to vibrate. Vortex shedding does not occur in other structures because attachments are used which cause turbulence in the wake of the structure and disrupt the formation of vortices. The equivalent static horizontal pressure range recommended for use in the design of cantilevered structures for the effects of vortex shedding was determined to be:

$$P_{VS} = \frac{0.613 V_c^2 C_d I_F}{2\beta} \quad (Pa) \qquad (2.4a)$$

$$P_{VS} = \frac{0.00118 V_c^2 C_d I_F}{2\beta} \quad (psf) \qquad (2.4b)$$

where V_c is the critical wind velocity expressed in m/s or ft/s, C_d is the drag coefficient, and β is the damping ratio.

Natural wind gusts result from the random variation in velocity and direction of air flow. The stress levels resulting from natural wind gusts are a function of the velocity of the wind. However, natural wind gusts do the most damage when they occur at a frequency approaching the natural frequency of the structural element causing resonance. Low velocity natural gusts occurring at a frequency near the natural structural frequency can result in higher stress levels than higher velocity gusts at a frequency different from the natural structural frequency due to dynamic amplification. Natural wind gusts most often control the fatigue design of luminaire structures. Project 10-38 studied the effect of natural wind gusts on cantilevered support structures and proposed the following equation for the equivalent static natural wind gust pressure range when based on a yearly mean wind speed of 5 m/s (11.25 mph):

$$P_{NW} = 250 C_d I_F \qquad (Pa) \qquad\qquad (2.5a)$$

$$P_{NW} = 5.2 C_d I_F \qquad (psf) \qquad\qquad (2.5b)$$

If more detailed natural wind gust data is available, the following equations can be used:

$$P_{NW} = 250 C_d \left(\frac{V_{mean}^2}{25}\right) I_F \quad (Pa) \qquad\qquad (2.6a)$$

$$P_{NW} = 5.2 C_d \left(\frac{V_{mean}^2}{125}\right) I_F \quad (psf) \qquad\qquad (2.6b)$$

where V_{mean} is the yearly mean wind speed in m/s or mph..

Truck gusts are wind loads on a structure that result from a truck passing underneath. The pressure is applied to the projected area of the structure in a plane parallel to the ground. Truck gust pressures also occur in a plane normal to the direction of the moving truck. However, this pressure is neglected because it typically has a smaller magnitude than the natural wind gust pressure. Based on studies of truck gust pressures, Project 10-38 proposed the following equations to approximate the equivalent static pressure range due to truck gusts:

$$P_{TG} = 1760 C_d \qquad (Pa) \qquad\qquad (2.7a)$$

$$P_{TG} = 36.6 C_d \qquad (psf) \qquad\qquad (2.7b)$$

Since luminaire structures have minimal exposed area in the plane parallel to the ground, truck gusts are not considered for fatigue design.

Project 10-38 included an extensive anchor bolt fatigue testing program. The purpose of the testing was to determine the lower bound constant amplitude fatigue limit (CAFL) of snug-tightened and fully-tightened anchor bolts loaded in axial tension. Also, the effects of bolt misalignment, maximum stress value, type of thread fabrication, and bolt grade on the fatigue resistance were considered. Table 2.2 shows the four different bolt types used in the fatigue

testing. Based on the test results, the following conclusions were reached about the fatigue resistance of anchor bolts:

1. In the finite life region, the Category E' fatigue curve should be used for the design of snug-tight anchor bolts and the Category E fatigue curve should be used for fully-tightened anchor bolts.

2. In the infinite life region, the CAFL corresponding to Category D should be used for both snug-tightened and fully-tightened anchor bolts. For design purposes, it is recommended that anchor bolts should be installed in the fully-tightened condition whenever possible.

3. Bending stresses of bolts misaligned up to 1:40 do not need to be considered in anchor bolt stress calculations as long as firm contact exists between the anchor bolt nut and base plate.

4. The maximum stress in the anchor bolts greatly influences fatigue strength. A decrease in the maximum stress below 60% of the yield strength improves the apparent fatigue strength and CAFL.

5. Anchor bolts fabricated with rolled threads had a higher fatigue resistance than those fabricated with cut threads when the magnitude of the maximum stress was low (approximately 30% of the minimum yield strength of the material).

6. Grade 55 and Grade 105 bolts show identical fatigue resistance when tested to the same maximum stress.

7. Grade 55 anchor bolts exhibit slighter higher fatigue resistance than Grade 105 when the ratio of maximum stress to yield stress for the two bolt grades is the same.

Project 10-38 also included static load testing to determine the relationship between support structure forces and anchor bolt stress. For various Moment:Torsion:Shear ratios, the flexure formula can be used to compute anchor bolt stresses if the base plate is stiff enough to prevent prying action. This applies for both straight and misaligned bolts. Also, if the exposed length of the bolt does not exceed 1 in., the bending stresses caused by horizontal shear forces and torsional moments may be ignored. If the exposed bolt length is greater than one bolt diameter, a fixed-fixed beam model for the bolt is recommended for computing bending stresses.

Table 2.2: Specimens used in anchor bolt fatigue testing (adapted from Dexter et al., 1998)

Specimen Series	Material Grade	Nominal Diameter (in)	Thread Series	Thread Type
H55	55	1.5	6UNC	Cut
F55	55	1.5	6UNC	Rolled
H105	105	1.5	6UNC	Cut
F105	105	1.5	6UNC	Rolled

The *1994 Specifications* recommended that the *AASHTO LRFD Bridge Design Specifications* (AASHTO, 1994) be used for cantilevered support structures designed for infinite life. However, many of the details used in cantilevered support structures differ substantially from those used in bridge structures. Therefore, Project 10-38 included a fatigue categorization of the standard details used in cantilevered support structures.

The fatigue categorization followed a procedure similar to that used in the *LRFD Bridge Design Specifications* and the *American Welding Society Specifications*. A nominal stress approach is used and the details are grouped into categories based on their relative fatigue resistance. A nominal stress approach means that the stress range used in the S-N curve is based on the nominal stress in the detail. The fatigue categories are shown in Table 2.3 along with the CAFL. Most of the details used in cantilevered support structures were not tested. Therefore, Project 10-38 assigned fatigue categories based on general understanding of fatigue behavior, prior research that led to fatigue curves in other specifications, structural failures resulting from fatigue damage, and engineering judgment. The resulting categorizations are found in Chapter 11 of the *2001 Specifications*.

Table 2.3: Fatigue detail categories and values of CAFL (Adapted from Dexter et al., 1998)

Detail Category	Steel CAFL (ksi)	Aluminum CAFL (ksi)
A	23.9	10.2
B	16.0	5.9
B'	12.0	4.6
C	10.0	4.1
D	7.0	2.5
E	4.5	1.9
E'	2.6	1.0
ET	1.2	0.4

Project 10-38 proposed importance factors for fatigue for each type of cantilevered support structure subjected to each type of dynamic wind load. The importance factors are reduction factors for the static load ranges that account for the conservative load ranges and allow the use of engineering judgment when applying those load ranges. Support structures were grouped into three categories based on importance as shown in Table 2.4. Importance factors were then assigned based on importance category, structure type, and dynamic wind load type as shown in Table 2.5. The importance factors were calibrated so that Category III structures designed per the proposed requirement have a reliability similar to a structure designed using the *1994 Specifications*.

Table 2.4: Definition of Importance Categories (Adapted from Dexter et al., 1998)

Importance Category	Definition
I	Critical cantilevered support structures installed on major highways
II	Other cantilevered support structures installed on major highways and all cantilevered support structures installed on secondary highways
III	Cantilevered support structures installed at low-risk locations

Table 2.5: Importance Factors for Fatigue (Adapted from Dexter et al., 1998)

Category		Importance Factor			
			Vortex	Natural	Truck
		Galloping	Shedding	Wind Gusts	Gusts
I	Sign	1.00	x	1.00	1.00
	Signal	1.00	x	1.00	1.00
	Luminaire	x	1.00	1.00	x
II	Sign	0.72	x	0.85	0.90
	Signal	0.64	x	0.77	0.84
	Luminaire	x	0.66	0.74	x
III	Sign	0.43	x	0.69	0.79
	Signal	0.28	x	0.53	0.67
	Luminaire	x	0.31	0.48	x

Note: x-Structure is not susceptible to this type of loading.

2.3.2 *NCHRP Report 469* (Dexter *et al.*, 2002)

Following the completion of Project 10-38, specific research areas were identified that would require more study. Those topics were addressed in the second project phase called Project 10-38 (2). Project 10-38 (2) addressed the following areas; verification of static pressure ranges for wind induced dynamic loads developed in Project 10-38 and assessment of design procedures developed in Project 10-38. The findings and recommendations from Project 10-38 (2) were published in *NCHRP Report 469: Fatigue-Resistant Design of Signal, Sign, and Light Supports*.

Project 10-38 concluded that the vortex shedding specifications only applied to symmetric poles that were tapered less than 0.14 in/ft. In structures that had a greater taper, the critical velocity at which lock-in would occur as predicted by Equation 2.2 or Equation 2.3 would be less than 5 m/s (11mph). At these critical velocities there would be insufficient energy to excite the structure. Also, lock-in can only occur over a critical range of diameters. Thus, in highly tapered poles, the length along which lock-in would occur would be short enough that the resulting stresses would not control the design. However, video provided by a luminaire manufacturer to the Project 10-38 (2) research team proved this argument to be incorrect.

The video showed a luminaire vibrating in double curvature with peak displacement about equal to the pole diameter. Vibration in double curvature means lock-in is occurring at a higher fundamental frequency and higher critical wind velocity. The critical velocity is high enough that when the equivalent static pressure is applied over a short length, it can still control the fatigue design. The *2001 Specifications* do not address vortex shedding lock-in at higher modes of vibration. Project 10-38 (2) recommended that all structures regardless of taper be checked for vortex shedding and that the equivalent static pressure should be applied over the range of the structure in which the diameter is within plus or minus 10% of the critical diameter.

Prior to Project 10-38 (2), it was thought that increasing the support structure stiffness was an effective way of preventing vortex shedding lock-in because it increased the natural frequency. However, since Project 10-38 (2) demonstrated that vortex shedding lock-in could occur in any of the first three modes of vibration, stiffening the structure would not prevent this phenomenon from occurring, but would decrease the stress ranges in critical details.

Based on an evaluation of the *2001 Specifications* and the instrumentation of a VMS in New Jersey, Project 10-38 (2) recommended changes to the provisions regarding truck induced wind gusts. Project 10-38 recommended applying the truck induced wind gust pressure over the entire length of a sign. However, more than one truck passing under a sign simultaneously is a rare occurrence. Therefore, Project 10-38 (2) recommended that the pressure only be applied to a 12 foot length of the sign. Project 10-38 (2) also recommended that the equation for the equivalent static truck gust pressure be changed to the following:

$$P_{TG} = 900C_d \qquad (Pa) \qquad\qquad (2.8a)$$
$$P_{TG} = 18.8C_d \qquad (psf) \qquad\qquad (2.8b)$$

The change was recommended because the previous equation was based on limited data. The newly proposed equations were based on data from an instrumented VMS in New Jersey that showed that the loads on the structure were much lower than those predicted by the Project 10-38 equation. Also, the previous equation was calibrated for an incorrect drag coefficient of 1.45. The new equation was calibrated to the correct drag coefficient of 1.7, which was used in the *2001 Specifications*.

Project 10-38 (2) determined that no change was needed to the equations for equivalent static pressure range due to galloping and natural wind gusts. Data from a test at Texas Tech University on a full scale signal structure showed that the previously proposed galloping equations were reasonable. Although no change was proposed to the equation, tests results showed that vibration mitigation techniques could reduce galloping induced vibrations by up to 35%. Therefore, Project 10-38 (2) recommended that the importance category for fatigue could be reduced from I to II if a mitigation technique was used. The three mitigation techniques were increasing structural stiffness, adding damping plates that alter aerodynamic properties of the structure, and using mechanical damping devices. Project 10-38 (2) also included a spectral finite element analysis of VMSs to verify the accuracy of the natural wind gust equation proposed in Project 10-38. The equation was deemed to be reasonable and no new recommendations were made.

When evaluating the recommendations from Project 10-38, Project 10-38 (2) determined that structures designed using the fatigue provisions performed as expected. Structures that were designed conservatively using previous codes were found to be adequate. Similarly, signal structures that had failed in the field did not meet the fatigue requirements of the *2001 Specifications*. Finally, design calculations performed in Project 10-38 (2) showed that it was more cost-effective to improve the connection detail than to increase the member size when a structure had to be redesigned to meet the fatigue provisions of the *2001 Specifications*.

2.3.3 *NCHRP Report 494* (Fouad, 2003)

NCHRP Project 17-10 was initiated to update all the non fatigue and vibration related chapters of the *1994 Specifications*. Project 17-10 (2) was the second phase of this project and was initiated to update the *1994 Specifications* to load and resistance factor format and to refine the provisions based on current research results. The findings of Project 17-10 (2) were published

in *NCHRP Report 494: Structural Supports for Highway Signs, Luminaires, and Traffic Signals*. Projects 17-10 and 17-10 (2) have not been discussed in detail because they do not relate directly to fatigue of cantilevered support structures. However, a change proposed by Project 17-10 (2) has implications on fatigue design. Project 17-10 (2) proposed a new equation for the drag coefficient of multisided tapered poles when the cross-section approaches a circular section. Multisided tapered poles are commonly used in luminaire and traffic signal support structures and the drag coefficient is used in the equations for the equivalent static pressure ranges due to vortex shedding, natural wind gusts, and truck gusts. The follow equations are proposed for the drag coefficient:

$$C_d = C_{dm} \ for \ r \leq r_m \qquad (2.9)$$

$$C_d = C_{dr} + (C_{dm} - C_{dr}) \frac{(r - r_r)}{(r_m - r_r)} \ for \ r_m < r < r_r \qquad (2.10)$$

$$C_d = C_{dr} \ for \ r \geq r_r \qquad (2.11)$$

where C_d is the drag coefficient to be used in the design, C_{dm} is the drag coefficient for the multisided section, C_{dr} is the drag coefficient for the round section, r is the ratio of the corner radius to the radius of the inscribed circle for the multisided cross-section, r_m is the ratio of the corner radius to the radius of the inscribed circle where the cross-section is considered multisided, and r_r is the ratio of the corner radius to the radius of the inscribed circle where the cross-section is considered round.

2.4 Experimental Fatigue Testing

The following section summarizes the results and conclusions of research efforts that performed fatigue testing of sensitive connection details in luminaires and other cantilevered support structures. Some of these research projects also included analytical work which will be discussed in this section instead of in Section 2.5. A summary of all the fatigue testing data can be found in Appendix 1.

2.4.1 Miki et al. (1981)

Miki et al. (1981) performed fatigue testing of socket connections for the California Department of Transportation and found that unequal leg fillet welds had greater fatigue resistance than equal leg fillet welds when the long leg is along the length of the tube. The unequal leg fillet welds were found to have a fatigue resistance slightly above Category E' and the equal leg fillet

welds had a fatigue resistance slightly below Category E'. The fatigue test data is shown in Figure 2.5.
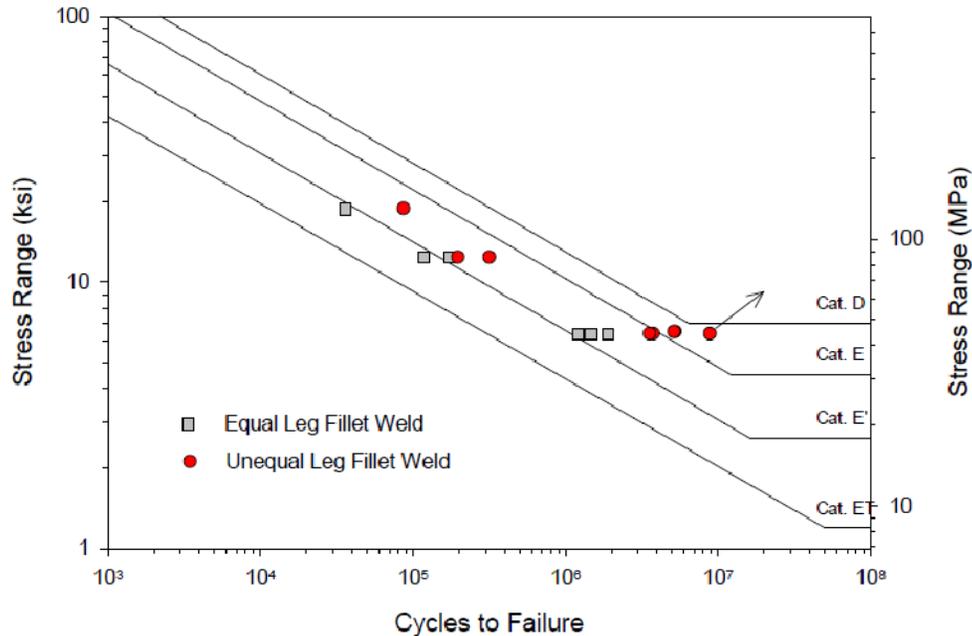
Figure 2.5: Fatigue test data of unequal and equal leg fillet welded socket connections (adapted from Dexter et al., 2006)

2.4.2 Johns (1998)

Johns (1998) studied the dynamic characteristics and fatigue resistance of aluminum luminaire support structures with shoe base pole socket connections. The research was in response to the failure of multiple aluminum luminaire supports on Route 147 in southern New Jersey. Finite element modeling and pull back testing were performed on both a cantilevered luminaire support structure and a straight luminaire support structure to determine the dynamic characteristics. Full scale experimental fatigue testing was performed on 6 cantilevered and 6 straight luminaire structures. Drawings of the cantilevered support structure and the straight support structure are shown in Figure 2.6 and Figure 2.7 respectively. The following is a brief synopsis of the findings and recommendations for improved fatigue performance.

Pull back tests were performed on both cantilevered and straight luminaire support structures. The stiffness of the cantilevered luminaire support structure was determined experimentally to

be 3.6 N/mm (20.6 lb/in) and analytically to be 3.4 N/mm (19.4 lb/in). The natural frequency for the second mode of vibration in the cantilevered support structure was determined experimentally to be 1.02 cycles/s and analytically to be 1.04 cycles/s. The damping ratio was determined experimentally to be 0.40% of critical. The second mode of vibration in a cantilevered luminaire support structure corresponds to in-plane vibration of the structure (tip of luminaire translates perpendicular to the direction of traffic). The stiffness of the straight luminaire support structure was determined analytically to be 3.6 N/mm (20.6 lb/in). The natural frequency for the first two modes of vibration, which are both cantilever bending with the difference being in-plane versus out-of-plane motion, were determined experimentally to be 0.74 cycles/s and analytically to be 0.85 cycles/s. The damping ratio was determined experimentally to be 1% of critical.

Johns (1998) performed full scale fatigue testing on 12 aluminum luminaire support structures. Six cantilevered support structures and six straight support structures were tested. All six straight support structures and one cantilevered support structure were mounted on a transformer base. The other five cantilevered support structures were bolted directly to the concrete foundation. When the transformer base was used, the access hole was oriented such that it would be subjected to maximum bending stresses.

Three of the seven transformer bases tested developed cracks. One specimen developed cracks at the top corner of the transformer base access hole where a notch and a sharp point were discovered on the edge of the access hole, which most likely caused the crack initiation. A second cracked transformer base specimen had cracks initiate in two places. One crack initiated in the transformer base wall opposite the access hole where it was seen afterwards that the wall was noticeably thinner due to excessive grinding. The other crack initiated at the back of the finger tabs in opposite corners of the base, which were used to bolt the transformer base to the foundation. The third cracked transformer base had cracking initiate in one of the long slotted holes that the shoe base bolts into. The tests were continued despite the transformer base cracking and the fatigue data for the transformer base was not analyzed. However, the importance of high quality fabrication in fatigue sensitive details was apparent from these tests.

Seven of the pole specimens tested developed cracking in the poles themselves or in the pole-to-shoe base welds. Semi-elliptical cracks developed at the weld toe of the pole-to-shoe base connection and propagated through the pole thickness around the circumference in four of the

seven specimens. These cracks were caused by bending stresses and the fatigue data for these specimens as well as the tests that did not fail (shown as run-outs) are plotted in Figure 2.8. The lower bound of the 97.5% confidence interval plots just below the Category E line in the infinite life region and between Category D and E in the finite life region. The other three specimens failed due to cracks that developed at the weld root. These cracks were caused by shear stresses in the weld that were aggravated by poor welding practices that resulted in effective weld sizes which were less than those specified. The fatigue data for the cracks that initiated at the weld toe are shown in Figure 2.9, where the lower bound of the 97.5% confidence interval is the Category F line used in the *Steel Design Handbook* (Dexter and Fisher, 1997).
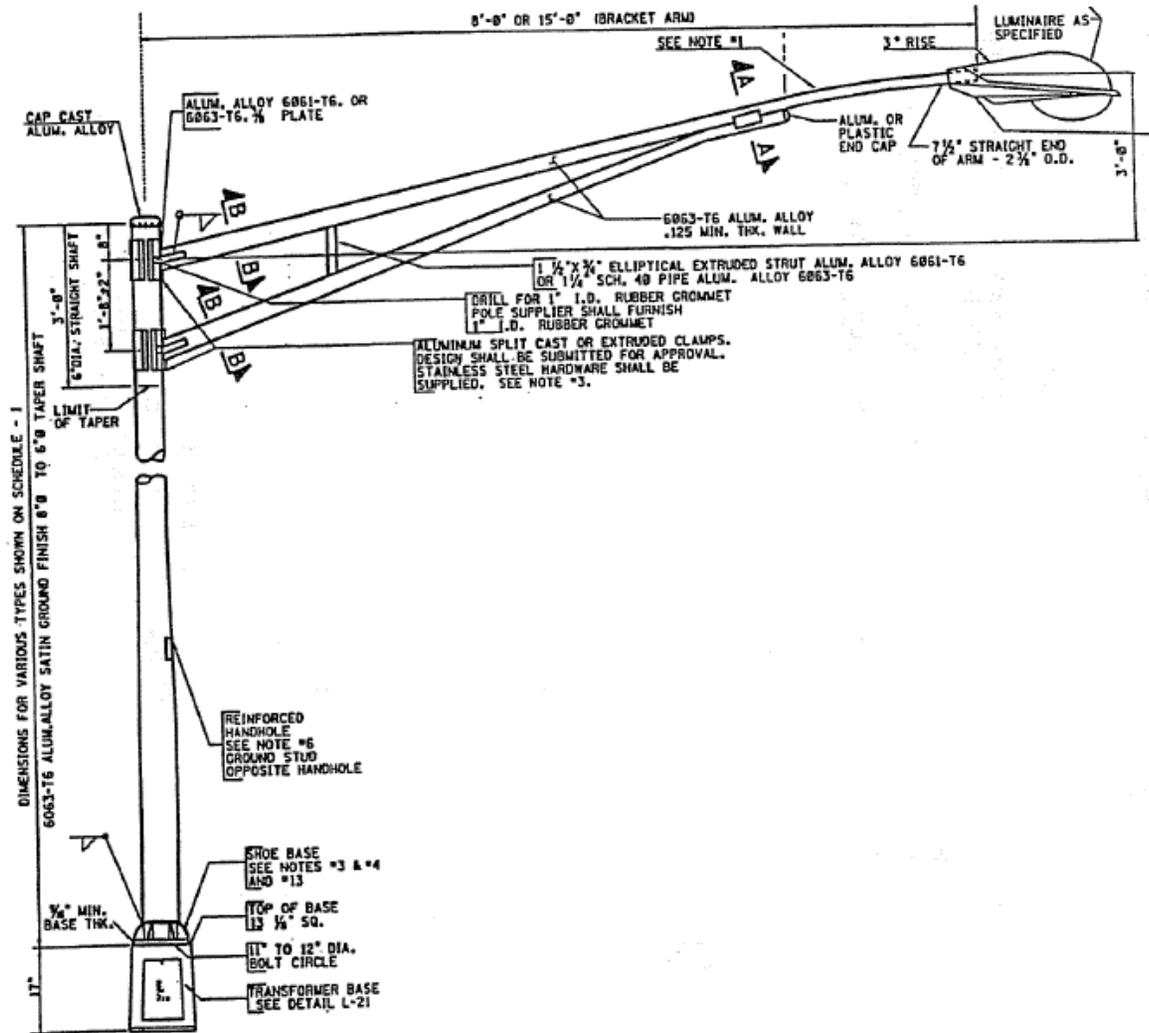
Figure 2.6: Drawing of cantilevered luminaire support structure (Johns, 1998)
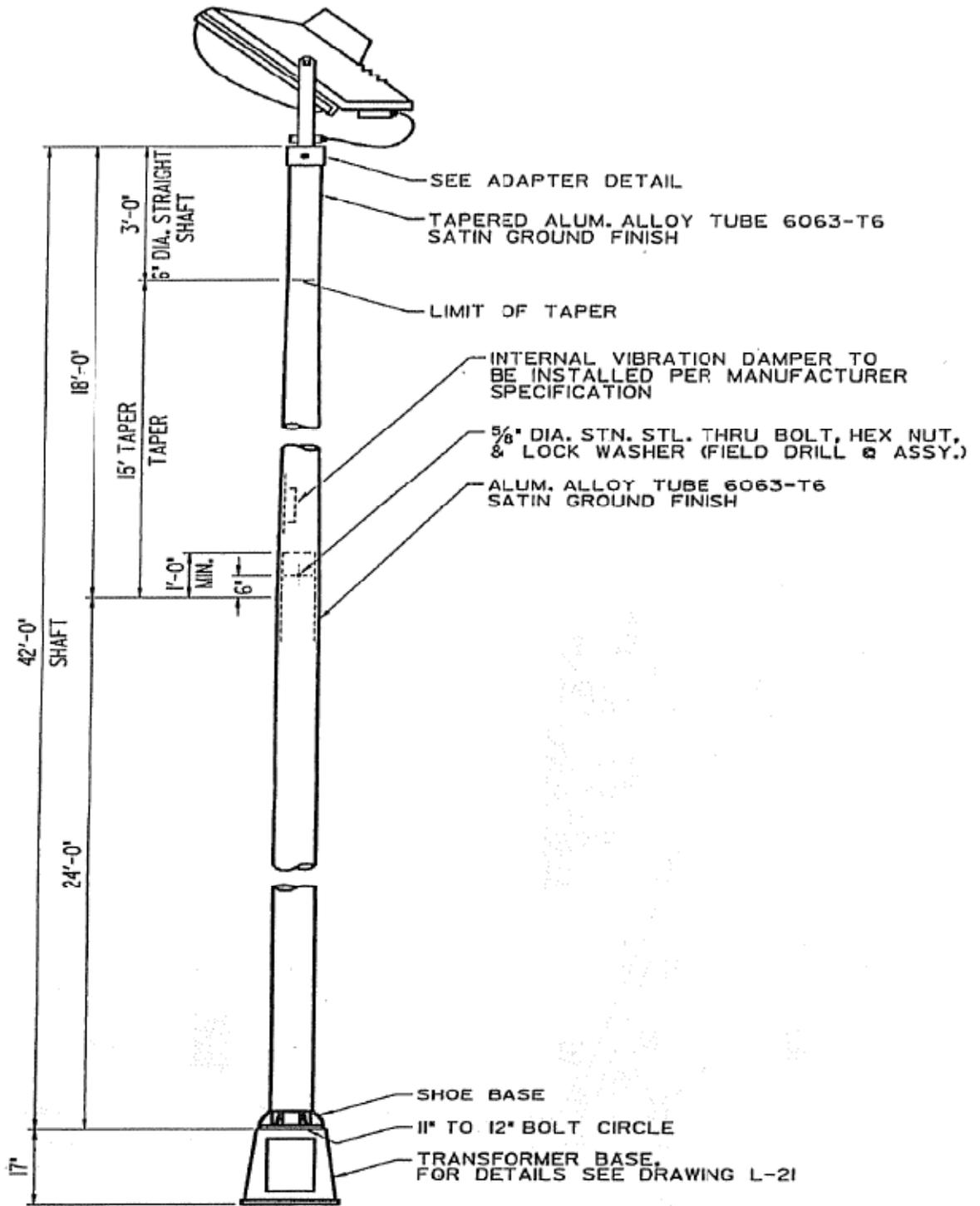
Figure 2.7: Drawing of straight luminaire support structure (Johns, 1998)

A few recommendations were made to improve the fatigue resistance of the shoe base connection: (i) the inside top edge of the shoe base could be beveled or an unequal leg fillet weld could be used to increase the distance of the weld leg along the pole resulting in lower shear stresses; (ii) the pole thickness and/or diameter could be increased to increase the section modulus of the pole cross-section and decrease the stress ranges in the wall of the pole; and (iii) care should be taken in the fabrication process to eliminate potential defects that can initiate fatigue cracks.
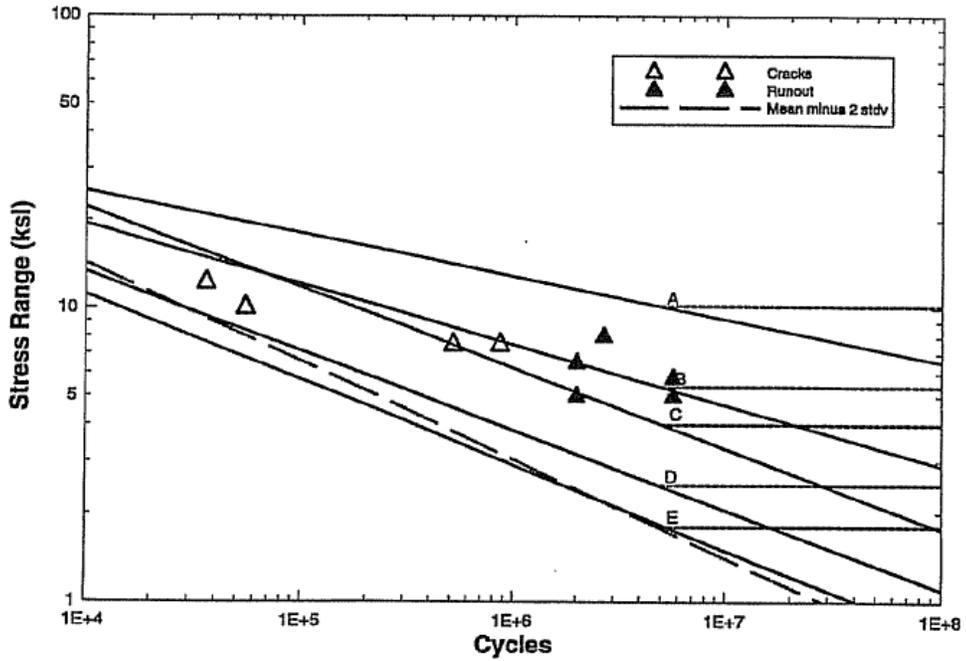
Figure 2.8: S-N plot for cracks through pole (Johns, 1998)
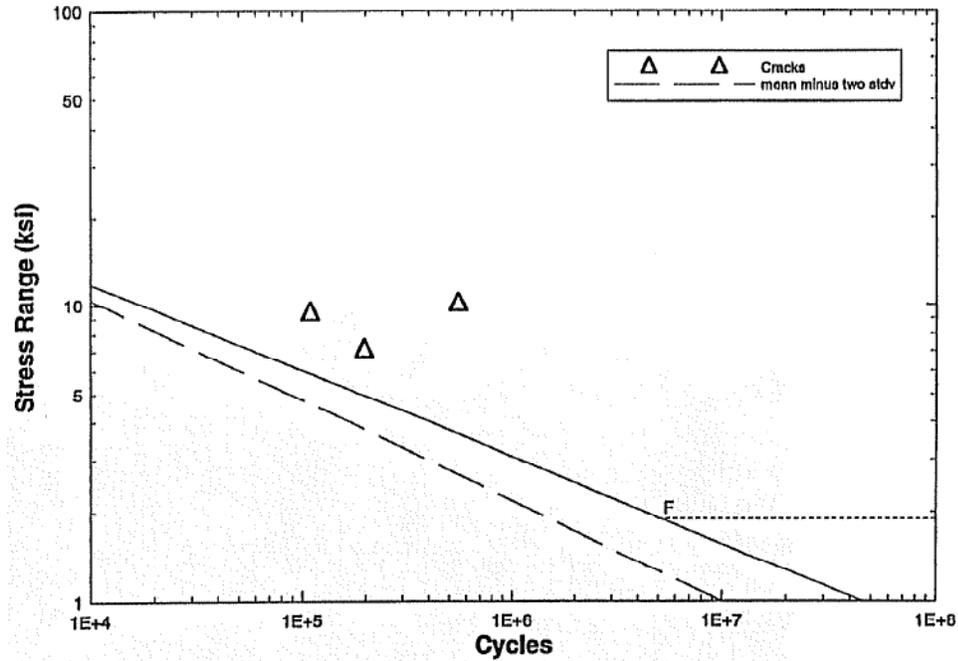
Figure 2.9: S-N plot for cracks that initiated at the weld root (Johns, 1998)

2.4.3 Gilani and Whittaker (2000b)

This project investigated the fatigue life of support structures for Changeable Message Signs (CMSs) or Variable Message Signs (VMSs), which are electronic signs that provide information to motorists. CMSs weigh about 2.5 kips and are typically supported by a cantilever inverted "L" structure as shown in Figure 2.10. Research into CMS fatigue behavior was initiated in response to the high cycle fatigue failure of a CMS support structure in southern California. This research included an experimental component (Gilani and Whittaker, 2000b) and an analytical component (Gilani and Whittaker, 2000a), which will be discussed in Section 2.5.
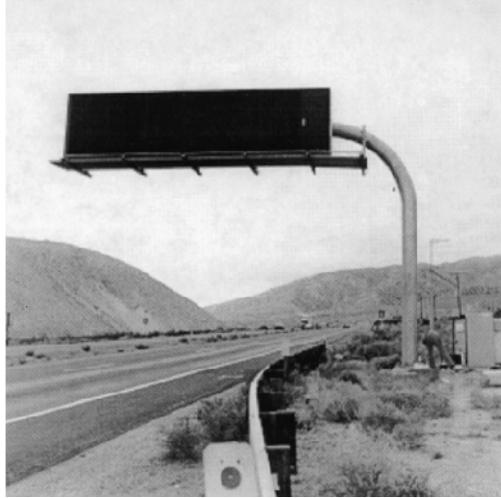
Figure 2.10: CMS in California (Gilani and Whittaker, 2000a)

Gilani and Whittaker (2000b) conducted a laboratory testing program as part of an extensive research project on CMS support structures. The laboratory test program consisted of 6 specimens: specimen AB1 was an as-built pole structure similar to that used for CMSs in the state of California; specimens MA1, MA2, and MA3 were mast arms taken from full CMS structures prepared for field installation; and specimens GR1 and CIP1 were pole structures that had pole-to-base plate connections retrofitted with gusset plates and incased in concrete respectively. High cycle fatigue loading was applied to each specimen to assess the fatigue life of the tube-to-transverse plate connections and determine the effectiveness of two retrofit procedures. A unidirectional load was applied to the tip of the pole and mast arm structures in the horizontal plane using a servohydraulic actuator and the test was run in displacement control.

Complete joint penetration (CJP) welded details were typically used for pole-to-base plate and mast arm-to-pole connections in CMSs. This detail was classified as a Category E' fatigue detail in *NCHRP Report 412* for two reasons: notches tend to form at the bottom of these details that can initiate cracks and the connection is difficult to inspect. Both visual and ultrasonic inspection of CJP pole-to-transverse plate connections can be difficult. The weld root is not visible if the backing ring is not removed, which is not typically done. Also, the backing ring can reflect ultrasonic waves and distort ultrasonic inspection readings.

Specimen AB1 was a cantilevered pole structure with a CJP welded pole-to-base plate connection. A 102 mm tall X 25 mm thick (4 in. X 1 in.) backing ring was tack welded to the

base plate. The pole had a 12.77 mm (½ in.) wall thickness and a 102 mm wide X 155 mm tall (4 in. X 6 in) conduit hole 457 mm (18 in.) above the base plate. The conduit hole was flame cut and the corners were not rounded. A stiffening tube was fillet welded to the perimeter of the conduit hole. The base plate was 70 mm (2.75 in.) thick and was bolted to the foundation with eight high strength anchor bolts. A drawing of the CJP welded pole-to-base plate connection is shown in Figure 2.11.
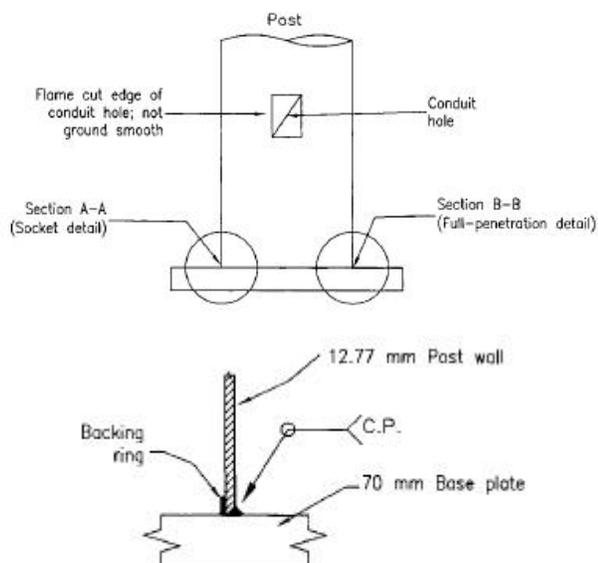
Figure 2.11: CJP welded pole-to-base plate detail (Gilani and Whittaker, 2000b)

The specimen was cycled at a nominal stress range of 81 MPa (11.8 ksi) about zero mean stress at the extreme tension fiber just above the tube-to-transverse plate weld. Visible cracks appeared after 1 million cycles at the corners of the conduit hole and by 1.2 million cycles the cracks propagated through the wall thickness and no longer had any tensile resistance as shown in Figure 2.12. The test continued until the specimen reached the Type I failure mode due to cracking around the conduit hole. The Type I failure mode was defined as a reduction in resistance of 90% of the maximum resistance at the target displacement. Since the test was run in displacement control, the Type I failure mode refers to an actuator load reading of 90% of the maximum (initial) actuator load reading at the test (actuator) displacement. The Type II failure mode was defined as propagation of cracks in the pole-to-base plate connection or mast arm-to-flange plate connection. Type I failure was reached at 2,700,000 cycles at which point numerous repairs were made to the structure and testing continued. The following repairs were made to the conduit hole:

26

1. the stiffening tube around the conduit hole was removed and the conduit hole corners were rounded and ground smooth;

2. 6 mm (¼ in.) thick holes were drilled at the ends of the crack to prevent further growth;

3. a V-shaped notch was cut along the entire length of all cracks with the short end of the notch on the inside of the pole;

4. a backing ring was tack welded to the inside of the pole along the length of the crack and the cutout was filled with weld material;

5. the repaired weld was ground flush with the outside of the pole;

6. a 305 mm X 610 mm X 16 mm (12 in. X 24 in. X 0.625 in.) patch plate was placed over the conduit hole and attached to the outside of the pole with a continuous fillet weld.
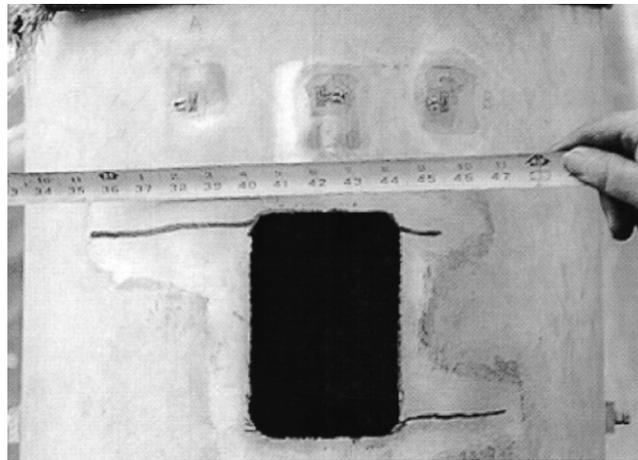
Figure 2.12: Cracking at the corners of the conduit hole in specimen AB1 (Gilani and Whittaker, 2000b)

When the testing was continued, new cracks appeared in the patch plate-to-pole fillet weld at 1.7 and 2.0 million cycles after the repairs were made. These cracks were filled with weld material and testing continued. By 2.1 million cycles after the repairs, cracks appeared in the heat affected zone (HAZ) of the pole-to-base plate connection. At 2.4 million cycles the cracks in the patch plate-to-pole fillet weld no longer had any tensile resistance. The test was eventually terminated at 2.7 million cycles when the resistance of the pole decreased to 90% of the maximum resistance at the target displacement (Type I Failure).

Figure 2.13 shows the longitudinal stress distribution at the bottom of the pole along the center of the conduit hole and the side opposite the conduit hole. Stresses along those lines from the finite element analysis performed by Gilani and Whittaker (2000a), which will be discussed in Section 2.5 are also included. The plot shows that the finite element model represented the stress distribution around the conduit hole effectively. Figure 2.14 shows the stress range along

line A at 32 mm (1.25 in.) and 686 mm (27 in.) above the base plate during the test. Little variation is seen in the stress range through the first million cycles. However, once cracks start to appear at the corner of the conduit hole the stress ranges decrease as the tensile resistance is reduced. The stress ranges rise at 1.2 million cycles after the repairs are made. At about 2.4 million cycles, the stress range along Line A at 32 mm (1.25 in.) above the base plate drops to nearly zero as cracking starts to occur in the HAZ of the CJP weld at the pole-to-base plate connection.
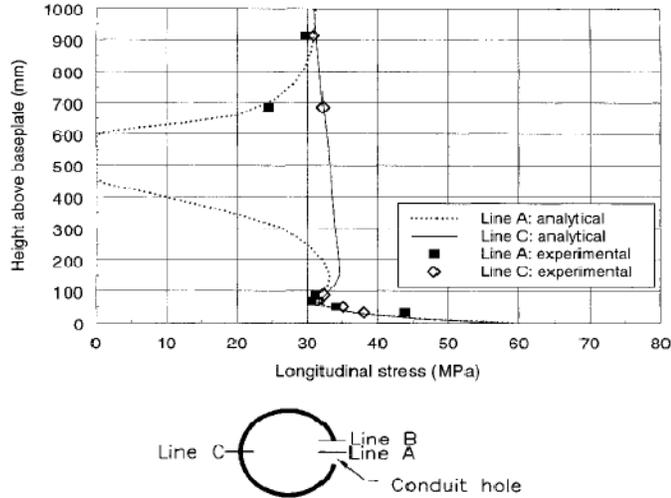
Figure 2.13: Longitudinal stress distribution at base of test pole (Gilani and Whittaker, 2000b)
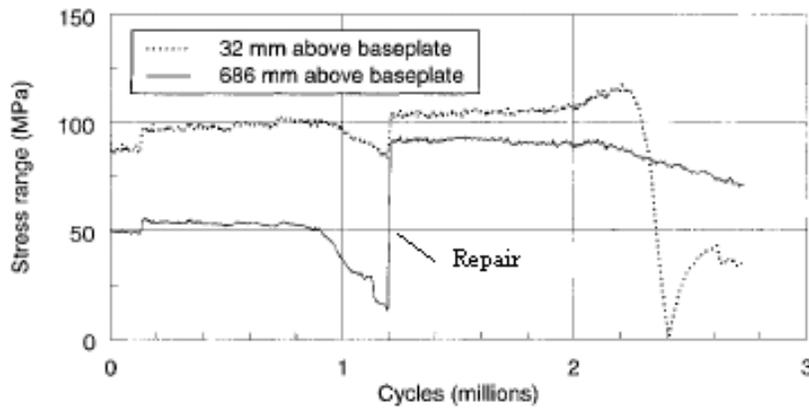
Figure 2.14: Change in stress range along line A throughout the duration of the test (Adapted from Gilani and Whittaker, 2000b)

The mast arm specimens were made from 457 mm (18 in.) diameter steel tubes with 9.5 mm (3/8 in.) wall thickness and had a 64 mm (2.5 in.) diameter conduit hole. The mast arms were

CJP welded with a backing ring to an annular flange plate with an inside diameter of 406 mm (16 in.), an outside diameter of 610 mm (24 in.), and thickness of 35 mm (1.38 in). The annular flange plates were slightly distorted due to welding to the test frame extension piece. The plate was flattened when bolted to the test frame and residual strains as high as two times the yield strain were recorded in the plate near the CJP weld. Ultrasonic testing was used to check the CJP welded mast arm-to-flange plate connections. Three flaws were detected in specimen MA1 and none were found in the other two specimens.

The mast arms were cycled at a stress range of 69 MPa (10 ksi). A crack was detected at 1.5 million cycles in the HAZ of specimen MA1 at the CJP welded connection next to one of the flaws found during initial ultrasonic testing. This was defined as a Type II failure mode. Testing continued until 2.8 million cycles when the resistance of specimen MA1 had dropped to 90% of the maximum resistance at the target displacement (Type I Failure). Specimens MA2 and MA3 were cycled 4 million times until the testing stopped. At this point, neither specimen MA2 nor MA3 had cracking in the mast arm-to-flange plate connection although some cracking was observed in MA3 around the conduit hole. Also, the resistance of specimens MA2 and MA3 never decreased below 90% of the maximum support structure resistance. Therefore, neither specimen reached the Type I or Type II failure mode.

The pole-to-base plate connection of specimen GR1 was a socket connection with eight 14 mm (0.56 in.) thick gusset stiffeners. The triangular gusset stiffeners were 102 mm (4 in.) wide at the base plate by 152 mm (6 in.) tall and fillet welded to the base plate and to the pole. A detail of this connection is shown in Figure 2.15. The specimen was cycled about a mean stress of 90 MPa (13 ksi) to simulate dead load and the stress range was 86 MPa (12.4 ksi). Two cracks propagated from the conduit hole at 60,000 cycles and eventually propagated into the gusset-to-pole welds. By 800,000 cycles, the resistance had dropped below 90% of the maximum resistance at the target displacement (Type I Failure). The poor performance of the gusset stiffened connection was attributed to two factors: (i) the location and size of the conduit hole and gusset stiffeners produced high stress concentrations below the conduit hole and (ii) large residual stresses resulted from the flame cutting of the conduit hole.
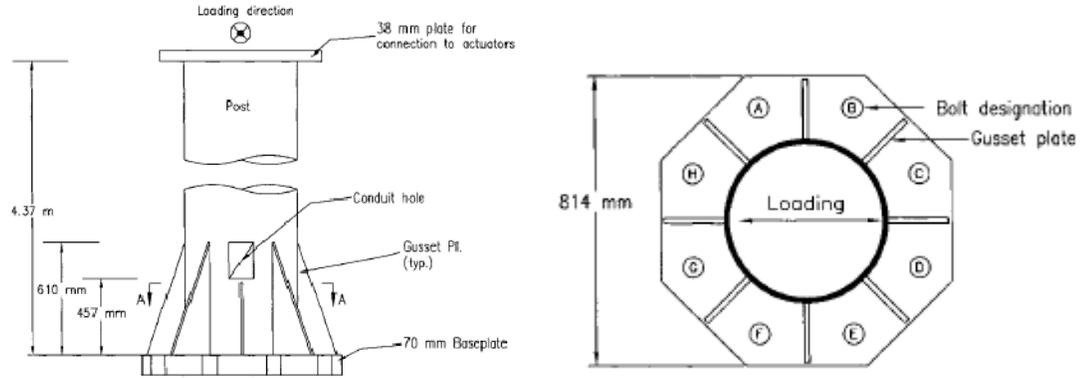
Figure 2.15: Profile and plan of gusset stiffened socket connection (Gilani and Whittaker, 2000b)

Specimen CIP1 had a 1.83 m (72 in.) tall by 1067 mm (42 in.) diameter concrete jacket with 16 21 mm (0.83 in.) diameter vertical bars grouted into the foundation as shown in Figure 2.16. The jacket was meant to increase the section modulus at the pole-to-base plate connection, increase the structural stiffness, and increase the mechanical damping. A pull back test was performed to determine the change in dynamic properties. The damping ratio increased from 0.3 to 1.5 percent of critical and the stiffness increased from 2.5 kN/mm (14 kips/in.) to 6.1 kN/mm (35 kips/ in.). Since the test structure only included the pole, the increase in damping ratio and stiffness would not be as high in an actual CMS with a concrete jacket. In the fatigue testing, the jacket effectively protected the CJP welded pole-to-base plate connection by reducing the stresses at the toe of the weld. After 4.5 million cycles no cracking was observed in the pole and the stress ranges were 20 times less than those in the non-retrofitted structure.

457 mm steel post

Drill and bond 16-22 mm rebar in 35 mm x 381 mm holes,

13 mm rebar @ 102 mm hoop

1.83 m

102x152 mm conduit hole

A

8-57 mm anchor bolts

Pedestal

Foundation

686 mm

1,067 mm OD annular concrete jacket

16-22 mm rebars, 2 per face of base plate, 380 mm deep drill and bond in 35 mm holes

13 mm bars @ 102 mm

8-57 mm anchor bolts

814 x 70 mm Octagonal baseplate

457 mm Post
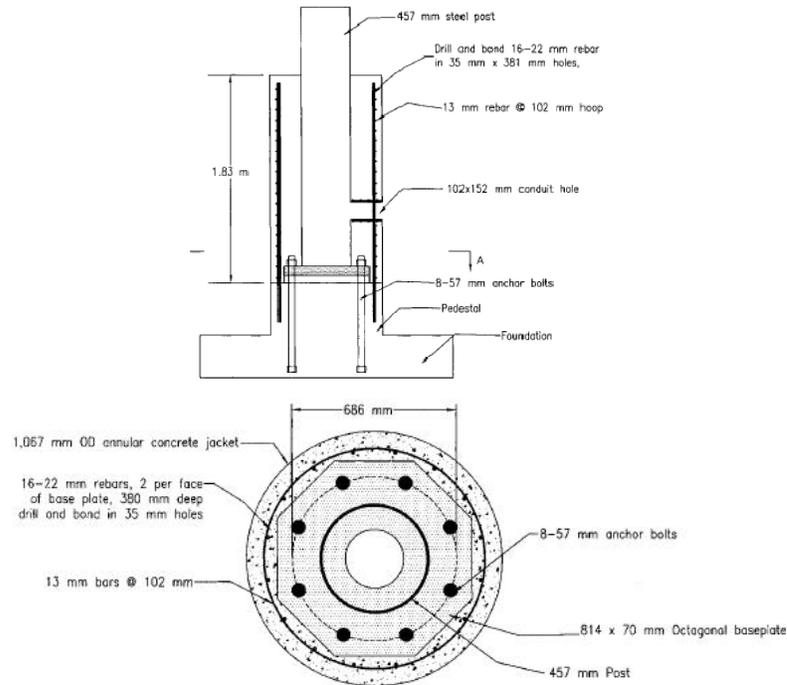
Figure 2.16: Profile and plan of CJP welded pole-to-base plate connection with concrete jacket (Gilani and Whittaker, 2000b)

2.4.4 Chen (2003)

Chen (2003) studied the causes of fatigue cracking in mast arms of signal support structures throughout the state of Missouri. The research included laboratory fatigue testing of five mast arm specimens with various weld details, in-service stress data collected through field instrumentation of two signal support structures, and metallurgical analysis of the failed laboratory specimens and field specimens. Also, a comparison was made between the design of the signal support structures from the *1994 Specifications* and the proposed (3rd Draft) *1999 Specifications*. The *1999 Specifications* was the first revision of the *1994 Specifications* to include the new provisions developed in *NCHRP Report 412*.

The fatigue test consisted of four circular and one octagonal mast arm specimens fabricated by three different manufacturers. The five mast arm specimens have a fillet welded socket mast arm-to-end plate connection. Two of the specimens utilized a new "fatigue resistant" unequal leg fillet weld design where the vertical and horizontal legs were equal to 1.83 and 1.57 times the weld throat distance, respectively. The five specimens were cycled at a stress range of 8 ksi

31

about a mean stress of 14 ksi as measured in the extreme tension fiber at the weld toe of the socket connection. All four circular specimens cracked at the weld toe on the top side (tension side) of the mast arm and the octagonal specimen cracked at the corner on the extreme tension side. The fatigue test results are shown in Table 2.6 and the mean of the test data is plotted against the AASHTO Category E' S-N curve in Figure 2.17.

Table 2.6: Fatigue test data for five mast arm specimens (Chen, 2003)

Mast Arm	Manufacturer	Weld Type	Failure Cycles	Comments
254682	Valmont	Old	1.8 million	None
BB 34970	Valmont	New	2.1 million	None
CB 12917	Valmont	New	0.4 million	Possible lack of fusion of weld
88791	Union Metals	Old	0.5 million	Flaw detected by Mag Particle prior to loading
9539 CL54	JEM	Old	0.0 million	Flaw detected by inspection prior to loading
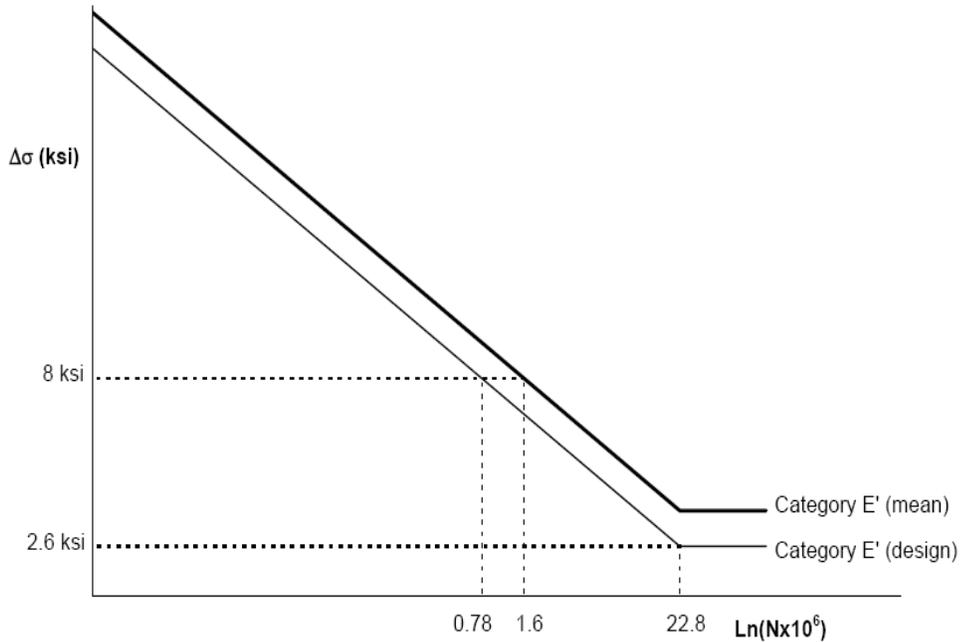
Figure 2.17: Mean of fatigue data for five mast arm specimens (Chen, 2003)

From the test data and metallurgical analysis of the laboratory and field specimens, a few conclusions were drawn about the connection detail. Cracking in the mast arms occurred at the weld toe of the mast arm-to-end plate connection and crack initiation was exacerbated by the occurrence of undercutting. Undercutting occurs when the base material is burned away at the toe of the weld causing a geometric stress concentration. Lack of penetration and fusion were also observed in the fillet welds. Also, the new "fatigue resistant" weld profile did not improve fatigue life and was susceptible to the same poor weld quality as the other specimens. Other potential defects affecting fatigue life such as residual stresses in the base material were not taken into consideration.

Chen (2003) checked signal support structures designed using the *1994 Specifications* against the new provisions developed in *NCHRP Report 412*. The mast arm specimens considered did not satisfy the new provisions and the member thicknesses needed to increase in size by at least a factor of two to meet the fatigue requirements. Finally, it was found that truck induced wind gusts controlled the fatigue design for signal support structures.

From the field instrumentation of two mast arms in-service, four important conclusions were drawn:

1. wind speed and the ratio of stress to the square of wind speed follow a lognormal distribution;
2. the average stress in the signal support structure with the longer mast arm was much higher than those with the shorter mast arm;
3. the amplitude of the horizontal vibration caused by natural wind gusts was three times greater than the vertical vibrations;
4. although not observed during instrumentation, the octagonal mast arms are potentially susceptible to galloping.

2.4.5 Palmatier and Frank (2005)

Palmatier and Frank (2005) initiated a research program to assess the effectiveness of ultrasonic impact treatment (UIT) when applied to signal structures. Prior research has shown that UIT can effectively improve the fatigue life of different welded details and is most effective when applied to a previously galvanized structure under dead load. For these reasons, UIT is particularly well-suited for field retrofit of signal structures. The purpose of this research was to

develop a procedure for UIT of signal structures in the field and to test the performance of signal structures retrofitted with UIT. UIT improves fatigue performance by increasing the weld radius which results in a better stress flow through the detail and a reduction in the SCF. The pictures shown in Figure 2.18 are fillet weld profiles at 10 times magnification before and after UIT. The cross-section of the treated weld shows an increase in weld radius, a decrease in the length of the weld leg, and a negligible effect on the global weld angle.

To better understand the process and application of UIT, the procedure was performed on two in-service signal structures in Denton, Texas. The mast arm-to-end plate and end plate-to-pole welds were both treated. The UIT was performed quickly and easily using a bucket truck with an electrical power generator. An illustration of this setup can be seen in Figure 2.19. The process took less than 40 minutes per arm and caused little disruption in traffic. The time breakdown for the two signal structures can be seen in Table 2.7. Palmatier and Frank (2005) recommended that the weld toe be treated in an arc between 90 and 180 $^{\circ}$s centered about the top of the mast arm. This recommendation was due to crack development at the top of the mast arm in previous laboratory testing. After UIT, the galvanizing should be repaired by applying zinc rich paint over the treated area. The final recommendation was that UIT should not be performed on poles with visible cracks since it was shown to have little impact on already cracked welds. Palmatier and Frank (2005) recommend that poles with visible cracks should be replaced rather than retrofitted.
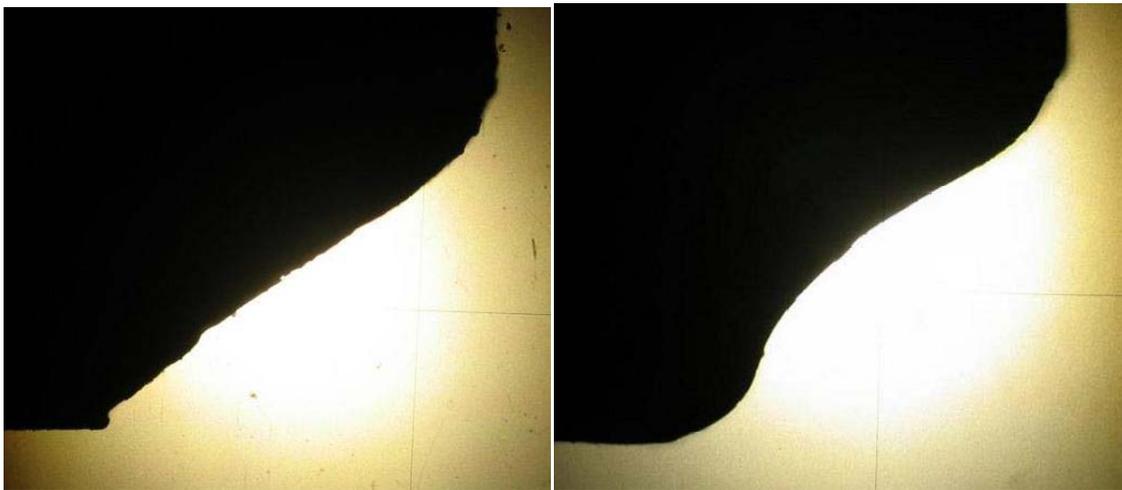
Figure 2.18: Weld profile before and after UIT (Palmatier and Frank, 2005)

Figure 2.19: Use of bucket truck for UIT (Palmatier and Frank, 2005)

Table 2.7: Time required to perform UIT on 2 specimens (Palmatier and Frank, 2005)

Location	Time (min)					
	Setup	UIT Application	Inspection and weld cleaning	Galvanization repair	Clean up	Total Time
Mast arm 1	11	6	2	3	2	24
Mast 1	-	6	3	4	0	13
					Total	33
Mast arm 2	5	6	2	3	2	18
Mast 2	-	7	3	4	4	18
					Total	36

The second component of the project described by Palmatier and Frank (2005) was experimental fatigue testing of eight different mast arm specimens. Two of the mast arm specimens were taken out of the field. One of the field specimens underwent UIT at the mast arm-to-transverse plate connection and at the transverse plate-to-pole connection after one year of service. That specimen was then removed 5 months after UIT application. The other field specimen was untreated and had been in-service for 10 years. The other six specimens were taken from the fabrication yard at TransAmerican where two had UIT applied to the mast arm-to-transverse plate connection and the other four were untreated. All specimens had 1.25 in.

35

thick end plates except the field specimen that had undergone UIT which had a 1 in. thick end plate. The fatigue test data for the eight specimens may be seen in Figure 2.20. "TA" refers to the four untreated specimens from the TransAmerican fabrication yard while "TAU" refers to the two treated specimens from the TransAmerican fabrication yard. "DU" and "DN" are the treated and untreated specimens pulled out of the field in Denton, Texas respectively.
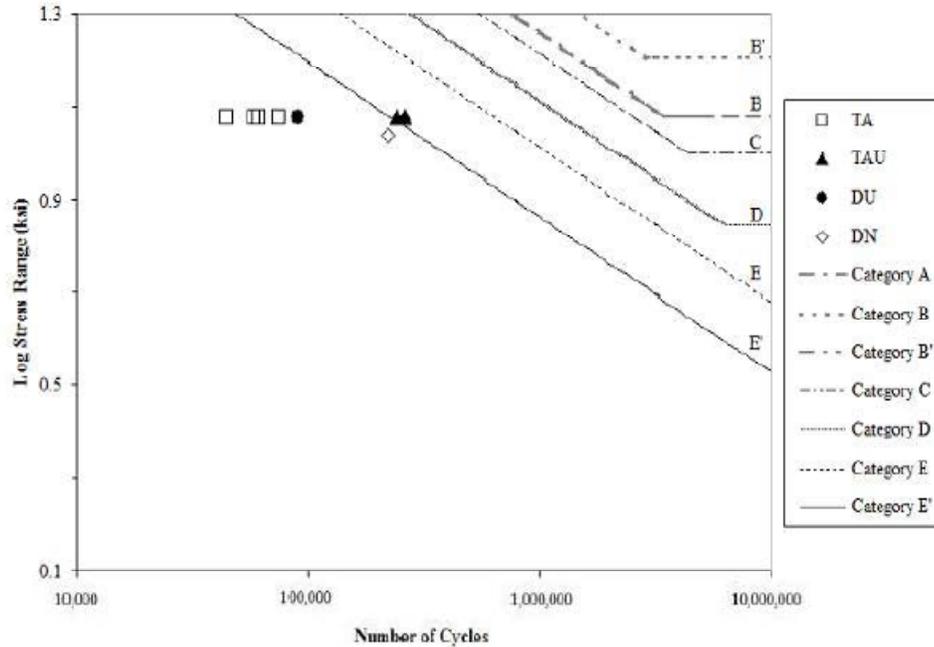
Figure 2.20: Fatigue data for University of Texas testing program (Palmatier and Frank, 2005)

The two treated specimens from the fabrication yard performed at the Category E' level while the four untreated specimens performed well below the Category E' level. The data from the field specimens was less conclusive. The treated field specimen did not perform nearly as well as the untreated field specimen. However, the untreated specimen had a thicker end plate. The thicker end plate drastically reduces stresses at the weld toe and improves the fatigue life of the detail as observed in other research (Connor *et al.*, 2004). Therefore, it was not possible to make a direct comparison between the two field specimens. The untreated field specimen performed comparably to the treated specimens from the fabrication yard even though they had the same end plate thickness. This unexpected result is most likely due to the fact that specimen DN had a smaller diameter mast arm than the fabrication yard specimens. The smaller diameter resulted in a lower end plate moment and smaller end plate deformations thus reducing the stresses at the weld toe.

Palmatier and Frank (2005) concluded that retrofit through UIT is a rapid and non-disruptive procedure to implement when the proper equipment is present. The testing program demonstrated that UIT is an effective method of improving the fatigue performance of the mast arm-to-pole connections in the specimens from the fabrication yard. Because of the different dimensions, it was not possible to compare the two field specimens considered. However, it was surmised that base plate thickness played a role in the difference in fatigue life.

2.4.6 Azzam (2006)

Azzam (2006) investigated the fatigue resistance of aluminum luminaire structures. Prior to this project, limited experimental fatigue data on connections typically used in aluminum luminaire poles was available. Azzam (2006) performed experimental fatigue testing of shoe base pole socket and through plate pole socket connections. Azzam (2006) also measured residual stresses in two fabricated details and performed finite element modeling of numerous pole socket connection configurations.

The testing program consisted of 19 shoe base pole socket connections and 10 through plate pole socket connections. The test samples were fabricated from 6063 series T4 temper aluminum alloy. The pole specimens for both connections were 10 ft. tall and had a diameter of 10 in. and a wall thickness of 0.25 in. The shoe base was 14 in. by 14 in. and 1 in. thick and the height of the shoe was 4.875 in. An unequal fillet weld leg was used for the shoe base-to-pole weld with a vertical length of 0.375 in. and horizontal length of 0.25 in. The dimensions of the shoe base pole socket connection are shown in Figure 2.21. The through plate pole socket connection used a 14 in. by 14 in. by 1 in. thick base plate made from 6061 series T6 temper aluminum alloy. The test displacement and stress range for each Specimen 1s shown in Table 2.8 where the "A" specimens refer to the shoe base pole socket connections and the "B" specimens refer to the through plate socket connections.
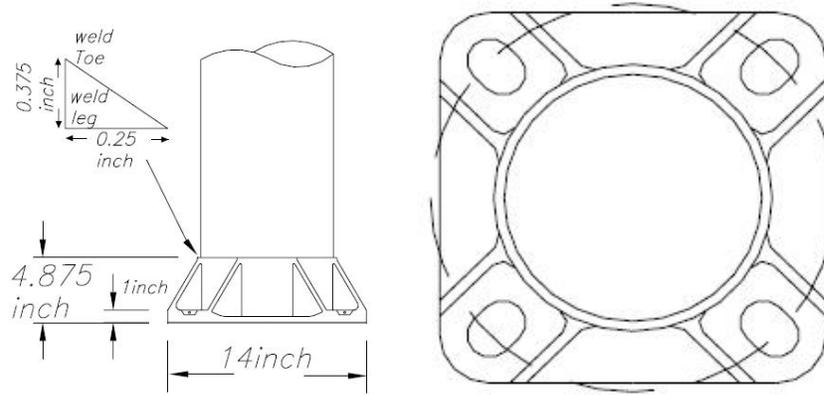
Figure 2.21: Dimensions of shoe base pole socket connection (Azzam, 2006)

Table 2.8: Stress ranges used in shoe base pole socket and through plate pole socket connection test specimens (Azzam, 2006)

Specimen Number	Displacement (in.)	Stress Range (ksi)	Specimen Number	Displacement (in.)	Stress Range (ksi)
A6	0.875	3.6	B3	0.5	2.0
A7	1.5	6.6	B4	0.5	2.2
A8	1.5	7.3	B5	0.875	3.5
A9	0.75	4.0	B6	0.875	4.5
A10	0.75	3.5	B7	0.25	0.9
A11	1.0	5.1	B8	0.25	0.9
A12	1.0	4.7	B9	0.875	1.0
A13	1.25	5.4	B10	0.875	2.0
A14	1.25	6.1	B11	0.875	1.4
A15	1.25	5.6	B12	0.875	2.9
A16	1.25	6.5			
A17	1.75	8.1			
A18	1.75	7.3			
A19	1.75	8.1			
A20	1.75	8.6			
A21	0.875	5.3			
A22	0.875	4.1			
A23	0.875	4.8			
A24	0.875	5.8			

All 19 shoe base pole socket connections had cracking in the shoe base-to-pole fillet weld. Most cracks developed in the weld toe at the furthest distance from the neutral axis and propagated through the thickness along the weld toe. In a few specimens, the cracks initiated in

the weld root and propagated through the weld throat. Figure 2.22 shows the fatigue data for
the 19 shoe base pole socket connections plotted against the AASHTO S-N curves. Also, the
lower bound of the 97.5 % confidence interval line is plotted. The lower bound line has a flatter
slope and intersects the AASHTO Category D, E, and E' curves in the finite life region. In the
infinite life region, the lower bound curve plots well above Category D. The shoe base pole
socket connection is a Category E detail in the *2001 Specifications*. The flatter line is most
likely due to the compressive residual stresses in the shoe base detail resulting from the
fabrication process.
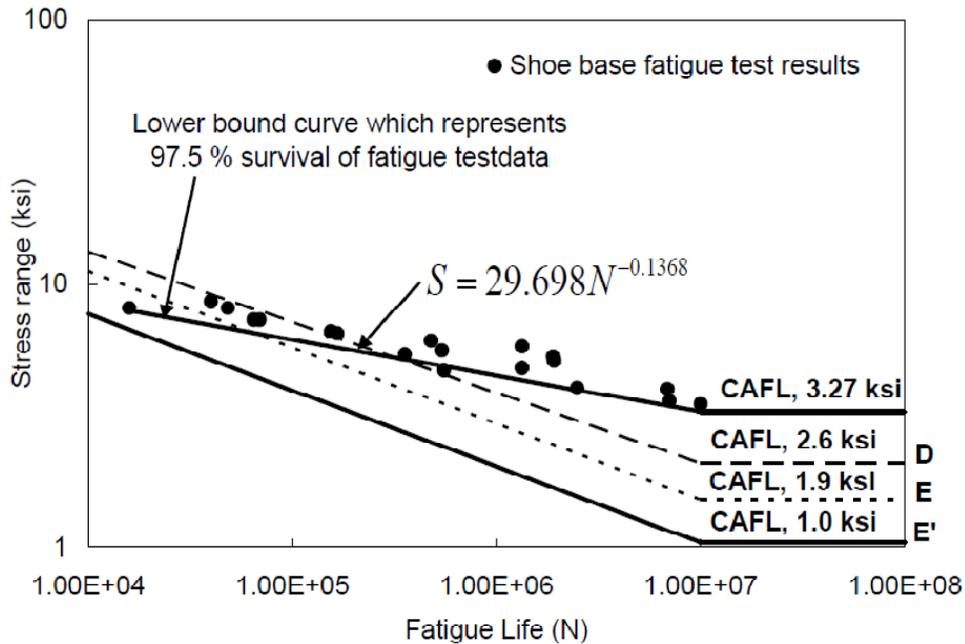
Figure 2.22: S-N plot for aluminum shoe base pole socket connection (Azzam, 2006)

All ten through plate socket connections had cracking in the weld toe of the socket connection.
The cracks initiated in the weld toe opposite the anchor bolts in 80% of the test specimens. This
cracking pattern is known as the butterfly trend, where the stress in the weld toe opposite the
anchor bolts is higher than the stress in the extreme tension fiber. This behavior occurs in
specimens with flexible base plates that induce additional local bending stresses in the pole
walls. Figure 2.23 shows the fatigue data for the 10 through plate pole socket connections
plotted against the AASHTO S-N curves. The lower bound of the 97.5% confidence interval
plots well below the AASHTO Category E' S-N curve. The *2001 Specifications* classify this
detail as Category E', which over predicts the fatigue resistance of the test specimens.
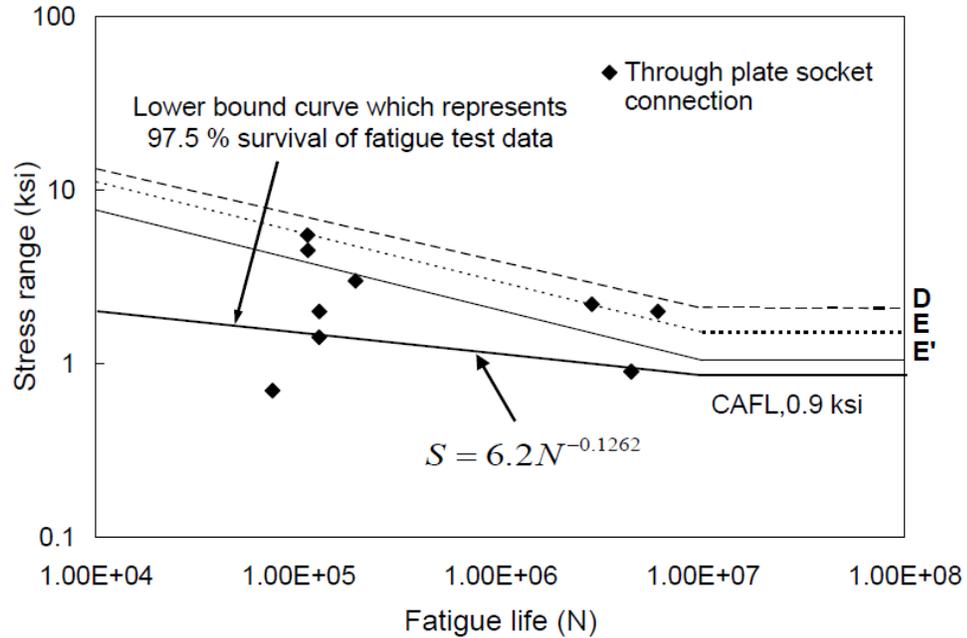
Figure 2.23: S-N plot for aluminum through base pole socket connection (Azzam, 2006)

Azzam (2006) experimentally studied the residual stresses in the two pole socket connections. Residual stresses can greatly impact fatigue resistance. Tensile residual stresses can reduce the fatigue life of a detail by acerbating crack growth and compressive residual stresses can increase the fatigue life by delaying crack initiation. In the shoe base connection, compressive residual stresses of up to 15 ksi were measured at the surface of the pole just above the weld toe. This is thought to be the cause of the flat slope in the fatigue curve. The tensile residual stresses in the bottom casting of the shoe base connection approached 31 ksi adjacent to the fillet weld, which is close to the yield stress of the material. Compressive residual stresses were measured in the outer surface of the pole wall just above the weld toe in the through plate socket connection. Beyond a depth of 0.025 in. in the pole wall, tensile stresses of up to 8 ksi were measured.

Azzam (2006) performed extensive finite element modeling of pole-to-base connections in ANSYS. A parametric study was done to determine the stress concentration factor (SCF) in the pole wall resulting from changes in the following five parameters:

1. base plate thickness in shoe base pole socket connection and through plate pole socket connection;
2. weld leg geometry in through plate pole socket connection;
3. hole diameter in base plate of through plate pole socket connection;

4. number of holes in base plate of through plate pole socket connection
5. gusset stiffener geometry in through plate pole socket connection.

The following is a brief synopsis of the findings from this parametric study.

From previous research, base plate flexibility greatly influences the fatigue resistance of the socket connection (Ocel, 2006). For the aluminum shoe base pole socket connections studied by Azzam (2006), the SCF in the pole wall at the connection with the shoe was not affected by the shoe base plate thickness. In this case, the SCF is the maximum normal stress in the tube wall divided by the nominal stress in the tube wall. Figure 2.24 shows the SCF for different shoe base plate thicknesses and as shown the SCF for a shoe base plate thickness of 1 in. is 1.4 and only decreases slightly for a shoe base plate thickness of 4 in.

The SCF in the tube wall for the through plate socket connection was greatly influenced by the base plate thickness. For a pole thickness of 0.3750 in. and a tube radius of 5 in., the SCF for a base plate thickness of 1 in. and 4 in. are 2.8 and 1.4 respectively. For a 4 in. radius pole with 0.375 in. wall thickness, the magnitudes of the SCF are greater: the SCF is 3.4 and 1.8 for base plate thicknesses of 1 in. and 4 in. respectively. Figure 2.25 shows the influence of base plate thickness on the SCF in the tube wall for a 4 in. radius tube and various tube wall thicknesses.

Azzam (2006) investigated the impact of fillet weld leg geometry on the SCF in the tube wall of a through plate pole socket connection. All models were run with a base plate thickness of 3 in. to reduce the effects of base plate flexibility. Various geometries of unequal and equal fillet welds were examined. For the unequal fillet weld legs, the horizontal length was 0.250 in. and the vertical length was varied between 0.250 and 0.563 in. For the equal fillet weld legs, the weld leg varied from 0.125 in. to 0.300 in. Figure 2.26 and Figure 2.27 shows the SCF in the tube wall at the weld toe for the unequal and equal leg fillet welds respectively. The results indicate that the SCF for a given unequal leg fillet weld is lower than that for an equal leg fillet weld and that as the vertical leg increases, the SCF decreases. Further, it was found that the 5 in. radius tube results in a lower SCF for all welds than the 4 in. radius.
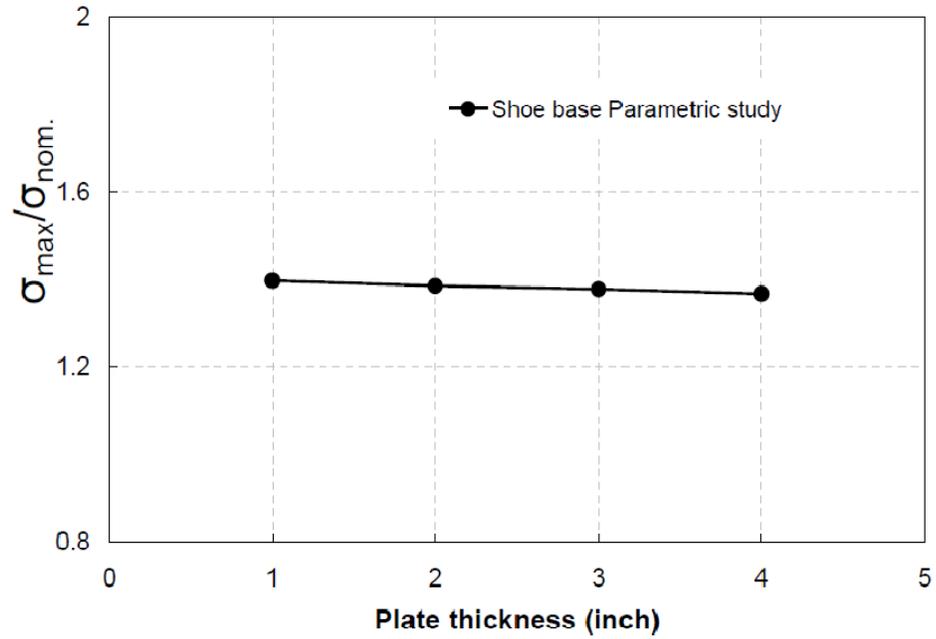
Figure 2.24: Plot of SCF for a given shoe base thickness (Azzam, 2006)
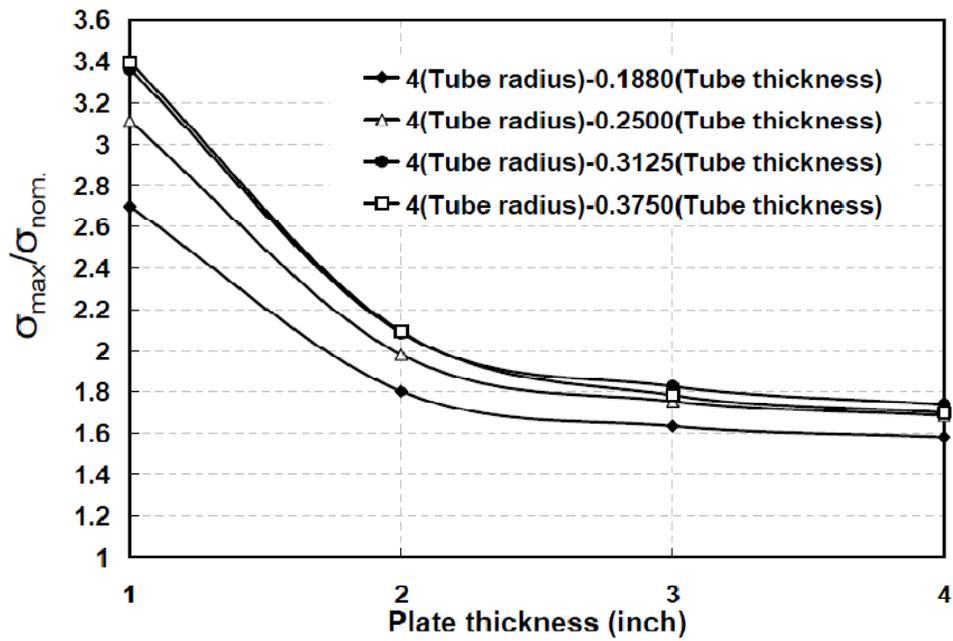
Figure 2.25: Plot of SCF for a given base plate thickness in through plate pole socket connection (Azzam, 2006)
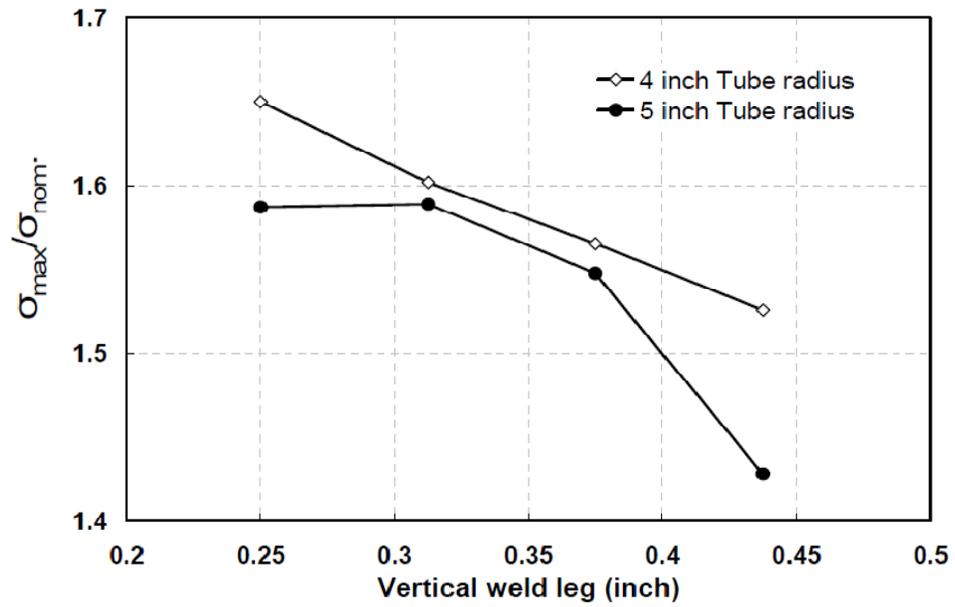
Figure 2.26: SCF in tube wall for a given length of vertical weld leg in unequal leg fillet weld (Azzam, 2006)
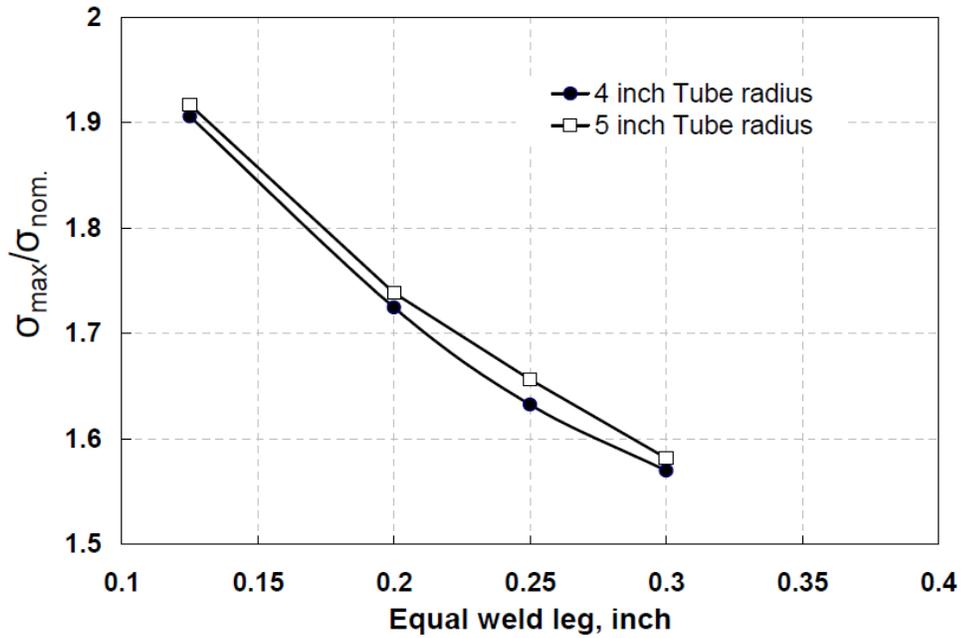
Figure 2.27: SCF in tube wall for a given length of weld leg in equal leg fillet weld (Azzam, 2006)

43

Azzam (2006) studied the effect of bolt hole diameter and number of bolt holes on the SCF in the pole wall in the through plate socket connection. The study showed that an increase in bolt diameter from 1 in. to 2.5 in. resulted in a 25% reduction in maximum longitudinal stress in the weld toe opposite the bolt area. When the number of bolt holes was increased from 4 to 8, the SCF in the pole wall decreased. The additional restraint provided in the 8 bolt hole configuration made the butterfly trend disappear and the maximum stress occurred at the locations furthest from the neutral axis as expected.

Azzam (2006) studied the stresses in the pole wall at the gusset tips for different sized gusset stiffeners used in through plate pole socket connections. Gusset stiffeners of length 2, 3, 4, 8, and 16 in. were considered for various base plate and tube thicknesses. Figure 2.28 and Figure 2.29 show the results of the parametric study for base plate thicknesses of 1 and 3 in respectively. The stresses remain constant once the vertical length of the stiffener exceeds 4 in. and the highest stresses were seen in the short gusset stiffeners. This data is contrary to the fatigue classifications in the *2001 Specifications*. The *2001 Specifications* categorizes a gusset stiffener with a length of less than 2 in. as Category C, between 2 and 4 in. as Category D, and greater than 4 in. as Category E.
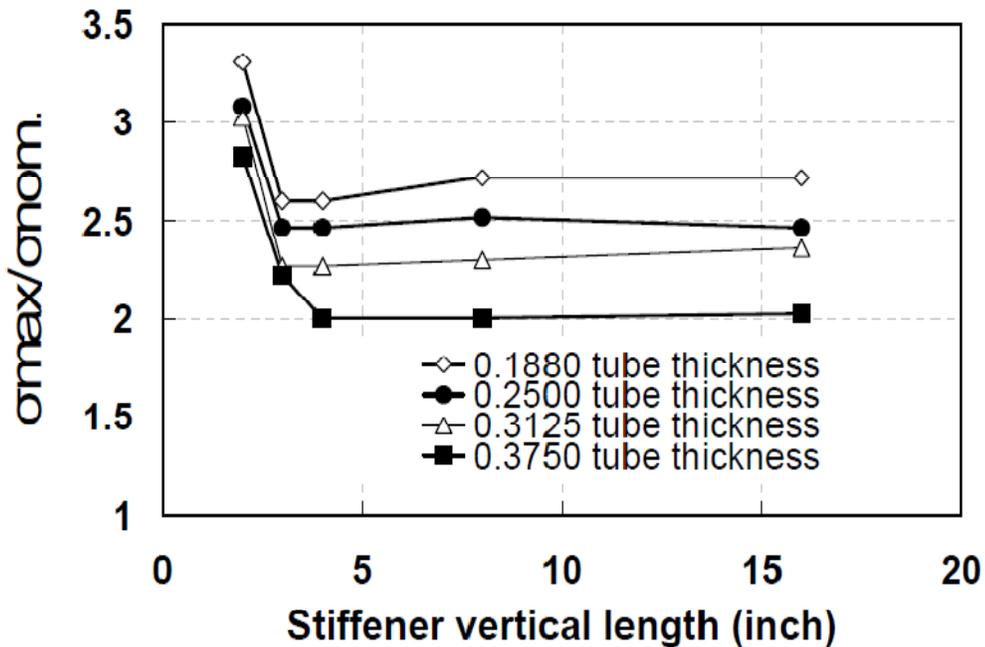
Figure 2.28: SCF in pole wall at the tip of gusset stiffener for different gusset sizes and 1 in. base plate thickness (Azzam, 2006)
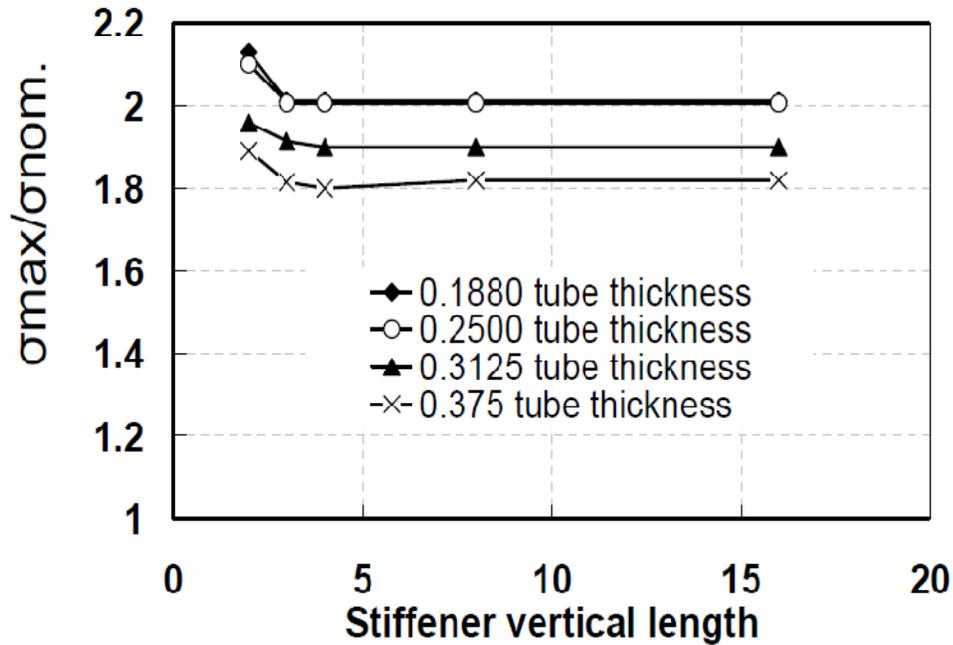
Figure 2.29: SCF in pole wall at the tip of gusset stiffener for different gusset sizes and 3 in. base plate thickness (Azzam, 2006)

2.4.7 Ocel *et al.* (2006)

Ocel *et al.* (2006) performed extensive fatigue testing on details typically used in cantilevered support structures. All specimens tested by Ocel *et al.* (2006) had octagonal mast arm and pole cross-sections because those were typically used by the Minnesota Department of Transportation (MnDOT). The fatigue testing program included mast arm-to-column connections, tube-to-transverse plate connections, transformer base details, and access hole details. The following is a discussion of the test specimens, fatigue test results, and comparisons to the fatigue classifications in the *2001 Specifications*.

Two general types of pole and mast arm structures were tested. Type I specimens used a built-up box mast arm-to-pole connection. This connection differed slightly from a standard box connection used with a circular pole as shown in the schematic in Figure 2.30. The Type I box connection consisted of a flange plate and two side plates. The flange plate was continuously fillet welded to the pole flat and the two side plates were fillet welded to the pole flat on each

side. The flange plate had four holes with nuts welded on the back for the mast arm base plate to bolt into. The box connection used with a circular pole contains two side plates, a top plate, a bottom plate, and a flange plate. The Type I box connection was thought to be advantageous because the flange plate bears directly on the pole creating a direct load path.
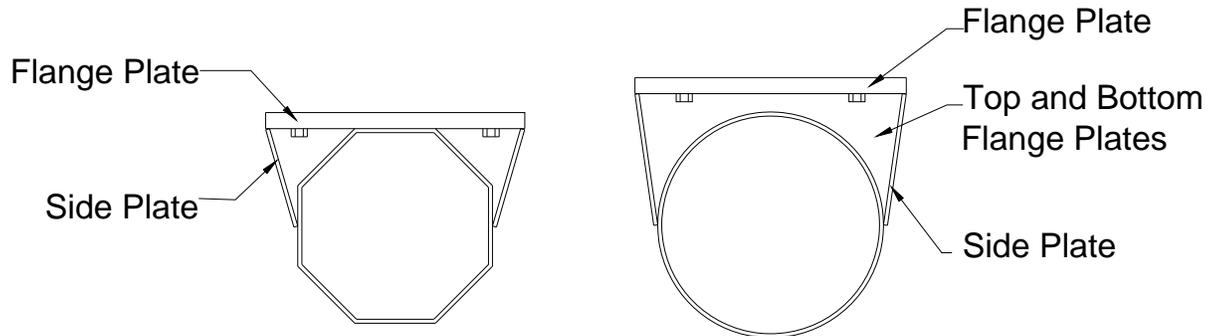
Figure 2.30: Schematic of Minnesota type box connection with octagonal pole and standard box connection with circular pole

The pole-to-base plate connection used in the Type I specimen was a fillet welded socket. MnDOT requires the use of a transformer base so it was included in the test setup to accurately represent the boundary conditions. Eight identical pole and mast arm specimens were used and the dimensions are shown in Figure 2.31. The eight mast arm specimens utilized two different tube-to-transverse plate connections. Four specimens used a triangular gusset stiffened socket connection and four used a CJP welded tube-to-transverse plate connection.

After testing began, a new specimen type was added called the Type I Long whose dimensions are shown in Figure 2.32. Type I Long specimens were added because the pole socket connections in the Type I specimen cycled in-plane performed poorly. Type I Long specimens had slightly different dimensions then the Type I specimens. The primary difference was that they had a 2.5 in. thick base plate where the Type I specimen had a 1.25 in. thick base plate. Of the four Type I Long specimens tested, two had a 0.1875 in. tube thickness and two had a 0.3125 in. tube thickness. The purpose of this additional specimen type was to investigate the improvement in fatigue resistance resulting from a thicker base plate.

The mast arm-to-pole connection in the eight identical Type II specimens utilized a mast arm that was CJP tube-to-tube welded to a small pole stub called a mast can as shown in Figure 2.33. The mast can had a slightly larger inside diameter than the outside diameter of the top of

the pole. The mast can was then slipped over the pole and the connection resists in-plane (deflection of mast arm tip is perpendicular to direction of traffic) moment through bearing of the mast can on the pole and out-of-plane (deflection of mast arm tip parallel to direction of traffic) moments through interlocking of the larger octagonal mast can fitting over the smaller octagonal pole. The Type II specimens also utilized an integrated transformer base.

The box connections used in the Type I specimens were initially tested in Reaction Frame I which was designed to cycle the mast arms (connected to the pole) in the three primary directions. Eight box connections were tested with three cycled in-plane, 4 cycled out-of-plane, and one cycled at 45 ^{o}s. The fatigue data for this connection is plotted against the AASHTO S-N curves in Figure 2.34. For the 3 Type I specimens cycled in-plane, the pole socket connection developed cracks and the testing had to be stopped. These three specimens were then moved to Reaction Frame III and testing continued. Reaction Frame III was built to complete the cycling of the in-plane box connections that did not crack in Reaction Frame I. Cracks in the in-plane specimen propagated at the intersection between the flange plate and pole tube. Also, the side plates buckled outwards causing cracking to initiate. Because cracks initiated at the intersection between the pole wall and the flange plate, the stress range was computed based on the moment of inertia of the weld group attaching the flange plate to the pole and side plates. This computation gave the nominal stress range at the intersection of the pole and flange plate. From the fatigue test data for the three box connections cycled in-plane, the lower bound of the 97.5% confidence interval was determined to be between Categories E' and ET. The *2001 Specifications* classified this detail as Category E' which is an over prediction of the fatigue resistance of the tested connection.

The 4 box connections (Type I specimens) cycled out-of-plane and 1 connection cycled at 45 ^{o}s all failed in Reaction Frame I. The fatigue cracks in these specimens initiated at the pole wall at the corner of the side plates. This cracking pattern was indicative of punching shear and was similar to what was seen in box connections with round poles. The stress range for these specimens was computed by converting the in-plane stress range to a membrane stress in the side plates. The membrane stress was then converted to a punching shear stress range in the pole. The lower bound of the 97.5% confidence interval for the four box connections cycled out-of-plane and one box connection cycled at 45 ^{o}s was slightly above Category K_2 which agrees with the *2001 Specifications*.

The three Type I socket connections tested in-plane in Reaction Frame I cracked before the box connection failed. The five remaining Type I specimens were cycled in Reaction Frame I until failure of the box connection and were cycled in Reaction Frame II until cracking of the socket connection. Once the socket connection cracked, the specimen was rotated so that the uncracked side would be subjected to tensile stresses and the cracked side to compressive stresses. This allowed the generation of two data points for each socket connection. There was concern that the high number of accumulated compression cycles might impact the fatigue resistance when the specimen was rotated, however, this was not the case in the Type I specimens.

Figure 2.31: Details for Type I pole, mast arm, and transformer base (Ocel et al., 2006)
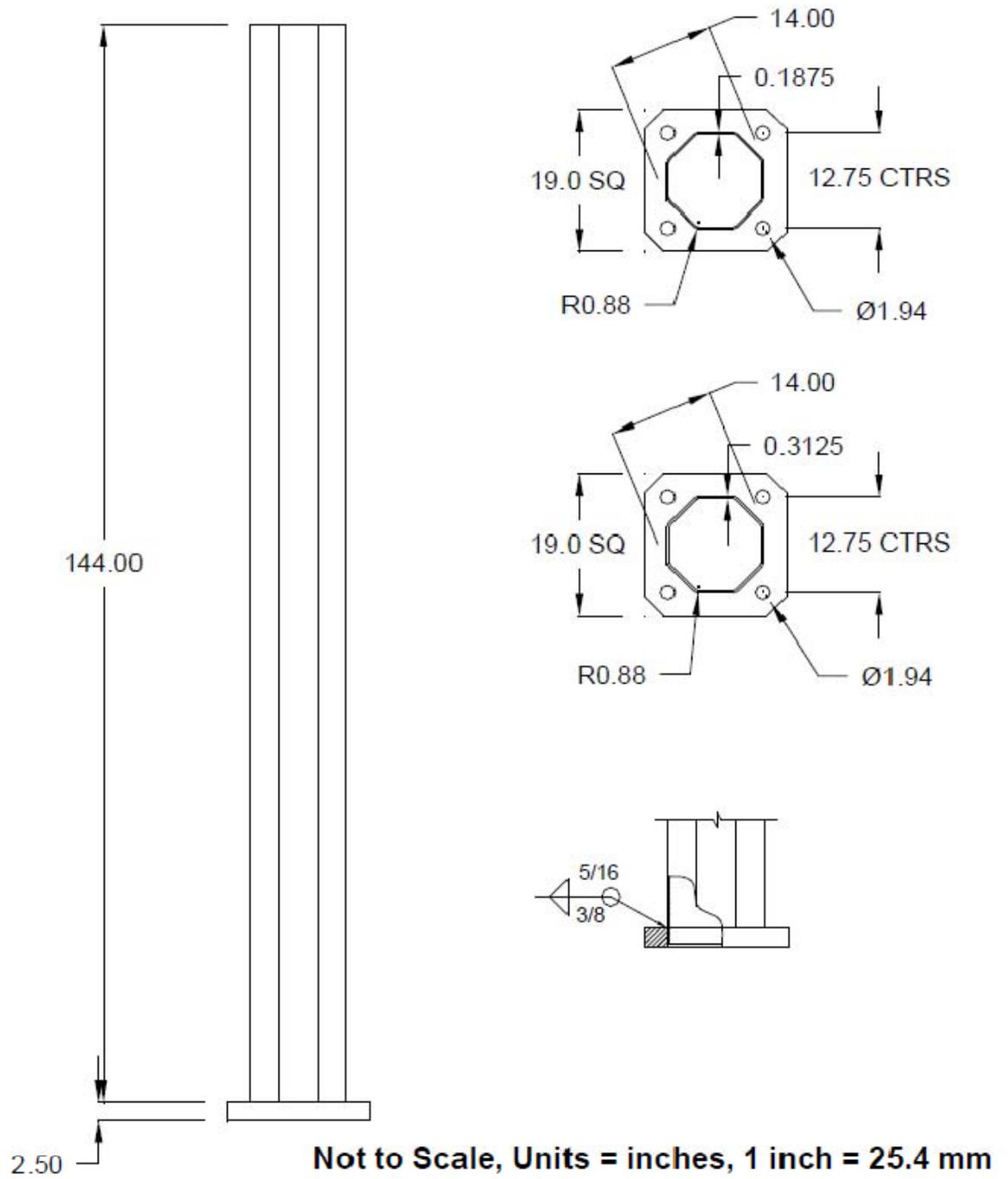
Figure 2.32: Details for Type I Long pole, mast arm, and transformer base (Ocel et al., 2006)

R0.88

11.60

0.3125

65.00

15°

6.25

30.00

100% FULL
PENETRATION

1/2

45°

CUT & FIT
MASTARM TO
MASTARM CAN

Mast Arm

Pole

3/8

H-BASE

24 1/2

14.0 DAC

26 1/2

Section B-B

12"
CTRS

(4) 2 3/16 DIA
ON 17 inch DIA BC

Section A-A

B   B

A   A
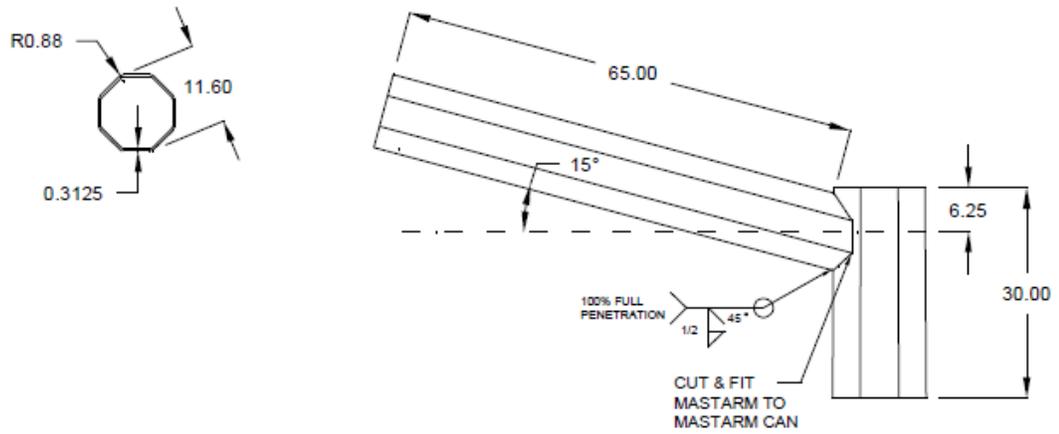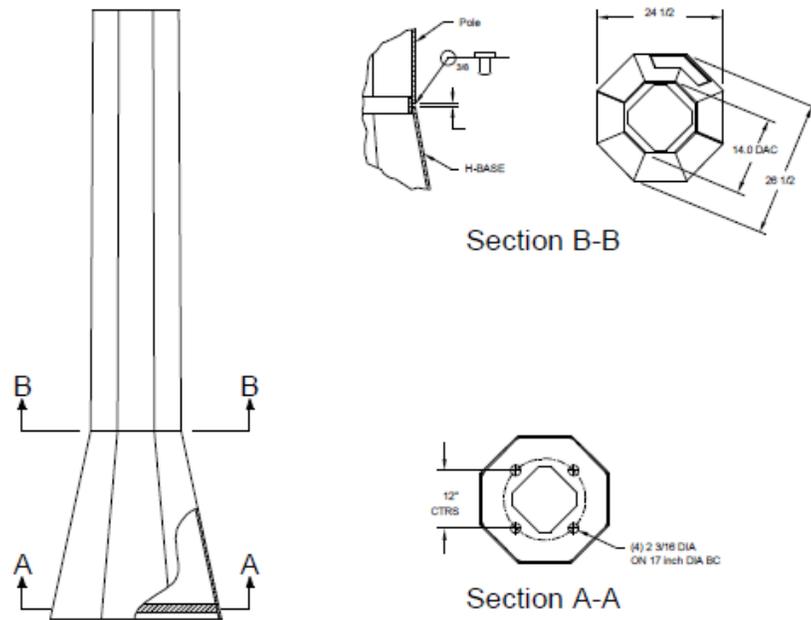
Pole

**Not to scale
units = inches
1 inch = 25.4 mm**

Figure 2.33: Details for Type II pole, mast arm, and transformer base (Ocel et al., 2006)
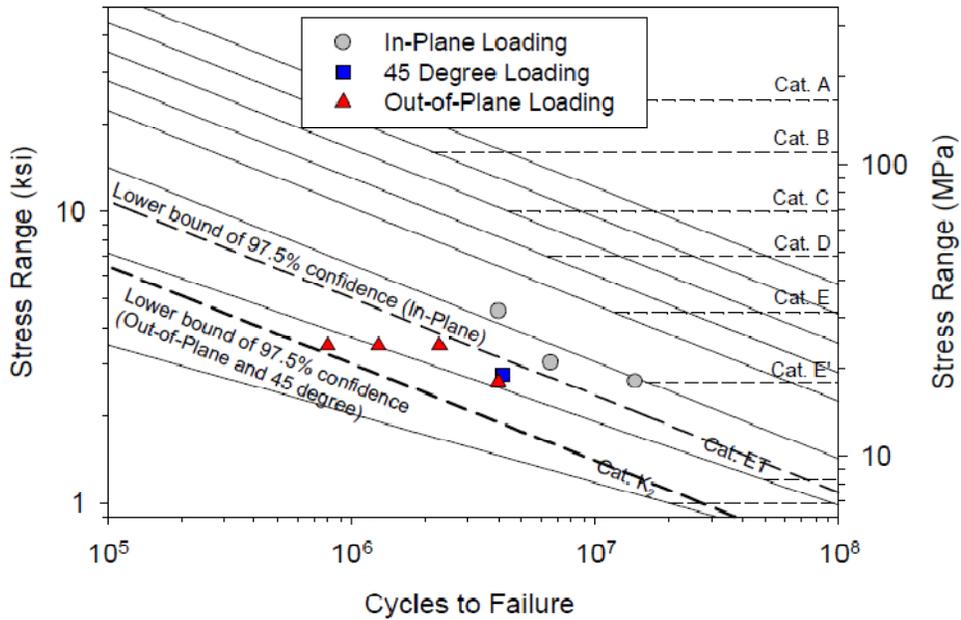
Figure 2.34: S-N plot for Type I box connection (Ocel et al., 2006)

The Type I socket connection had a 1.25 in. thick base plate and the pole had a 14 in. corner-to-corner dimension with 0.3125 in. thick tube walls. The fatigue data for the socket welded connection is shown in Figure 2.35 against the AASHTO S-N curves. Cracking initiated in all tested specimens at the pole bends on the extreme tension side. Most cracks initiated in the tube side weld toe and progressed into the tube wall. Other cracks initiated in the root of the socket weld and grew through the thickness of the weld. The lower bound of the 97.5% confidence interval intersects the K_2 curve. The *2001 Specifications* categorize this detail as Category E' so it over predicts the fatigue resistance of this detail by two categories.
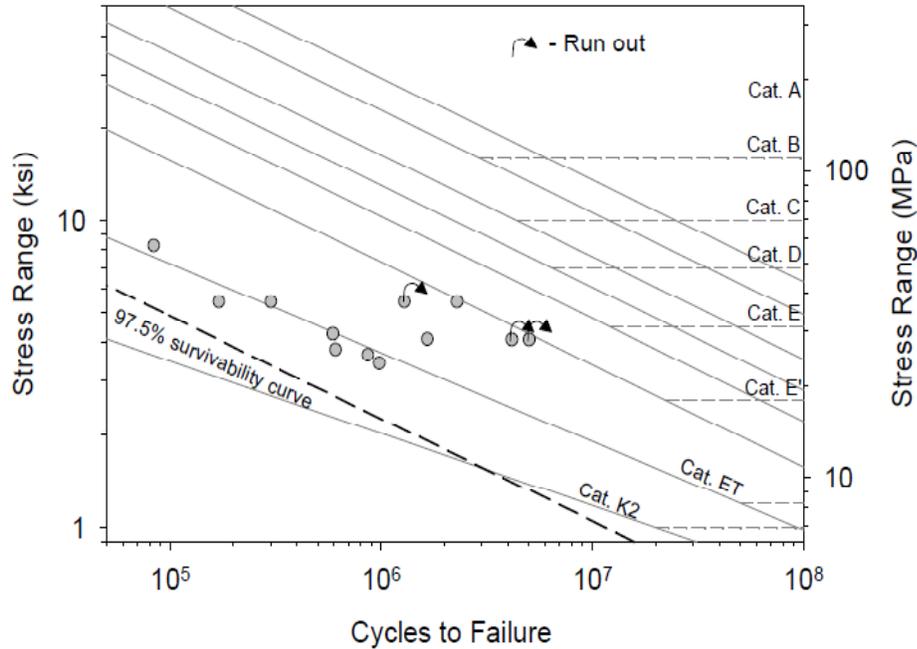
Figure 2.35: S-N plot for Type I socket connection (Ocel et al., 2006)

The Type I Long socket connections were tested to investigate the improvement in fatigue resistance resulting from a thicker base plate. Four Type I Long specimens were tested and each had a base plate thickness of 2.5 in. Two of the specimens had a tube wall thickness of 0.3125 in. and the other two had a wall thickness of 0.1875 in. The four Type I Long specimens were tested in Reaction Frame II and then rotated and tested again. Interestingly, while testing each specimen twice did not affect the thin base plate specimens, it did impact the fatigue resistance of the thick base plate specimens. For this reason, the second side specimens were neglected and a regression analysis was not performed. The fatigue data points for the thick base plate specimens with wall thicknesses of 0.3125 in. and 0.1875 in. are plotted against the AASHTO S-N curves in Figure 2.36 and Figure 2.37 respectively. The specimens with a 0.3125 in. wall thickness performed better than Category E and the 0.1875 in. tube thickness specimens performed better than Category E'. This is a two to three category improvement over the 1.25 in. thick base plate specimens and more in line with the Category E' classification in the *2001 Specifications*.
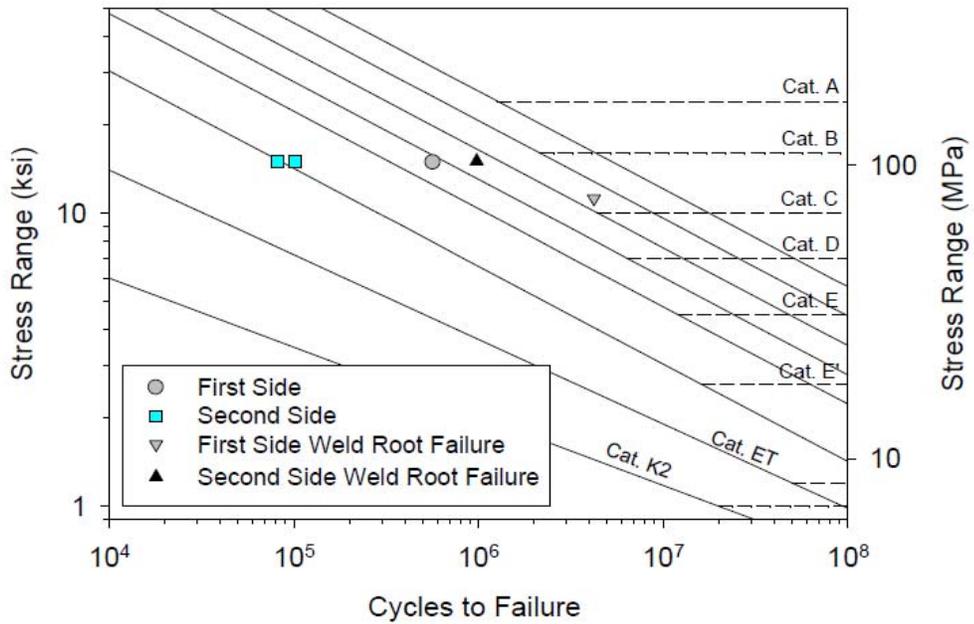
Figure 2.36: S-N plot for Type I Long socket connection with 2.5 in. thick base plate and 0.3125 in. thick tube wall thickness (Ocel et al., 2006)
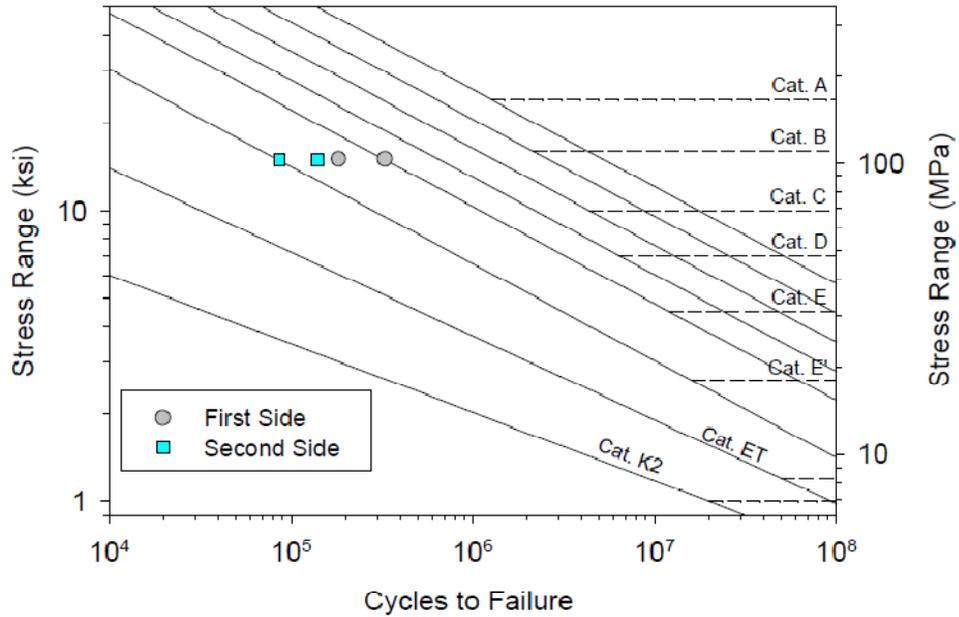
Figure 2.37: S-N plot for Type I Long socket connection with 2.5 in. thick base plate and 0.1875 in. thick tube wall thickness (Ocel et al., 2006)

The fatigue testing program included an investigation of hammer peening as a retrofit and repair technique for socket connections in cantilevered support structures. Hammer peening uses a pneumatic chisel to put compressive residual stresses into the weld toe. The residual

54

compressive stress reduces the magnitude of the tensile stress when the weld is cycled and therefore improves the fatigue life of the detail. Hammer peening has been shown to be effective when applied after fabrication and before erection and when applied to surface cracks under dead load.

Hammer peening retrofit was applied to 5 of the thin base plate socket connections and hammer peening repair was applied to 3 of the cracked thin base plate specimens. Figure 2.38 and Figure 2.39 show the fatigue data for the retrofitted and repaired socket connections respectively. The hammer peen repaired structures had the counter reset to zero once the crack was repaired. The 97.5% lower bound confidence interval for the retrofitted connections was between Categories E and E'. This is a marked improvement over the untreated thin base plate socket connections. The 97.5% lower bound confidence interval for the repaired structures is just above Category ET. This is a one category improvement over the untreated thin base plate socket connection. From these tests, hammer peening appears to be an effective retrofit and repair procedure for fillet welded socket connections.
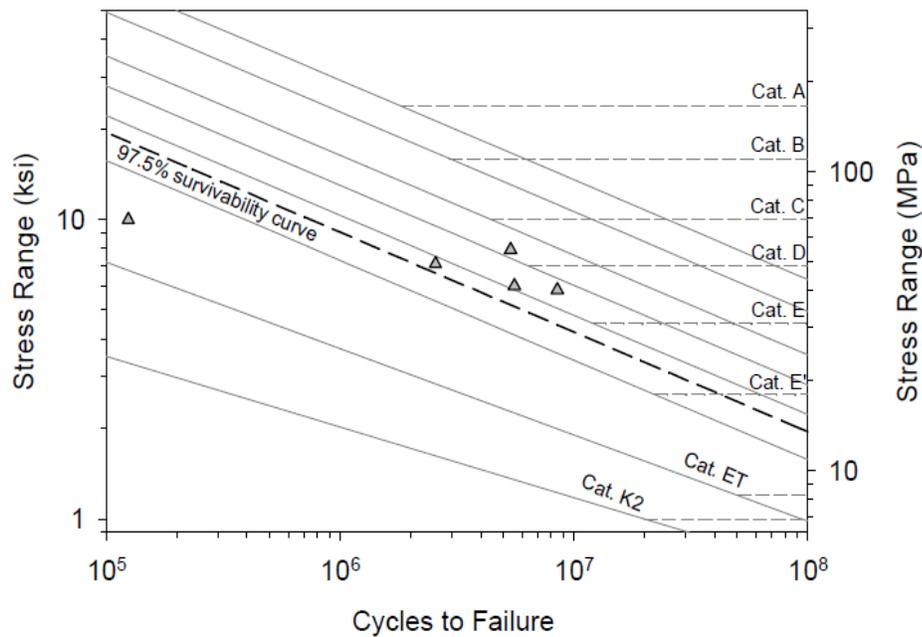
Figure 2.38: S-N plot for hammer peen retrofitted 1.25 in. thick base plate socket connection (Ocel et al., 2006)
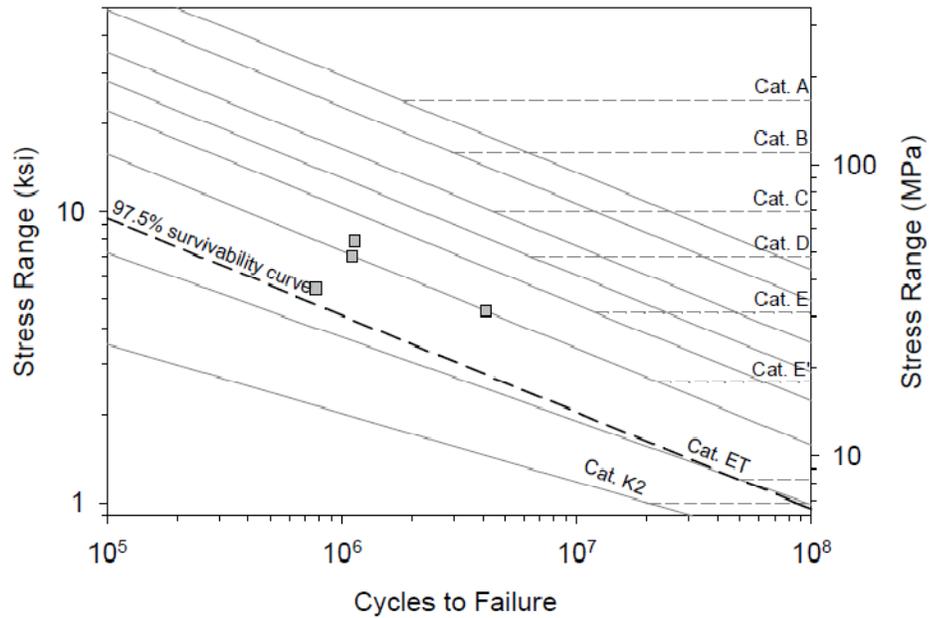
Figure 2.39: S-N plot for hammer peen repaired 1.25 in. thick base plate socket connection (Ocel et al., 2006)

Four Type I mast arm specimens with triangular gusset stiffened socket connections were tested. Like the other socket connections, both sides of the connection were tested. Triangular gusset stiffeners improve the connection detail by increasing the section modulus at the base of the pole and by moving the critical fatigue cracking location to the tip of the gusset. However, in the four tested specimens, the gusset stiffeners did not prevent cracking at the socket weld toe. When the pole cracked at the socket weld toe, the crack was hammer peen repaired so that the fatigue resistance of the gusset tip could be determined. Cracks in the gusset stiffener initiated in the top weld toe and propagated into the tube wall. Two of the specimens simultaneously cracked at the weld toe at the tip of the gusset stiffener and at the bottom weld to the base plate. The fatigue data for this connection is shown in Figure 2.40 plotted against the AASHTO S-N curves. The 97.5% lower bound confidence interval for the gusset tip is slightly above Category E. This is consistent with the *2001 Specifications*. The 97.5% lower bound confidence interval for the gusset stiffened socket connection is above Category ET. This represents a one category improvement over the unstiffened socket connection.
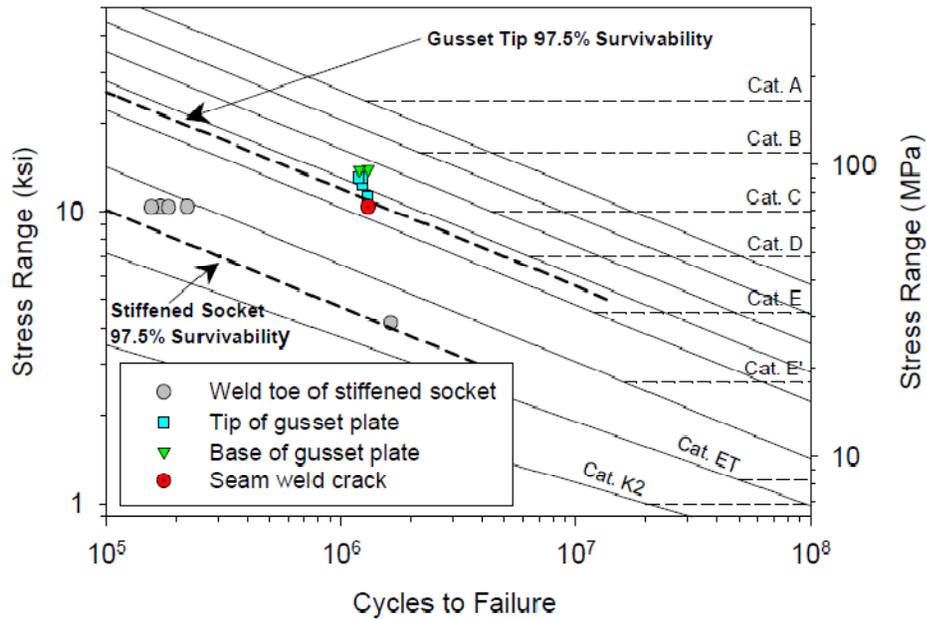
Figure 2.40: S-N plot for triangular gusset stiffened socket connection (Ocel et al., 2006)

Four Type I mast arm specimens had CJP welded tube-to-transverse plate connections. Like the previous connections, both sides were tested. Figure 2.41 shows the fatigue data for the CJP welded specimens plotted against the AASHTO S-N curves. Cracks initiated at the pole bends on the extreme tension side. The lower bound of the 97.5% confidence interval is between Categories E and E'. The *2001 Specifications* categorizes a CJP tube-to-transverse plate weld with the backing bar not welded to the base plate as Category E'. Therefore, the test data agrees with the fatigue resistance predicted by the *2001 Specifications*.
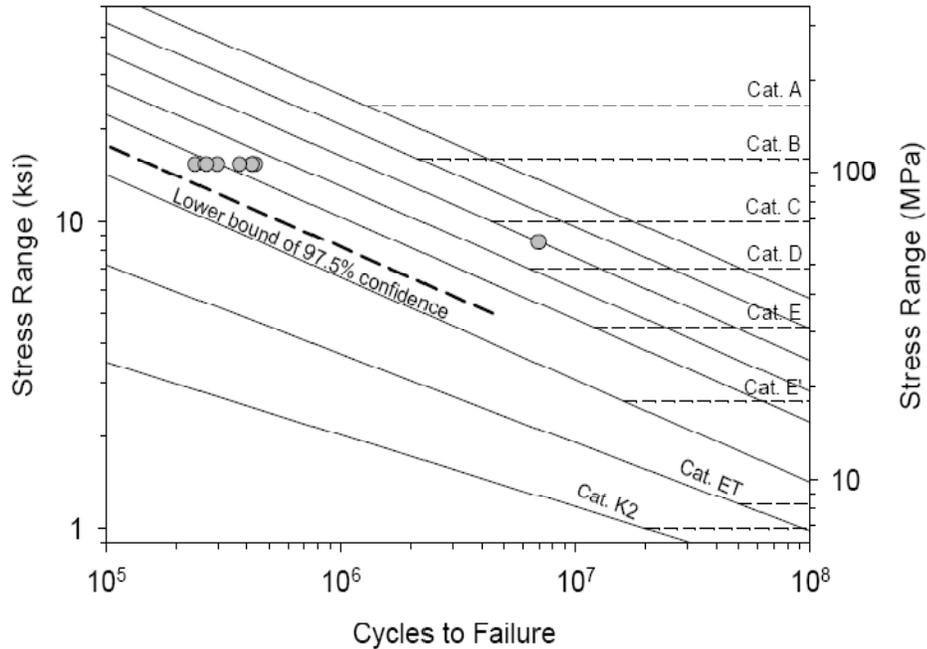
Figure 2.41: S-N plot for Type 1 mast arm CJP tube-to-transverse plate weld (Ocel et al., 2006)

Eight Type II octagonal tube-to-tube CJP welded mast arm-to-mast can connections were cycled in Reaction Frame I where three specimens were cycled in-plane, four out-of-plane, and one at 45 ºs. The fatigue data for the eight Type II specimens is plotted against the AASHTO S-N curves in Figure 2.41. Cracks initiated in all eight specimens on the mast can side of the weld indicating punching shear. Although many tube-to-tube connections had been tested in other projects, none had been used in a mast arm to mast can connection. The detail is not classified in the *2001 Specifications* and the closest detail is the fillet welded tube-to-tube connection. Since this detail is CJP welded with a backing bar, it would be expected to perform slightly better than the fillet welded connection. The *2001 Specifications* require two checks for the tube-to-tube fillet welded connection. The stress range in the branching member (mast arm) must have a Category ET resistance to ensure that the tube is thick enough to prevent a crack at the weld. Punching shear in the chord member (the mast can) must also be checked against Category K_2. Since all test specimens failed in punching shear, the fatigue stress range used was the punching shear stress range in the mast can. The lower bound of the 97.5% confidence interval plots slightly above K_2 resistance. Therefore, classification of the CJP tube-to-tube weld as Category K_2 would be sufficient.

58
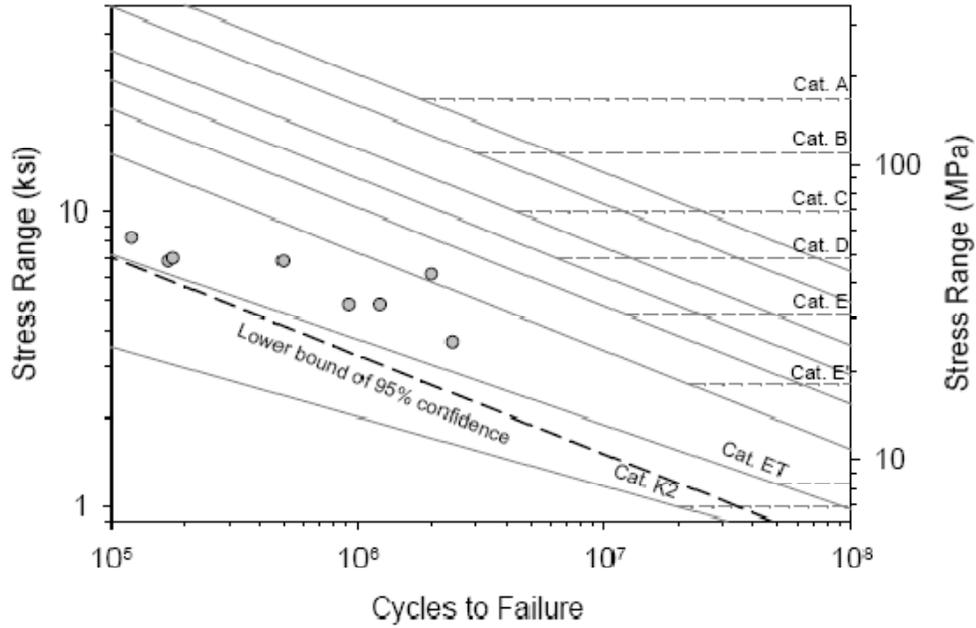
Figure 2.42: S-N plot for Type 2 mast arm to mast can CJP tube-to-tube weld (Ocel et al., 2006)

The Type I specimens were cycled with the transformer base still attached to represent the true boundary conditions. Although cracking of the transformer base in the Type I specimens was not investigated explicitly, cracks appeared in two of the specimens at the access hole detail. The first specimen that cracked was cycled in-plane and the access hole was located at the neutral axis of the cross-section corresponding to in-plane bending. The cracking in this Specimen 1s shown in Figure 2.43. The second specimen that cracked was cycled out-of-plane. The induced torsion from the out-of-plane loading caused large shear deformations at the corner of the access hole.

Figure 2.43: Fatigue cracking at the corner of the access hole (Ocel et al., 2006)

The two critical fatigue locations in the Type II specimens were the CJP weld between the pole and the integrated transformer base and the access hole detail. In all specimens, cracking occurred at the bottom corners of the access hole. Cracks initiated in one of two locations. The first type of crack initiated at the flame cut corner of the access hole and then propagated horizontally into the transformer base as shown in Figure 2.43. The second type of crack initiated at the fillet weld connecting the stiffening ring to the base plate. The fatigue data for the Type II specimens is shown in Figure 2.45 plotted against the AASHTO S-N curves. The stress ranges used were based on the net section properties of the access hole. The *2001 Specifications* do not include this exact detail. However, it classifies holes and cutouts to be Category D and the stiffening details to be Category E. The lower bound of the 97.5% confidence interval intersects the Category K_2 curve.
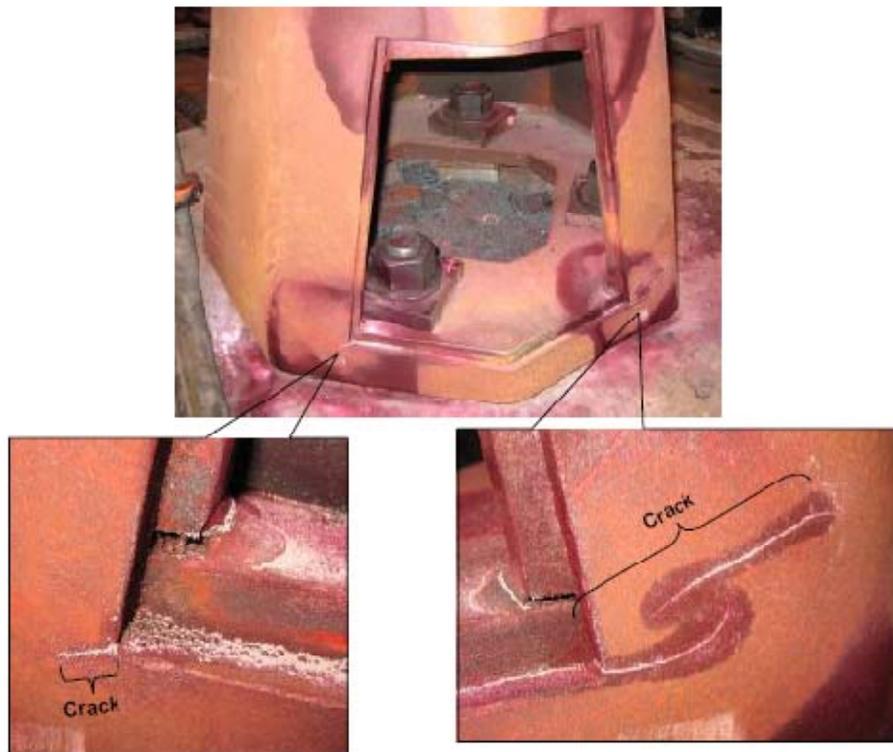
Figure 2.44: Cracking in access hole of Type 2 integrated transformer base (Ocel et al., 2006)
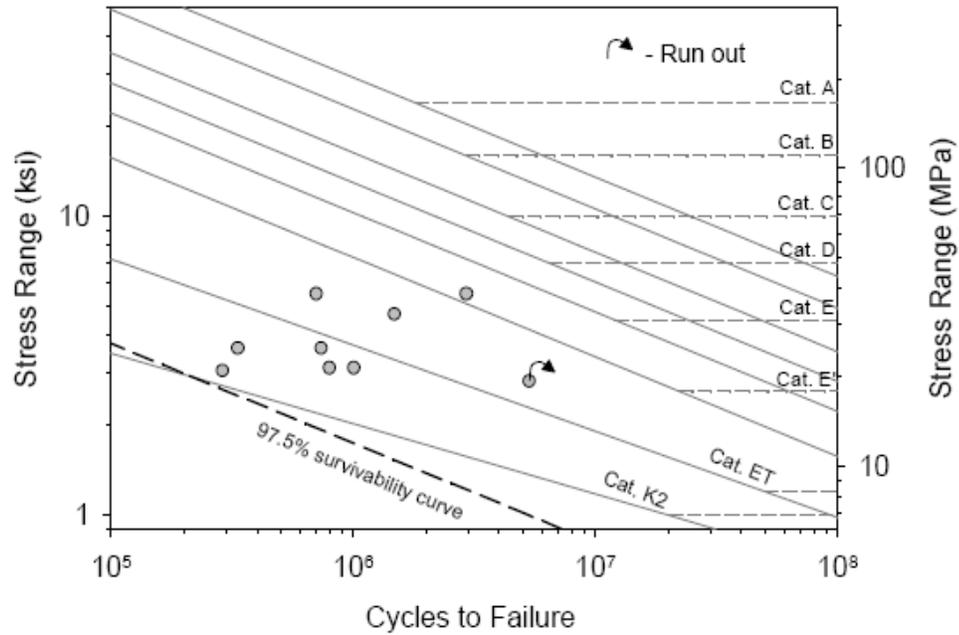
Figure 2.45: S-N plot for Type 2 pole (Ocel et al., 2006)

2.4.8 Rios (2007)

Rios (2007) performed full-scale fatigue testing on standard details used for pole-to-base plate connections in HML structures. The research was initiated in response to the fatigue failure of numerous HML structures around the United States that were designed using the *2001 Specifications*. The following four pole-to-base plate connection details were tested; fillet welded socket connection, Wyoming CJP detail, Texas CJP detail, and stool base connection detail. The pole specimens that were used were 24 in. diameter steel tapered tubes with 0.3125 in. wall thickness.

A total of sixteen specimens were tested using the four pole-to-base plate connection details, two bolt layouts, and four plate thicknesses. A matrix of the test specimens is shown in Table 2.9. Ten fillet welded socket connections as shown in Figure 2.46 were tested, all having unequal leg fillet welds and various base plate thicknesses and bolt layouts. Two different CJP welded details shown in Figure 2.46 were tested and are denoted the Wyoming CJP detail and

the Texas CJP detail. The Wyoming CJP detail used a backing bar that was fillet welded to the base plate and the weld root was sealed with a fillet weld from the top of the backing ring to the pole. The pole is then CJP welded to the base plate with an unequal leg reinforcing fillet weld on top. The Texas CJP detail did not use a backing ring to avoid the possibility of acid getting caught in between the base plate and pole wall during galvanizing. The pole base is butted up against the base plate and a fillet weld is made on the inside of the pole to the base plate and a CJP weld is then made from the pole to the base plate with an unequal leg reinforcing fillet weld on top.

Two specimens with a retrofitted socket connection called a stool base were also tested and are shown in Figure 2.47. The stool base detail consists of two vertical stiffening plates on each side of the bolt that are welded to a cap plate. The cap plate is welded to the pole wall and the anchor rods are threaded through the stool base and bolted down onto the cap plate. The actual pole-to-base connection is identical to the fillet welded connection detail.

Cracks in the fillet welded pole socket connections initiated at the weld toe in the extreme tension fiber and propagated around the pole. Specimens were determined to have failed when the resistance at the target displacement was reduced to 90% of the maximum resistance. Typically, cracks propagated 15 to 20 inches along the weld when failure was reached. It was found that the number of bolt holes and the base plate thickness had a major effect on the fatigue resistance. When the number of bolts was increased from 8 to 12, the fatigue life doubled in the 1.5 in. thick base plate specimens and almost tripled in the 2 in. thick base plate specimens. In the base plate specimens with 8 bolts, the fatigue life increased by 3.5 times when the base plate thickness was increased from 1.5 in. to 2 in. and increased by 10 times when the base plate thickness increased from 1.5 in. to 3 in.

All CJP welded specimens failed due to cracking that initiated at the weld toe of the CJP weld in the extreme tension fiber. Cracks propagated about 15 in. to 20 in. before failure was reached. The CJP welded details had better fatigue resistance than the fillet welded socket connection details and the Texas detail had 2 to 2.5 times the fatigue life of the Wyoming detail. However, because the Wyoming detail had a 2 in. thick base plate and the Texas detail had a 3 in. thick base plate, the fatigue life of the two CJP welded details cannot be directly compared due to the difference in base plate flexibility. The two stool base specimens tested had an 8 bolt hole pattern with a 2 in. thick base plate. Cracks propagated in these specimens at the toe of the

cap plate-to-pole fillet weld and propagated along the weld toe and into the pole wall. The fatigue resistance of this detail exceeded that of the fillet weld detail and the two CJP welded details.

Table 2.9: Test matrix for full scale HML connection specimens (Adapted from Rios, 2007)

Base Plate Size (in.)	Weld Type	Number of Specimens	
		8 bolts	12 bolts
1.5	Fillet	2	2
2.0	Fillet	2	2
2.0	CJP	2 (WY)	---
2.0 (with Stools)	Fillet	2	---
3.0	Fillet	2	---
3.0	CJP	---	2 (TX)
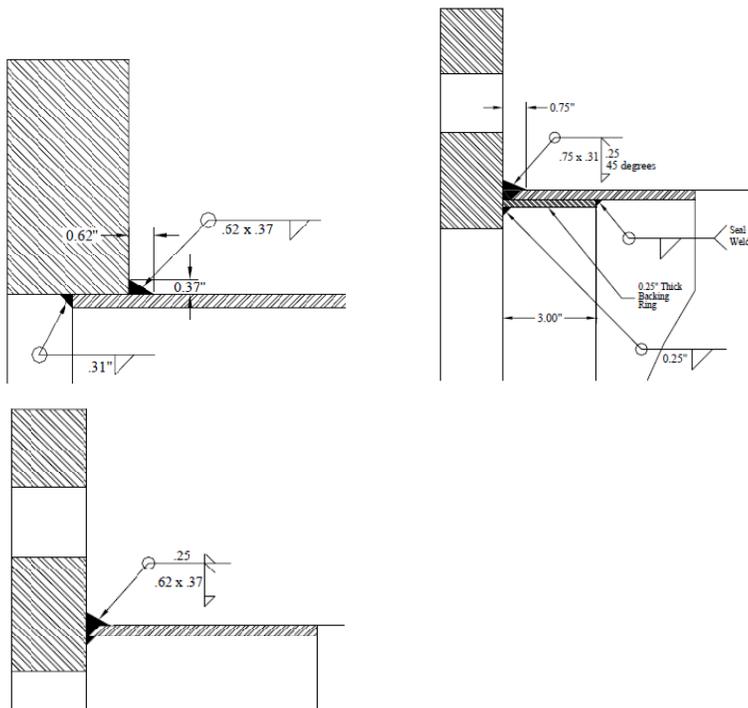
Figure 2.46: Drawings of fillet welded socket connection, Wyoming CJP connection, and Texas CJP connection (Rios, 2007)
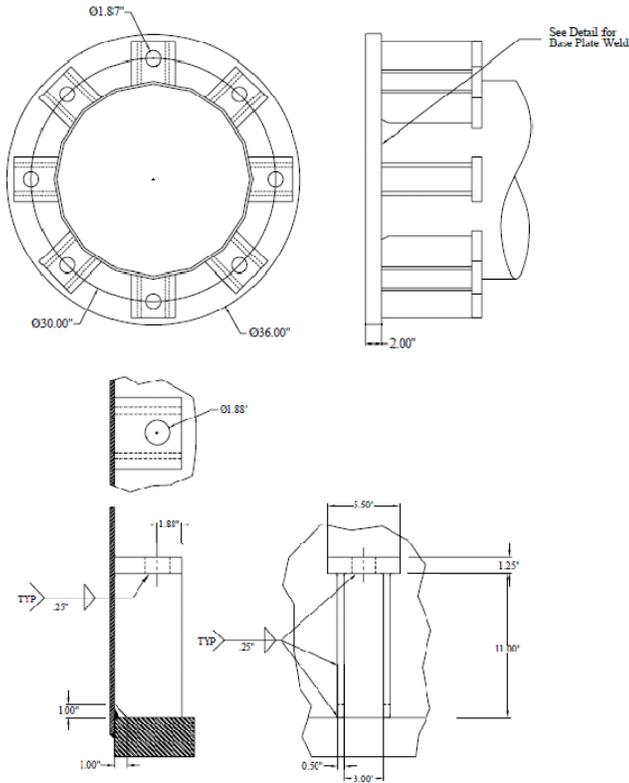
Figure 2.47: Drawing of stool base connection (Rios, 2007)

Figure 2.48 shows the fatigue data for all specimens plotted against the AASHTO fatigue life curves. The *2001 Specifications* classify all pole socket connections as Category E'. The tested pole socket connections performed well below Category E' regardless of base plate thickness and number of bolts. The *2001 Specifications* classify the CJP welded connections as Category E. The two tested CJP connections also performed below Category E regardless of base plate thickness and number of bolts. The data for the stool base connection plots close to the Category E line.
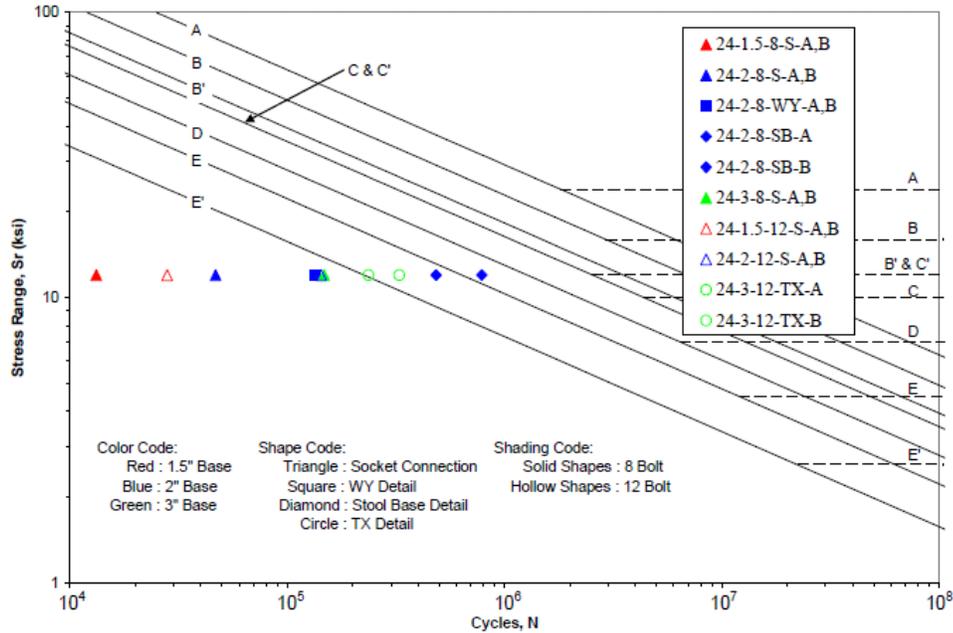
Figure 2.48: S-N curve for all connection details tested (Rios, 2007)

2.5 Analytical Fatigue Research

This section summarizes the analytical research pertaining to the fatigue life of luminaire support structures. The section includes finite element models developed for different types of support structures, development of reliability based methods for predicting, and the development of equations to account for the effect of base plate flexibility on fatigue life.

2.5.1 Foley *et al.* (2004)

This project was initiated in response to numerous failures of HML and bridge sign support structures as well as cracking in welded hollow structural shapes (HSS) in the state of Wisconsin. The purpose of the research was to determine a method for predicting the remaining life of fatigue sensitive details, determine the cause of cracking in failed support structures, establish rational inspection intervals, and recommend changes to HML design procedures that would improve performance. The development of a model to predict remaining life will be discussed in detail in Chapter 6.

An extensive finite element analysis of HML structures was initiated to determine the cause of cracking. The model was developed using ANSYS and included both modal analysis to determine the dynamic characteristics and stress analysis to determine the SCF in fatigue sensitive details. Based on the models, three important conclusions were drawn about the fatigue resistance of HML structures. The first conclusion was that the variation in base plate thickness had a much greater impact on the dynamic behavior of the structure than the standoff height of anchor rods. When the base plate was less than 1.5 in. thick, the higher mode frequencies differentiated greatly from the fixed base condition. This was not the case when anchor rod standoff heights were varied. The second important conclusion was that the eight anchor rod configuration performed much better than the four anchor rod configuration. The stresses in the mast walls were 40% greater with the four bolt configuration and the eight bolt configuration displayed a more uniform stress flow in the anchor rod connection. It was recommended that four anchor rod configurations should be avoided in HML structures. The third conclusion was that the SCF at the base of the HML should be considered for the static design of welds. The finite element analysis determined an SCF of 2.4 and 3.1 at the base of the two HML support structures modeled and it is recommended that a value of 3.0 be used.

It was also determined that HML structures need not be designed for vortex shedding lock-in. Vortex shedding lock-in did not occur during a one hour field observation of an HML structure subjected to 35 mph wind speeds. Due to decreasing shaft diameters, first mode vibrations due to natural wind gusts dominate the response. Ignoring vortex shedding lock-in greatly simplifies the design of these structures. The HML structures considered easily reached the 50 year design life when degradation of the cross-section due to corrosion was neglected. While corrosion of the anchor bolts is a concern, the design life model predicted a 264 year life for the anchor bolts. Therefore, even an anchor bolt with a reduced cross-section due to corrosion should not fail. Furthermore, if detailed inspection occurs during the welding and erection processes, inspection intervals of much longer than 2 years can be used for HMLs during their design service life.

2.5.2 Gilani and Whittaker (2000a)

Gilani and Whittaker (2000a) address the field monitoring of CMSs and analytical studies of critical details used in CMS support structures. The design fatigue stress range of a prototype CMS support structure was determined using the *1994 Specifications* and *NCHRP Report 412*.

66

The prototype structure had the dimensions shown in Figure 2.49. The mounting height of the CMS for the prototype structure was equal to the maximum height amongst all CMSs in California at the time so that maximum stress ranges would be computed. The *1994 Specifications* used static equivalent pressures to represent the wind loads and the prototype structure satisfied the strength, deflection, vibration, and fatigue requirements. However, the *1994 Specifications* did not include galloping in the fatigue design. The fatigue stress range computed using *NCHRP Report 412* was 7.3 ksi for the CJP welded pole-to-base plate connection and galloping was the controlling wind induced phenomena. The stress range of 7.3 ksi was higher than the CAFL for a Category E' detail, which was the classification for the CJP welded tube-to-transverse plate connection (2.6 ksi).
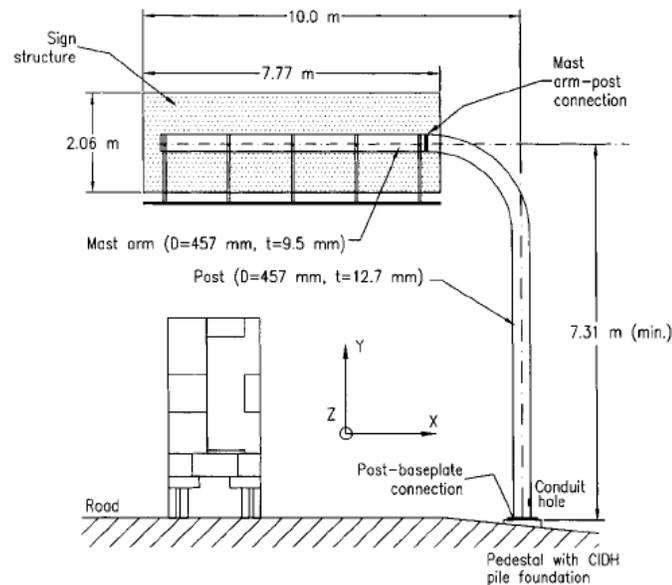
Figure 2.49: Dimensions used for CMS prototype (Gilani and Whittaker, 2000a)

Caltrans instrumented numerous CMSs located in high wind regions of California to determine the dynamic properties and response to wind loading. Gilani and Whittaker (2000a) participated in two of those studies. The first study was a pull-back test on a CMS support structure on Route 58 and the second study was continuous monitoring of a CMS support structure on Interstate 15 subjected to natural wind loads. The pull-back test consisted of pulling and quickly releasing the CMS support structure in the direction parallel to the direction of traffic to determine the dynamic characteristics. The first fundamental frequency and damping ratio were found to be 1.04 Hz and 0.7% respectively. The second fundamental frequency and damping ratio were found to be 1.10 Hz and 0.5% respectively. The first mode

shape corresponded to displacement of the mast arm in the vertical plane and the second mode shape corresponds to displacement of the mast arm in the horizontal plane. The location of strain gages, wind speed history, and stress history as recorded in strain gage SG1 are shown in Figure 2.50, Figure 2.51, and Figure 2.52.
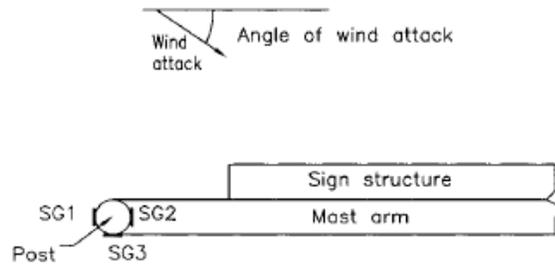
Figure 2.50: Instrumentation layout (Gilani and Whittaker, 2000a)
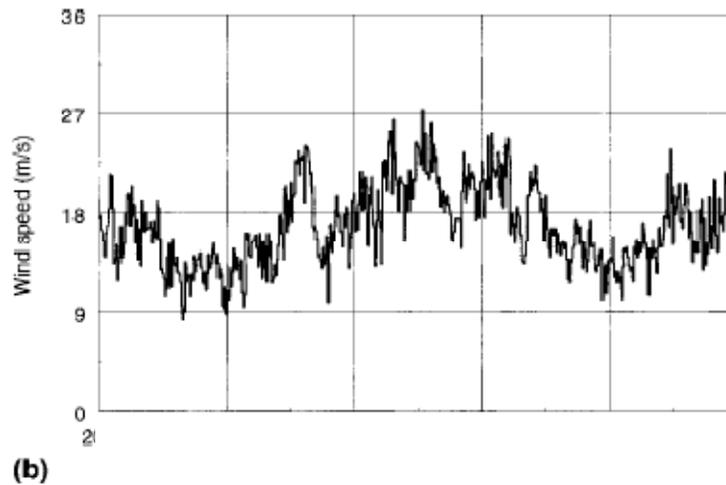
Figure 2.51: Recorded wind speed (Gilani and Whittaker, 2000a)
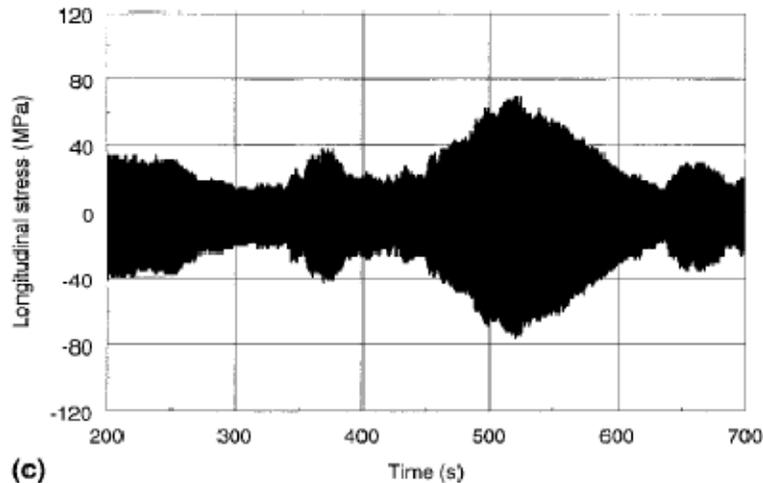
Figure 2.52: Longitudinal stress history in strain gage SG1 (Gilani and Whittaker, 2000a)

In Figure 2.52 dynamic amplification can be seen between 460 and 520 seconds. In this 60 second period, there is no major change in wind speed while the longitudinal stress amplitude increases. During this period of instability, the frequency of vibration was 1.04 Hz, which was consistent with the frequency of first mode vibration. Since vortex shedding was rarely seen in this type of structure, it was concluded that the dynamic amplification could be attributed to galloping. The maximum longitudinal stress range measured was 20 ksi (137.9 MPa). This stress range was higher than the equivalent static stress range computed for this structure using both the *1994 Specifications* (0.8 ksi) and almost double the value computed using *NCHRP Report 412*. Furthermore, this nominal stress range in the pole-to-base plate connection was significantly higher than the CAFL for a CJP welded tube-to-transverse plate detail.

A finite element analysis was performed on the bottom of the pole structure to determine the location and magnitude of stress concentrations. The model used eight-node solid elements and was performed in SAP2000. The finite element mesh used is shown in Figure 2.53. A single 1 kip unidirectional horizontal load was applied in the direction perpendicular to the face of the conduit hole. The analysis was performed with two different values for Poisson's ratio; 0.3 and 0. The longitudinal and von Mises stress distributions along three different paths for the model run with a Poisson's ratio of 0.3 are shown in Figure 2.54 and Figure 2.55 respectively. The values predicted by elementary beam theory (EBT) are also included. Figure 2.56 defines the paths used in the two plots. The flexural stresses along line B exceed those predicted by EBT by a factor of 3 at the conduit hole. The highest stress range was located at the conduit hole. The stress at the base connection was about 60% higher than predicted by EBT. This was most

69

likely due to restraint from the base plate which caused a nonlinear longitudinal and von Mises stress distribution in the pole. To confirm this, the Poisson's ratio in the model was changed to zero to eliminate the base plate restraint. This reduced the longitudinal and hoop stresses at the base of the pole. However, the stresses were still higher than predicted by EBT.
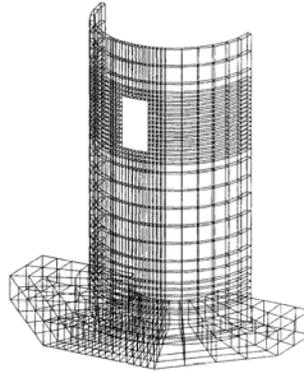
Figure 2.53: Finite element model of the bottom of the pole (Gilani and Whittaker, 2000a)
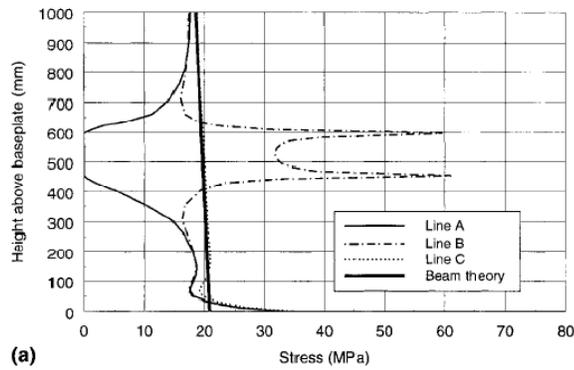
Figure 2.54: Longitudinal stress distribution in bottom of the pole (Gilani and Whittaker, 2000a)
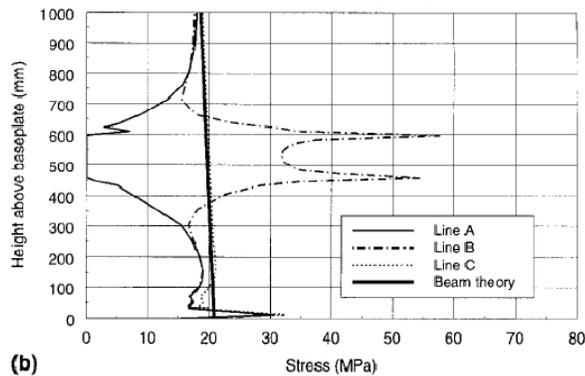
Figure 2.55: von Mises stress distribution in bottom of the pole (Gilani and Whittaker, 2000a)
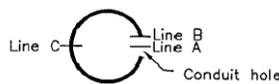
Figure 2.56: Definition of paths used in stress distributions (Gilani and Whittaker, 2000a)

A model was also developed to investigate the effect of conduit hole geometry on the SCF. Three different cutout geometries were modeled into a thick rectangular plate: a 4 in. wide by 6 in. tall rectangular hole, a 4 in. wide by 6 in. deep rectangular hole with 1 in. radius corners, and a 4 in. diameter circular hole. The three geometries produced SCFs of 3.5, 2.8, and 3.0 respectively. Since there was not a major variation in the SCF for different geometries, it was determined that geometry of a conduit hole did not have a major impact. However, a smaller conduit hole was found to have a smaller SCF regardless of geometry.

A third model was developed to investigate the effectiveness of implementing a gusset stiffened socket connection for reducing the stresses near the base plate. A steel pole from a CMS with a socket pole-to-base plate connection was modeled with 8 triangular gusset plates welded to the pole and base plate. Figure 2.57 shows a profile view and Figure 2.58 shows a plan view of the connection. A detail of the typical socket connection is shown in Figure 2.59. One of the gusset plates was cut shorter to accommodate the conduit hole. The gusset stiffeners reduced the longitudinal and von Misses stresses at locations away from the conduit hole including the pole-to-base plate weld. Stresses at the tips of the gusset stiffeners were not significantly larger than those in the unstiffened pole. However, at the location below the conduit hole and above the adjacent gusset stiffener, the maximum stress levels were not reduced from the case without stiffeners.
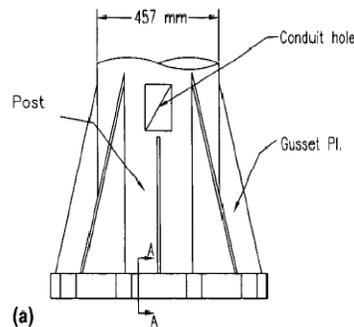
Figure 2.57: Profile of gusset stiffened socket connection (Gilani and Whittaker, 2000a)
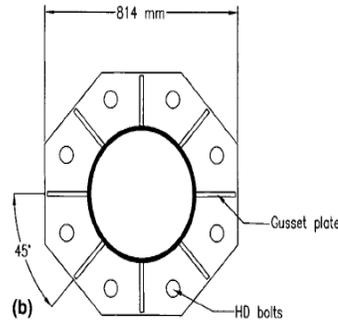
Figure 2.58: Plan of gusset stiffened socket connection (Gilani and Whittaker, 2000a)
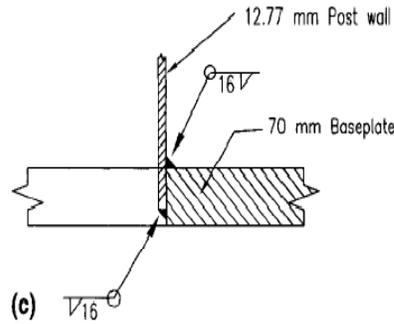
Figure 2.59: Socket connection detail (Gilani and Whittaker, 2000a)

2.5.3 Goode and van de Lindt (2007)

Goode and van de Lindt developed a reliability based framework for the design of HML structures. The framework relied on the results of dynamic response histories from finite element analyses. The forcing function in the response history analysis was determined from the drag term in Morrison's equation which relates the force caused when a fluid flows around a stationary slender body to the force on that body. The equation of motion for an HML structure subjected to wind induced forces is:

$$M\ddot{x} + C\dot{x} + Kx = \frac{1}{2}\rho_{air}AC_d u(t)|u(t)| \tag{2.12}$$

where M is the mass matrix, C is the damping matrix, K is the stiffness matrix, ρ_{air} is the mass density of air, A is the tributary projected area, C_d is the drag coefficient, and $u(t)$ is the wind velocity vector. The stress ranges resulting from the forcing function were determined using the finite element model and the expected damage over a time T was computed using the equation proposed by Crandall and Mark (1963):

$$E[D(T)] = \frac{v_o^+}{c}\left(2\sqrt{2}\sigma_y\right)^b \Gamma(1 + \frac{b}{2}) \tag{2.13}$$

where σ_y is standard deviation of the stress process, Γ is the gamma function, v_o^+ is the upcrossing rate of the stress process, and b and c are fatigue constants related to the material and base connection detail of the structure. Those constants were determined from the following equation:

$$NS^b = c \tag{2.14}$$

where N is the number of cycles at a stress range S. Finally, the Crandall and Mark equation was set equal to the damage accumulation equation proposed by Miner (1945):

$$F_{life} = \frac{1}{\sum_{i=1}^{n} F_i P_{Oi}} \tag{2.15}$$

where P_{Oi} is the probability of occurrence of the wind force for the ith wind speed causing the associated damage in Equation 2.13. The wind velocities used in the time history analysis were based on data obtained from NOAA and an assumed lognormal distribution for which the probability density function of wind velocities can be expressed as:

$$f_U(u) = \frac{1}{\sqrt{2\pi}\xi u}\exp\left[-\frac{1}{2}(\frac{\ln(u)-\lambda}{\xi})^2\right] \tag{2.16}$$

where the ξ is the lognormal standard deviation and λ is the lognormal mean. From these analyses, design charts were developed so that a level of HML reliability could be determined for given HML dimensions and wind conditions. The results of the reliability based framework were then compared to computer simulations and performed favorably.

2.5.4 Hall and Connor (2008)

Hall and Connor (2008) studied the impact of base plate thickness in pole socket connections and proposed a procedure for incorporating base plate thickness into the fatigue design provisions of the *2001 Specifications*. Base plate flexibility has a major impact on the SCF at the weld toe due to local bending stresses and it has been shown in previous experiments to impact fatigue life. The following is a summary of the procedure proposed by Hall and Connor (2008) for including base plate flexibility in fatigue design computations.

The procedure uses a flexibility parameter to relate the stiffness of the base plate to the SCF in the weld toe of the socket connection. The stiffness parameter is based on the assumption that the stiffness of the base plate correlates to the stiffness of an isolated portion of the base plate.

$$K = \frac{12S^3}{BT^3} \tag{2.17}$$

where S is the clear spacing between anchor nuts, B is the width of the base plate "beam" cross-section, and T is the base plate thickness and all dimensions are in mm. A graphic of these definitions is shown in Figure 2.60. The SCF for fatigue design is then computed using the following equation:

$$A_{FATDES} = 0.577(K + 14.926)^{0.347} \qquad (2.18)$$

This equation is based on a best fit curve relating the base plate stiffness parameter to the SCF in previous tests. The stress range for design is then determined using the following equation:

$$S_{rdesign} = \frac{A_{FATTEST}}{A_{FATDES}} * CAFL \qquad (2.19)$$

where $A_{FATTEST}$ is the stress range amplification factor from a fatigue test and $CAFL$ is the constant amplification fatigue limit determined from the *2001 Specifications*.
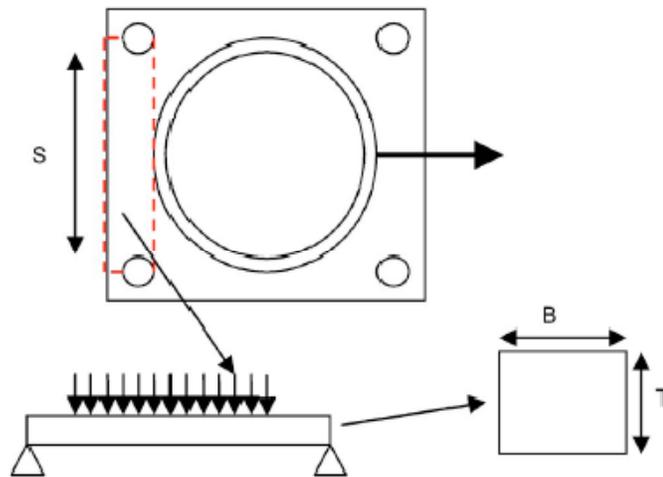
Figure 2.60: Definition of terms for the stiffness parameter equation (Hall and Connor, 2008)

2.5.5 Caracoglia and Velazquez (2008)

Caracoglia and Velazquez (2008) performed non-destructive field testing and finite element modeling to determine the dynamic characteristics of different luminaire structures. Table 2.10 shows the matrix of pole specimens studied. The dynamic characteristics for the first five modes of vibration for all four specimens were computed using a finite element model and analytical methods and are shown in Table 2.11. Free decay vibration tests were performed on

74

each specimen to determine the first and second mode vibration characteristics which are also shown in Table 2.11 and Table 2.12.

Using the experimental and analytical results, the following conclusions were drawn regarding the susceptibility of these structures to various wind induced phenomena. Steel and aluminum alloy poles generally have a fundamental frequency between 1 and 2 Hz and are not susceptible to high stress ranges resulting from natural wind gusts. Deflections were determined to be less than 5% of the length and maximum stresses were determined to be less than 70% of yield stress for 50 year return period winds. The GFRP luminaire was susceptible to vibrations of up to 10% of the length. Steel poles were not susceptible to vortex shedding in the fundamental mode because of the high mass or in the second mode because the frequency was around 5 Hz. Aluminum poles are more susceptible to vortex shedding and the use of mitigation devices was recommended. GFRP poles are not susceptible to vortex shedding. Steel poles are generally not susceptible to galloping because the critical wind velocities are higher than the 50 year return period winds. However, aluminum and GFRP poles above 13 m (42.2 ft) are susceptible to galloping.

Table 2.10: Pole specimens studied (Adapted from Caracoglia and Velazquez, 2008)

Specimen	Pole Material	Cross Section	Height m (ft)	Wall Thick. mm (in)	Base OD mm (in)	Top OD mm (in)	Damping Device
A	ASTM A595 Steel	16-sided	12.2 (40.3)	4 (0.1575)	241 (9.49)	102 (4.02)	---
B	GFRP Composite	circular	12.8 (42.2)	4 (0.1575)	254 (10.0)	127 (5.00)	---
C	GFRP Composite	circular	13.7 (45.2)	4 (0.1575)	254 (10.0)	152 (5.98)	1st Mode Damper
D	6063-T6 Aluminum	circular	12.2 (40.3)	6 (0.2362)	254 (10.0)	152 (5.98)	2nd Mode Damper

Table 2.11: Dynamic characteristics for first five modes (Caracoglia and Velazquez, 2008)

Mode	f_{jx} (Hz)	FE f (Hz)	Tests (Hz)	Diff. (%)	f_{jx} (Hz)	FE f (Hz)	Tests (Hz)	Diff. (%)
Specimen A: $\delta_D = 4$ mm, $M_L = 0$					Specimen A: $\delta_D = 4$ mm, $M_{(L1)} = 36$ kg			
1	1.78	1.79	1.63	−0.6	1.25	1.26	1.14	−1.0
2	7.97	8.01	7.20	−0.5	6.17	6.23	6.30	−1.0
3	20.10	20.19	–	−0.5	16.77	16.92	–	−0.9
4	38.16	38.21	–	−0.1	33.33	33.53	–	−0.6
5	62.23	61.90	–	0.5	55.87	55.90	–	−0.1

Details: Steel, $L = 12.2$ m, $D_{top} = 102$ mm, $D_{bot} = 241$ mm.

Mode	f_{jx} (Hz)	FE f (Hz)	Tests (Hz)	Diff. (%)	f_{jx} (Hz)	FE f (Hz)	Tests (Hz)	Diff. (%)
Specimen B: $\delta_{D,eq} = 6$ mm, $M_L = 0$					Specimen B: $\delta_{D,eq} = 6$ mm, $M_{(L1)} = 36$ kg			
1	1.40	1.39	1.20	0.6	0.73	0.78	0.63	−6.4
2	6.63	6.63	5.35	0.0	4.81	4.88	4.98	−1.4
3	17.05	17.01	–	0.3	13.90	13.96	–	−0.5
4	32.60	32.37	–	0.7	28.14	28.11	–	0.1
5	53.32	52.64	–	1.3	47.55	47.25	–	0.6

Details: GFRP, $L = 12.8$ m, $D_{top} = 127$ mm, $D_{bot} = 254$ mm, $d_{D,eq} = 6$ mm.

Mode	f_{jx} (Hz)	FE f (Hz)	Tests (Hz)	Diff. (%)	f_{jx} (Hz)	FE f (Hz)	Tests (Hz)	Diff. (%)
Specimen C: $\delta_{D,eq} = 8$ mm, $M_L = 0$					Specimen C: $\delta_{D,eq} = 8$ mm, $M_{(L2)} = 14$ kg			
1	1.19	1.19	1.12	−0.3	0.94	0.92	0.90	2.4
2	6.03	6.04	5.97	−0.2	5.01	5.00	5.05	0.2
3	15.83	15.82	–	0.1	13.70	13.72	–	−0.1
4	30.47	30.33	–	0.4	27.11	27.14	–	−0.1
5	49.98	49.46	–	1.0	45.33	45.23	–	0.2

Details: GFRP, $L = 13.7$ m, $D_{top} = 152$ mm, $D_{bot} = 254$ mm, $\delta_{D,eq} = 8$ mm.

Mode	f_{jx} (Hz)	FE f (Hz)	Tests (Hz)	Diff. (%)	f_{jx} (Hz)	FE f (Hz)	Tests (Hz)	Diff. (%)
Specimen D: $\delta_D = 5$ mm, $M_L = 0$					Specimen D: $\delta_D = 5$ mm, $M_{(L2)} = 14$ kg			
1	1.79	1.80	1.66	−0.5	1.45	1.39	1.21	4.3
2	9.10	9.16	8.58	−0.7	7.67	7.54	6.56	1.7
3	23.91	24.01	–	−0.4	20.91	20.76	–	0.7
4	46.00	45.97	–	0.1	41.32	41.07	–	0.6
5	75.47	74.87	–	0.8	69.03	68.39	–	0.9

Details: Aluminum, $L = 12.2$ m, $D_{top} = 152$ mm, $D_{bot} = 254$ mm.
FE: Finite Elements.

Table 2.12: Experimental results (Caracoglia and Velazquez, 2008)

Specimen		Luminaire mass (kg)	f_{1x} (Hz)[a]	$\zeta_{1x,Stuct}$ (%)[b]	f_{2x} (Hz)[a]	$\zeta_{2x,Stuct}$ (%)[b]
A	No damper	0.0	1.63	1.08	7.20	0.54
		35.8	1.14	0.85	6.30	0.46
B	No damper	0.0	1.19	1.07	5.35	0.52
		35.8	0.63	0.92	4.98	0.56
C	No damper	0.0	1.12	0.65	5.98	0.76
		13.0	0.90	0.48	5.05	0.53
	Chain damper	0.00	1.11	3.67	5.93	1.25
		13.0	0.89	2.87	5.03	1.40
D	No Damper	0.0	1.66	0.35	8.58	0.62
		12.7	1.22	0.27	6.29	0.46
	Chain damper	0.0	1.63	3.03	8.51	1.20
		12.7	1.21	1.36	6.32	1.16

[a] f_1 and f_2 derived by comparison FFT analysis with direct identification.
[b] ζ_1 and ζ_2 derived through comparison among different identification methods (Section 5).

Chapter 3 Experimental Setup

3.1 General

The following chapter describes the experimental design and setup used for luminaire support structure testing in the Structural Research Lab (SRL) at the University of Washington (UW). The objective of the experimental program was to assess the remaining service life of existing luminaire support structures in the state of Washington. The experimental program included both static and high cycle fatigue testing of two luminaire pole specimens. Specifically, the following section will describe the luminaire pole specimen selection process, provide details of the test specimens and setup, and summarize the instrumentation scheme.

3.2 Testing Program Objective

To make an accurate prediction of remaining service life for a given luminaire pole, three primary components are necessary; (1) a model must be developed that uses wind data from a specific location to estimate the number of cycles at different stress ranges in specific luminaire details over a given period of time, (2) a determination of the fatigue resistance of the given luminaire, and (3) a damage accumulation model that combines the first two components to predict the remaining life. The first component is beyond the scope of this project but the additional research needed to address it is summarized in Chapter 6. The testing program described here is directed at the second component and there is considerable research available in the literature to address the third component. The purpose of the testing program is to determine the behavior of characteristic luminaire poles subjected to static and high cycle horizontal loads and to assess the fatigue resistance of the critical details.

Two luminaires will be tested, which makes the scale of the testing program too small to produce static and high cycle fatigue data with a high ^{o} of statistical certainty. However, the static and high cycle fatigue testing program will provide useful data. The static testing data will provide an understanding of the flow of stress through the pole and around critical details and geometric discontinuities. SCFs can be determined and locations where high stress ranges may initiate fatigue cracking can be identified. An understanding of the static behavior will help to understand the high cycle fatigue behavior and potentially identify areas where retrofit

or repair procedures could reduce stress ranges and delay crack initiation. The high cycle fatigue data can be compared to the *2001 Specifications* to determine the applicability of the fatigue classifications to the characteristic luminaire pole being tested. The high cycle fatigue testing will also identify fatigue failure modes in the characteristic test poles and identify the locations of crack initiation and patterns of crack propagation. Common fabrication and welding defects that can cause crack initiation to develop may also be identified. Construction of a fatigue testing frame in the University of Washington SRL will also provide the Washington State Department of Transportation (WSDOT) with the capability of performing further luminaire pole testing in the future.

The static and fatigue testing will only cycle the luminaire pole and not the connected mast arm. Previous luminaire failures in the state of Washington occurred at the pole-to-base plate connection. Other failure modes identified in Chapter 2 such as failure of the mast arm-to-pole connection have not been observed in luminaires in Washington. Therefore, the fatigue testing will be focused on the pole-to-base connection, anchor bolts, and stiffened hand hole connection. Note that fatigue demand is influenced by the particular mast arm and pole combination; however, the fatigue resistance of the pole-to-base connection and other critical details is not. Once a fatigue resistance is determined for a given detail, an S-N curve can be used with a damage accumulation equation to estimate the remaining life of a specific pole and mast arm combination.

3.2 Selection of Luminaire Support Structure Test Specimens

Three primary criteria were developed to ensure that the test specimens would allow for an accurate assessment of the remaining service life. The test specimens had to be representative of luminaire poles currently in the field, be susceptible to high stress ranges from wind induced phenomena, and have a known service history. The importance of the three criteria will be discussed in greater detail along with a description of the selected test specimens.

Before discussing the three selection criteria, the availability of luminaire poles in good condition must be addressed. The availability of luminaire poles had as much of an impact on test specimen selection as the three criteria. The remaining life of damaged and/or corroded poles was beyond the scope of this research. Therefore, the test specimens could not have any damage beyond expected wear for an in-service luminaire pole. Also, poles that were currently

in-service would be difficult to remove from the field for testing. The selection of poles was limited to those available at the WSDOT bone yard. Poles in the bone yard were removed from the field to make way for construction or were removed because they were damaged. The test specimens chosen were the specimens in the bone yard that best satisfied the three selection criteria.

The first criterion was that the test specimen had to be representative of existing luminaire poles in the state of Washington. Since only two poles were tested, it was important that they were similar to the largest sample of poles possible. However, this posed a couple of challenges. WSDOT does not have an inventory of poles used throughout the state, and the poles are often fabricated by different manufacturers and had different dimensions, service conditions, and connection details. Those two factors made it difficult to quantitatively identify representative luminaire poles.

Instead, the determination of representative pole structures was made from information received by WSDOT field employees, data available from recent projects, and observations of poles at the WSDOT bone yard. From these sources, the following general pole characteristics were determined to be representative of the majority of luminaire poles in the state of Washington including:

1. 40 foot mounting heights with 12 foot mast arms;
2. slip fit mast arm-to-pole connections;
3. made of galvanized steel;
4. tapered poles with a circular cross-section;
5. CJP welded pole-to-base plate connection;
6. three sided base plate with breakaway base.

This list of general characteristics was used as a guideline for selecting the two test specimens from the WSDOT bone yard. The last important piece of information resulting from the qualitative assessment was that all luminaire failures occurred at the pole-to-base connection. From the literature, failure is expected in one of four places; the slip fit mast arm-to-column connection, the hand hole, the anchor bolts, or the pole-to-base plate connection. All these fatigue limit states could be tested with the exception of the mast-to-pole connection.

The second criterion was that the test specimens had to be subject to high fatigue stress ranges from wind induced phenomena while in-service. Specific combinations of poles and mast arms were identified that resulted in high fatigue stress ranges in the pole-to-base connection. An example is the best way to demonstrate susceptible combinations. WSDOT has a list of approved luminaire pole and mast arm combinations that were designed by different manufacturers in accordance with the *2001 Specifications*. The luminaire pole and mast arm combinations are displayed in a chart that gives all dimensions for a given mounting height and arm length. Table 3.1 shows a chart of approved combinations designed and manufactured by Valmont Industries.

The fatigue stress ranges for the Valmont Industries approved pole and mast arm combinations were computed using the *2001 Specifications* and assuming Fatigue Importance Category III. The calculations include a standard luminaire and standard highway sign and assume a double mast arm configuration. The standard luminaire has a projected vertical frontal area of 3.3 ft^2, a drag coefficient of 0.5, and a center of pressure located at the mounting height. The standard highway sign has a projected vertical frontal area of 10 ft^2, a drag coefficient of 1.2, and center of pressure located 9.5 ft. from the pole base. Since the poles were tapered, the controlling wind induced phenomenon was natural wind gusts. Figure 3.1 shows the stress ranges computed for all combinations in the Valmont Industries chart at the pole-to-base connection and an example calculation can be found in Appendix 2. The CAFL for AASHTO Category E is also plotted because the pole-to-base connection is CJP welded with the backing ring welded to the pole. Three important conclusions can be drawn from these fatigue stress range computations.

First, for a given mounting height, the stress range in the pole-to-base connection increases as the mast arm length increases. The natural wind gust pressure range is applied over the entire vertical projected area and luminaires with longer mast arms will have more vertical projected area than those with shorter mast arms. Therefore, specimens with longer mast arms will have larger moments at the pole-to-base connection for a given mounting height. Since all poles for a given luminaire mounting height have the same pole diameter and taper, there are specific combinations of mounting height and mast arm length that produce the largest bending stress range.

The second conclusion drawn from the stress range calculations for typical Valmont Industries manufactured WSDOT poles is that the stress range increases as the mounting height increases up to a height of 50 ft. As the mounting height increases, the vertical projected area and the lever arm increase causing the moment at the pole-to-base connection also to increase. However, as the luminaires get taller, the section modulus at the base increases as the diameter at the base increases. Since the nominal stress ranges shown from Figure 3.1 are computed at the pole base using the flexure formula:

$$\sigma = \frac{M}{S} \tag{3.1}$$

where M is the moment and S is the section modulus, it is clear that as the mounting height increases, the moment, section modulus, and fatigue stress range increase at the pole base. Therefore, it can be concluded that for the list of pole and mast arm combinations considered here, the increase in stress range resulting from a higher mounting height is greater than the increase in resistance from the increase in section modulus. It is important to note that this trend does not continue at the 50 ft. mounting height. At this height, Valmont Industries switches to a pole with a larger wall thickness, which significantly increases the section modulus.

The third conclusion drawn from Figure 3.1 is that the "DS90-WA-16S(D)-40" combination, which has the 40 ft. mounting height and 16 ft. arm length is the most susceptible to high fatigue stress ranges in this list of luminaires from Valmont Industries. This pole and mast arm combination represents the "sweet spot" just before the wall thickness increases. Valmont Industries reduces the maximum usable highway sign area for this combination from 10 ft^2 to 5 ft^2. The example was carried out simply to illustrate how critical mast arm and pole combinations can be identified from a given list of pole configurations or standard plans. While the experiments described here were only concerned with testing the lower portion of the luminaire poles, it is important to consider these critical combinations when selecting test specimens and when developing a framework to identify potentially critical luminaire support structures in the WSDOT inventory.

Table 3.1: List of approved pole and mast arm combinations manufactured by Valmont Industries

QTY.	CATALOG DESCRIPTION	H1 NOMINAL MOUNTING HEIGHT (±0'-6") "A"	ARM DESCRIPTION				POLE DESCRIPTION			
			ARM LENGTH "B"	ARM SHAFT			BASE O.D. "F"	TOP O.D. "G"	SHAFT LENGTH "H"	WALL GAUGE "J"
				BASE O.D. "C"	TOP O.D. "D"	LENGTH "E"				
	DS90-WA-6S (D)-30	30'-0"	6'-0"	5.41"	3.77"	11'-8"	8.05"	4.94"	22'-3"	11
	DS90-WA-8S (D)-30	30'-0"	8'-0"	5.41"	3.52"	13'-6"	8.05"	4.94"	22'-3"	11
	DS90-WA-10S (D)-30	30'-0"	10'-0"	5.41"	3.26"	15'-4"	8.05"	4.94"	22'-3"	11
	DS90-WA-12S (D)-30	30'-0"	12'-0"	5.41"	3.00"	17'-2"	8.05"	4.94"	22'-3"	11
	DS90-WA-14S (D)-30	30'-0"	14'-0"	5.41"	2.75"	19'-0"	8.05"	4.94"	22'-3"	11
	DS90-WA-16S (D)-30	30'-0"	16'-0"	5.41"	2.40"	21'-6"	8.05"	4.94"	22'-3"	11
	DS90-WA-6S (D)-35	35'-0"	6'-0"	5.41"	3.77"	11'-8"	8.75"	4.94"	27'-3"	11
	DS90-WA-8S (D)-35	35'-0"	8'-0"	5.41"	3.52"	13'-6"	8.75"	4.94"	27'-3"	11
	DS90-WA-10S (D)-35	35'-0"	10'-0"	5.41"	3.26"	15'-4"	8.75"	4.94"	27'-3"	11
	DS90-WA-12S (D)-35	35'-0"	12'-0"	5.41"	3.00"	17'-2"	8.75"	4.94"	27'-3"	11
	DS90-WA-14S (D)-35	35'-0"	14'-0"	5.41"	2.75"	19'-0"	8.75"	4.94"	27'-3"	11
	DS90-WA-16S (D)-35	35'-0"	16'-0"	5.41"	2.40"	21'-6"	8.75"	4.94"	27'-3"	11
	DS90-WA-6S (D)-40	40'-0"	6'-0"	5.41"	3.77"	11'-8"	9.45"	4.94"	32'-3"	11
	DS90-WA-8S (D)-40	40'-0"	8'-0"	5.41"	3.52"	13'-6"	9.45"	4.94"	32'-3"	11
	DS90-WA-10S (D)-40	40'-0"	10'-0"	5.41"	3.26"	15'-4"	9.45"	4.94"	32'-3"	11
	DS90-WA-12S (D)-40	40'-0"	12'-0"	5.41"	3.00"	17'-2"	9.45"	4.94"	32'-3"	11
	DS90-WA-14S (D)-40	40'-0"	14'-0"	5.41"	2.75"	19'-0"	9.45"	4.94"	32'-3"	11
	DS90-WA-16S (D)-40	40'-0"	16'-0"	5.41"	2.40"	21'-6"	9.45"	4.94"	32'-3"	11
	DS90-WA-6S (D)-50	50'-0"	6'-0"	5.41"	3.77"	11'-8"	10.85"	4.94"	42'-3"	10
	DS90-WA-8S (D)-50	50'-0"	8'-0"	5.41"	3.52"	13'-6"	10.85"	4.94"	42'-3"	10
	DS90-WA-10S (D)-50	50'-0"	10'-0"	5.41"	3.26"	15'-4"	10.85"	4.94"	42'-3"	10
	DS90-WA-12S (D)-50	50'-0"	12'-0"	5.41"	3.00"	17'-2"	10.85"	4.94"	42'-3"	10
	DS90-WA-14S (D)-50	50'-0"	14'-0"	5.41"	2.75"	19'-0"	10.85"	4.94"	42'-3"	10
	DS90-WA-16S (D)-50	50'-0"	16'-0"	5.41"	2.40"	21'-6"	10.85"	4.94"	42'-3"	10

S - SINGLE ARM   (D) - DOUBLE ARM   POLE AND ARM DATA
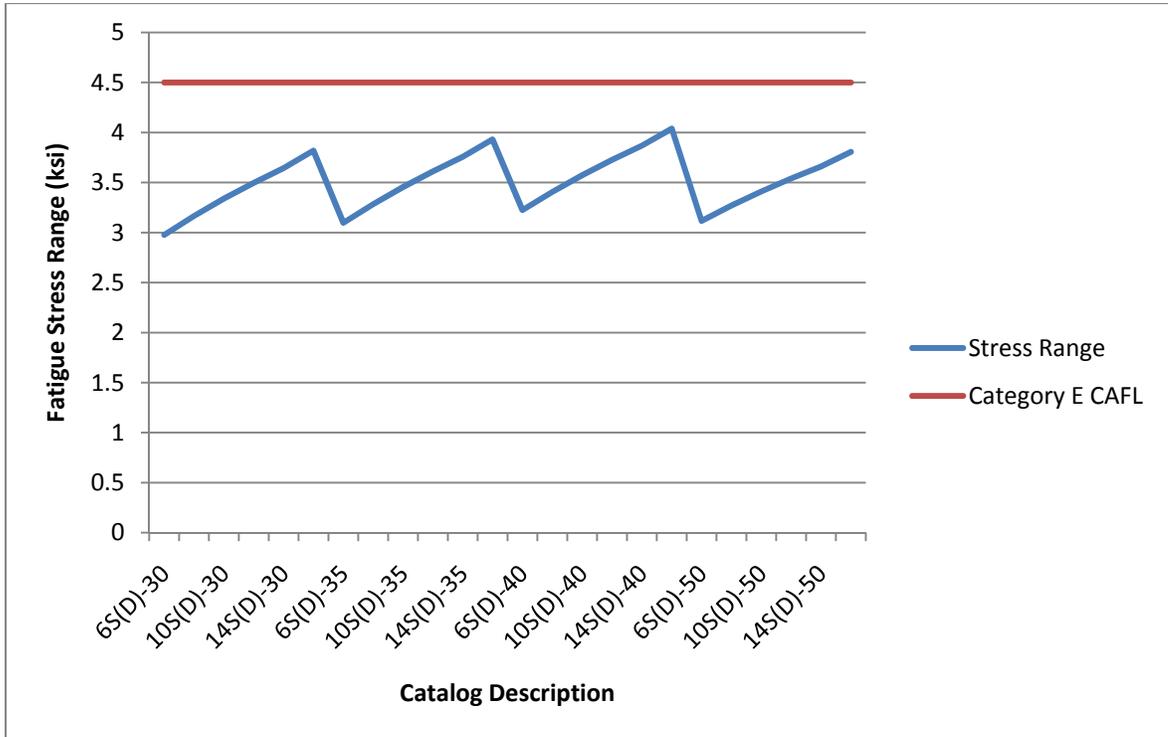
Figure 3.1: Nominal stress ranges at pole-to-base plate connection for Valmont Industries approved detail

The third criterion used for test specimen selection was that the test specimens must have reasonably well-known service histories, including locations and dates of installation. The stress range and number of cycles the selected luminaires had previously been subjected to is a function of the mean yearly wind speed and frequency of gusts. Mean yearly wind speed and frequency of gusts are a function of location. Therefore, location has a major impact on the stress range and number of cycles that the tested connection had been subjected to. A pole located in a region where the natural wind gusts produce few stress cycles above the CAFL of the connection will perform better in the laboratory than one that has seen many cycles above the CAFL. This information is important to calibrate test data so it can be compared to poles in other locations. The date of installation and date of removal are similarly important for approximating the number of stress cycles the structure has been subjected to prior to being tested in the laboratory.

3.3 Description of Test Specimens

Using the three selection criteria described above, two identical poles were selected from the WSDOT bone yard. The poles were recently removed from Washington State Route 16 for a new construction project. The selected luminaire poles were made out of 0.1280 in. thick galvanized steel. The poles had a taper of 0.108 in./ft. and an outside diameter of 9.43 in. at the base. The test specimens were originally part of a mast arm and pole combination with a mounting height of 40 ft. and mast arm length of 12 ft. The poles were cut in the WSDOT bone yard to a height of 15 ft. for transportation purposes. Specimen 1 and Specimen 2 were then cut to heights of 89.375 in. and 87.375 in. respectively at the SRL. These heights allowed the specimens to fit in the test frame and ensured that the ratio of bending moment to shear force remained sufficiently high.

The test specimens had a CJP welded pole-to-base plate connection with a fillet weld over the top. The CJP weld utilized a 1 in. tall by 0.25 in. thick backing ring that was tack welded to both the base plate and pole. The fillet weld was an unequal leg with a horizontal dimension of 0.375 in. and a vertical dimension of 0.5 in. A drawing of the tube-to-transverse plate weld is shown in Figure 3.2. The pole has a flame cut opening called a hand hole that provides access

to the utilities inside the pole with a centerline located 15.125 in. above the base plate in Specimen 1 and 13.750 in. above the base plate in Specimen 2. The pole height and hand hole location are the only geometric difference between the two specimens. The hand hole opening is an oval with a top and bottom curve radius of 2 in. The hand hole is stiffened with a 2.5 in. deep by 0.5 in. thick oval stiffening plate that is CJP welded to the inside of the hole. The hand hole is oriented on the side opposite the mast arm on a single armed pole and is above the single bolt side of the base plate. The only other detail on the bottom of the poles are CJP welded tube-to-tube splices located 7 in. above the base plates. These allow the pole-to-base plate connection to be shop welded.
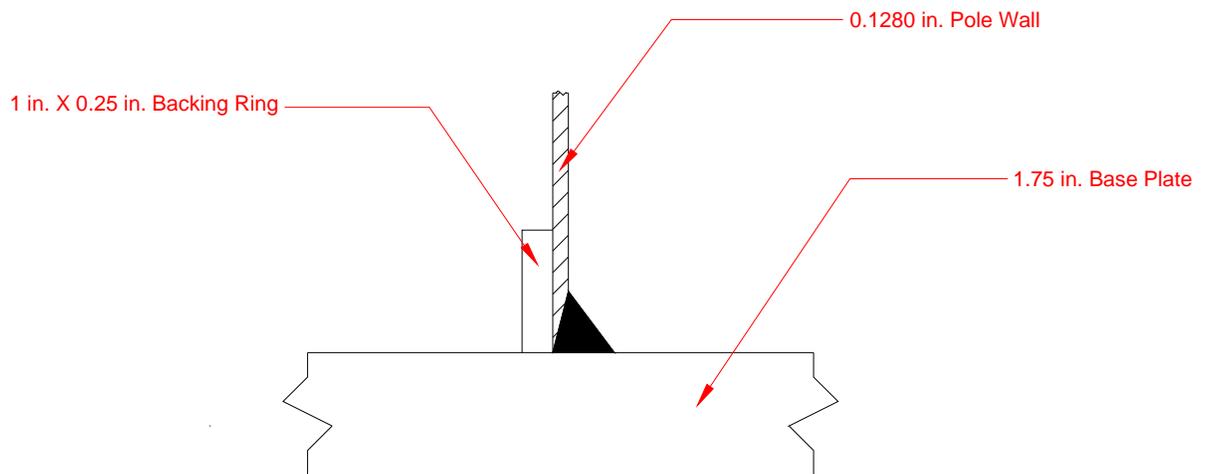
Figure 3.2: Detail of CJP welded pole-to-base plate connection

The base plate is a 1.75 in. thick steel triangular plate with a 6 in. diameter cutout in the center. A drawing of the base plate is shown in Figure 3.3. A keeper plate and a breakaway base are bolted below the base plate. The purpose of the breakaway plate is to prevent the pole from falling on vehicles when impacted. However, the breakaway plate was not used when testing the pole because the nominal stresses in the critical details were computed with the fixed base assumption. Bolting the base plate directly to the foundation better approximated the fixed boundary condition and would give a more accurate representation of the remaining fatigue life in critical details of the two luminaire poles.
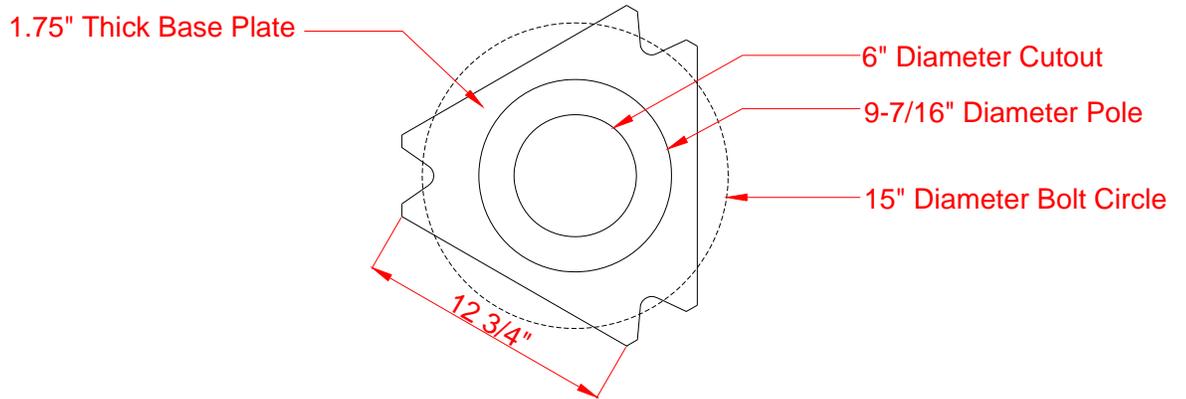
Figure 3.3: Schematic of triangular pole base plate

3.4 Test Setup

The test setup consisted of four primary components; (1) the reaction frame, (2) the actuator-to-pole connection beam, (3) the pole mounting plate, and (4) the hydraulic actuator. Figure 3.4 shows a schematic and Figure 3.5 shows a photograph of the full test frame. A description of the individual components is provided in the following section.
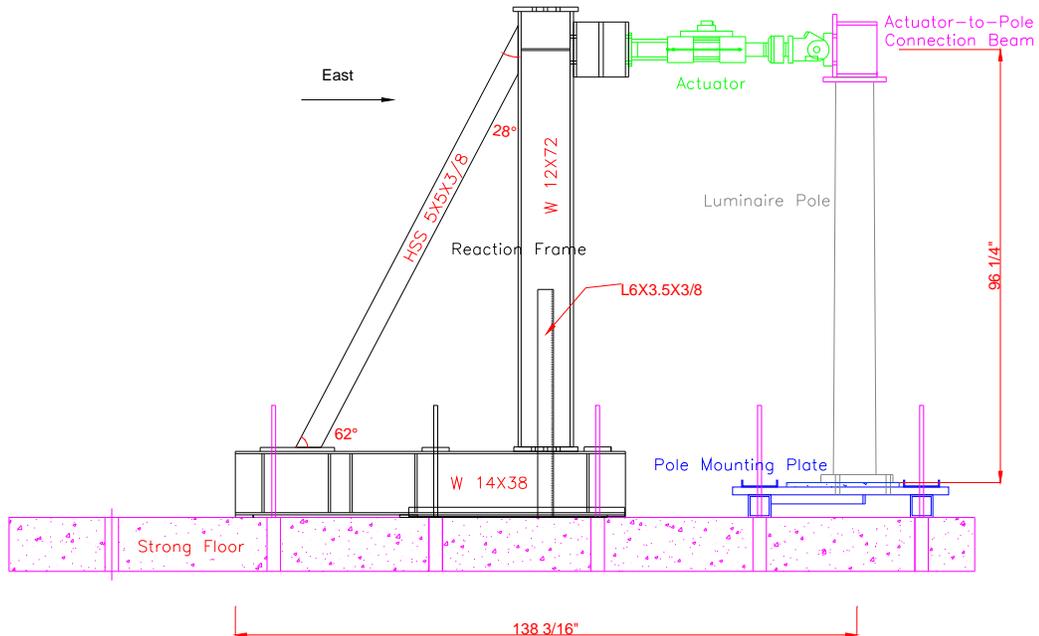
Figure 3.4: Profile view of test setup

Figure 3.5: Photograph of test setup with MTS controller

The purpose of the reaction frame was to ensure that no in-plane or out-of-plane deflection occurred at the west end of the actuator. The reaction frame had to be stiff enough to prevent any substantial deflection and had to have a fatigue resistance necessary to survive the testing of the two specimens. The reaction frame consisted of two W14x38 floor beams situated at a center-to-center spacing of 8.77 in. and seated on bearing plates on the strong floor. The frame was anchored to the strong floor by three 0.875 in. diameter threaded rods which passed between the two floor beams. The threaded rods were spaced at 36 in. and were threaded into holes 30 in. below the strong floor. The nuts at the top of the threaded rods sat on bearing plates that were welded to the two floor beams and the anchor rods were tensioned to 7 kips. The pretension provided the necessary normal force to ensure that the horizontal friction force between the steel floor beam and the concrete strong floor was large enough to resist the actuator force and prevent slip of the reaction frame.

A 105 in. tall W 12x72 column section was bolted to the floor beams with 3 snug-tightened A325 bolts on both sides of the web. A 106 in. long HSS 5X5X3/8 tube section was fillet welded to the floor beam on one end and to the flange of the column at the other end at an angle

of 62 °s above horizontal to provide in-plane resistance. A 62 in. long L 6X3.5X3/8 section was fillet welded to a channel section sitting on the strong floor on one end and to the web of the column at the other end at an angle of 54 °s above the horizontal to provide out-of-plane resistance. The channel sitting on the floor was bolted to the strong floor by two 0.875 in. diameter threaded rods which were tensioned to keep the channel section in place on the strong floor. A 12 in. W 12X72 stub beam was bolted to the column 89 in. above the floor beam. The stub beam was used to move the actuator away from the reaction frame so that it bolted to the pole close to its neutral length. The stub beam was heavily stiffened by 1 in. thick transverse stiffeners. Transverse stiffeners were also welded to the column section at the location where the stub beam was bolted to the column.

The actuator-to-pole connection beam was a 9 in. long section of a W 12X72 shape as shown in Figure 3.6. The actuator-to-pole connection beam had a 1in. thick mounting plate continuously fillet welded all around to the front of the beam. The mounting plate had holes that matched the holes on the actuator swivel. A 1 in. thick welding plate was then bolted to the bottom of the actuator-to-pole connection beam to provide a clean welding surface for the two test specimens. The top of the luminaire pole was continuously fillet welded to this plate. The connection beam ensured that the horizontal actuator load was directly applied to the top of the pole. Figure 3.6 also shows a photograph of the assembled connection beam.
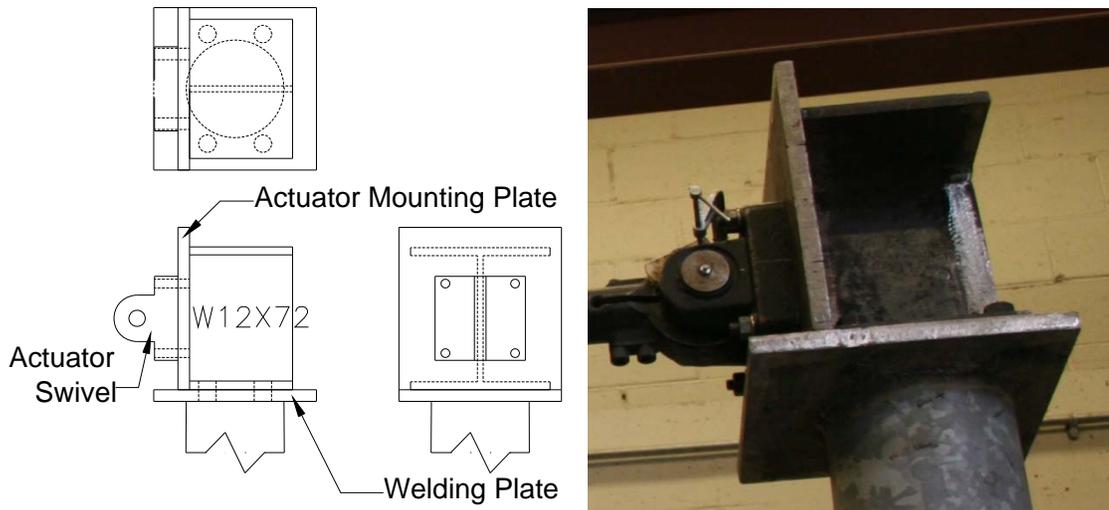
Figure 3.6: Schematic and photograph of the actuator-to-pole connection

The purpose of the luminaire pole mounting plate was to raise the pole base plate off the strong floor so that the anchor bolts were accessible from underneath the base plate for the two test specimens. To preserve the fixed base boundary condition, no rotation of the pole mounting plate could occur during testing. The pole mounting plate was studied comprehensively to develop a design that would both eliminate rotation and still allow access to the anchor bolts. A finite element model in MSC Marc was developed to determine the rotational stiffness of different mounting plate configurations, the final version of which is shown in Figure 3.7. The performance criteria for the luminaire pole mounting plate was such that the deflection at the tip of the pole due to rotation of the mounting plate had to be less than 10% of the expected elastic displacement resulting from the applied actuator force.
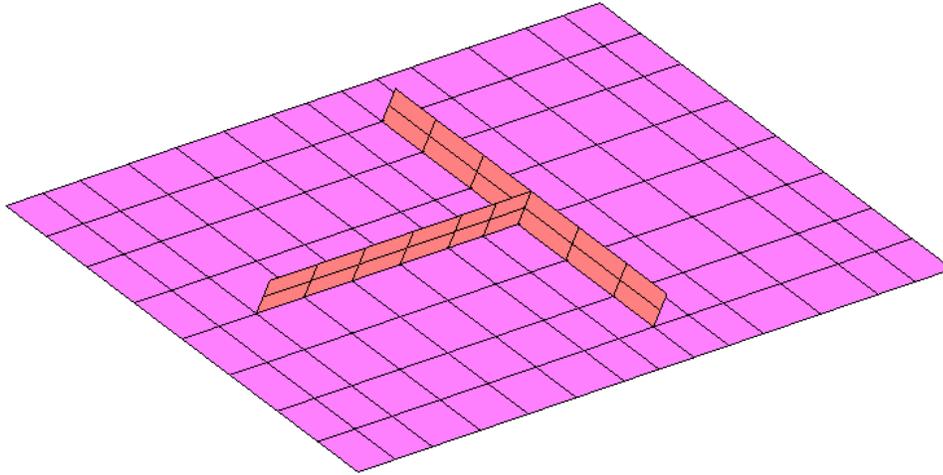
Figure 3.7: Finite element mesh of the luminaire pole mounting plate

The final design for the luminaire pole mounting plate consisted of a 24 in. X 48 in. X 1.75 in. thick steel plate seated on and fillet welded to two 2 ft. HSS 5X5X3/8 sections spaced at 36 in. and is shown in the schematic in Figure 3.8 and the photograph in Figure 3.9. The two HSS sections had wall stiffeners welded on to prevent buckling of the tube wall when the threaded rods were tensioned. Both a longitudinal and a transverse stiffener were welded to the bottom of the pole mounting plate in a "T" configuration. The longitudinal stiffener was 24 in. X 2 in. X 0.5 in. thick and the transverse stiffener was 20.5 in. X 2 in. X 0.5 in thick. Three 1.25 in. diameter holes were drilled in a triangular configuration to receive the anchor bolts. Two C 8X1.5X3/8 channel sections were placed on top of the mounting plate at 36 in. spacing to provide additional stiffness to the plate although they were not included in the finite element

model. Two 1 in. diameter threaded rods were used on each side to connect the channel, mounting plate, and HSS tube section to the strong floor. The threaded rods were tensioned to 7 kips to prevent any slip of the luminaire pole mounting plate assembly. Each specimen was leveled, squared with the actuator, and a base of hydro stone was poured between the luminaire base plate and the luminaire mounting plate. This was done to ensure that the pole would be plumb and that the luminaire base plate would be sitting on a uniform bearing surface.
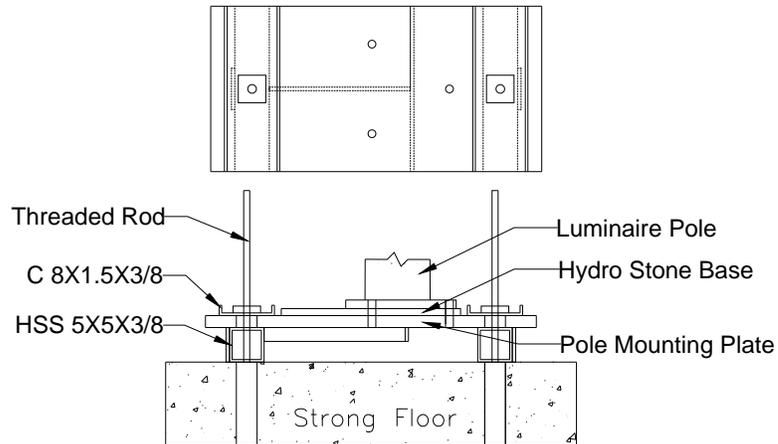
Figure 3.8: Schematic of pole mounting plate

Figure 3.9: Photograph of assembled luminaire pole mounting plate

The actuator used was an MTS 244.21 hydraulic actuator which has an 11 kip capacity and 6 in. stroke. The actuator is fatigue rated and can be run at the required frequencies. The actuator was used with a pedestal base on the reaction frame side and a swivel end on the luminaire pole side. A schematic and photograph of the actuator are shown in Figure 3.10. The testing was

run in load control, which is ideal for fatigue testing where the applied actuator force must remain constant throughout the test to ensure a constant nominal stress range. Displacement control causes problems for fatigue testing because the load decreases when the stiffness of the structure decreases. When run in load control, the nominal stress range will be constant and the displacement will increase as the stiffness of the specimen decreases. The actuator ran at a frequency of 2.0 Hz at a load range of 1.24 kips about a mean of 0 kips in Phase I and at a frequency of 0.6 Hz and 1.0 Hz at a load range of 2.48 kips about a mean of 0 kips in Phase IIa and Phase IIb respectively. These values corresponded to a stress range at the extreme tension fiber at the CJP weld toe of 13.78 ksi and 27.56 ksi in Specimen 1 during Phase I and Phase II respectively and 13.72 ksi and 27.44 ksi in Specimen 2 during Phase I and Phase II respectively. The slight decrease in the stress range in Specimen 2 is because slightly more hydro stone was used in Specimen 2 than in Specimen 1 slightly reducing the distance from the actuator centerline to the CJP weld toe.
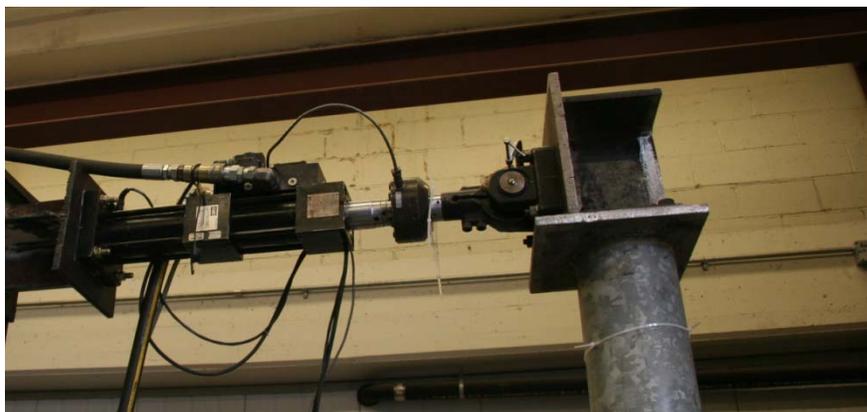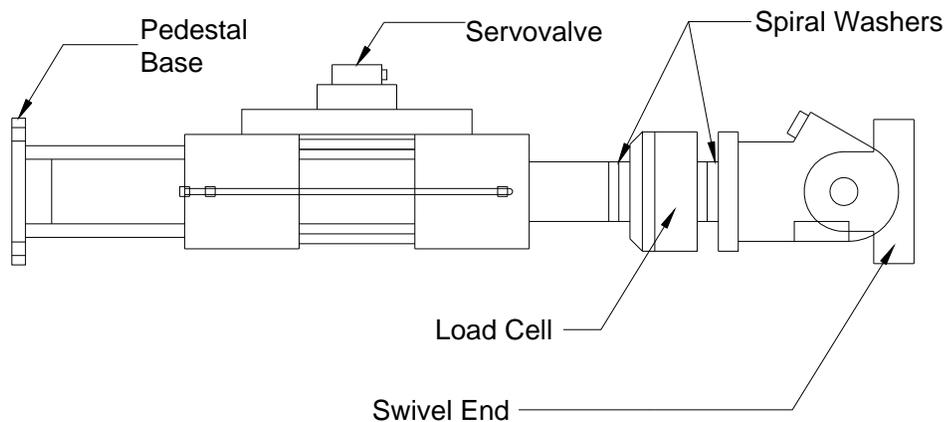
Figure 3.10: Schematic and photograph of MTS 244.21 hydraulic actuator

3.5 Specimen Installation Procedure

A specific procedure was followed for installation of the luminaire pole specimens to ensure that the specimens were properly aligned with the actuator centerline and leveled. This was necessary to ensure that no out of plane bending or torsional effects would occur in the pole specimen causing the nominal stress ranges to deviate from the computed values.

1. The pole specimens were cut to size (89.375 in. for Specimen 1 and 87.375 in. for Specimen 2) and bolted down to the luminaire pole mounting plate.
2. The actuator-to-pole connection beam was then balanced on top of the luminaire pole and bolted to the actuator swivel.
3. The actuator-to-pole connection beam was leveled using shims and aligned with the actuator centerline.
4. The top of the luminaire pole was tack welded to the welding plate on the bottom of the actuator-to-pole connection beam.
5. The actuator-to-pole connection beam was unbolted from the actuator swivel and the pole base plate was unbolted from the luminaire pole mounting plate.
6. The luminaire pole specimen (with the actuator-to-pole connection beam now connected with a tack weld) was removed from the test frame and set horizontally on the ground.
7. The shims were removed and the top of the luminaire pole was continuously fillet welded to the welding plate on the bottom of the actuator-to-pole connection beam.
8. The luminaire pole specimen with the welded actuator-to-pole connection beam was then placed back into the reaction frame and bolted to the actuator swivel but not to the luminaire pole mounting plate.
9. The luminaire pole was then picked up by the crane and maneuvered so that the actuator swivel was leveled and the pole was plumb.
10. Shims were then placed underneath the base plate and the anchor bolts were tightened.
11. Hydro stone was poured underneath the base plate to ensure a consistent bearing surface between the pole base plate and the pole mounting plate.

3.6 Instrumentation Scheme

An extensive instrumentation scheme was used to determine the static flow of stresses through the pole and to track the material behavior throughout the duration of the high cycle fatigue tests. Four types of instruments were used in the testing setup; strain gages, string potentiometers, Duncan potentiometers, and inclinometers. The instrumentation setup had five primary purposes:

1. verify that the force in the load cell produced the expected nominal strains in the pole as computed by the flexure formula;
2. track the stress flow around critical details and determine SCFs;
3. measure the material degradation at various locations throughout the duration of the test;
4. measure the deflected shape of the pole;
5. ensure no slip occurs in the testing frame.

The following is a description of the strain gage and potentiometer layouts used. Drawings of the exact instrument locations are included as well as a description of the purpose of individual instruments.

Slightly different strain gage layouts were used for Specimen 1 and Specimen 2. 38 uniaxial strain gages were used for Specimen 1 and 32 uniaxial strain gages and 5 strain gage rosettes were used for Specimen 2. The strain gages were concentrated around the pole base and at the hand hole. The geometry and welding at the CJP welded tube-to-transverse plate connection and the hand hole opening causes stress concentrations and are the most likely locations for crack initiation. The strain gage data was to:

1. determine the variation in stress between the inside and the outside of the pole wall;
2. determine the SCF at the weld toe;
3. determine the stress in the backing ring;
4. determine whether the maximum stresses at the weld toe occur at the extreme fibers from the neutral axis or if the butterfly trend is evident as identified in previous research;
5. determine the stress along a path in the extreme tension fiber on the pole wall opposite the hand hole and compare it to EBT and finite element analysis.

Table 3.2 shows the list of strain gages used in each test. Figure 3.11 shows the location of the cross-sections on the pole where the strain gages are located and Figure 3.12 and Figure 3.13 shows the strain gage layout at the individual cross-sections and hand hole respectively. Since the luminaire poles behaved elastically, the strain data could easily be converted to stress by multiplying by the modulus of elasticity of steel (29,000 ksi). Different layouts were used in Specimen 1 and Specimen 2. Specimen 1 had a higher concentration of gages at the pole base and used uniaxial strain gages around the hand hole. Specimen 2 used fewer strain gages at the pole base but used strain gage rosettes around the hand hole and a line of strain gages between the base plate and the mid-height of the pole at the 90 and 270 $^\circ$ cross-section locations.

Identical potentiometer layouts were used for the two test specimens and are shown in Figure 3.14 and Figure 3.15 for the Duncan potentiometers and the string potentiometers and inclinometers, respectively. The list of potentiometers used is shown in Table 3.3. Thirteen potentiometers were used for each test including the MTS load cell and MTS LVDT. Three string potentiometers were used at heights of 38 in., 72 in., and 92.375 in. above the luminaire pole mounting plate. The purpose of the string potentiometers was to determine the deflected shape of the pole during testing and to compute the pole stiffness. These measurements also made it possible to determine the decrease in stiffness as the pole began to crack. The string potentiometer at 92.375 in. above the base plate connected to the web of the actuator-to-pole connection beam. Since the actuator-to-pole connection beam was considered to be rigid, the deflection in this string potentiometer could be used to verify the MTS LVDT readings. Two inclinometers were used to determine the pole rotation at 36 in. and 84 in. above the base plate. Finally, six Duncan potentiometers were used to measure the slip in critical elements of the test setup. The Duncan potentiometers measured slip of the pole base plate, vertical deflection of the pole mounting plate, and slip of the HSS 5X5X3/8 bearing tubes. The data from the Duncan potentiometers was checked to make sure no significant deflection or slip was occurring during testing and was not used for any of the test data analysis.

Table 3.2: Strain gage list

Gage Designation	Gage Type	Gage Location	Test Specimen 1	Test Specimen 2
BR_1	Uniaxial	Backing Ring Inside 90 Degrees	X	
BR_2	Uniaxial	Backing Ring Inside 300 Degrees	X	
WT_3	Uniaxial	Weld Toe Outside 30 Degrees	X	
WT_4	Uniaxial	Weld Toe Outside 60 Degrees	X	X
WT_5	Uniaxial	Weld Toe Outside 90 Degrees	X	X
WT_6	Uniaxial	Weld Toe Outside 120 Degrees	X	X
WT_7	Uniaxial	Weld Toe Outside 150 Degrees	X	
WT_8	Uniaxial	Weld Toe Outside 210 Degrees	X	
WT_9	Uniaxial	Weld Toe Outside 240 Degrees	X	X
WT_10	Uniaxial	Weld Toe Outside 270 Degrees	X	X
WT_11	Uniaxial	Weld Toe Outside 300 Degrees	X	X
WT_12	Uniaxial	Weld Toe Outside 330 Degrees	X	
1.5_13	Uniaxial	1.5 in. Above Base Plate Inside 90 Degrees	X	X
1.5_14	Uniaxial	1.5 in. Above Base Plate Inside 300 Degrees	X	X
2.625_15	Uniaxial	2.625 in. Above Base Plate Outside 30 Degrees	X	
2.625_16	Uniaxial	2.625 in. Above Base Plate Outside 60 Degrees	X	X
2.625_17	Uniaxial	2.625 in. Above Base Plate Outside 90 Degrees	X	X
2.625_18	Uniaxial	2.625 in. Above Base Plate Outside 120 Degrees	X	X
2.625_19	Uniaxial	2.625 in. Above Base Plate Outside 150 Degrees	X	
2.625_20	Uniaxial	2.625 in. Above Base Plate Outside 210 Degrees	X	
2.625_21	Uniaxial	2.625 in. Above Base Plate Outside 240 Degrees	X	X
2.625_22	Uniaxial	2.625 in. Above Base Plate Outside 270 Degrees	X	X
2.625_23	Uniaxial	2.625 in. Above Base Plate Outside 300 Degrees	X	X
2.625_24	Uniaxial	2.625 in. Above Base Plate Outside 330 Degrees	X	
5.5_25	Uniaxial	5.5 in. Above Base Plate Outside 60 Degrees	X	X
5.5_26	Uniaxial	5.5 in. Above Base Plate Outside 90 Degrees	X	X
5.5_27	Uniaxial	5.5 in. Above Base Plate Outside 120 Degrees	X	X
5.5_28	Uniaxial	5.5 in. Above Base Plate Outside 240 Degrees	X	X
5.5_29	Uniaxial	5.5 in. Above Base Plate Outside 270 Degrees	X	X
5.5_30	Uniaxial	5.5 in. Above Base Plate Outside 300 Degrees	X	X

Gage Designation	Gage Type	Gage Location	Test Specimen 1	Test Specimen 2
5.5_31	Uniaxial	5.5 in. Above Base Plate Inside 90 Degrees	X	X
5.5_32	Uniaxial	5.5 in. Above Base Plate Inside 300 Degrees	X	X
8.0_33	Uniaxial	8.0 in. Above Base Plate Outside 90 Degrees		X
8.0_34	Uniaxial	8.0 in. Above Base Plate Outside 270 Degrees		X
9.25_35	Uniaxial	9.25 in. Above Base Plate Outside 90 Degrees		X
9.25_36	Uniaxial	9.25 in. Above Base Plate Outside 270 Degrees		X
13.0_37	Uniaxial	13.0 in. Above Base Plate Outside 270 Degrees		X
16.0_38	Uniaxial	16.0 in. Above Base Plate Outside 270 Degrees		X
20.0_39	Uniaxial	20.0 in. Above Base Plate Outside 90 Degrees		X
20.0_40	Uniaxial	20.0 in. Above Base Plate Outside 270 Degrees		X
45.0_41	Uniaxial	45.0 in. Above Base Plate Outside 90 Degrees	X	
45.0_42	Uniaxial	45.0 in. Above Base Plate Outside 270 Degrees	X	
48.0_43	Uniaxial	48.0 in. Above Base Plate Outside 90 Degrees		X
48.0_44	Uniaxial	48.0 in. Above Base Plate Outside 270 Degrees		X
HH_45	Rosette	Top of Hand Hole 180 Degrees		X
HH_46	Rosette	Top of Hand Hole 135 Degrees		X
HH_47	Rosette	Top of Hand Hole 90 Degrees	X (Uniaxial)	X
HH_48	Rosette	Top Left of Hand Hole 0 Degrees		X
HH_49	Rosette	Top Left of Hand Hole 45 Degrees		X
HH_50	Rosette	Top Left of Hand Hole 90 Degrees		X
HH_51	Rosette	Top Right of Hand Hole 180 Degrees		X
HH_52	Rosette	Top Right of Hand Hole 135 Degrees		X
HH_53	Rosette	Top Right of Hand Hole 90 Degrees		X
HH_54	Rosette	Left of Hand Hole 180 Degrees		X
HH_55	Rosette	Left of Hand Hole 135 Degrees		X
HH_56	Rosette	Left of Hand Hole 90 Degrees	X (Uniaxial)	X
HH_57	Rosette	Right of Hand Hole 0 Degrees		X
HH_58	Rosette	Right of Hand Hole 45 Degrees		X
HH_59	Rosette	Right of Hand Hole 90 Degrees	X (Uniaxial)	X
HH_60	Uniaxial	Bottom of Hand Hole	X	
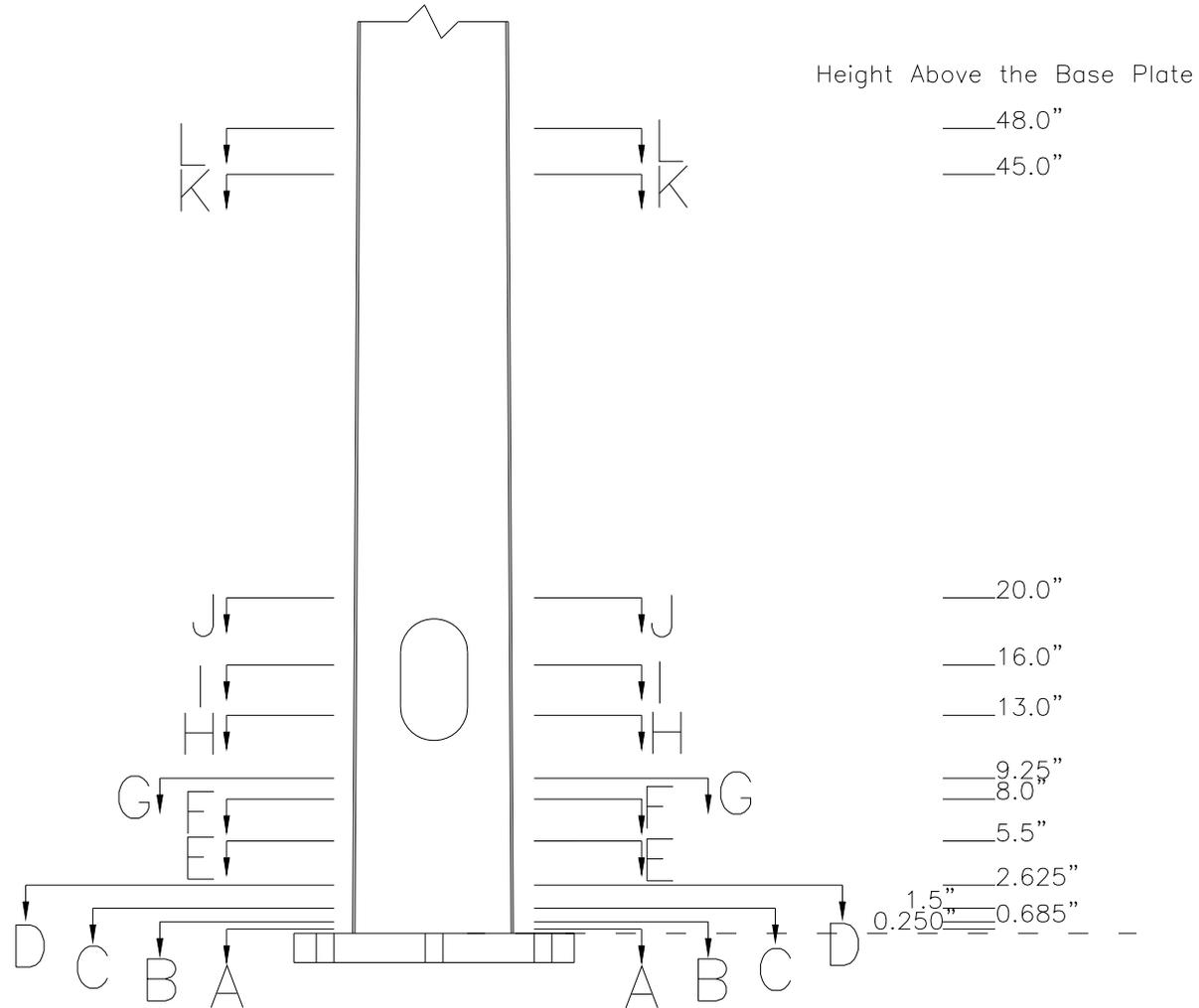
Figure 3.11: Location of pole cross-sections
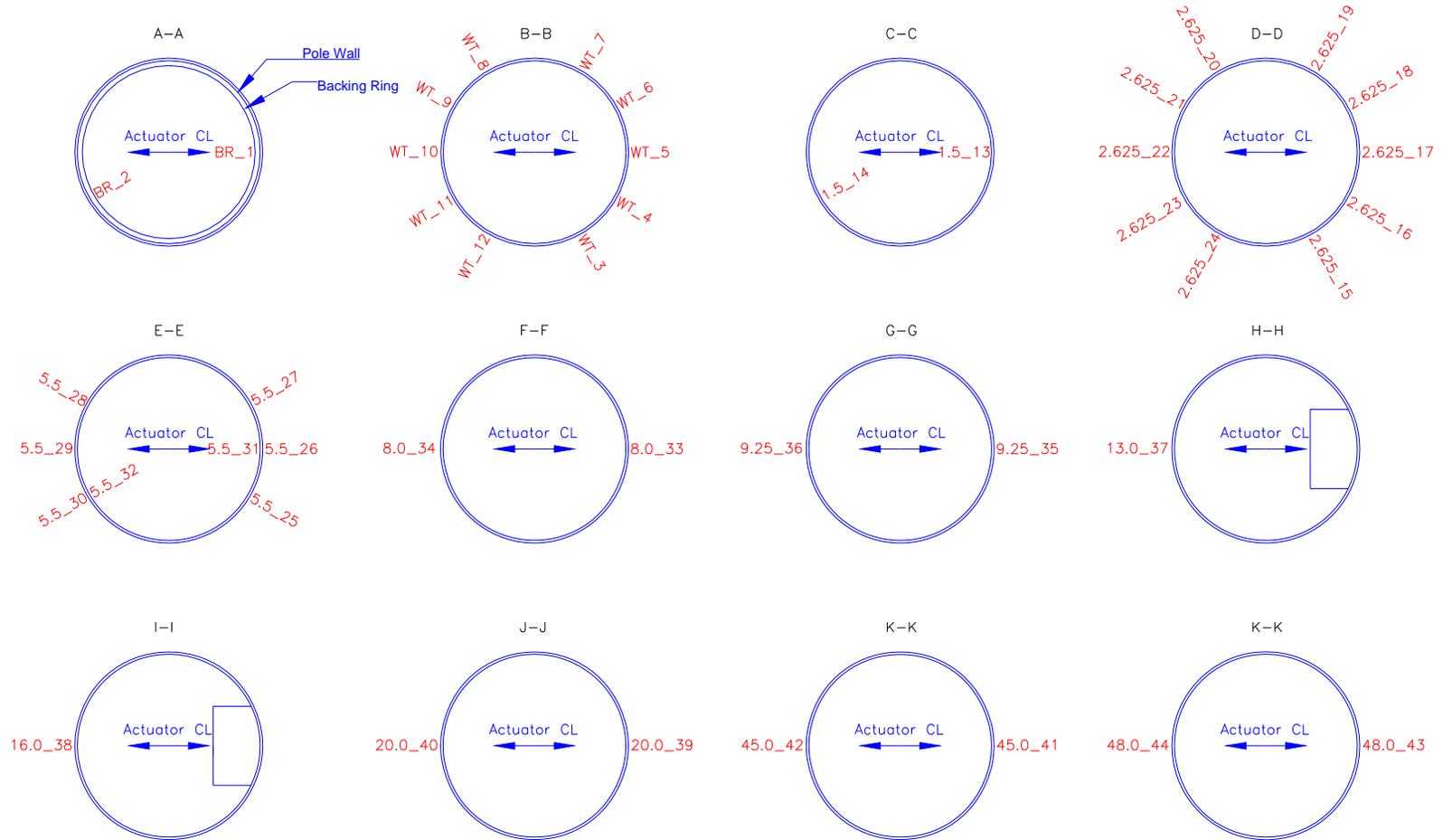
Figure 3.12: Strain gage locations at cross-sections
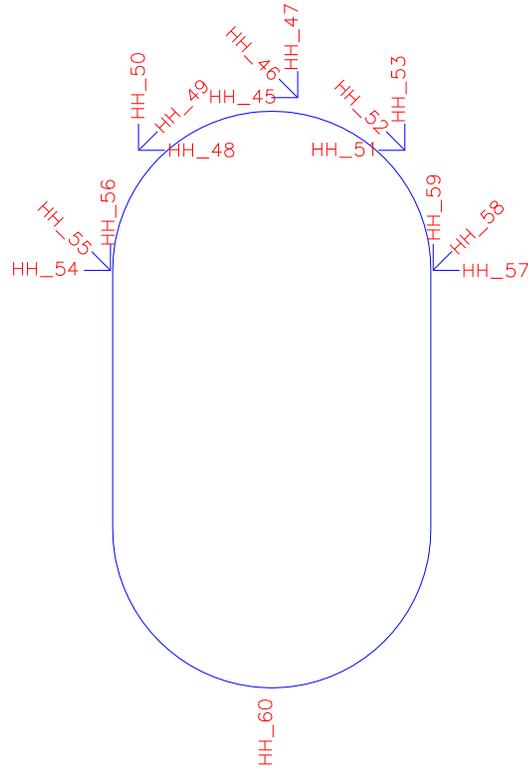
Figure 3.13: Strain gage locations at the hand hole

Table 3.3: List of potentiometers used

Potentiometer Designation	Potentiometer Type	Purpose
MTS_LC_1	Load Cell	Load Cell
MTS_LVDT_2	LVDT	LVDT
HSS_NE_DUNC_3	Duncan	Measures Slip of HSS Bearing Tube
HSS_SE_DUNC_4	Duncan	Measures Slip of HSS Bearing Tube
PLT_W_DUNC_5	Duncan	Measures Plate Deflection
PLT_E_DUNC_6	Duncan	Measures Plate Deflection
BP_SW_DUNC_7	Duncan	Measures BP Slip
BP_NW_DUNC_8	Duncan	Measures BP Slip
38_SP_9	String	Measures Pole Deflection
72_SP_10	String	Measures Pole Deflection
STUB_SP_11	String	Measures Pole Deflection
36_INC_12	Inclin.	Measures Pole Rotation
84_INC_13	Inclin.	Measures Pole Rotation
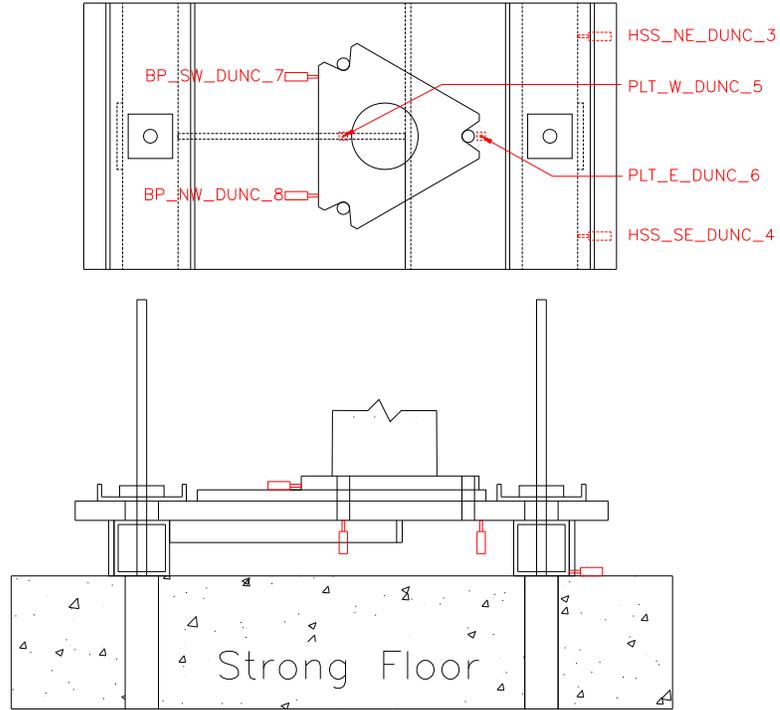
Figure 3.14: Location of Duncan potentiometers used at pole base
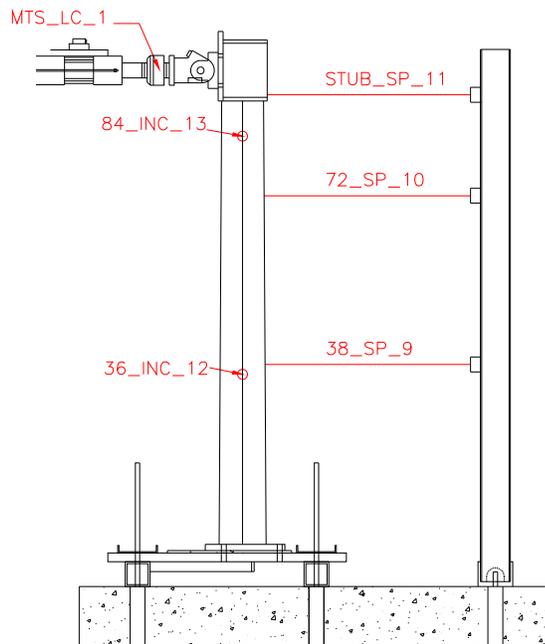
Figure 3.15: Location of string potentiometers and inclinometers used on pole

Chapter 4 Experimental Program and Observations

4.1 Overview

This chapter discusses the testing protocol, problems that occurred during testing and observations that were made during the testing.

4.2 Initial Quasi-Static Testing

Each specimen was subjected to 5 cycles of quasi-static loading prior to the start of the fatigue testing. The purpose of the quasi-static testing was to check the instrumentation and to obtain a baseline for the stress distribution, stiffness, and SCFs. Loading for the quasi-static testing was done in force control with the target load being the same as used for Phase I of the fatigue testing described below, which was an actuator load of 0.620 kips pushing to the east and 0.620 kips pulling to the west generating a base moment of 59.2 kip-in. in Specimen 1 and 58.9 kip-in. in Specimen 2. Both specimens behaved elastically and all instruments were found to be fully functional.

The quasi-static test results are presented in Chapter 5 and are presented as strain gage and potentiometer readings taken during these initial cycles. The actual data points used were the readings taken in the strain gages and potentiometers at a load cell reading of 0.600 kips pushing to the east and 0.600 kips pulling to the west. The load cell readings used for the data analysis were chosen slightly below the peak load to avoid any effects resulting from the actuator changing directions.

4.3 Initial Fatigue Loads

Following the quasi-static testing, each specimen was subjected to constant amplitude fatigue loading to estimate the remaining fatigue life of critical luminaire pole details. Selection of the

fatigue load magnitude involved two criteria: (i) the loading should be well below that needed to cause yielding in the critical details, and (ii) the loading should be large enough to ensure that a reasonable number of cycles could be expected to cause failure. Thus, to determine the actuator load used for fatigue testing, the fatigue resistance of the critical details in the specimens had to be estimated. Once the fatigue life was estimated, an actuator load could be determined that would produce the desired nominal stress in the critical details. However, no previous fatigue test data existed for luminaire poles with a triangular base plate detail similar to those tested. Therefore, the fatigue life couldn't be predicted from previous experimental data. Instead, the fatigue provisions of the *2001 Specifications* were used to estimate the fatigue life of the test specimens.

The fatigue life of the critical details in the test specimens was estimated using the nominal stress approach in the *2001 Specifications* and the 50% confidence interval S-N curve parameters for the AASHTO fatigue detail categories determined by Ginal (2003). The pole-to-base plate connection was classified as CJP welded with an attached backing ring. The hand hole detail was classified as a longitudinal attachment with a CJP weld, in which the main member is subjected to longitudinal loading with a length (distance from top of hand hole to bottom) greater than 12 times the thickness of the stiffener or 4 in. when the thickness of the stiffener is less than 1 in. Both details were classified as Category E. Since the nominal stress at the CJP weld toe was greater than at the termination of the hand hole, the CJP weld toe was determined to be the location that would fail first. Failures of the CJP welded pole-to-base plate connection were observed in the field which seemed to validate this conclusion. The anchor bolts were also checked using the *2001 Specifications* to ensure that they would not fail before cracks initiated in the pole-to-base plate connection or the hand hole stiffener.

The nominal stress range at the CJP weld toe was computed using the flexure formula where the moment was equal to the actuator force times the distance from the weld toe to the centerline of the actuator. An actuator load range of 1.240 kips about a mean load of 0 kips was found to produce a nominal stress range at the CJP weld toe of 13.78 ksi in Specimen 1 and 13.72 ksi in Specimen 2 about a mean stress of 0 ksi. Using the nominal stress range, the number of cycles to failure for the AASHTO Category E CJP welded tube-to-transverse plate detail was determined to be approximately 653,500 for Specimen 1 and 662,100 for Specimen 2. Again, the predicted number of cycles to failure for Specimen 2 was higher than Specimen 1 because extra hydro stone was used slightly reducing the moment at the CJP weld toe. Even though the

hand hole opening proved to be the critical test detail in Specimen 1, the test loads for Specimen 2 were still calibrated based on fatigue failure at the CJP weld toe. At this load range the actuator could be run at a frequency of 2.0 Hz resulting in a run time of 91 hours in Specimen 1 to complete 653,500 cycles and 92 hours in Specimen 2 to complete 662,100 cycles which was determined to be a reasonable time span for testing. These computations assumed that no previous accumulated fatigue damage occurred in the field.

4.4 Changes in Fatigue Loads

During the testing, it became clear that the critical details in both specimens significantly surpassed the fatigue life predicted by the 50% confidence interval AASHTO Category E S-N curve developed by Ginal (2003). At a stress range of 13.78 ksi at the CJP weld toe, Specimen 1 reached 1,362,627 cycles with no crack initiation or reduction in stiffness while the predicted fatigue life was 653,504 cycles. At a stress range of 13.72 ksi at the CJP weld toe, Specimen 2 reach 2,429,211 cycles with no crack initiation or reduction in stiffness while the predicted fatigue life was 662,116 cycles.

After 1,362,627 cycles in Specimen 1 and 2,429,211 cycles in Specimen 2, the actuator load range was doubled to produce a stress range in the extreme tension fiber at the CJP weld toe of 27.56 ksi and 27.44 ksi in Specimen 1 and Specimen 2 respectively about a mean stress of 0 ksi to expedite crack initiation and propagation. Once the stress range was increased, an equivalent stress range was computed based on the AASHTO stress life equation:

$$S_{eq} = \left[\frac{n_1 + n_2}{\frac{n_1}{S_1^{-m}} + \frac{n_2}{S_2^{-m}}}\right]^{\frac{-1}{m}} \tag{4.1}$$

where n is the cycle count for a given phase, S is the stress range for a given phase, and m is the slope of the fatigue curve, which for the AASHTO S-N curves is equal to 3. The testing was then continued until crack initiation or significant reduction in stiffness was identified. The loading pattern for the two specimens is shown in Table 4.1, where Phase I contains cycles at an actuator load range of 1.24 kips and Phase II contains cycles at an actuator load range of 2.48 kips. At the larger load level, a reduced cycle frequency was used for Specimen 1 and Specimen 2. For Specimen 2, the frequency was increased part way through Phase II.

TECHNICAL REPORT STANDARD TITLE PAGE

Table 4.1: Overview of fatigue test parameters

	Fatigue Test Phase I	Fatigue Test Phase IIa	Fatigue Test Phase IIb
Specimen 1			
Actuator Load Range (kips)	1.24	2.48	---
Actuator Frequency (Hz)	2	0.6	---
Stress Range (ksi)	13.78	27.56	---
Cycle Start	1	1,362,628	---
Cycle End	1,362,627	1,499,587	---
Specimen 2			
Actuator Load Range (kips)	1.24	2.48	2.48
Actuator Frequency (Hz)	2	0.6	1
Stress Range (ksi)	13.72	27.44	27.44
Cycle Start	1	2,429,212	2,534,793
Cycle End	2,429,211	2,534,792	2,570,302

4.5 Data Acquisition

The data acquisition program used for the testing was National Instruments Labview. A virtual instrument designed specifically for fatigue testing was used. The virtual instrument had two recording modes; continuous and periodic recording. Continuous recording mode allowed a limited number of channels to be recorded throughout the duration of testing. Periodic recording mode allowed for data channels to be recorded at a defined cycle interval for a defined recording duration. Some problems occurred with the virtual instrument resulting in a loss of some experimental data for certain cycles. On five separate occasions, the virtual instrument shut down while the function generator for actuator control was still running and the actuator was still cycling the specimen resulting in data not being recorded for some cycles. The following is a summary of why this occurred and the process used to determine the number of missed cycles.

The virtual instrument writes the continuous data to a file that grows in size as the test progresses. Five channels were used for the continuous recording and the virtual instrument limits the size of the continuous data file to 1.5 gigabytes. When the test ran consistently for multiple days at a frequency of 2 Hz, the file size limit was exceeded and the virtual instrument

shut off while the function generator continued to cycle the actuator. This limitation was not initially known and led to shut down of the virtual instrument on three occasions. On two other occasions, the power supply to the virtual instrument was accidently shut off due to other laboratory activities. When the virtual instrument shut down while the function generator continued to run and cycle the specimen. The following procedure was followed to compute the missed cycles:

1. The voltage on the MTS actuator controller was immediately checked to ensure that the load was in the proper range and the function generator and specimen loading was stopped;
2. The exact shutdown time was immediately recorded;
3. The output data file was opened and the last recorded cycle number and time was identified;
4. The time that passed between the shutdown and last recorded data cycle was computed and then multiplied by the frequency and added to the last recorded cycle count to determine the last actual cycle.

The current number of cycles following an accidental virtual instrument shutdown was computed from:

$$n_c = n_{LR} + (t_c - t_{LR}) * f_{test} * 3600 \qquad (4.2)$$

where n_{LR} is the number of the last recorded cycle by the virtual instrument, t_{LR} is the time of the last recorded cycle converted to hours, t_c is the time at which the function generator was manually stopped converted to hours, and f_{test} is the test frequency in cycles/second at which the last recorded cycle occurred. When converting times to hours, 3:56:03 PM would be recorded as 15.93 hours. Using this method, a few cycles might potentially be missed due to slight errors in actuator frequency and the exact recorded times. However, when considering the magnitude of the number of test cycles, in the millions, the few missed cycles that may result from the above procedure are negligible. Further, no shutdowns occurred while the specimens were damaged. There was no difference in the behavior of the specimens before or after the shutdowns and all instruments read similar values before and after.

4.6 Other Experimental Challenges

Some other challenges were encountered during the long duration of fatigue testing and will be briefly discussed. These challenges led to delays in testing but did not have a significant effect on the test data. The most persistent challenge was that the temperature of the hydraulic fluid used to power the actuator was too high to be able to run the test. When this occurred, the test had to be shut down until the hydraulic fluid cooled. In the SRL, there are two large pumps in the basement that provide hydraulic power to the entire facility. The cooling system for these pumps is insufficient for long duration testing, especially when the volume of hydraulic fluid circulated is low, as it was for this testing. Since a small actuator and small displacements were necessary, only a small fraction of the hydraulic fluid in the system was cooled during each loading cycle resulting in numerous situations of overheating. This situation was aggravated by the presence of somewhat old hydraulic fluid in the system. The old hydraulic fluid was presumed to have particulate matter in it which increases pipe friction and heat in the system. To mitigate this challenge, the filters had to be changed frequently during testing.

Another issue encountered during the testing of Specimen 2 was that some friction was observed in the swivel assembly at the end of the actuator. This friction resulted in the swivel locking up during fatigue testing. This was fixed by taking the swivel assembly apart and lubricating the bearing. There was concern that the friction in the swivel assembly was causing inaccurate load cell readings. However, a voltmeter reading the control signal verified that the load cell reading and control signal were the same.

Additional pauses in testing were necessary for random maintenance and because other tests were running in the laboratory. Table 4.2 and
Table 4.3 show the test log for Specimens 1 and 2 respectively. An entry exists for every instance that the virtual instrument was stopped and restarted and instances when the cycle counts were adjust per Equation 4.2 are noted.

Table 4.2: Test log for Specimen 1

Start Date	Start Time	Start Cycle	End Date	End Time	End Cycle
5/19/2009	1:35:03 PM	0	5/19/2009	3:59:17 PM	17,605
5/19/2009	4:20:00 PM	17,606	5/21/2009	12:03:00 PM	325,325*
5/21/2009	12:44:55 PM	325,326	5/22/2009	4:38:29 PM	527,155*
5/22/2009	4:55:48 PM	527,156	5/22/2009	6:38:43 PM	540,258
5/23/2009	11:24:04 AM	540,529	5/23/2009	9:39:07 PM	562,323
5/23/2009	9:54:36 PM	562,324	5/25/2009	9:05:00 AM	813,050
5/25/2009	9:24:16 AM	813,051	5/26/2009	8:49:12 AM	1,161,040
5/26/2009	10:16:39 AM	1,161,041	5/27/2009	7:57:10 PM	1,362,627
6/2/2009	1:49:35 PM**	1,362,628	6/2/2009	3:57:21 PM	1,365,431
6/2/2009	4:40:59 PM	1,365,432	6/4/2009	7:16:33 AM	1,443,855
6/8/2009	8:36:13 PM	1,443,856	6/9/2009	10:53:55 PM	1,499,587
*The virtual instrument stopped recording while the function generator					
was still running, the missed cycles were computed using method					
described in Chapter 4					
**Actuator load range increased from 1.240 kips to 2.480 kips, frequency					
decreased from 2 Hz. to 0.6 Hz					

Table 4.3: Test log for Specimen 2

Start Date	Start Time	Start Cycle	End Date	End Time	End Cycle
7/10/2009	5:23:18 PM	0	7/10/2009	5:29:00 PM	683
7/10/2009	6:00:57 PM	684	7/10/2009	6:46:54 PM	4,551
7/10/2009	6:53:27 PM	4,552	7/10/2009	9:08:07 PM	20,311
7/10/2009	9:23:34 PM	20,312	7/12/2009	12:41:26 PM	296,149
7/12/2009	12:47:20 PM	296,150	7/13/2009	7:29:16 PM	506,621
7/13/2009	7:44:34 PM	506,622	7/13/2009	7:48:00 PM	507,033
7/13/2009	7:51:51 PM	507,034	7/14/2009	8:38:31 PM	681,071
7/15/2009	11:39:50 AM	682,072	7/15/2009	3:29:01 PM	707,946
7/15/2009	3:50:34 PM	707,947	7/15/2009	3:53:00 PM	708,239
7/17/2009	7:28:16 PM	708,240	7/17/2009	8:26:42 PM	715,128
7/17/2009	8:36:53 PM	715,129	7/18/2009	4:20:54 AM	769,498
7/18/2009	10:30:06 PM	769,499	7/18/2009	10:36:00 PM	770,207
7/18/2009	10:46:05 PM	770,208	7/18/2009	10:53:00 PM	771,037
7/18/2009	11:15:10 PM	771,038	7/18/2009	11:24:32 PM	772,520
7/20/2009	10:10:20 AM	772,521	7/20/2009	11:06:22 AM	779,245
7/20/2009	11:10:10 AM	779,246	7/20/2009	11:28:43 AM	781,285
7/20/2009	11:31:12 AM	781,286	7/20/2009	12:14:56 PM	786,439
7/22/2009	12:04:00 PM	786,440	7/22/2009	10:37:11 PM	860,721
7/23/2009	11:04:43 AM	860,722	7/23/2009	3:19:57 PM	890,682
7/23/2009	4:00:49 PM	890,683	7/23/2009	4:04:00 PM	891,065
7/23/2009	4:06:30 PM	891,066	7/26/2009	6:09:49 PM	1,362,161
7/26/2009	6:17:34 PM	1,362,162	7/27/2009	8:02:52 PM	1,514,600
7/27/2009	8:33:29 AM	1,514,601	7/28/2009	12:08:00 PM	1,626,742*
7/28/2009	12:28:15 PM	1,626,743	7/29/2009	2:05:28 AM	1,735,102
7/29/2009	8:51:58 AM	1,735,103	7/29/2009	1:51:04 PM	1,770,030
7/30/2009	9:02:25 AM	1,770,031	7/30/2009	11:21:11 AM	1,786,683
8/3/2009	11:05:36 AM	1,786,684	8/3/2009	6:46:57 PM	1,828,620
8/3/2009	6:55:29 PM	1,828,621	8/3/2009	8:41:55 PM	1,841,156
8/3/2009	8:46:03 PM	1,841,157	8/5/2009	4:07:37 PM	2,162,570*
8/5/2009	11:25:37 PM	2,162,571	8/7/2009	4:52:00 PM	2,429,211
8/13/2009	4:56:21 PM	2,429,212	8/14/2009	12:33:21 PM	2,470,611
8/19/2009	6:31:52 AM	2,470,612**	8/19/2009	4:41:20 PM	2,495,876
8/20/2009	4:08:00 PM	2,495,877	8/21/2009	1:43:08 PM	2,508,786*
8/24/2009	11:26:04 AM	2,508,787	8/25/2009	12:56:28 AM	2,534,644
8/31/2009	2:55:55 PM	2,534,645	8/31/2009	3:00:00 PM	2,534,792
8/31/2009	3:14:56 PM	2,534,793	9/1/2009	12:59:48 AM	2,566,475
9/1/2009	11:37:50 AM	2,566,476	9/1/2009	12:42:24 PM	2,570,302
*The virtual instrument stopped recording while the function generator					
was still running, the missed cycles were computed using method					
described in Chapter 4					
**Actuator load range increased from 1.240 kips to 2.480 kips, frequency					
decreased from 2 Hz. to 0.6 Hz					

4.7 Specimen 1 Observations

No cracks or reduction in stiffness were identified in Specimen 1 in the first 1,362,627 cycles. At this point, the actuator load was doubled to a range of 2.480 kips. Cracking was first identified in the upper right corner of the hand hole in Specimen 1 as shown in Figure 4.1 at 1,406,676 cycles. Since cracking initiated before it was visually observed, the strain gage data was reviewed to find the exact cycle count at which cracking was initiated. Crack initiation was identified by plotting the strain versus cycle count in the cycles preceding the observation of cracking. In the plot, a significant reduction in the tensile strain can be observed at 1,369,708 cycles marking the instance of crack initiation. Since fatigue failure is defined as the point of crack initiation in Chapter 5, this cycle count was used in the fatigue data plots instead of the cycle count at which cracking was first observed.

After the first identification of cracks, the testing continued until 1,499,587 cycles when significant degradation in stiffness of the pole had occurred and the test was ended. At this point, the crack opened up between 1/16 and 1/8 of an in. in tension and had grown to approximately 10 in long. The crack propagated in both directions around the radius of the upper portion of the hand hole offset from the edge by about 0.5 in. The crack was just beyond the edge of the hand hole stiffener where a weld between the stiffener and the pole was located. After propagating around the top of the hole, the crack then began travelling horizontally away from the hole and grew around the perimeter of the pole.

After the testing, critical details were inspected for fatigue damage. No damage was observed in the CJP welded tube-to-transverse plate connection or the anchor bolts. This was unexpected since fatigue failure at the tube-to-transverse plate connection had been observed in the state of Washington and was determined to be the critical location for fatigue by the provisions of the *2001 Specifications*. After testing, the pole was cut into several pieces to inspect the interior for damage in the pole wall and to get a better view of the fabrication quality. No other locations of crack initiation or additional propagation of the hand hole cracks were identified.
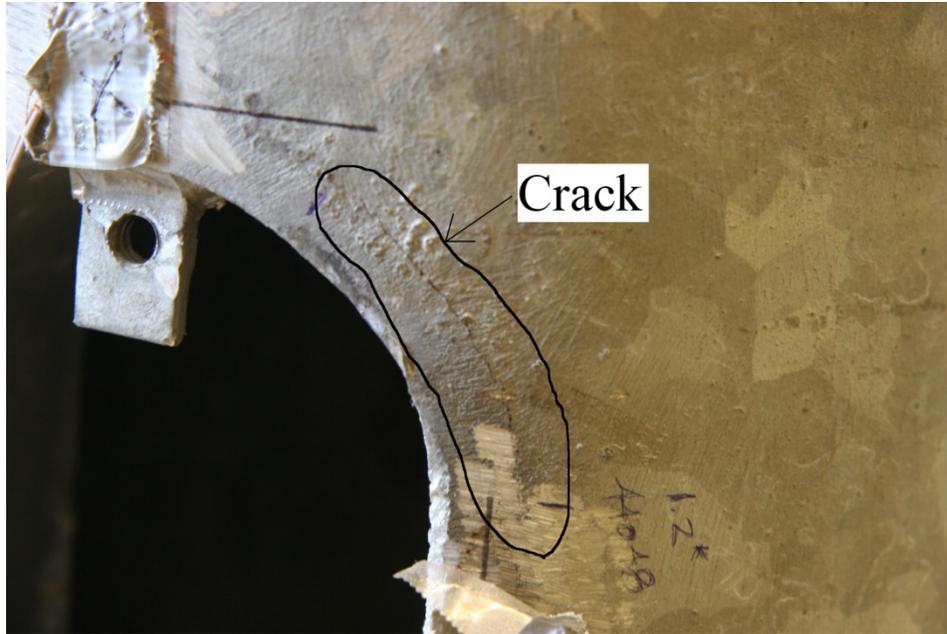
Figure 4.1: Hand hole of Specimen 1 at 1,362,627 cycles

4.8 Specimen 2 Observations

No cracks or reduction in stiffness were identified in Specimen 2 in the first 2,429,211 cycles. Once this point was reached, the actuator load was doubled to a range of 2.480 kips. Cracking was first identified in the lower left corner of the hand hole at 2,508,949 cycles and it propagated rapidly growing 2 in. by cycle 2,564,070. Figure 4.2 shows the crack loaded in tension during cycle 2,508,949. A second crack initiated in the upper right corner of the hand hole and was first identified at 2,557,552 cycles. This crack also grew rapidly and by cycle 2,564,070, the crack had grown an inch since initial identification. Figure 4.3 shows the second crack when loaded in tension during cycle 2,557,552. Testing was finally terminated at 2,570,302 cycles when the specimen's stiffness had degraded significantly and cracks were observed to open approximately 1/8 in. when in tension. Using the same procedure as explained for Specimen 1, the cycle at which crack initiation occurred was determined to be 2,501,088 from the strain gage data.

Both cracks initiated at about the same location on opposite corners of the hand hole and about a ½ in. away from the opening. Again, this distance corresponds to the interface between the hand hole stiffener and the pole wall. The critical details were inspected after testing was complete and no fatigue damage was found at the CJP welded pole-to-base plate connection or

in the anchor bolts. The pole cross-sections were cut into pieces to check the inside for any signs of crack initiation and none were found. Further, the strain gage data was reviewed to see if any other signs of crack initiation were present (gages showing compression but not tension) and none were found.

An important point should be made about the CJP welded tube-to-transverse plate connection and the anchor bolts. Because the test was terminated at 2,557,552 cycles and no cracking was found in the CJP weld or the anchor bolts, does not necessarily mean that number of cycles at the previously computed nominal stress range. Because the hand hole is located higher up on the pole than the other two details, cracking at the hand hole will relieve the stresses at the details below it. Therefore, inclusion of any fatigue cycles after initial cracking at the hand hole in the other details would cause the fatigue resistance to be over predicted due to the reduction in stress range.
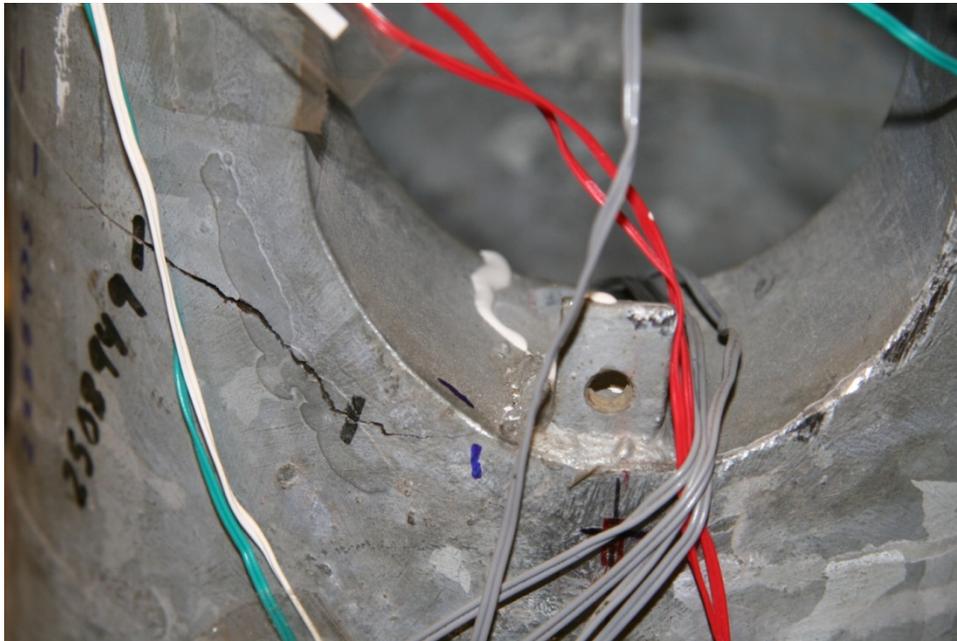
Figure 4.2: Cracking in Specimen 2 at lower left corner of the hand hole after 2,508,949 cycles
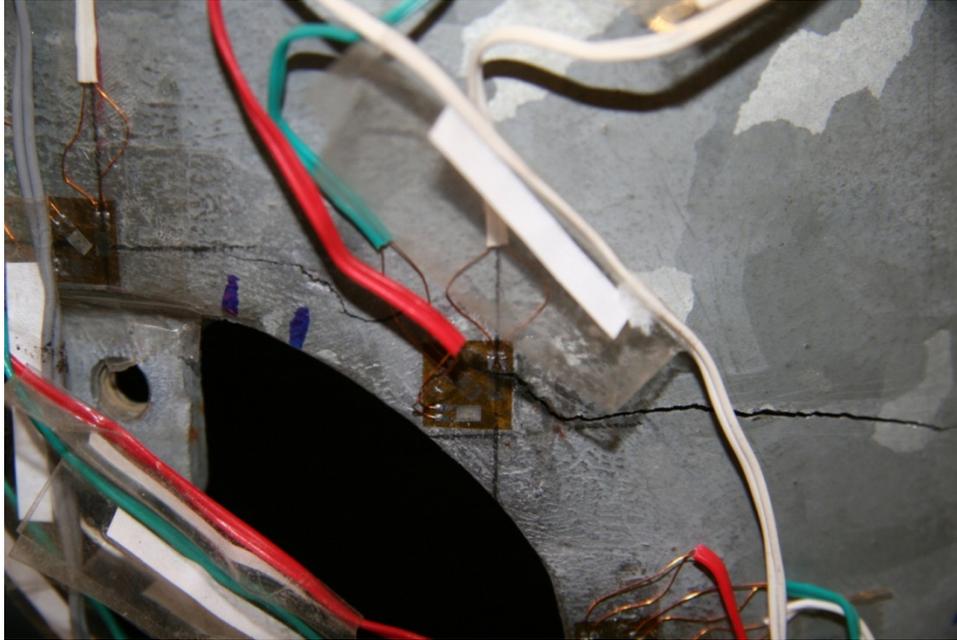
Figure 4.3: Cracking in Specimen 2 at the upper right corner of the hand hole at 2,557,552 cycles

Chapter 5 Experimental Results and Analysis

5.1 General

This chapter presents the results and analysis of the static and high cycle fatigue testing of two previously in-service luminaire poles. Section 5.2 focuses on the static testing of the two specimens, presenting strain gage data and interpretation. Section 5.3 discusses the potentiometer data and Section 5.4 discusses the fatigue testing results and presents a comparison of the results to previous the fatigue provisions of the *2001 Specifications*.

5.2 Static Testing Results and Analysis

The following section presents the results of the static testing and analysis of the data. The results, presented in the form of strain gage readings, are categorized by the location of the strain gages. Charts for each location are presented which contain the related strain gage readings, computation of the EBT strains, and local SCFs. Seven specific issues will be discussed in relation to fatigue of the luminaire support structure:

1. Comparison of strain gage readings in undisturbed regions to those predicted by EBT;
2. Measured stress in the backing ring at the pole-to-base plate connection;
3. Flow of stresses from the pole to the CJP weld to the base plate to the foundation and possible presence of the butterfly effect;
4. Variation of strain along the height of the pole and comparison to EBT;
5. Principle stresses around the hand hole and angle of rotation;
6. Computation of SCFs at critical locations ;
7. Stresses on the inside of the tube wall compared to the outside of the tube wall.

5.2.1 Uniaxial Strain Gage Data

Uniaxial strain gage data is presented in the following sections for Specimens 1 and 2. Two readings are taken for each specimen. Strain gage readings are taken at both 0.600 kips loading to the east and 0.600 kips loading to the west. Loading to the east refers to the actuator pushing (load cell compression) on the specimen causing eastward deflection of the luminaire and the

hand hole side of the pole is in compression. Loading to the west refers to the actuator pulling (load cell tension) the specimen causing westward deflection of the luminaire and the hand hole side of the pole is in tension. The strain gage readings are presented in microstrain and negative strain gage readings correspond to compressive strain and positive strain gage readings correspond to tensile strain. Since the static testing remains within the proportional limit for steel, the uniaxial strain gage data can be converted to uniaxial stress by multiplying by the Young's modulus of steel (29,000 ksi). The absolute value of the strains at the gage locations computed using EBT are also presented. The EBT strains are computed using the section dimensions and the flexure formula. In two locations, the hand hole and the backing ring, modified section properties are used and will be discussed in greater detail in the individual section. In all other locations, the section properties are computed from the nominal specimen dimensions presented in Chapter 3. Finally, the SCFs for both loading to the east and west are presented which are computed by dividing the actual recorded strain by the EBT strain.

5.2.2 Mid-height Strain Gage Readings

The mid-height strain gage data is shown in Table 5.1. Strain gages were placed in both Specimen 1 and 2 near the mid-height at both the 90 and 270 ^{o} cross-section locations. The purpose of these strain gages was to verify that the actuator load produced the expected strains. This ensured that both the actuator load cell readings and the nominal section properties used to compute the EBT strain were correct. The strain gages were placed near the mid-height of the specimens because this location was far enough from any geometric discontinuities or connection details to prevent any deviation from the strains predicted by EBT. From the strain data, it can be seen that the recorded strains are within 12% of the EBT strain value. Considering the small actuator loads used in this testing, the recorded strains match the EBT strains sufficiently well.

Table 5.1: Mid-height strain gage readings

Gage Location	Loading East Strain (µε)	Loading West Strain (µε)	Abs. EBT Strain (µε)	Loading East SCF	Loading West SCF
Specimen 1					
45.0 in. Above BP Out. 90 Degrees	-0.135	0.137	0.134	1.01	1.02
45.0 in. Above BP Out. 270 Degrees	0.129	-0.124	0.134	0.97	0.93
Specimen 2					
48.0 in. Above BP Out. 90 Degrees	-0.120	0.114	0.125	0.96	0.91
48.0 in. Above BP Out. 270 Degrees	0.119	-0.110	0.125	0.95	0.88

5.2.3 Backing Ring Strain Gage Readings

The backing ring strain gage data is shown in Table 5.2. Strain gages were placed on the backing ring at the 90 and 300 ^{o} cross-section locations on Specimen 1. Ideally, the gages would have been placed at the 90 and 270 ^{o} cross-section locations. However, due to the presence of weld material from the pole seam weld at the 270 ^{o} cross-section location, it was not possible to place a line of strain gages on the backing ring and inside the pole in this location. Since it was favorable to have a line of strain gages at the same cross-section location on the inside, the 300 ^{o} cross-section location was chosen. The purpose of these gages was to determine whether any stress flowed through the backing ring and into the base plate.

The only connection between the inside of the pole and the backing ring is a 1.5 in. tack weld at the 260 ^{o} cross-section location. The bottom of the backing ring was fillet welded to the pole base plate. For computing the EBT strains in the backing ring, the pole and backing ring were considered completely composite, i.e., they were treated as a single hollow tube section. The combined section had an outside diameter equal to the nominal outside diameter and a thickness equal to the sum of the pole thickness and the backing ring thickness. Computing the EBT strain in this way assumes that there is a sufficient mechanical connection between the pole and the backing ring. With only a 1.5 in. tack weld, this was not the case. However, the EBT strains computed for the composite section provide values for comparison. Nonetheless, it should be it should be noted that this is a location of high stress concentration. Therefore, if the actual section behaved compositely, the strain reading should be substantially higher than the EBT strain calculation, which does not consider stress concentration.

The strain gage data in Table 5.2 shows that some stress flows through the backing ring but the magnitude is quite low. The maximum stress computed using the strain gage data was 1.64 ksi in compression at the 90 ^{o} gage during loading to the east. Interestingly, the 90 ^{o} gage reads higher than the 300 ^{o} gage for loading in both directions despite the fact that the pole-to-backing ring tack weld is on the other side of the neutral axis. The presence of the tack weld causes some stress to flow through the backing ring but the magnitude is quite small. It is unclear why larger strains are observed away from the tack weld; however, since the magnitudes are so low and the EBT strains are conservative, the backing ring strains were not considered critical. Further, since backing ring strains were so small in Specimen 1, no strain gages were placed on the backing ring in Specimen 2.

Table 5.2: Backing ring strain gage readings

Gage Location	Loading East Strain ($\mu\varepsilon$)	Loading West Strain ($\mu\varepsilon$)	Abs. EBT Strain ($\mu\varepsilon$)	Loading East SCF	Loading West SCF
Specimen 1					
Backing Ring Inside 90 Degrees	-0.056	0.054	0.078	0.72	0.69
Backing Ring Inside 300 Degrees	0.009	-0.024	0.067	0.14	0.36

5.2.4 Outside Base of Pole Strain Gage Readings

A high concentration of strain gages were placed around the pole base in Specimen 1 and Specimen 2. In Specimen 1, rings of 10 strain gages were placed on the outside of the pole at 0.625 in. above the base plate (weld toe) and 2.625 in. above the base plate, and 6 gages were placed 5.5 in. above the base plate. In Specimen 2, rings of 6 strain gages were placed at those same locations. The strain gage readings for Specimens 1 and 2 are shown in Table 5.3 and Table 5.4 respectively.

Table 5.3: Base of pole Specimen 1 strain gage readings

Gage Location	Loading East Strain (με)	Loading West Strain (με)	Abs. EBT Strain (με)	Loading East SCF	Loading West SCF
Specimen 1					
Weld Toe Outside 30 Degrees	-0.108	0.111	0.115	0.94	0.97
Weld Toe Outside 60 Degrees	-0.230	0.225	0.199	1.16	1.13
Weld Toe Outside 90 Degrees	-0.262	0.270	0.230	1.14	1.17
Weld Toe Outside 120 Degrees	-0.194	0.204	0.199	0.97	1.03
Weld Toe Outside 150 Degrees	-0.105	0.110	0.115	0.91	0.96
Weld Toe Outside 210 Degrees	0.127	-0.102	0.115	1.10	0.89
Weld Toe Outside 240 Degrees	0.265	-0.253	0.199	1.33	1.27
Weld Toe Outside 270 Degrees	0.201	-0.201	0.230	0.87	0.87
Weld Toe Outside 300 Degrees	0.239	-0.230	0.199	1.20	1.15
Weld Toe Outside 330 Degrees	0.129	-0.101	0.115	1.12	0.88
2.625 in. Above BP Out. 30 Degrees	-0.130	0.128	0.113	1.15	1.13
2.625 in. Above BP Out. 60 Degrees	-0.203	0.197	0.196	1.04	1.00
2.625 in. Above BP Out. 90 Degrees	-0.221	0.219	0.226	0.98	0.97
2.625 in. Above BP Out. 120 Degrees	-0.183	0.181	0.196	0.93	0.93
2.625 in. Above BP Out. 150 Degrees	-0.091	0.096	0.113	0.81	0.84
2.625 in. Above BP Out. 210 Degrees	0.124	-0.098	0.113	1.09	0.87
2.625 in. Above BP Out. 240 Degrees	0.211	-0.211	0.196	1.08	1.08
2.625 in. Above BP Out. 270 Degrees	0.227	-0.251	0.226	1.01	1.11
2.625 in. Above BP Out. 300 Degrees	0.208	-0.203	0.196	1.06	1.04
2.625 in. Above BP Out. 330 Degrees	0.119	-0.092	0.113	1.05	0.82
5.5 in. Above BP Out. 60 Degrees	-0.209	0.206	0.191	1.09	1.08
5.5 in. Above BP Out. 90 Degrees	-0.198	0.194	0.220	0.90	0.88
5.5 in. Above BP Out. 120 Degrees	-0.196	0.197	0.191	1.03	1.03
5.5 in. Above BP Out. 240 Degrees	0.190	-0.189	0.191	0.99	0.99
5.5 in. Above BP Out. 270 Degrees	0.191	-0.200	0.220	0.86	0.91
5.5 in. Above BP Out. 300 Degrees	0.159	-0.153	0.191	0.83	0.80

Table 5.4: Base of pole Specimen 2 strain gage readings

Gage Location	Loading East Strain (με)	Loading West Strain (με)	Abs. EBT Strain (με)	Loading East SCF	Loading West SCF
Specimen 2					
Weld Toe Outside 60 Degrees	-0.203	0.194	0.198	1.02	0.98
Weld Toe Outside 90 Degrees	-0.235	0.229	0.229	1.03	1.00
Weld Toe Outside 120 Degrees	-0.191	0.186	0.198	0.96	0.94
Weld Toe Outside 240 Degrees	0.251	-0.240	0.198	1.27	1.21
Weld Toe Outside 270 Degrees	0.207	-0.200	0.229	0.90	0.88
Weld Toe Outside 300 Degrees	0.209	-0.193	0.198	1.05	0.97
2.625 in. Above BP Out. 60 Degrees	-0.192	0.182	0.195	0.98	0.93
2.625 in. Above BP Out. 90 Degrees	-0.189	0.186	0.225	0.84	0.83
2.625 in. Above BP Out. 120 Degrees	-0.183	0.177	0.195	0.94	0.91
2.625 in. Above BP Out. 240 Degrees	0.198	-0.194	0.195	1.01	1.00
2.625 in. Above BP Out. 270 Degrees	0.173	-0.168	0.225	0.77	0.75
2.625 in. Above BP Out. 300 Degrees	0.188	-0.179	0.195	0.97	0.92
5.5 in. Above BP Out. 60 Degrees	-0.172	0.165	0.190	0.91	0.87
5.5 in. Above BP Out. 90 Degrees	-0.184	0.175	0.219	0.84	0.80
5.5 in. Above BP Out. 120 Degrees	-0.173	0.169	0.190	0.91	0.89
5.5 in. Above BP Out. 240 Degrees	0.183	-0.179	0.190	0.97	0.94
5.5 in. Above BP Out. 270 Degrees	0.211	-0.205	0.219	0.96	0.94
5.5 in. Above BP Out. 300 Degrees	0.186	-0.178	0.190	0.98	0.94

The high concentration of strain gages at the base served three primary purposes:

1. To identify cracking in the CJP welded pole-to-base plate connection before it is observed. When cracks initiate, the tensile capacity is reduced and can be indicated by the strain gage data before the cracking is visible.
2. To determine the SCF at the weld toe and at locations slightly above the weld toe which can help to predict the likelihood of crack initiation in a given location. The SCF can also be used to determine the effect of base plate flexibility as will be discussed in greater detail in the analysis of the fatigue data.
3. To identify the flow of stresses from the pole to the base plate to the foundation. Previous research has shown that the flow of stresses can deviate from that predicted by the flexure formula at the pole-to-base connection in specimens with thin flexible base plates. The high concentration of strain gages at the base may help identify any similar trends in the test specimens which have thick triangular base plates.

The strain gage data in Table 5.3 and Table 5.4 show that the SCF at the 90° location on the cross-section at the weld toe is equal to 1.14 and 1.17 in Specimen 1 and 1.03 and 1.00 in Specimen 2 for loading to the east and west respectively. At the 270° location, the SCF at the

weld toe is equal to 0.87 and 0.87 in Specimen 1 and 0.90 and 0.88 in Specimen 2 for loading to the east and west respectively. Two important observations can be made from the SCFs. The first observation is that the data shows a major deviation from the strain predicted by EBT. Since the 90° and 270° gages are the same distance from the neutral axis, the strains should theoretically be the same. As expected, there is a stress concentration due to the geometric discontinuity, but the fact that it only occurs on one side of the cross-section must be explained. The second observation is that the strain gage data at the 90° location in Specimen 1 shows a major stress concentration but no stress concentration exists at that location in Specimen 2 despite having identical dimensions. The potential explanations for this behavior are discussed below.

One possible explanation for the difference between the 90° and 270° strains is that the butterfly trend is occurring. The butterfly trend occurs when the maximum tensile stress at the base of the pole occurs at the location adjacent to the anchor bolts in tension rather than at what would be the pole's extreme tension fiber. In essence, the anchor bolts, which are not in line with the loading plane, attract load away from the extreme tension fiber. This trend causes a stress profile which differs from that predicted by EBT since the location on the cross-section farthest from the neutral axis does not have the maximum tensile stress. However, this trend has primarily been identified in poles with square thin base plates with socket connections and four anchor bolts. The test specimens have 1.75 in. thick triangular base plates with CJP welded pole-to-base plate connections and three anchor bolts; however, the larger SCFs for the 90° gage location and smaller SCFs for the 270° gage location are consistent with the butterfly effect, at least for loading such that the gages are in tension. Recall that a single anchor bolt was located adjacent to the 90° gage while two anchor bolts were present at the 210 and 330° cross-section locations on the other side.

If the butterfly trend was occurring and the double bolt side was in tension, the bolts would attract load away from the 270° cross-section location similar to what is seen in a square base plate. In this case, the strain should be higher in the 240° and 300° gages which were observed in both Specimen 1 and 2. However, when the single bolt side is in tension, the bolt is located in line with the 90° gage. Unlike with rectangular base plates, when the single bolt side is tension, it attracts load through the 90° cross-section location. In this case, higher tensile stresses would be expected on the single bolt side when in tension, which is what was observed in Specimen 1 but not in Specimen 2. However, there are two observations that are inconsistent

with the presence of the butterfly trend. While the SCF values of less than unity in the 270°

gages when in tension may be indicative of the butterfly trend, the fact that those SCFs remain

low when the 270° location is in compression is not. The butterfly trend should not apply to the

compression side of the pole. In compression, the transfer of load from the pole base plate to

the pole mounting plate is through bearing. Assuming a uniform bearing surface, the maximum

compression stress should be at 270°. Further, the butterfly trend has been observed only in

specimens with flexible base plates. The base plates used in the test specimens would generally

not be considered flexible since they are 1.75 in. thick.

The second reason why the strain gage data may be deviating from the EBT strain distribution is

due to imperfections in the specimen alignment and uniformity of the contact area between the

base plate and pole mounting plate that was attached to the strong floor. It's possible that the

luminaire poles and/or base plates were bent when removed from the field or during service.

This might also explain why the poles were out of plumb when they arrived at the SRL.

Distortion of the base plate similar to that shown in Figure 5.1 would have resulted in strain

gage readings similar to those in Table 5.3 and Table 5.4. Another possible imperfection is that

the bearing surface between the pole base plate and the hydro stone was non-uniform. This

could also explain the difference in the strain gage readings in the 90° gage for loading to the

east (compression) between Specimen 1 and 2. When installed in the test frame, the base plates

were shimmed so that the pole was plumb and the anchor bolts were tightened enough to hold

the pole into place. Hydro stone was then poured and allowed to harden after which the anchor

bolts were tightened. It's possible that either the base plate or the hydro stone surface was

slightly distorted causing a bearing surface near the bolts but a small gap halfway between the

two bolt holes. Both possibilities would result in a load path in both compression and tension

that would reduce the stresses at the location farthest from the neutral axis.
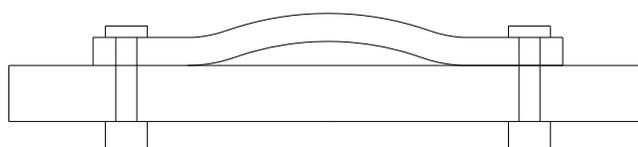
Figure 5.1: Possible base plate distortion

The third possible explanation for the unanticipated strain measurements is flexibility in the

pole mounting plate attached to the strong floor. The most flexible location of the pole

mounting plate is halfway between the holes for the two anchor bolts on the west side of the

base plate. This location is directly underneath the extreme fiber of the pole. If this location was deforming, the stress in the extreme fiber at the weld toe on the west side of the specimen would be slightly relieved. However, potentiometer measurements of pole mounting plate deformation were very small, making it unlikely that there was enough plate deformation to cause stress relief at the 270° location of the pole.

A radial plot of the absolute value of the stresses in Specimen 1 for both loading to the east and west are shown in Figure 5.2 and Figure 5.3 respectively. The absolute value of stresses in Specimen 2 for both loading to the east and west are shown in Figure 5.4 and Figure 5.5 respectively. The same data is also shown on a scatter plot for Specimen 1 in Figure 5.6 and Specimen 2 in Figure 5.7. Two interesting trends are observed from these figures. In Specimen 1 at 2.625 in. above the base plate, the stress in the 270 ^{o} gage is not less than the 240 and 300 ^{o} gages. However, in Specimen 2 the strain in the 270 ^{o} gage at 2.625 in. above the base plate is lower than the 240° and 300° gages. For Specimen 2, it isn't until 5.5 in. above the base plate that the 270° strain gage reads higher than the 240 and 300° gages. This trend is true in both tension and compression. A difference in stress distribution between Specimens 1 and 2 was not expected since they have almost identical geometries. The only difference is the location of the hand hole which was closer to the base plate in Specimen 2 by 1.35 in. Therefore, it is possible that the stresses might be disturbed due to the geometric discontinuity of the hand hole. However, the hand hole is centered on the 90° side of the cross-section, yet the trend appears at the 270° cross-section location. It is possible that the redistribution of stresses due to the hand hole opening occurs throughout the cross-section causing a disturbance at the 270° location.

Another observation is the presence of a disturbance at 5.5 in. above the base plate. The 60°, 90°, and 120° gages for both specimens recorded strains that are closer to each other relative to what is predicted by EBT. Also, the 60° and 120° gages at 5.5 in. recorded strains that were larger than those at 2.625 in. Again, this is most likely due to the proximity of the 5.5 in. gages to the hand hole, which was 4.4 in. above them. The last observation is that the stresses are larger at the 240° gage at the weld toe than at the 300° gage in both Specimen 1 and Specimen 2. Initially, it was though that this could be an alignment issue with the test frame. However, since this trend does not appear anywhere above the weld toe, it seems an alignment issue was not the cause. It's possible that the anchor bolt at the 210° location was tighter than the bolt at the 330° location. However, it's unlikely that this trend would appear in both specimens if that was truly the case.
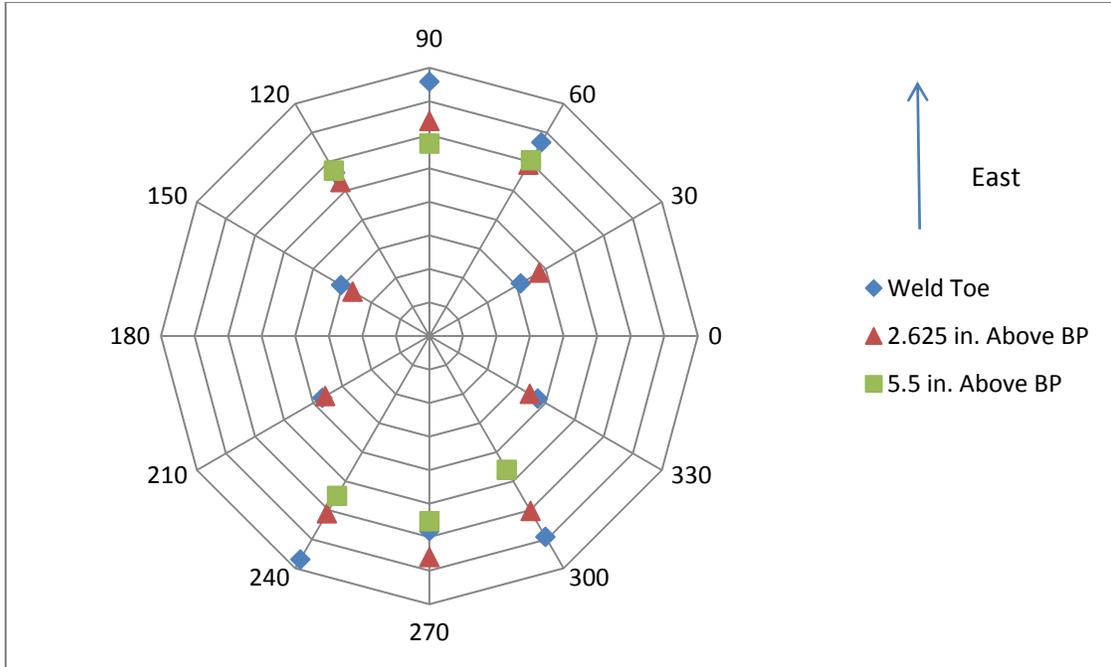
Figure 5.2: Radial plot of the absolute value of stress in Specimen 1 subjected to loading to the east of 0.600 kips (actuator centerline is on 90o and 270o line, hand hole is located at 90o, and each radial bar equals 1 ksi)
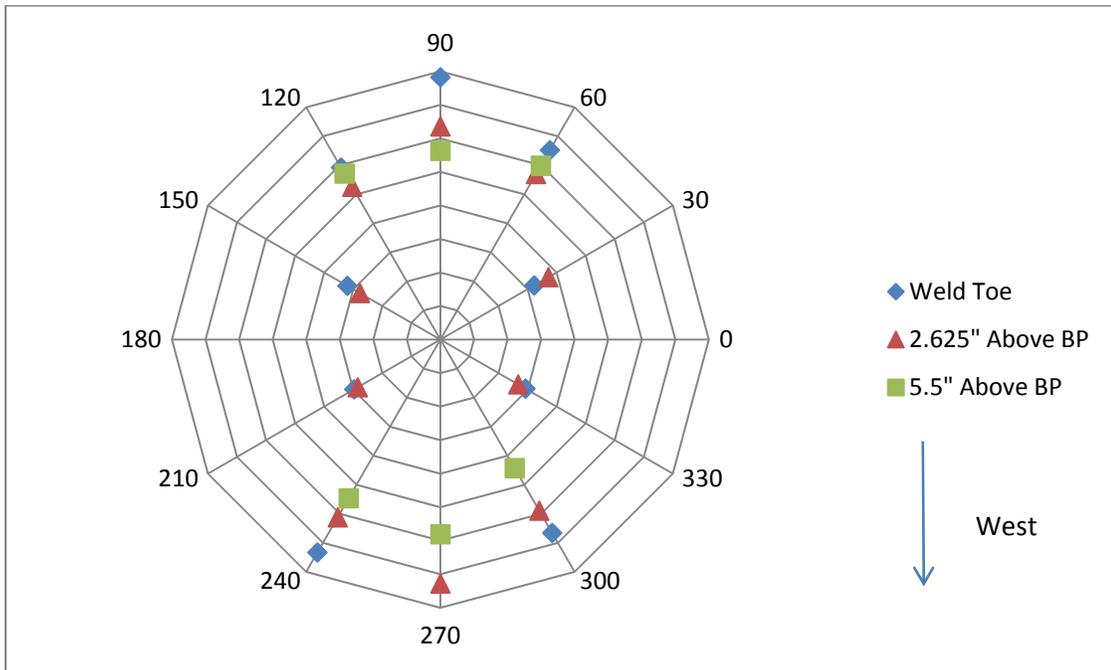
Figure 5.3: Radial plot of the absolute value of stress in Specimen 1 subjected to loading to the west of 0.600 kips (actuator centerline is on 90o and 270o line, hand hole is located at 90o, and each radial bar equals 1 ksi)
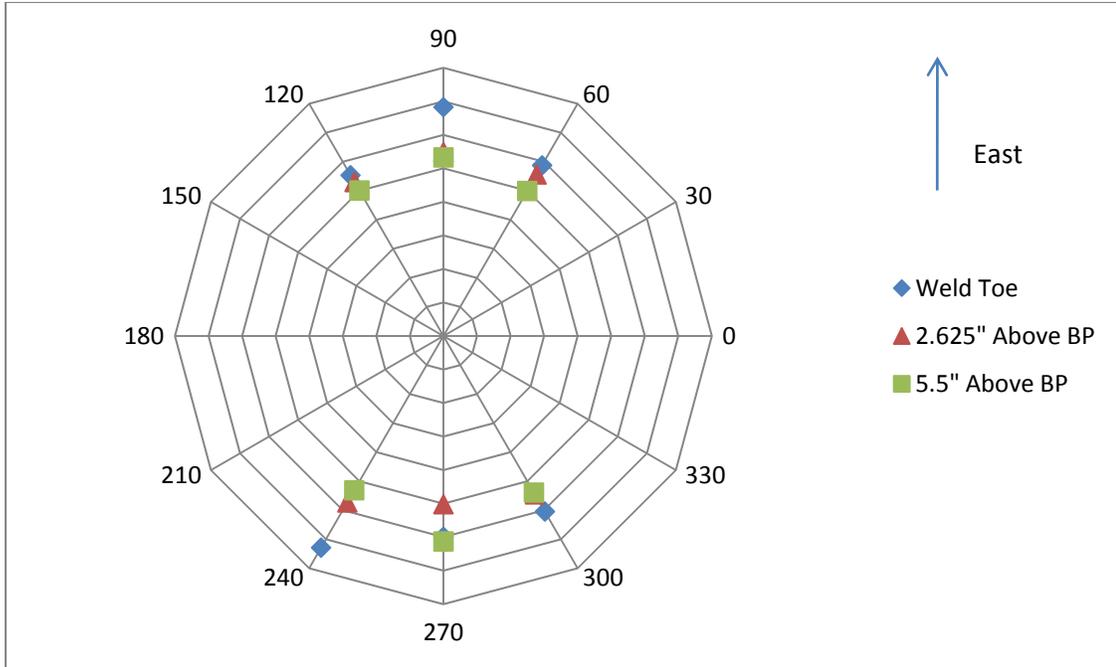
Figure 5.4: Radial plot of the absolute value of stress in Specimen 2 subjected to loading to the east of 0.600 kips (actuator centerline is on 90o and 270o line, hand hole is located at 90o, and each radial bar equals 1 ksi)
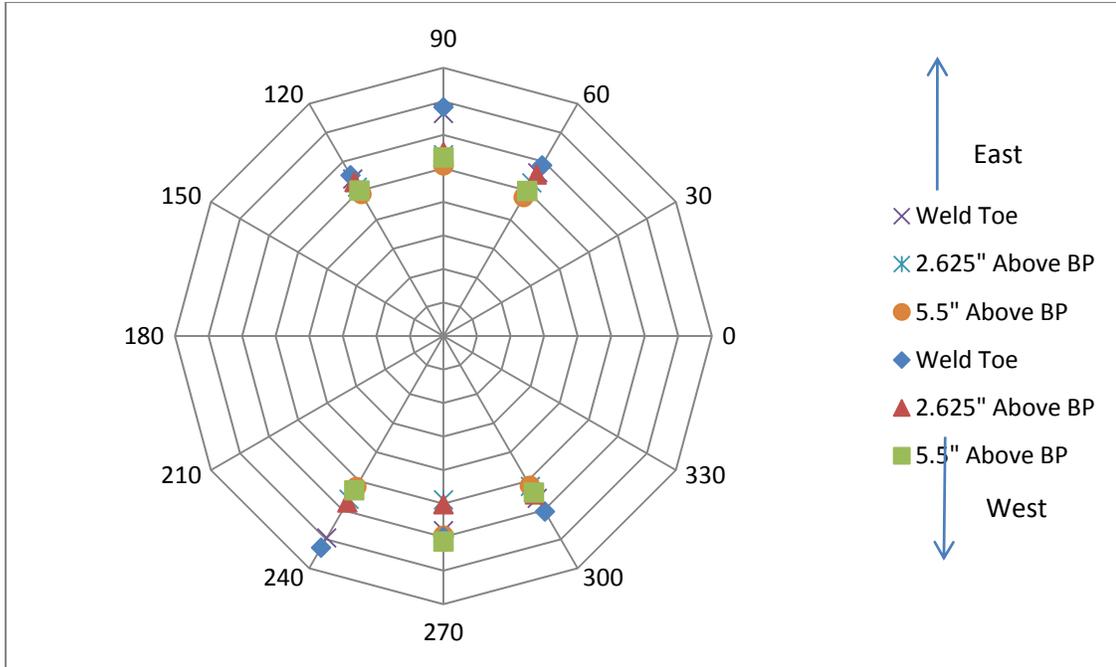
Figure 5.5: Radial plot of the absolute value of stress in Specimen 2 subjected to loading to the west of 0.600 kips (actuator centerline is on 90o and 270o line, hand hole is located at 90o, and each radial bar equals 1 ksi)
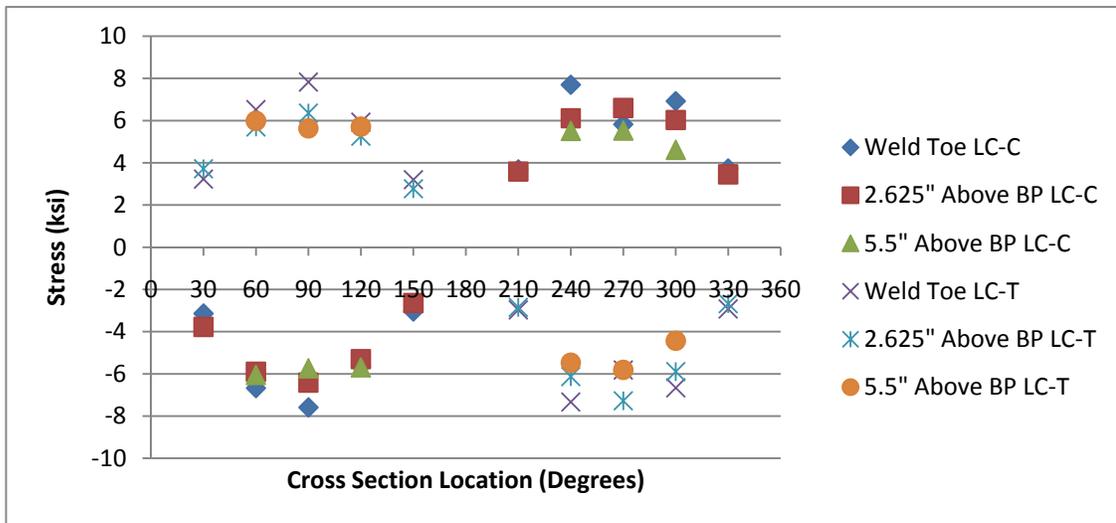
Figure 5.6: Stresses in Specimen 1 at the base of the pole

123
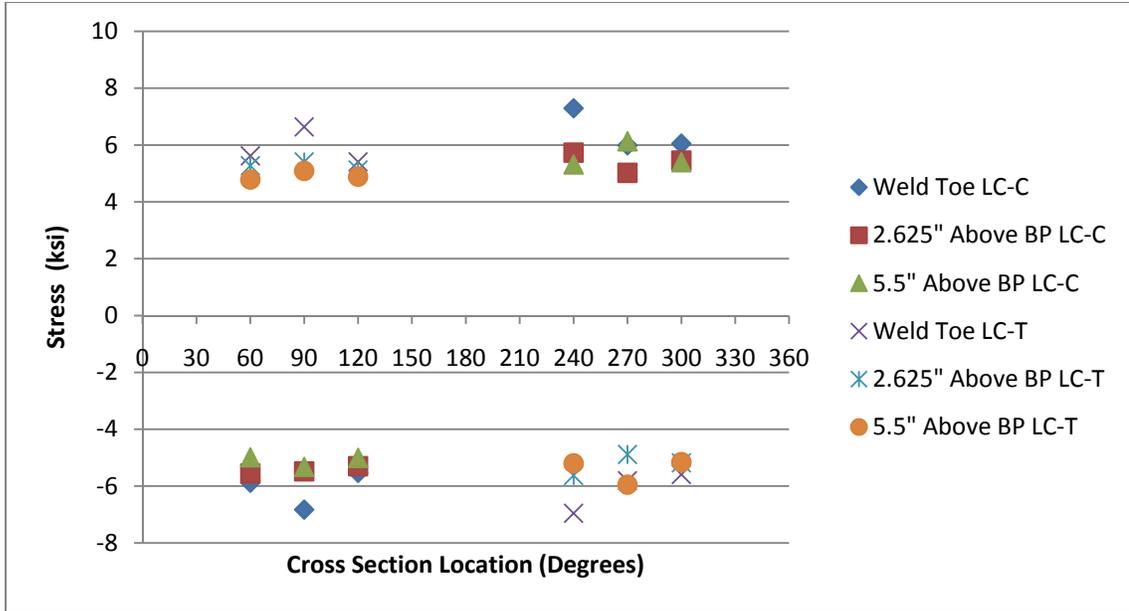
Figure 5.7: Stresses in Specimen 2 at the base of the pole

5.2.5 Longitudinal Strain Gages

Table 5.5 shows strains measured at gages placed at various distances from the base plate at the 90° and 270° cross-section locations in Specimen 2. The purpose of these gages was to determine the variation of the longitudinal stress along the pole height. This strain gage data was combined with the previously discussed data from the 90 and 270 $^{\circ}$ locations to plot the variation of longitudinal stress along the height as shown in Figure 5.8 and Figure 5.9 for Specimen 2 subjected to loading to the east and west respectively. Recall that the bottom of the hand hole is located at 9.90 in. above the base plate and the top of the hand hole is located 17.60 in. above the base plate and that it is centered at 90°. As expected, the geometric discontinuities at the pole-to-base plate connection and at the hand hole cause the measured stress to vary significantly from the stress predicted by EBT. The figures highlight the locations along the 90° and 270° paths where the measured stress significantly exceeds and is less than the EBT stress. A few important observations are discussed below.

Examining the stress results for the 90° gage locations, it is observed that they are similar for both loading directions. The stresses at weld toe significantly exceed those predicted by EBT as discussed in previous sections. The stress then drops significantly below the EBT stress as the gages get closer to the bottom of the hand hole. The stress immediately above the hand hole is also well below the EBT stress. Clearly the stresses are flowing around the hand hole opening,

resulting in longitudinal stresses that are well below the EBT stresses immediately above and below the hand hole. At gages significantly above the hand hole, the stress approaches the EBT stress. Note that there were no gages between the top of the hand hole and mid-height of the pole. In this region a linear transition has been assumed which may not be accurate. This assumption makes the stress variation along the pole's length at the 90° cross-section location look like it remains well below the EBT stress up to a height of 40 in. above the base plate. If more gages were placed between the top of the hand hole and mid-height of the pole, the stress would approach the EBT stress as the gages got farther above the hand hole.

Examining the stresses at the 270° cross-section location shows that those are also similar for loading in both directions. The stress at the weld toe and immediately above it is slightly below the EBT stress as previously discussed. At 5.5 in. above the base plate, the stress is higher than the EBT stress. At this location, the strain gage is significantly far above the base plates that the impact of the anchor bolts and base plate geometry does not affect the strain. Interestingly, the stress opposite the hand hole is well below the EBT stress. The EBT stress plotted at the hand hole is not computed using a reduced section and if a reduced section was used, the EBT stress would be larger since the cross-section's moment of inertia would decrease. The reduction in stress on the side opposite the hand hole was not expected. However, it may be attributed to the large stiffeners welded around the hand hole, which increased the cross section at this location. Above the hand hole, the stresses begin to approach the EBT stress.

Table 5.5: Stress along height gages in Specimen 2

Gage Location	Loading East Strain ($\mu\varepsilon$)	Loading West Strain ($\mu\varepsilon$)	Abs. EBT Strain ($\mu\varepsilon$)	Loading East SCF	Loading West SCF
Specimen 2					
8.0 in. Above BP Out. 90 Degrees	-0.084	0.080	0.214	0.39	0.37
8.0 in. Above BP Out. 270 Degrees	0.133	-0.128	0.214	0.62	0.60
9.25 in. Above BP Out. 90 Degrees	0.052	-0.052	0.212	0.24	0.25
9.25 in. Above BP Out. 270 Degrees	0.174	-0.179	0.212	0.82	0.85
13.0 in. Above BP Out. 270 Degrees	0.178	-0.171	0.204	0.87	0.84
16.0 in. Above BP Out. 270 Degrees	0.193	-0.187	0.198	0.98	0.94
20.0 in. Above BP Out. 90 Degrees	-0.123	0.120	0.189	0.65	0.63
20.0 in. Above BP Out. 270 Degrees	0.182	-0.175	0.189	0.96	0.93
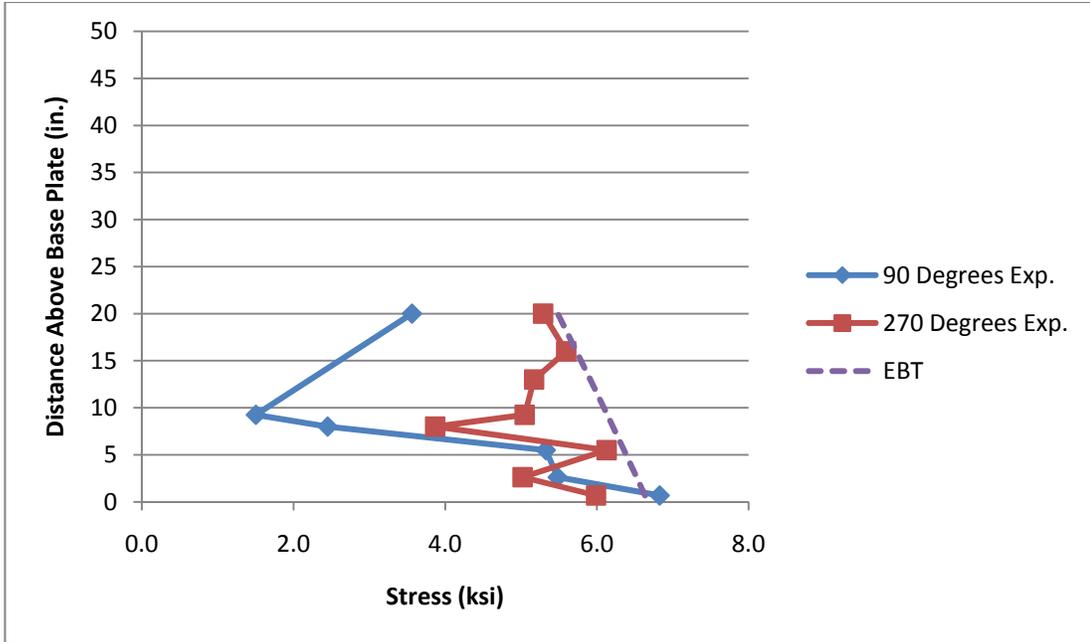
Figure 5.8: Stress distribution along height of Specimen 2 for loading to the east (the hand hole is located between 9.9 in. and 17.6 in. and the 90o side is in compression)
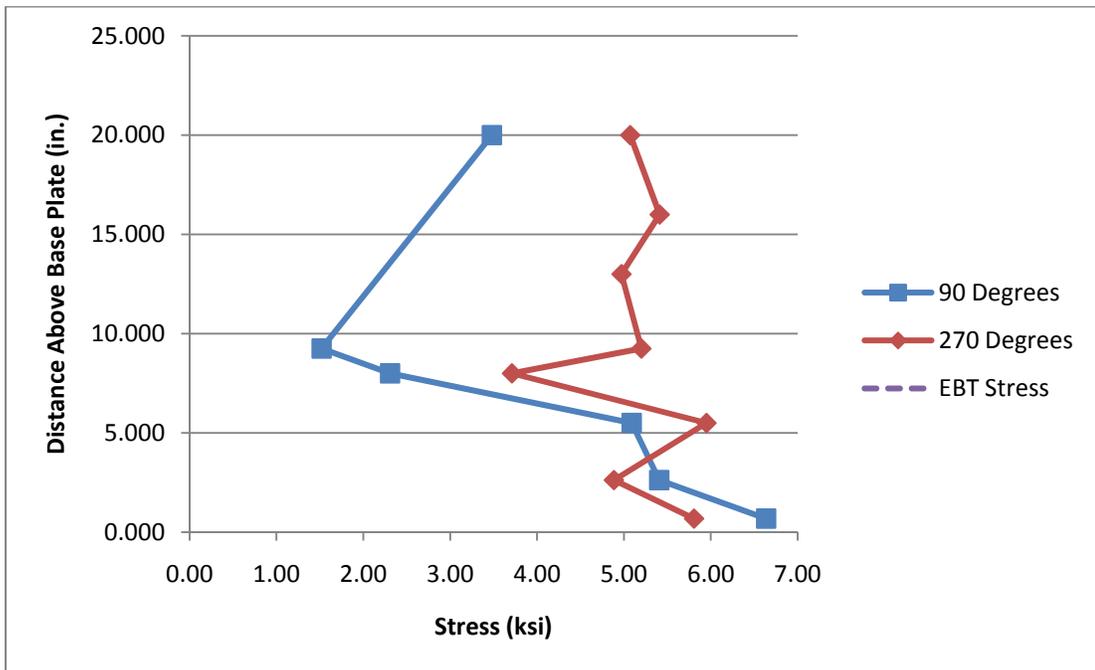
Figure 5.9: Stress distribution along height of Specimen 2 for loading to the west (the hand hole is located between 9.9 in. and 17.6 in. and the 90o side is in tension)

5.2.6 Hand Hole Gages

Table 5.6 shows the strain gage readings from the gages used around the hand hole in Specimen 1 and Specimen 2. Four uniaxial strain gages were used in Specimen 1. Since cracking initiated at the top of the hand hole in Specimen 1 (and Specimen 2), 5 rosettes were placed around the top of the hand hole in Specimen 2 to determine the biaxial state of stress at specific locations. Figure 5.10 and Figure 5.11 show the principal stresses in Specimen 2 for loading to the east and west respectively. Two important conclusions can be drawn from the magnitude of the principal stresses and the rotation angles.

In Specimen 1, a crack initiated on the upper right corner of the hand hole. In Specimen 2, a crack initiated in the lower left corner of the hand hole but a second crack initiated on the upper right corner. The actual location of crack initiation was located between the upper right corner gage and the right gage. Due to the crack initiation in this location, high stress ranges are expected. The maximum principal stresses computed from the rosette strains at the top right corner of the hand hole are 5.17 ksi in compression for loading to the east and 5.25 ksi in tension for loading to the west. The maximum principal stresses calculated from the strain rosette at the right side of the hand hole are 8.67 ksi in compression for loading to the east and 8.37 ksi in tension for loading to the west. The location where cracking initiated in Specimen 2, the bottom left hand corner, was most likely subjected to an even higher stress range since this location was farther down on the pole where the bending moment was larger.

The magnitude of the stress range is important when compared to the stress range at the CJP weld toe. The *2001 Specifications* characterize both the hand hole connection and the pole-to-base plate connection as Category E details. Since both details have the same fatigue resistance, the detail subjected to the highest stress ranges should be the critical location. The magnitude of the measured stress range in the hand hole exceeds the measured stress range at the CJP weld toe. Therefore, it makes sense that crack initiation occured at the hand hole. However, using EBT and the *2001 Specifications* cracking would be expected to initiate at the CJP weld toe first. This is discussed in greater detail below.

The *2001 Specifications* use a nominal stress approach for fatigue design where the stress ranges used in the S-N curves are computed using EBT and stress concentrations are assumed to be accounted for through physical testing to establish the fatigue detail categories. There are two methods in the literature for computing the nominal stresses at the hand hole from EBT. The first method was used in the design examples for luminaires in *NCHRP Report 412* and is the most simplistic. This method uses the net section properties and moment immediately below the hand hole to compute the nominal stress range. Using this method for the dimensions of Specimen 2 and an actuator load of 0.600 kips, the stress range computed is 12.2 ksi. Since the geometric SCF is unknown, this cannot be directly compared to the measured stress ranges. However, since the nominal stress at the CJP weld toe would be 13.26 ksi from EBT, the hand hole stress range from EBT would incorrectly lead the designer to believe that the CJP weld toe was the critical location for fatigue.

The second method of computing the nominal stress range is to use the reduced section properties at the location where cracking initiates. When using reduced section properties, the nominal stress range is again computed using EBT. Instead of using the net section, the hand hole cutout and hand hole stiffener are included in the computation of the section modulus. However, this method also provides misleading results. When using this method, the stress range is 25.2 ksi which may better approximate the actual stress range. Since the stiffener is so thick, it moves the neutral axis of the cross-section towards the hand hole, reducing the distance from the pole wall to neutral axis causing an increasing the section modulus. From these two methods, it is clear that using EBT to compute nominal stresses does not identify the critical fatigue detail. The rosette data shows that there is a biaxial state of stress around the hand hole that is not adequately accounted for in EBT or in the detail classification.

The strain rosette data shows two other interesting trends. Since cracking at the top of the hand hole occurred on the right hand side in both tests, it would be expected that the higher stress range would be found on the right side. The stress range computed from the top right gage was higher than that from the top left gage. However, the stress range from the left gage was greater than from the right gage. This could be due to gage misalignment since there is a high strain gradient in this region and a slight misalignment of the strain gages could greatly impact the data. The rotation angle of the principle stresses is also important to notice. It can be seen that the cracks propagate approximately parallel to the principle compressive stress and perpendicular to the direction of principle tensile stress. Although this is not exact, since the

cracks will propagate through imperfections in the material where stress is concentrated, it is a logical path for propagation given the rosette data.

Table 5.6: Hand hole strain gage readings

Gage Type	Gage Location	Loading East Strain (με)	Loading West Strain (με)
	Specimen 1		
Uniaxial	Top of Hand Hole 90 Degrees	-0.061	0.064
Uniaxial	Left of Hand Hole 90 Degrees	-0.242	0.241
Uniaxial	Right of Hand Hole 90 Degrees	-0.224	0.222
Uniaxial	Bottom of Hand Hole	-0.041	0.045
	Specimen 2		
Rosette	Top of Hand Hole 180 Degrees	0.013	-0.011
Rosette	Top of Hand Hole 135 Degrees	-0.018	0.019
Rosette	Top of Hand Hole 90 Degrees	-0.030	0.031
Rosette	Top Left of Hand Hole 0 Degrees	0.042	-0.040
Rosette	Top Left of Hand Hole 45 Degrees	-0.105	0.099
Rosette	Top Left of Hand Hole 90 Degrees	-0.152	0.149
Rosette	Top Right of Hand Hole 180 Degrees	0.012	-0.015
Rosette	Top Right of Hand Hole 135 Degrees	-0.125	0.122
Rosette	Top Right of Hand Hole 90 Degrees	-0.166	0.171
Rosette	Left of Hand Hole 180 Degrees	0.058	-0.054
Rosette	Left of Hand Hole 135 Degrees	-0.079	0.078
Rosette	Left of Hand Hole 90 Degrees	-0.295	0.284
Rosette	Right of Hand Hole 0 Degrees	0.060	-0.055
Rosette	Right of Hand Hole 45 Degrees	-0.059	0.057
Rosette	Right of Hand Hole 90 Degrees	-0.288	0.276
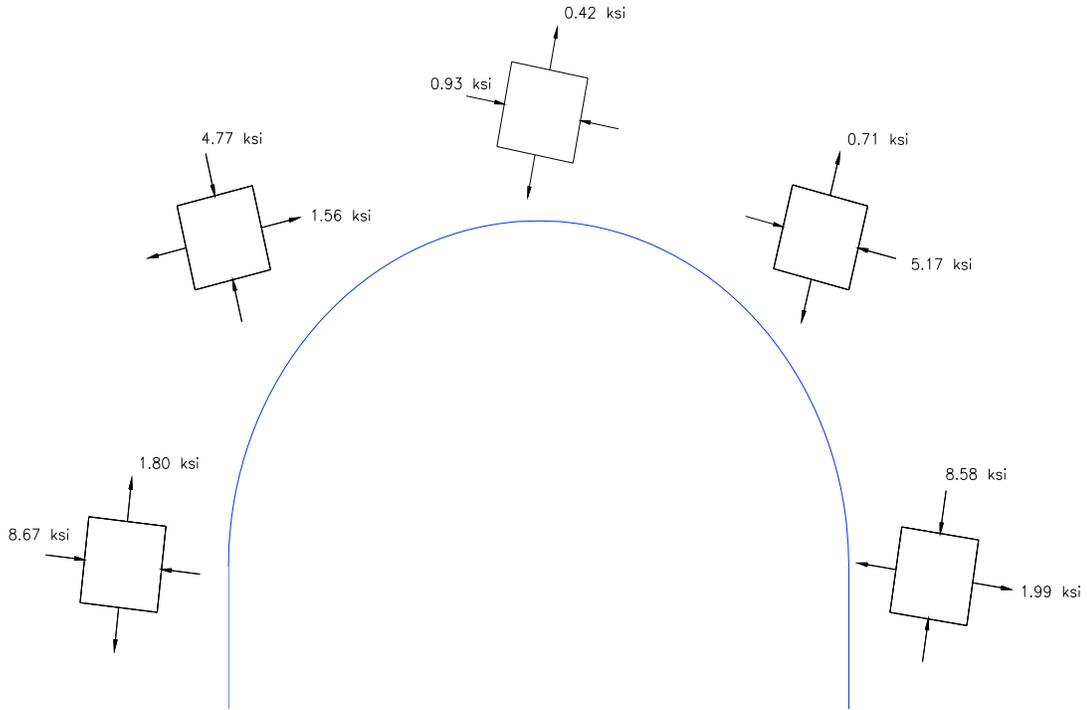
Figure 5.10: Principal stress distribution around the top of the hand hole in Specimen 2 for loading to the east (hand hole side in compression)
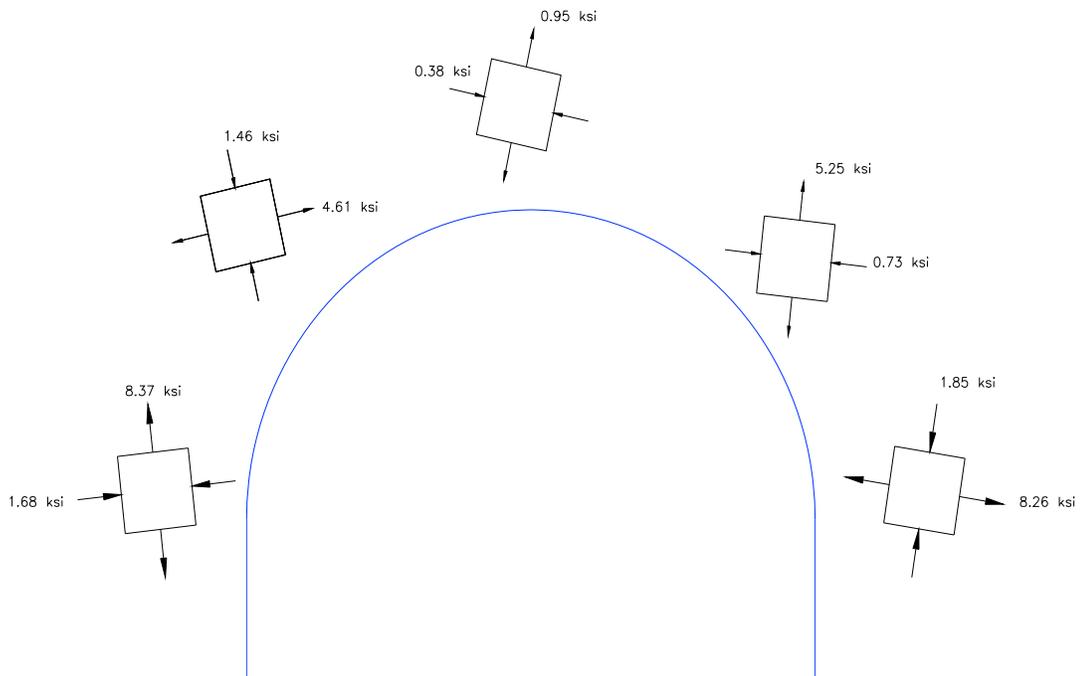
Figure 5.11: Principal stress distribution around the top of the hand hole in Specimen 2 for loading to the west (hand hole side in tension)

5.2.7 Interior Gages

Table 5.7 shows the strain gage data for the two strain gages placed on the inside of the pole. The purpose of the strain gages was to determine whether the strain through the thickness of the pole wall. It was speculated that in tension, the strain at the bottom inside of the pole should be reduced since the stress has to flow outward through the weld and to the anchor bolts; however, this was not apparent in the data. In socket connections where fillet welds are used, such a stress flow has been observed, but here the specimens has CJP welds to their base plates and no relief of interior stresses was observed. Interestingly, there are some high SCFs at 5.5 in. above the base plate, which may be due to proximity to the pole splice or the seam weld.

Table 5.7: Inside strain gages

Gage Location	Loading East Strain ($\mu\varepsilon$)	Loading West Strain ($\mu\varepsilon$)	Abs. EBT Strain ($\mu\varepsilon$)	Loading East SCF	Loading West SCF
Specimen 2					
1.5 in. Above Base Plate Inside 90 Degrees	-0.196	0.190	0.227	0.86	0.84
1.5 in. Above Base Plate Inside 300 Degrees	0.140	-0.204	0.197	0.71	1.04
5.5 in. Above Base Plate Inside 90 Degrees	-0.221	0.217	0.219	1.01	0.99
5.5 in. Above Base Plate Inside 300 Degrees	0.293	-0.302	0.190	1.54	1.59

5.3 String Potentiometers and LVDT

The LVDT and string potentiometers were used to measure the load-deflection behavior of the luminaire pole. Figure 5.12 and Figure 5.13 show the best fit linear load-deflection behavior for Specimens 1 and 2. Specimen 1 has a stiffness of 2.934 kips/in. and Specimen 2 has a stiffness of 2.857 kips/in. The slightly larger stiffness of Specimen 1 is most likely due to the hand hole being higher up on the pole where the moment is less.
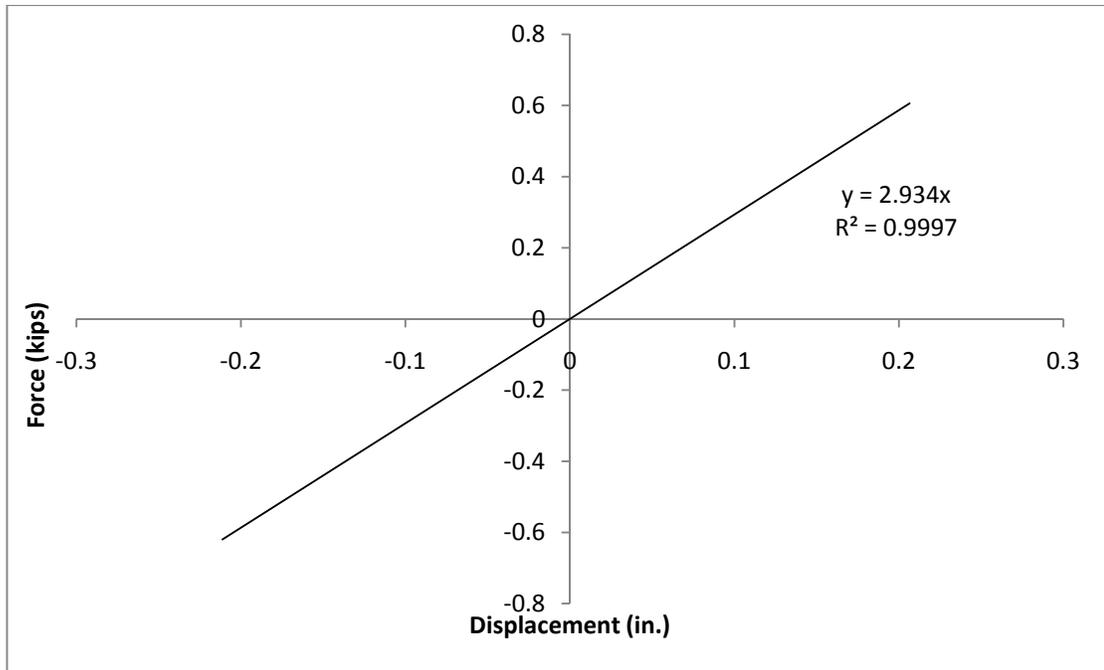
Figure 5.12: Load deflection behavior for Specimen 1
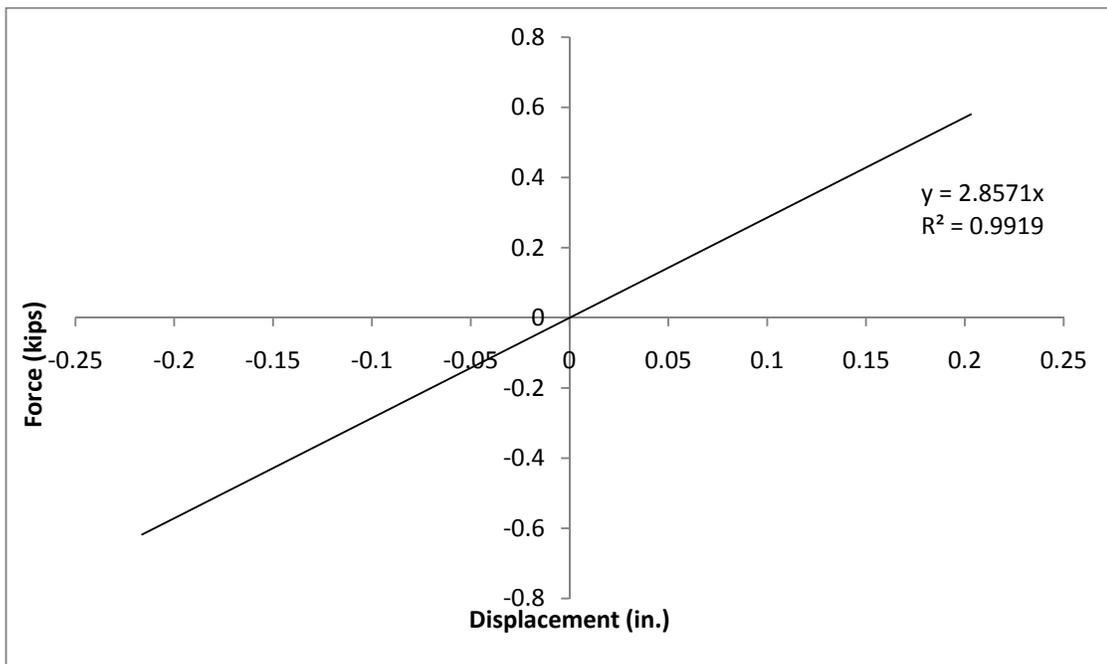
Figure 5.13: Load deflection behavior for Specimen 2

5.4 Fatigue Data

This section examines the results from the high cycle fatigue testing of two previously in-service WSDOT luminaire poles. The poles tested included CJP welded pole-to-base plate connections, stiffened hand holes, and anchor bolts. As described in previous sections, failure occurred by way of cracking at the hand hole which started at the hand hole corners and propagated outwards. The experimental fatigue life of the luminaire pole details will be compared to both the 50% and 95% confidence intervals developed by Ginal (2003).

5.4.1 Equivalent Nominal Stress Ranges

Since two different stress ranges were used per specimen during testing, equivalent nominal stress ranges were computed using Miner's equivalent stress from Equation 4.1. Nominal stresses are used to compare the fatigue data to AASHTO design values; therefore, the stress ranges at the pole-to-base plate connection were computed using EBT. For the hand hole, the stress ranges were computed at the tension fiber just below the hand hole opening using the section properties of the pole determined per the design examples in *NCHRP Report 412*. The nominal forces in the anchor bolts were computed using the moment of inertia of the bolt group. The forces on the single bolt side of the base plate were used since the force range in that bolt was double the force range in the two bolts on the double bolt side. The net tension area used to calculate anchor bolt stress area was computed using the following equation from the *2001 Specifications*:

$$A_s = \frac{\pi}{4}[d - \frac{0.97432}{n_t}]^2 \qquad (5.1)$$

where d is the nominal bolt diameter and n_t is the number of threads per inch. Since the bolts were installed in a snug-tight condition, it was assumed that no axial compressive stress was developed. Table 5.8 shows the nominal stress ranges for the different phases of testing in the different luminaire details under consideration and the computation of the equivalent nominal stress range.

Table 5.8: Equivalent stress ranges and cycle counts

Detail	Phase I Stress Range (ksi)	Phase I Cycle Count	Phase II Stress Range (ksi)	Phase II Cycle Count	Eq. Stress Range (ksi)	Eq. Cycle Count
Specimen 1						
CJP Weld Toe	13.78	1,362,627	27.56	1,369,708	13.94	1,369,708
Hand Hole	12.51	1,362,627	25.02	1,369,708	12.66	1,369,708
Anchor Bolt	8.69	1,362,627	17.38	1,369,708	8.79	1,369,708
Specimen 2						
CJP Weld Toe	13.71	2,429,211	27.42	2,501,088	14.57	2,501,088
Hand Hole	12.60	2,429,211	25.20	2,501,088	13.39	2,501,088
Anchor Bolt	8.64	2,429,211	17.28	2,501,088	9.18	2,501,088

5.4.2 Design for Finite Life and Infinite Life

An S-N curve can be divided into two regions; an infinite life region and a finite life region. Figure 5.14 shows an example of an S-N curve and illustrates the two regions. The finite life region represents the part of the curve which has a negative slope (in log-log space) and the infinite life region represents the part of the curve which has zero slope (in log-log space). Recall that the *2001 Specification* use an infinite life approach for the design of luminaire support structures.

With an infinite life approach, the CAFL, the stress range at the zero slope part of the curve in the infinite life region, is determined from experimental data. Nominal stress ranges for critical details are then limited to the CAFL for that detail classification. This approach works well for luminaire support structures subjected to wind loading where it is difficult to accurately compute the number of cycles at various stress ranges that the critical details will be subjected to during the service life of the pole. With a finite life approach, the fatigue stresses at critical details are large enough to be in the finite life region of Figure 5.14. A specific design life is typically used to compute a maximum service level stress range and corresponding number of cycles. These are then checked against the specific S-N curve for the detail's fatigue classification to ensure that the number of cycles doesn't exceed the fatigue limit for the expected stress range. This approach is commonly used in bridge design where the stress cycles are caused by vehicular traffic and can be accurately computed for the service life of the structure.

Although the infinite life approach is used for the fatigue design of luminaire structures testing was performed with stresses above the CAFL to ensure a finite life and reasonable test duration.

Thus, the fatigue data will be compared with the AASHTO S-N curves for both the 50% and 95% confidence intervals for various fatigue categories. The 50% confidence interval represents the actual mean number of cycles before failure at a given stress range for a given detail category. The 95% confidence interval is typically used for design when a finite life approach is used. If 100 specimens are tested for a given fatigue category at a given stress range, 95 should exceed the number of cycles represented by the 95% confidence interval S-N curve. The CAFL for a specific fatigue category does not change for a given confidence interval as it is independent of the number of cycles.
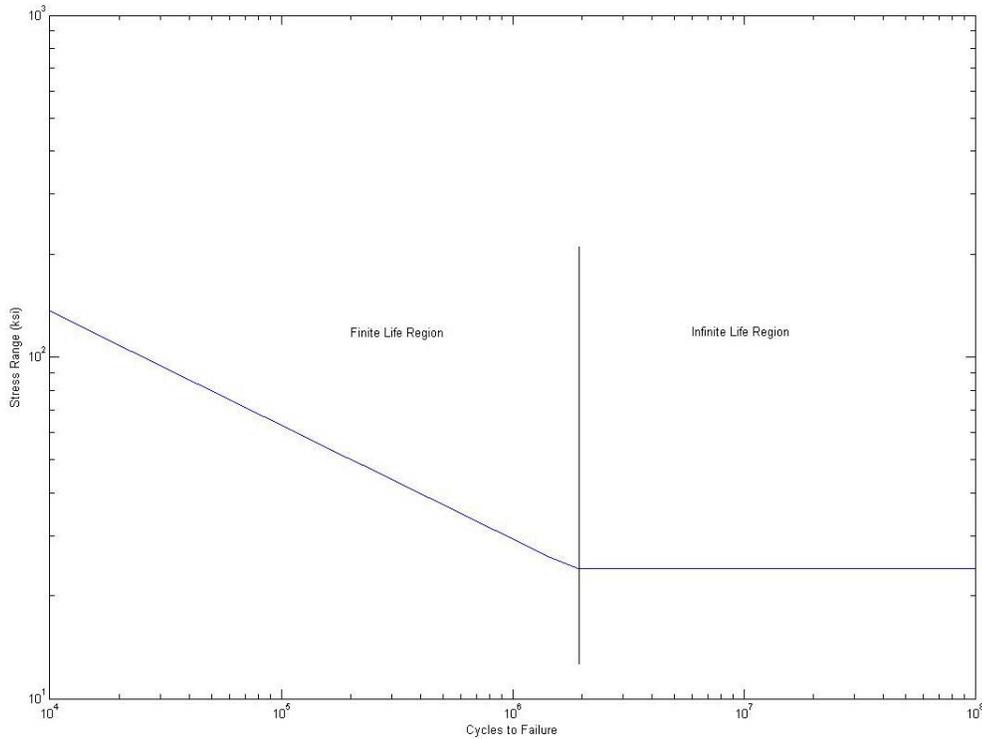
Figure 5.14: Example fatigue curve illustrating finite and infinite life regions

5.4.3 Fatigue Test Results for CJP Welded Tube-to-Transverse Plate Connection

The fatigue data for the pole-to-base plate connection in the two luminaire pole specimens is shown in Figure 5.15 with AASHTO S-N curves for fatigue categories D, E, and E'. Both specimens developed cracking at the hand hole prior to crack initiation in the CJP weld toe. Even though testing continued after crack initiation at the hand hole, cycle counting at the CJP

weld toe stopped and a run-out point was recorded because the cracking at the hand hole relieves the stresses at the CJP weld toe. Continuing to count cycles beyond the development of hand hole cracking would over predict the fatigue resistance of the pole-to-base plate connection. The run-out point for Specimen 1 exceeds the 50% confidence Category E curve and the 95% confidence Category D curve and Specimen 2 exceeds the 50% confidence Category D curve. Recall that the pole-to-base plate connection detail is classified as Category E in the *2001 Specifications*.

Two important considerations must be included in the discussion of the fatigue resistance of the CJP welded connection. First, the two pole specimens were removed from the field after 20-30 years of service. When tested in the SRL, the cycle counter was started at zero because there was no way of determining the number of accumulated fatigue cycles the pole was subjected to during service. However, the poles were subjected to fatigue loading in the field. Therefore, it is likely that a new pole received from the shop would perform better than the test specimens. Second, the data points were run-outs and don't represent points fatigue failure of the pole-to-base connection. Pole test inspection and analysis of the strain gage data showed no damage at the CJP weld toe. Therefore, it is presumed that the specimens could have been subjected to additional cycles before crack initiation.

Based on the test results and discussion above, it can be concluded that the two characteristic luminaire specimens performed better than predicted by the *2001 Specifications*. It is possible that if the hand hole crack had been repaired in Specimen 1 and testing continued, the number of cycles accumulated could have approached the number reached in Specimen 2. Thus, considering that Specimens 1 and 2 had identical connections to their base plates, that both had been in-service for 20-30 years, and that neither base plate connection failed, a Category D assignment may be reasonable for the CJP welded pole-to-base plate connection.

Several reasons why the pole-to-base plate connection performed better than expected are possible. The first is base plate flexibility, which as described in the literature review, impacts the fatigue resistance. Stiff base plates will reduce the SCF at the CJP weld toe which improves the fatigue resistance. Previous projects have described base plate flexibility in terms of thickness and the triangular base plates used here were both 1.75 in. thick, which would be considered stiff base plates. Base plate flexibility can also be described in terms of the distance from the anchor bolts to the pole wall where a base plate with anchor bolts located close to the

pole wall will be stiffer than one where the anchor bolts are farther from the pole wall. The triangular base plate configuration used in these luminaire pole specimens makes it possible for the anchor bolts to be located very close to the pole wall increasing the base plate stiffness. These factors could lead to stiff base plates relative to those for which a Category E classification is found adequate.

The second possible reason for the unexpectedly high fatigue resistance at the pole-to-base plate connection is the presence of a large weld there. Both specimens had a CJP weld with an unequal leg fillet weld over the top with leg sizes of 0.375 in. horizontal and 0.5 in. vertical. This fillet weld was larger than those in many tests described in the literature. The larger weld provides a better load path from the pole wall to the base plate reducing the SCF at the CJP weld toe and reducing the need for perfect CJP welds.

A third possible explanation for the high fatigue resistance is that the data was simply a result of the statistical variability in fatigue data. The *2001 Specifications* use one S-N curve to describe all CJP welded tube-to-transverse plate connections with attached backing rings. However, there are many factors impacting the fatigue resistance of the connection. Variables such as base plate flexibility, pole wall thickness, fabrication quality, size of the fillet weld over the top, and the location of other geometric discontinuities all impact the fatigue resistance of a specific connection. Therefore, the results discussed here indicate that the *2001 Specifications* seem to use a conservative fatigue classification for these details.
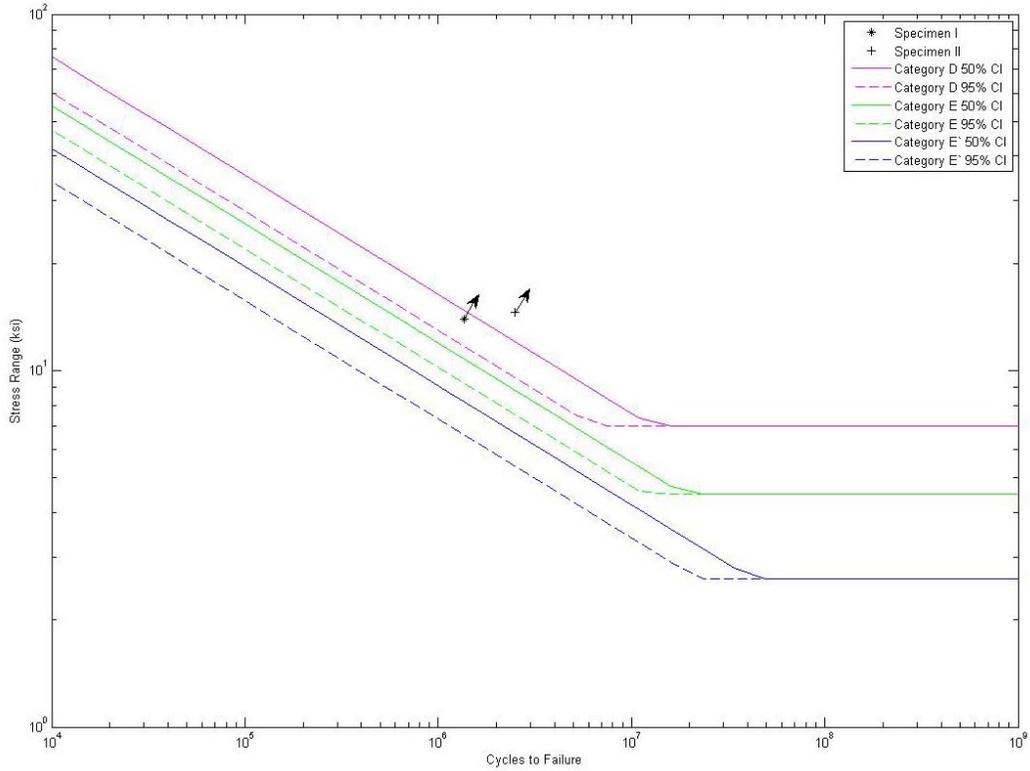
Figure 5.15: Fatigue data for CJP welded pole-to-base plate connection (arrows indicate run-out)

5.4.4 Hand Hole Detail

The two experimental fatigue data points for the hand hole connection are shown in Figure 5.16 with the 50% and 95% confidence interval AASHTO S-N curves. These data points represent actual fatigue failures rather than run-outs. The fatigue resistance of Specimen 1 exceeds the 50% confidence Category E curve and the 95% confidence Category D curve. The fatigue resistance of Specimen 2 exceeds the 50% confidence Category D curve. After crack initiation, the testing was continued and for both specimens and a significant number of additional cycles were applied before degradation in stiffness was observed. The experimental data points shown in Figure 5.16 correspond to the first cycle when cracks were identified. Note that the hand hole detail used in both specimens is classified as a Category E detail in the *2001 Specifications*.

As shown in Figure 5.16, the fatigue resistance of Specimen 1 was close to that of Category E while the fatigue resistance of Specimen 2 exceeded that of a Category E detail. When

interpreting these results it is important to consider the orientation of the pole in the laboratory relative to that in the field. In the laboratory, the hand hole was the critical connection on the pole and since the hand hole was located in the plane of loading, it was subjected to the maximum tensile and compressive stresses possible. However, in the field this is not necessarily the case. Typically, the hand hole is located in the same plane as the mast arm, either on the same side or on the opposite side. If the controlling wind induced phenomenon for luminaire support structures is natural wind gusts like it was for those tested here, the maximum stress are generated by wind pressure applied to the largest possible exposed area. For this reason, the highest magnitude stresses are from natural wind gust pressures in the out-of-plane direction, i.e. orthogonal to the mast arm. For such loading, the hand hole hand hole will be located on the neutral axis of the pole's cross section where the stress range will be small. Ensuring that the hand hole is either on the same side or the opposite side of the pole as the mast arm(s) will drastically reduce the stresses in the hand hole and delay the onset of fatigue failure.
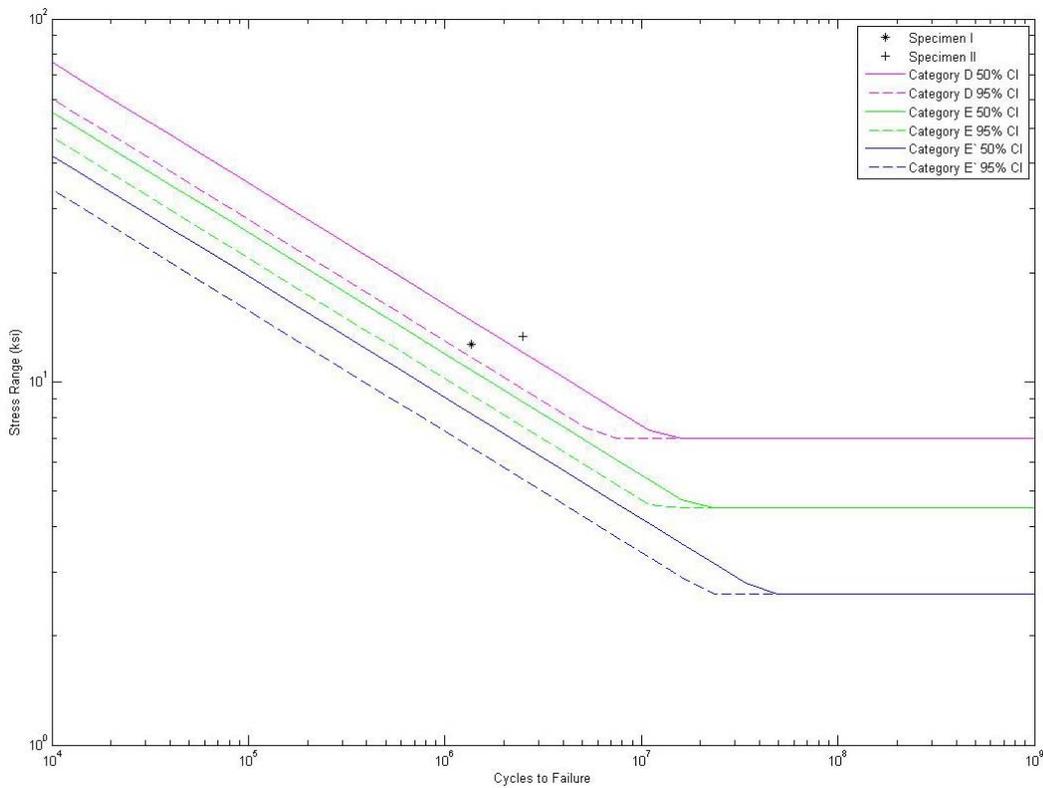
Figure 5.16: Fatigue data for hand hole connection

5.4.5 Anchor Bolt Connections

The two fatigue data points for the anchor bolts loaded in axial tension are shown in Figure 5.17. Like the pole-to-base plate connection data, cycle counting was discontinued once cracking initiated in the hand hole and a run-out point was recorded. Since the anchor bolts are below the hand hole, cracking of the hand hole will reduce the axial tensile stress in the anchor bolts causing the fatigue resistance to be over predicted. Because of the relatively low stress range in the anchor bolts, meaningful conclusions cannot be drawn from the run-out data points. The run-out point for Specimen 1 exceeded the 50% confidence interval Category E' curve and Specimen 2 exceeded the 50% confidence Category E fatigue curve. The anchor bolt subjected to axial tension is a Category D detail in the *2001 Specifications*.
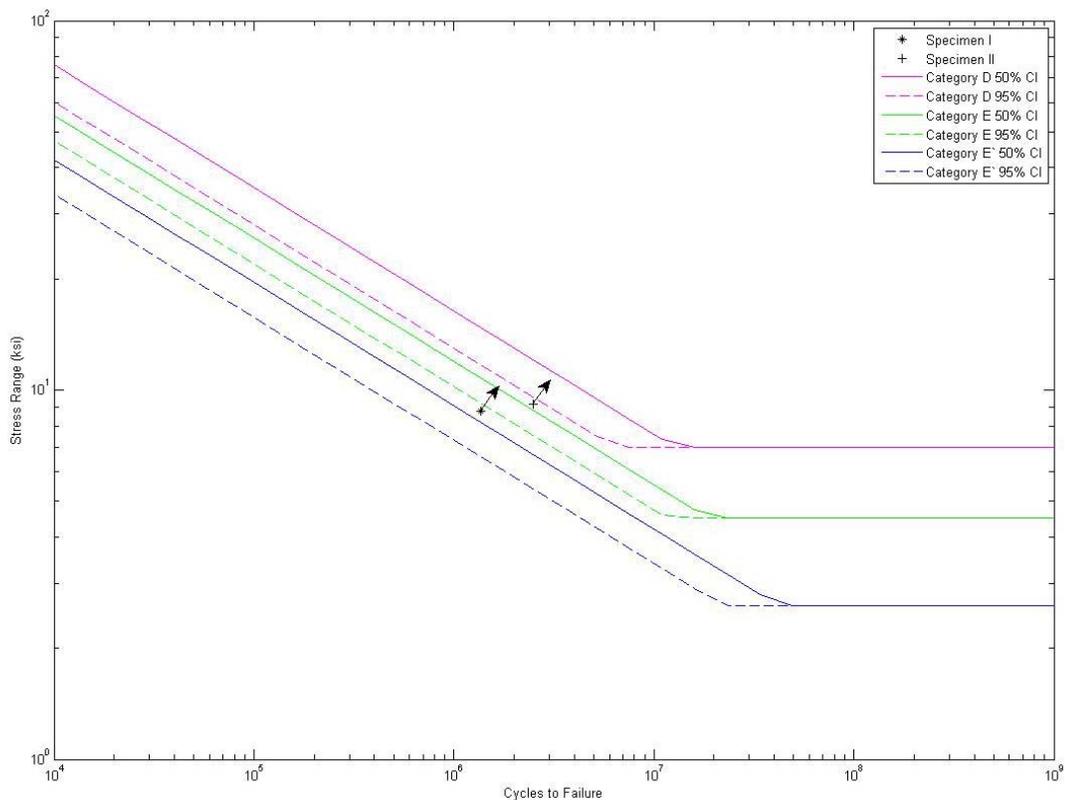
Figure 5.17: Fatigue data for anchor bolts (arrows indicate run-out)

Like the hand hole connection, orientation of the triangular base plate in the field should be considered. The single bolt side of the triangular base plate is typically located on the same side of the mast arm. Thus, the axial tension in that anchor bolt will be zero when the luminaire deflects out-of-plane where the largest possible area is exposed to the natural wind gust pressure inducing the largest possible bending moment at the pole's base. However, the three anchor bolt layout dictates that the other two bolts would reach nearly the same tensile stress when cycled with out-of-plane wind loadings. In the laboratory, the single bolt side was in the plane of loading. Therefore, the anchor bolt on the single bolt side was subjected to twice the tensile stress of the anchor bolts on the double anchor bolt side because it was twice as far from the neutral axis as shown in Figure 5.18. This was done in the laboratory to increase the stress range in the single bolt. Again, attention to the orientation of luminaire details installed in the field can "protect" them from high fatigue stress ranges.
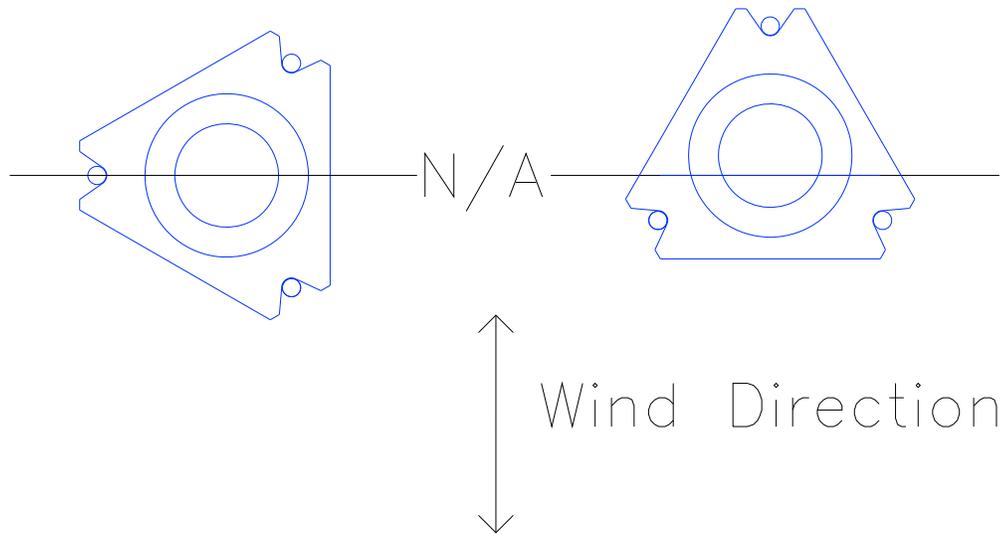
Figure 5.18: Base plate orientation used in the field (left) and in the laboratory (right).

Chapter 6 Finite Element Analysis

6.1 Overview

A finite element model of the pole base in Specimen 2 was developed using the finite element program MSC Marc Mentat 2008. The purpose of the finite element model was to verify the stresses measured by the instrumentation during the quasi-static testing and to perform a parametric study analyzing the effect on the base plate thickness, anchor bolt radius, and thickness of the hand hole stiffener on the stresses in the pole wall. A simplistic model of the characteristic pole and mast arm combination was developed in SAP 2000 to determine the dynamic characteristics.

6.2 Development of the Model

The model uses the element type 75 which is defined as a 4 node thick shell element with global displacements and rotations as degrees of freedom and bilinear interpolation is used for coordinates, displacements, and rotations (Marc, 2008). The simplistic element formulation makes it ideal for use with the non-linear springs used to represent the boundary conditions utilized in this model. The model consisted of 5,837 shell elements of varying thickness to model the base plate, the pole wall, and the hand hole stiffener. Only the bottom 30 in. of the pole were modeled which was sufficient to include the hand hole and went far enough above the hand hole that resulting geometric discontinuities effecting the stress distribution would not occur. The top nodes at the pole were connected to a restrained node by which a rigid beam element was used. A horizontal force of 0.600 kips and moment of 39 kip-in. were applied in both directions to the restrained node to represent the 0.600 kip force applied at the actuator centerline during the quasi-static testing. All elements were defined as having a steel material type with a Young's modulus of 29,000 ksi and a Poisson's ratio of 0.30. The individual components of the model will be summarized.

A picture of the finite element mesh used to model the pole base is shown in Figure 6.1. The triangular pole base plate was made up of shell elements with a thickness of 1.75 in. The indentations in the base plate for the anchor bolts were not modeled. The nodes at the third locations of the triangular base plate at a distance of 7 in. from the center of the pole had all 6

degrees of freedom fixed to model the restraint provided by the anchor bolts. The luminaire pole was modeled as a cylindrical surface made up of 3shell elements with a radius of 4.715 in. and a thickness of 0.1280 in. Although the actual luminaire was lightly tapered, a non-tapered section was used to simplify the analysis. The mesh was highly refined at the interface between the base plate and the pole to ensure the high strain gradient was captured. The hand hole was then modeled by removing elements on the surface of the pole wall and attaching them to a curve in the shape of the hand hole. The nodes on the edge of the curve were then translated 2.5 in. into the pole and elements were formed and meshed to model the stiffener. The hand hole stiffener was made up of shell elements that were 0.5 in. thick. The mesh at the interface between the hand hole opening and the stiffener was highly refined to capture the behavior in this location.

The behavior of the pole base plate bearing on the hydro stone was modeled by using non-linear springs. 1,260 identical non-linear springs were attached to each node on the base plate and were connected to a ground and only provided resistance in the vertical direction. The non-linear springs were defined with a bilinear force-displacement curve that was extremely stiff in compression and had almost zero stiffness in tension. The purpose of the non-linear spring was to simulate the behavior in which the hydro stone is extremely stiff in compression but does not restrain the base plate from lifting off.
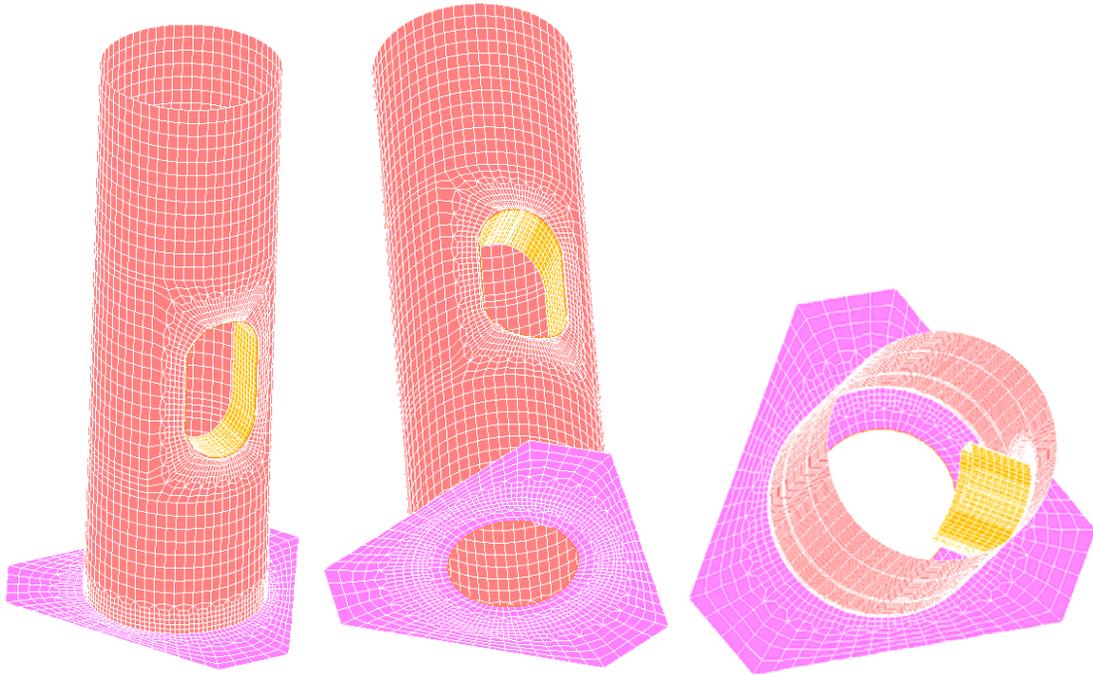
Figure 6.1: Finite element mesh of luminaire pole base

To simplify the analysis the pole was modeled as a non tapered cylinder with the diameter at the pole base (9.43 in.) used along the length. The pole was modeled using a cylinder. The displacement was fixed at the three sides of the base plate at the locations corresponding to the bolt holes. A contact body was used to represent the bearing surface between the pole base plate and the hydro stone surface used in the laboratory. The bottom of the pole base plate was defined as a deformable body and the hydro stone bearing surface was defined as a rigid contact body. It should be noted that since shell elements were used instead of solid elements, the weld could not be modeled. Instead, the model only represents the geometric stress concentration.

6.3 Validation of Model

To validate the model, stresses at the weld toe and along the height of the pole were plotted for different levels of mesh refinement. When performing the mesh refinement, the hand hole wasn't included in the model. This was done because the hand hole was meshed manually and was not possible to automatically refine. Therefore, the mesh refinement was done on the pole model without the hand hole. Once an acceptable level of refinement was determined, the hand

hole was inserted into the model. A finer mesh was used around the hand hole and then built out to the more course pole mesh determined using the convergence study.

Four different models were tested with increasingly finer meshes. For each mesh, the longitudinal bending stresses at the weld toe and along the height of the pole at the 90° and 270° locations were measured. The weld toe stresses were measured at the lowest location on the pole at which the intersection of the base plate and pole did not cause distorted stress readings. Figure 6.2 and Figure 6.3 show the longitudinal bending stresses at the weld toe and along the height of the pole for different levels of refinement respectively. 2800 elements showed acceptable convergence and was used for the final mesh. However, the stresses at the 90 degree location were lower than for 11,520 elements. To eliminate this, a finer mesh was used at the intersection between the base plate and pole and then built out so that the stresses at the base plate would be modeled. Based on this method, it was determined that acceptable refinement existed to model the behavior in locations where high strain gradients existed.
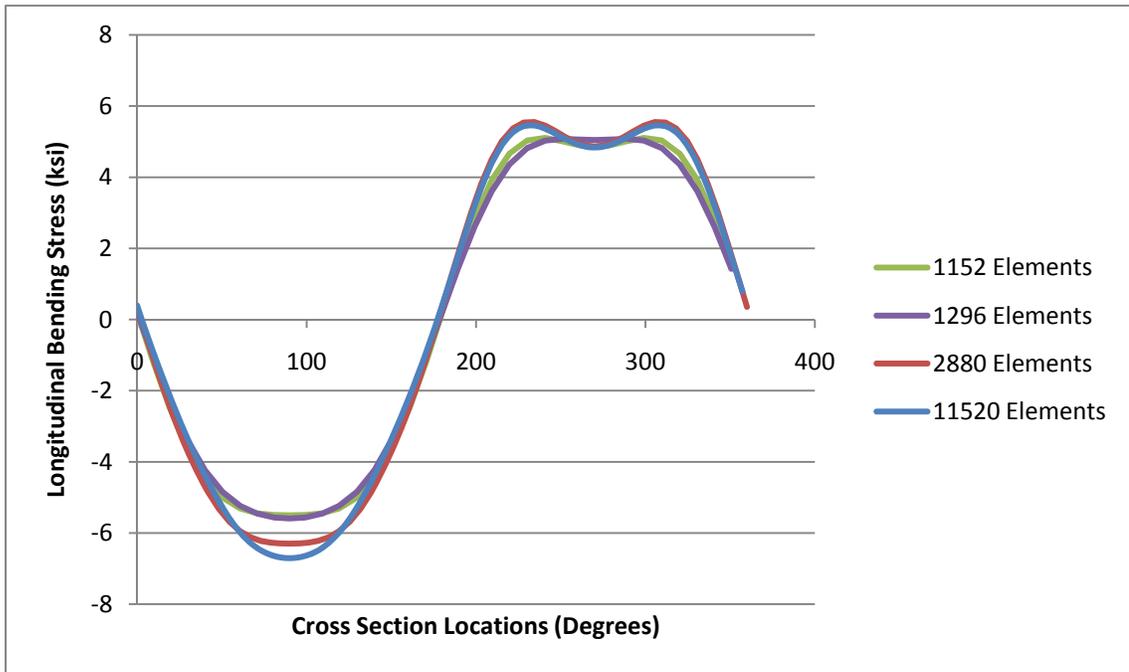
Figure 6.2: Weld toe stresses at different levels of mesh refinement

146
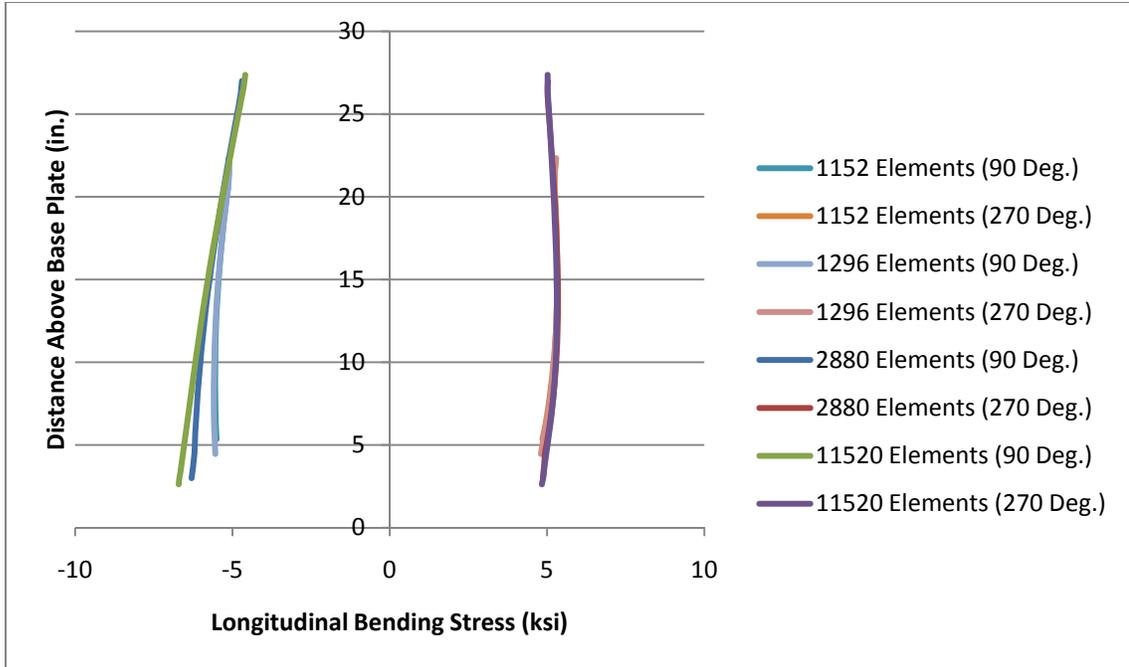
Figure 6.3: Stresses along height of pole for different levels of mesh refinement

The stresses around the circumference of the pole were extracted from the analysis to see if the behavior matched the experimental data. Figure 6.4 shows the longitudinal bending stresses computed at the weld toe in the model and from the experiment. Two interesting trends can be observed. The first trend is that the experimental stress readings show good agreement in the 60° and 120° gages but fall short in the 90°, 240°, 270°, and 300° gages. The source of this error is most likely found in the strain gage installation or in the effect of bearing surface. The strain gages can't be placed exactly at the weld toe and instead are approximately 1/8 in. or ¼ in. above the weld toe. However, since this is a region of high strain gradient, this slight distance could cause the reduction in stresses that are seen in the experimental data. The other possible explanation is that the finite element analysis does not include the CJP and fillet welds used in the experimental setup. The large welds in the test specimens smooth out the flow of stresses and reduce the impact of the geometric discontinuity.

The other trend is that the reduction in strain at the 270° measured experimentally also shows up in the finite element analysis. However, from the model it can be seen that the stresses at 270° are significantly lower than at 90° for both cycles. This is probably due to the fact that the 270° location is just above the most flexible part of the base plate. The presence of the butterfly

effect is the most likely the reason for the reduction in stress at 270º in the experimental data and in the finite element model.
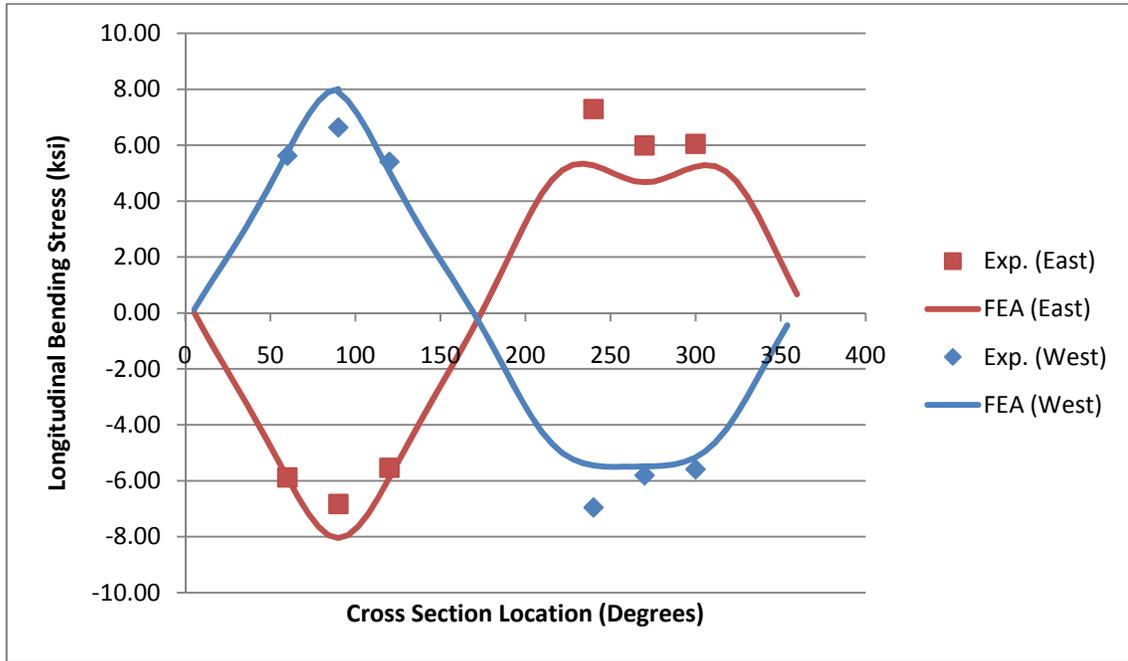
Figure 6.4: Longitudinal bending stresses around the weld toe

6.4 Parametric Study

6.4.1 Impact of Base Plate Thickness

As shown in previous tests, base plate thickness influences the stress concentration factor at the weld toe. However, it was presumed that the effect of base plate thickness on a triangular base plate might be different. For that reason, a parametric study was performed to determine the variation in the SCF at the weld toe when the base plate thickness was varied. In the finite element model, the thickness of the shell elements on the base plate were varied from 1.25 in. to 3.00 in and the longitudinal bending stress was computed at the weld toe. The loading was applied both to the east and to the west and the maximum compressive and tensile stresses at the weld toe were determined. The standard pole dimensions explained above were used at all other locations. Table 6.1 shows the SCFs computed for the different cycles and base plate thicknesses and Figure 6.6 shows a plot of that data.

Table 6.1: SCFs at the weld toe computed from finite element analysis

Base Plate Thickness (in.)	Loading East (Double Bolt Side in Tension)		Loading West (Single Bolt Side in Tension)	
	Maximum Tensile SCF	Maximum Compressive SCF	Maximum Tensile SCF	Maximum Compressive SCF
1.25	1.17	1.90	1.94	1.43
1.50	1.19	1.75	1.72	1.35
1.75	1.22	1.60	1.60	1.30
2.00	1.25	1.51	1.52	1.27
2.25	1.27	1.45	1.47	1.27
2.50	1.29	1.41	1.42	1.29
2.75	1.30	1.38	1.39	1.30
3.00	1.31	1.35	1.36	1.31

As expected from the literature, the base plate thickness has a large effect on the SCF at the weld toe. Two important trends should be pointed out. The tensile SCF on the double bolt side actually increases for loading to east while the compressive SCF on the single bolt side decreases as the plate gets thicker. For loading to the west, the tensile SCF on the single bolt side decreases and the compressive SCF on the double bolt side decreases and then levels off as the base plate thickness increases. This is most likely a cause of the boundary conditions between the base plate and the hydro stone. As the double bolt side goes in tension and the base plate wants to pull up, there is nothing restraining that vertical deformation. However, as the base plate gets stiffer, the restraint of the base plate is restraining the bottom of the pole causing high stresses to occur. However, for the west cycle this behavior is not seen because the base plate bears on and restrains the pole wall. Like with square base plates, the thickness of the triangular base plate significantly effects the SCF at the weld toe at the base of the pole and therefore will effect the fatigue resistance of the luminaire support structure. It can be seen that the effect of base plate thickness starts to level off at above 2.5 in.
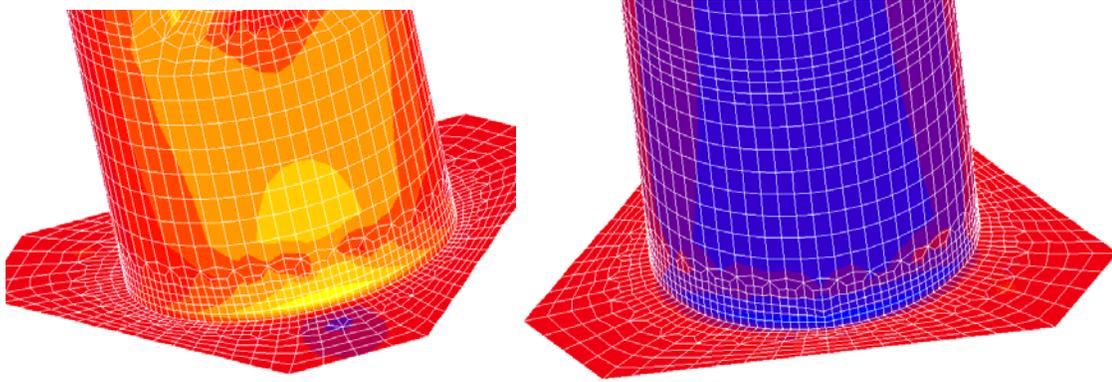
Figure 6.5: Stress contours in the pole base for loading to the west
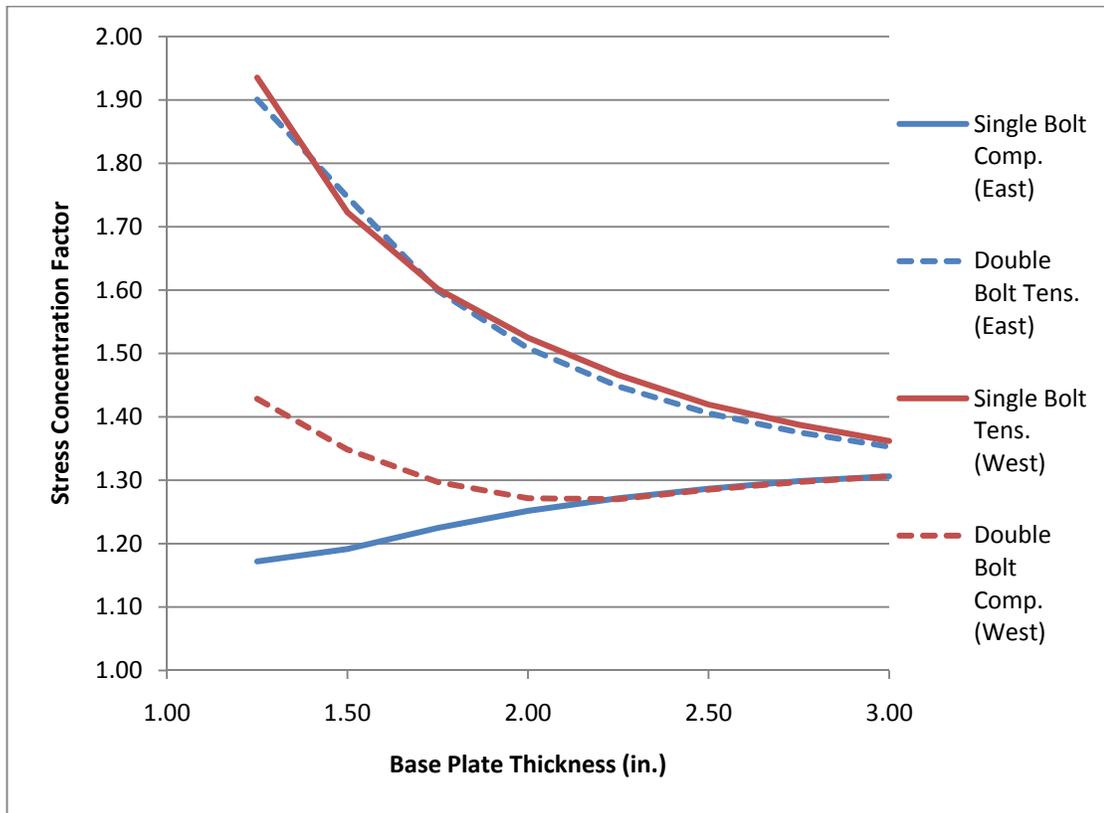
Figure 6.6: SCF at the weld toe for different base plate thicknesses

6.4.2 Thickness of Hand Hole Stiffener

Since cracking initiated around the perimeter of the hand hole, the effect of the hand hole stiffener was studied. The length of the hand hole stiffener remained at 2.5 in. but the thickness

of the stiffener was varied by changing the thickness of the stiffener shell elements. All other dimensions remained the same. The maximum (tensile) and minimum (compressive) principle stress in the pole wall around the perimeter of the hand hole was recorded for the loading east and west cycles respectively. In every situation, the controlling principle stresses occurred at the bottom side of the hand hole where the curved portion intersects the straight portion. The principle stresses are shown in Table 6.2 and plotted in Figure 6.7. The thicker hand hole stiffener significantly reduced the stresses in the pole wall adjacent to the hand hole for both cycles. However, the effect of the increased stiffener thickness is reduced as the stiffener thickness approaches 1 in.

Table 6.2: Maximum principle stress for loading to the west and minimum principle stress for loading to the east in the pole wall at the perimeter of the hand hole

	Loading East--Double Bolt Side in Tension	Loading West--Single Bolt Side in Compression
Hand Hole Stiffener Thickness (in.)	Maximum Principle Stress at Hand Hole (ksi)	Minimum Principle Stress at Hand Hole (ksi)
0.125	-16.16	15.83
0.250	-13.59	13.36
0.375	-11.82	11.66
0.500	-10.70	10.57
0.750	-9.23	9.15
1.000	-8.50	7.95
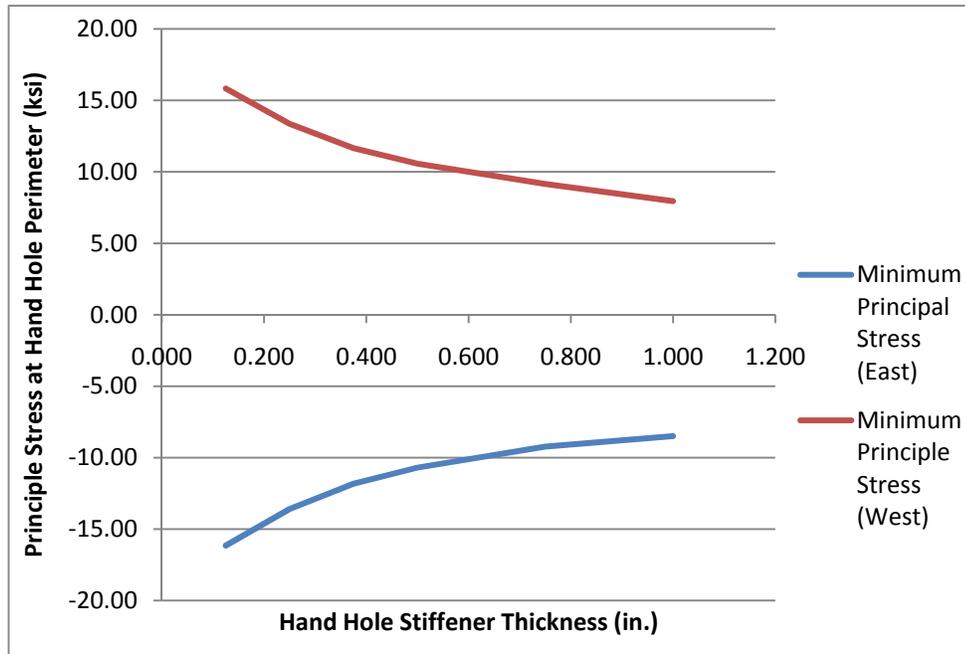
Figure 6.7: Principle stresses in the pole wall adjacent to the hand hole stiffener

6.4.3 Bolt Hole Radius

The effect of the bolt hole radius on the longitudinal bending stress at the weld toe of the pole to base plate connection was considered. The bolt hole radius was changed by moving the locations of the nodes that are fixed for all 6 degrees of freedom radially towards and away from the center of the pole but the number of bolts (three) remained the same. Essentially, this changes the stiffness of the base plate by changing the unsupported length. However, when modeled, the bolt radius did not have a major impact on the SCF at the weld toe. The analysis was run for a 1.75 in. thick base plate and it is possible that for a more flexible base plate the bolt hole radius may have had a bigger impact. With that said, the designer should always move the bolts as close to the pole as possible while leaving room for tightening.

Bolt Radius (in.)	Loading East--Double Bolt Side in Tension		Loading West--Single Bolt Side in Tension	
	Maximum Tensile SCF	Maximum Compressive SCF	Maximum Tensile SCF	Maximum Compressive SCF
6.25	1.22	1.60	1.60	1.30
6.81	1.24	1.62	1.62	1.32
7.38	1.25	1.64	1.64	1.33
7.94	1.26	1.66	1.66	1.34

6.4.4 Dynamic Characteristics

A simple modal analysis of the characteristic luminaire pole structure was used in SAP2000 to determine the dynamic properties. The pole dimensions were a 40 ft. mounting height, 12 ft. mast arm, and the same pole dimensions were used as in the test specimens. The dynamic characteristics are shown in the Table 6.3.

Table 6.3: First five mode shapes of characteristic luminaire support structure

Mode Number	Period (sec)	Frequency (Hz)
1	0.900	1.11
2	0.854	1.17
3	0.341	2.93
4	0.291	3.44
5	0.086	11.57

Chapter 7 Development of a Framework for Estimation of Remaining Fatigue Life

7.1 Overview

The fatigue design of luminaire support structures is challenging because they are subjected to variable amplitude loading and the actual number of cycles and corresponding stress ranges seen in the field are difficult to predict. The infinite life approach to fatigue design of luminaires adopted in the *2001 Specifications* is an effective way to ensure that luminaire support structures have the required fatigue resistance even though the number of cycles and corresponding stress ranges are unknown. However, the fatigue design provisions in the *2001 Specifications* provide no guidance for determining the remaining life of an in-service luminaire support structure. Since the majority of in-service luminaire support structures in the state of Washington were designed prior to the development of the *2001 Specifications* and with little attention to fatigue resistance, an estimate of the remaining life would be highly beneficial. A remaining life estimate would provide a way to prioritize the replacement of luminaires, focus inspection efforts on at-risk luminaires, and assess the impact of additional signage which increases exposed area and fatigue stresses.

To estimate the remaining life of an in-service luminaire, a sophisticated framework must be developed that reflects the uncertainty in both the wind loading and luminaire fatigue resistance. The development of such a framework requires four components; (1) a wind pressure model capable of probabilistic representation of the wind pressure for use in dynamic analysis; (2) a structural model of a particular luminaire where dynamic pressures can be applied and probabilistic estimates of cycle counts at various stress ranges can be made; (3) equations for the fatigue resistance of specific luminaire details including estimates of uncertainties, and (4) a damage accumulation model. The following chapter describes the framework for developing a model to estimate remaining life applied specifically to luminaire support structures in the state of Washington. The framework is based on work by Foley et al. (2004) and their investigation of the remaining life of sign bridge structures. This section outlines the framework for remaining life estimation and identifies specific areas where additional data and/or research is necessary to fully implement it. A flow chart summarizing specific components of the framework is shown in Figure 7.1.
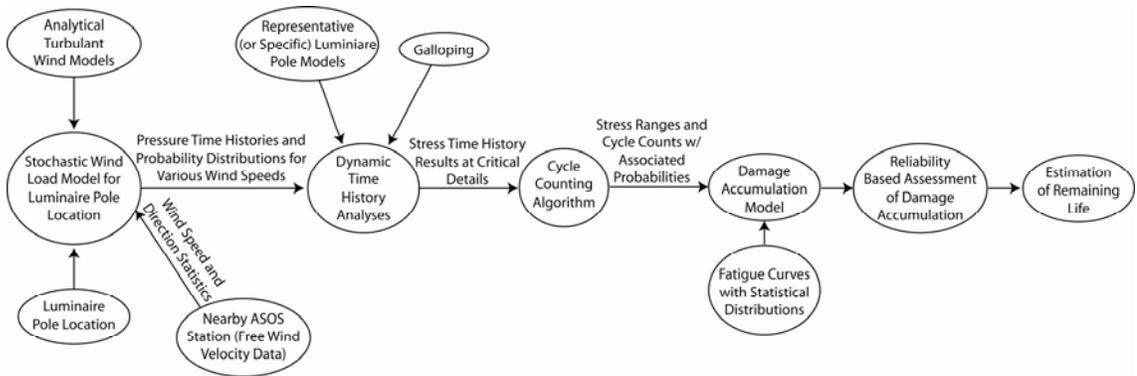
Figure 7.1: Flow chart of the necessary components for estimating the remaining fatigue life

7.2 Determination of Pressure Time Histories and Probability Distributions

To estimate the applied loads that a luminaire will be subjected to during its service life, wind pressure time histories must be developed that probabilistically represent peak wind velocity and its geographic distribution across the state. Accepted methods for generating wind time histories that consider both the mean wind velocity and wind gusts are applied with wind speed data collected from weather stations across the state.

7.2.1 Conversion of Weather Station Data to Probabilistic Distributions of Velocity and Direction

The probability that a specific wind event will occur must be computed based on weather station data. The National Oceanographic and Atmospheric Association (NOAA) maintains a large number of weather stations throughout the state of Washington. A map of the weather stations in the state of Washington is shown in Figure 7.2. Each station continuously measures free wind velocity and direction, with wind velocities recorded as mean wind speeds over a given time interval. From this data, two histograms can be developed to determine the probability of a specific wind event occurring at a specific site. The first is the frequency of occurrence of a mean 5-second wind velocity within predefined velocity bins. The second is the frequency of occurrence of a specific wind direction for each of the mean 5-second wind velocity bins. Examples of these two types of histograms are shown in Figure 7.3. Using the wind station data, conditional probabilities can be computed for all possible wind events at a

specific location. For example, the histograms enable the estimation of the probability that a mean 5-second wind velocity between 7.5 and 12.5 mph at a direction between 55 and 65 $^{\circ}$'s will occur at a specific location.

Map generated by NOAA's National Climatic Data Center, 2008
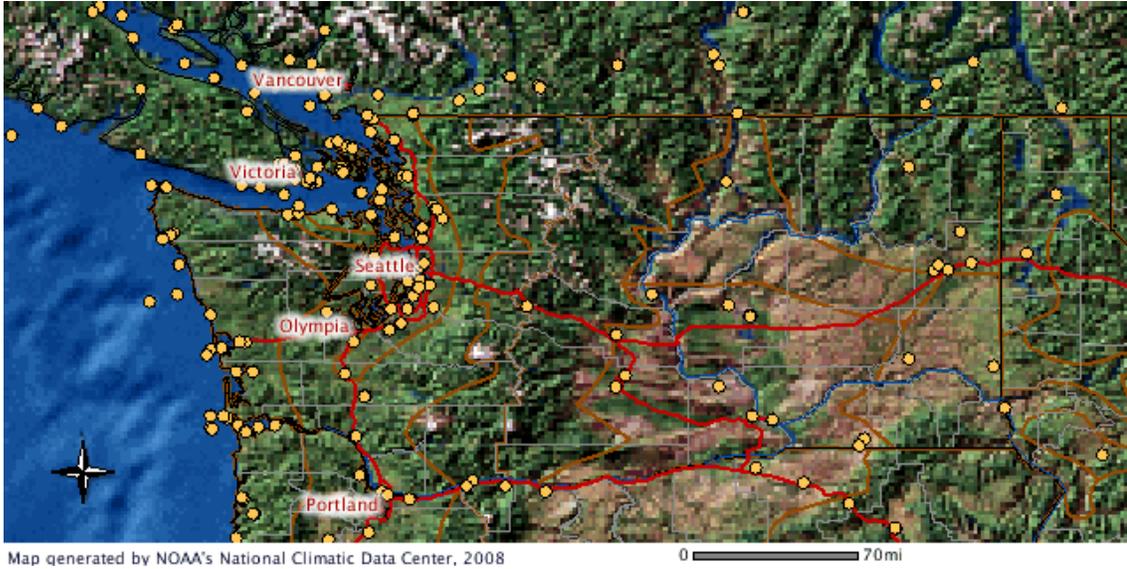
Figure 7.2: NOAA weather stations in the site of Washington
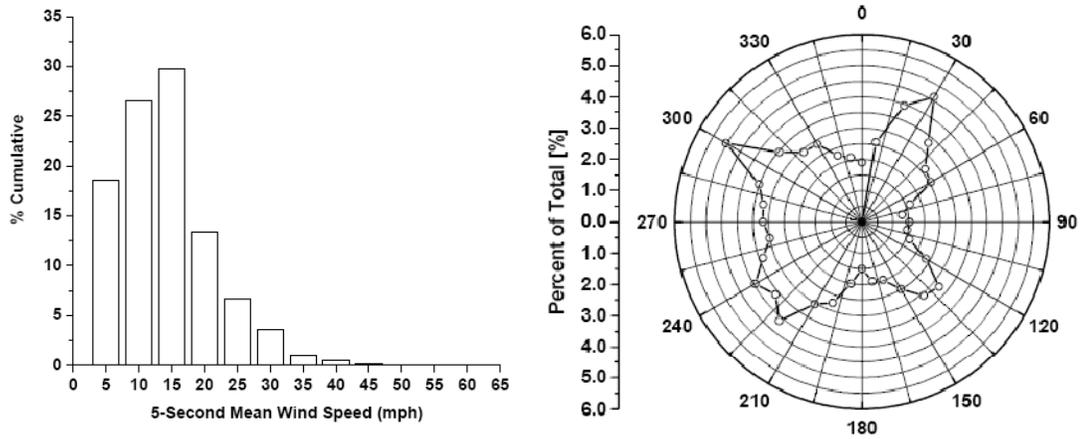
Figure 7.3: Histograms showing the mean wind speed probability and directional probability at a mean 5-second wind speed of 15 mph (Ginal, 2003)

7.2.2 Conversion of Mean Wind Speeds to Turbulent Wind Time Histories

The weather station data provides a probabilistic representation of the mean 5-second wind speed and direction. However, the turbulent wind component must also be included as well as the variation of wind speed with time, i.e. wind time histories. Both components are necessary for capturing the dynamic response of the luminaire support structure. A modified frequency spectrum model can be used to represent the turbulent wind component in the frequency domain, where the power spectral density is approximated by (Kaimal, 1972):

$$S_K(f) = \frac{200 U_*^2 * z}{\overline{U_z}(1 + \frac{50fz}{\overline{U_z}})^{5/3}} \tag{7.1}$$

where $\overline{U_z}$ is the desired mean wind speed at a height z above the surface, f is the frequency, and U_* is the shear velocity, which accounts for turbulence. Using the power spectral density function, the random turbulent wind speed component of the time history can be developed using (Iannuzzi and Spinelli 1987; Levy 1996; Shinozuka and Jan 1972):

$$u_z(t) = \sum_{k=1}^{N} \sqrt{2S_K(f_k)\Delta f} \cos(2\pi f + \varphi_K) \tag{7.2}$$

$$f_k = k\Delta f \tag{7.3}$$

and N is the number of frequencies at which frequency spectrum S_K is evaluated, f_k is the specific frequency, Δf is the assumed frequency increment, t is the assumed time value, and φ_K is a Gaussian random number distributed between 0 and 2π, chosen for each specific frequency. This summation creates a random turbulent wind time history centered about the mean wind velocity, with a broad range of frequency content. For 5-second mean wind velocities, a 5-second long time history would be produced. Note that multiple time histories for each mean velocity may be produced from this stochastic process.

7.3 Structural Modeling and Fatigue Life Estimation

The next step in the procedure is to apply individual time histories to the structure and determine the number of cycles at each given stress range in more specific detail during the 5-second time interval. This step requires development of a finite element model of the specific luminaire support structure capable of undergoing time history analysis, a counting procedure that can record the number of cycles at each stress range during the interval, and a damage accumulation law that estimates the remaining life of the structure based on the annual number of cycles at each stress range.

7.3.1 Determining Stress Ranges from Random Wind Time Histories

To use the wind time histories developed in the previous section, a finite element model of the structure must be developed for use in the time history analyses. The random wind time history can then be applied to the structure and a stress history at the specific details of interest recorded. The analysis would then be repeated at all desired wind speeds and for variable wind directions. The number of cycles at a given stress range can then be determined from the stress history output from the model. Typically, a rain flow counting procedure would be used since it is the most simplistic procedure to program, produces reasonable results, and is generally an accepted approach.

Once the number of cycles and corresponding stress ranges are determined for the wind time histories associated with various wind velocities, the number of cycles occurring in a given year at each stress range must be determined. This is done by multiplying the number of cycles at a given stress range in the five second interval by both the number of 5-second intervals in a year (6,307,200) and the probability that the mean wind speed will be at the specified magnitude and direction. This will give the total number of cycles that occurred at each stress range for each year the luminaire support structure is in-service, accounting for the statistical distribution of wind load.

7.3.2 Determining the Remaining Life Using Linear Damage Accumulation Law

With the yearly demand estimated, the remaining life of the structure can be computed using a damage accumulation law and the AASHTO stress-life equations. The damage accumulation law is simply a method of combining the damage due to cycles at each stress range to estimate the total damage due to the complete loading history. A linear damage accumulation law by Palmgren and Miner (1945) has been used in the literature and has been shown to give adequate results. The Palmgren and Miner damage accumulation law simply states that the total damage is equal to the sum of the fractional damage at each stress range. A damage accumulation equal to unity represents fatigue failure of the structure. The damage accumulation law is represented by the following equation:

$$\sum D_i = \sum \frac{n_i}{N_i} \qquad (7.4)$$

where n_i is the number of cycles accumulated at stress range S_i and N_i is the number of cycles at stress range S_i that would cause fatigue failure. The number of cycles at a given stress range that would cause fatigue failure is determined using the AASHTO stress life equation:

$$N_i = AS_i^{-m} \qquad (7.5)$$

where A is the x-intercept of the fatigue curve in log-log space and m is the slope of the fatigue curve in log-log space (taken as 3 for AASHTO S-N curves). The damage accumulation is then computed by taking the ratio of the number of cycles accumulated at each given stress range determined using the time history analyses to the number of cycles to failure at each given stress range computed using the stress life equation.

This procedure must be considered in a probabilistic sense. Using the stress life equation parameters determined by Ginal (2003) and shown in Table 7.1, a confidence interval can be associated with an S-N curve for a specific fatigue detail category. When applying this procedure, the confidence interval associated with the stress life equation is the same confidence interval applied to the damage accumulation. In other words, if a 95% confidence interval stress life equation is used, the corresponding damage computed using the linear damage accumulation law also has a 95% confidence interval. Basically, the number of cycles to failure computed using the stress life equation is a random variable but the number of cycles accumulated computed using the time history analyses is not. Applying the confidence interval associated with the stress life equation to the damage accumulation law drastically reduces the complexity of the model while still producing acceptable results.

Table 7.1: S -N design curve parameters for AASHTO fatigue classifications (Ginal, 2003)

Detail Category	Confidence Level	S_{rD} (ksi)	A_D $(x10^8)$	$CAFL_D$
D	20%	14.50	61.0	7,000
E	20%	10.25	21.5	4,500
E'	20%	7.98	10.2	2,600
D	50%	13.00	43.9	7,000
E	50%	9.50	17.1	4,500
E'	50%	7.20	7.46	2,600
D	70%	11.95	34.1	7,000
E	70%	9.00	14.6	4,500
E'	70%	6.67	5.93	2,600
D	95%	10.30	21.9	7,000
E	95%	8.10	10.6	4,500
E'	95%	5.80	3.90	2,600

7.3 Other Considerations

7.3.1 Site Specific Variations

The NOAA site data provides a recording of the wind data and direction in an open location. However, the site conditions for luminaire poles vary considerably and this will impact the wind loading. If the luminaire is located on the leeward side of a hill where it will be sheltered from the wind, the wind data for an open location would likely over predict the magnitude of the mean wind velocity the specific luminaire is subjected to. Conversely, if a luminaire is located between buildings where a wind tunnel effect is likely to occur, the nearest weather station might under predict the magnitude of the wind speed. Therefore, it would be beneficial to observe and report the specific site characteristics of newly installed luminaires or existing luminaires that could potentially cause the wind behavior to deviate from that which would be reported at the nearest weather station. Adjustments of wind station data based on observed site conditions can be made using approximations from ASCE 7 (2005).

7.3.2 Need for Additional Fatigue Testing of Specific WSDOT Details

If a large scale project is taken on to assess the remaining life of a large inventory of poles, it would be beneficial to do fatigue testing of the specific details under consideration instead of

using the fatigue classifications in the *2001 Specifications*. As described previously, the classifications are meant to encompass all details in a certain category and are meant to be conservative for design purposes. Fatigue testing of specific details of interest in the WSDOT inventory would further refine the model by utilizing a more representative model of the variation in stress life.

7.3.3 Consideration of Fluid-Structure Interaction

As described in the literature review, luminaire support structures are potentially susceptible to vortex shedding. However, inclusion of vortex shedding into the analytical model would drastically increase the complexity as it includes fluid-structure interaction. While analyzing luminaire models explicitly for the effects of vortex shedding is not practical, the amplified stress ranges resulting from vortex shedding lock-in could be approximated when the correct conditions are present. For cycles generated from specific wind velocities where vortex shedding lock-in is known to occur, a multiplier could be used to amplify the stress ranges. The multiplier would have to include the probability that vortex shedding occurs at the selected wind velocities and directions. Recall that vortex shedding is only a concern for luminaire support structures without a taper or with a very small taper.

7.3.4 Validation of Remaining Life Model

Validation of the framework for estimating the remaining life of luminaire support structures is necessary. To do this, each component of the framework would be validated individually. Field monitoring of the response of luminaire support structures to dynamic wind loading would provide data for validation of the analytical models. Monitoring of wind speeds and directions near the luminaires would provide data to validate the dynamic wind pressure time histories. Laboratory fatigue tests would help to establish more representative fatigue life data for common WSDOT details. Finally, examining case studies of luminaire failures would provide opportunities to investigate the framework in its entirety. In those cases, the framework could be used to assess the probability of luminaire pole fatigue.

Chapter 8 Conclusion and Recommendations

8.1 Summary

Fatigue sensitive details in luminaire support structures are subjected to complex variable amplitude stress ranges throughout their service life. The complex stress histories result from natural wind gusts and the highest stress ranges occur when the wind gust frequency approaches the fundamental frequency of vibration of the support structure. Vortex shedding lock-in can also produce high stress ranges in non-tapered or lightly tapered luminaire support structures. The complexity of the loading has resulted in the use of an infinite life nominal stress approach for fatigue design of luminaire support structures as recommended by considerable research and required by the *2001 Specifications*. Equations for the equivalent static pressure range due to natural wind gusts and vortex shedding lock-in (when applicable) are used to compute the nominal fatigue stress range in critical details. The computed stress range must be below the constant amplitude fatigue limit (CAFL) for the detail classifications where the CAFL is the stress range at which the slope of the idealized fatigue curve is zero in log-log space.

An extensive literature review was conducted and numerous retrofit and repair techniques for luminaire support structures were identified. Ultrasonic impact treatment (UIT) is an effective method for retrofitting or repairing socket connections to improve the fatigue life if applied when the structure is under dead load and prior to crack initiation. Gusset stiffeners can also be used to retrofit pole socket connections if the vertical dimension is sufficiently long. However, careful analysis is necessary since cracks can initiate at the tip of the stiffeners. A repair technique was successfully used for crack at the corner of a hand hole opening. Holes were drilled at the ends of the crack and a V-shaped notch was cut along the length of the crack, filled with weld material, and ground flush. A patch plate was continuously fillet welded over the repaired area.

A few important conclusions were reached with regard to improving fatigue life of luminaire support structures:

1. The SCF at the weld toe of a pole socket connection can be significantly reduced by using a stiff base plate.

2. The SCF at the weld toe of a pole socket connection can be reduced by doing any of the following; decreasing the pole thickness, increasing the vertical weld leg size in an unequal leg fillet weld or the leg size in an equal leg fillet weld, and increasing the number of anchor bolts in the base plate.

3. CJP welded pole-to-base plate connection have better fatigue resistance than pole socket connections.

4. Critical fatigue locations and general behavior in aluminum and steel luminaire support structures are the same but modified fatigue curves should be used for design.

5. Poor fabrication techniques will accelerate crack initiation and reduce fatigue life.

Two previously in-service luminaire poles with triangular base plates and three anchor bolt configurations that are common in Washington were tested to determine their remaining fatigue resistance. The connection details tested in the characteristic poles were already classified in the *2001 Specifications*. However, those classifications characterize the fatigue resistance of a wide variety of details with one fatigue curve and are for new poles. The purpose of the fatigue testing was to determine the resistance of the specific details common in older support structures in Washington. From the literature, fatigue cracking can initiate in four details on luminaire support structures; the pole-to-base plate connection, the hand hole stiffener, the anchor bolts, and the mast arm-to-pole connection. Since fatigue failures at the mast arm-to-pole connection have not been reported in Washington, the experimental focus was on the other three locations. The fatigue resistance of the three tested details is summarized below along with conclusions from the quasi-static testing.

The experimental specimens both had CJP welded pole-to-base plate connections with fillet welds over the top and a backing ring. The detail was classified as Category E in the *2001 Specifications* but the test specimens exceeded that resistance despite being in-service for 20-30 years. The fatigue resistance of Specimen 1 exceeded the 50% confidence Category E fatigue curve as well as the 95% confidence Category D fatigue curve and Specimen 2 exceeded the 50% confidence Category D fatigue curve. Further, these data points were run-outs as failure around the hand hole controlled the fatigue life of both specimens. No damage was observed at the pole-to-base plate connection indicating that more cycles could have been accumulated before initiation of fatigue cracking.

The quasi-static testing indicated stress concentration factors (SCFs) as high as 1.33 were present in the CJP weld toe at the 240° cross-section location and as high as 1.17 at the 90° cross-section location. The high tensile SCFs were attributed to the presence of the butterfly trend where stresses at the 240° and 300° cross-section locations may be as large or larger than those at the 270° cross-section location. The butterfly trend is due to the presence of two anchor bolts on one side of the base plate, adjacent to the 240° and 300° cross-section locations. When that side is in tension, the anchor bolts attract stress away from the location on the cross-section farthest from the neutral axis (270°). Similarly, when the side of the specimen adjacent to the single bolt was in tension, a high SCF was recorded due to stress being attracted towards the single bolt. The single anchor bolt was in line with the cross-section location farthest from the neutral axis on one side of the pole (90°). Unexpectedly high compressive SCFs were measured at the CJP weld toe away from the extreme tension fiber on the side of the cross-section adjacent to the two anchor bolts. Several possible reasons for this behavior were postulated, with the most likely reason being that a more uniform bearing surface existed adjacent to the anchor bolts.

Two factors were identified that could have contributed to the high experimental fatigue resistance of the CJP welded pole-to-base plate connection. First, the CJP weld had a large unequal leg fillet weld over the top of it. This large fillet weld smoothed the flow of stresses from the pole walls to the base plate reducing geometric stress concentration. The other factor was the presence of a stiff base plate. As shown in previous research, a stiff base plate can drastically reduce the stresses at the weld toe. However, it should be noted that the high SCFs at the weld toe and presence of the butterfly trend are behaviors that are consistent with more flexible base plates.

Selecting the two test specimens was difficult because no inventory of in-service luminaire poles existed. Instead, poles were selected from the WSDOT bone yard with input from field engineers about the types of luminaire dimensions and details typically used. A procedure was developed to identify critical combinations of poles and mast arms that would be susceptible to high fatigue stress ranges. Both experimental specimens used similar stiffened hand holes for access into the pole with the hand hole in Specimen 2 being closer to the base plate than the hand hole in Specimen 1. The hand hole stiffeners were classified as Category E fatigue details in the *2001 Specifications* and their experimental fatigue life was found to exceed the fatigue life implied by that category. The fatigue life of the hand hole detail in Specimen 1 exceeded

the 50% confidence Category E fatigue curve and the 95% confidence Category D fatigue curve. The fatigue life of Specimen 2 exceeded the 50% confidence Category D curve. Cracking in Specimen 1 initiated in the upper right hand corner of the hand hole and propagated around the perimeter of the hand hole at the interface between the welded hand hole stiffener and the pole wall. Cracking in Specimen 2 initiated in the bottom left corner and propagated in a similar manner to the crack in Specimen 1. High principle tensile stresses were recorded in the upper left and right corners of the hand hole and their orientation was consistent with the observed cracking pattern. The observed fatigue cracking was most likely due to: (i) the presence of an excessively thick hand hole stiffener that restrained the deformation and caused high stresses in the adjacent pole wall and (ii) the presence of the stiffener weld and associated brittle material in the zone of high stresses.

Both test specimens utilized 5 in. long 1 in. diameter A325 anchor bolts. The fatigue testing of the anchor bolts was inconclusive because of the low stress ranges achieved during testing. The anchor bolt was classified as a Category D detail in the *2001 Specifications* and the run-out point for the anchor bolt in Specimen 1 exceeded the 50% confidence Category E' fatigue curve. The anchor bolt in Specimen 2 exceeded the 50% confidence Category E fatigue curve when testing was stopped. Due to the run-out, it is not possible to say whether the resistance exceeded Category D.

8.2 Recommended Inspection Protocol

The development of a sophisticated methodology to estimate the remaining life of luminaire support structures would be highly beneficial. However, developing the necessary components of such a methodology would require a substantial effort. In the meantime, focused inspection efforts of in-service luminaire support structures could be beneficial in predicting and/or extending their remaining life and prioritizing replacement. The following is a summary of inspection actions that would help achieve these goals:

1. Prior to onsite inspection, the procedure discussed in Chapter 3 to identify detail and support structure combinations that are susceptible to the highest stress ranges can be carried out. To utilize this procedure, a review of older luminaire drawings or survey of details from the field is necessary. Once critical support structures are identified, they can be cross-referenced with wind speed maps for the state to identify regions where the

critical older poles may be subjected to larger wind loads. These identified luminaire support structures should be prioritized for inspection.

2. The identified luminaire support structures should be inspected for crack initiation at four critical locations: the pole-to-base plate connection, the stiffened hand hole, the anchor bolts, and the mast arm-to-pole connection. Inspecting the mast arm-to-pole connection would require the use of special equipment to lift the inspector up high enough to visibly inspect. However, this is the least critical of the four locations and would only require inspection if there are concerns about specific details. The anchor bolts should be inspected for crack initiation and for tightness. The weld toe at the base plate connection and the corners of the hand hole should be visibly inspected for crack initiation. Crack initiation in any of those locations would be grounds for immediate removal.

3. Inspect the critical fatigue sensitive details for the presence of fabrication defects. Excessive grinding, notches, or poor weld quality accelerate crack initiation and can drastically reduce the fatigue life of specific details.

4. Investigate the site conditions for luminaire support structures identified as critical. The importance of site specific weather observations was stated in Chapter 6. Luminaires may have wind shelter from natural or manmade elements or they may be more exposed to wind or wind tunneling effects. Luminaire support structures that have already exceeded their service life and are in locations where site specific conditions increase local wind speeds even if no cracking is present.

5. Through this research it has become clear that WSDOT's record keeping with respect to luminaire support structures is insufficient. Drawings, locations, orientation of mast arms, and the installation dates of support structures are critical in establishing estimates of remaining life and determining the impact of increased exposed area due to additional attachment of signs. As part of a general inspection of luminaires, some of this data could be collected and organized providing a valuable resource for future inspection and replacement decision making.

8.3 Support Structure Orientation Considerations

Support structure orientation is important for newly installed luminaire support structures and for existing structures. In the laboratory testing, the hand hole was oriented so that it was centered about the extreme bending fiber of the cross-section and was subjected to the largest

stresses possible. However, if the hand hole is oriented on the same side or 180° from the mast arm it will be located on the neutral axis when the highest bending stresses occur, i.e. when the natural wind gusts occur normal to the plane of the mast arm. In the approved WSDOT details for new luminaires, the hand hole is located on the same side as the mast arm and the practice should be continued. During inspection and identification of poles susceptible to fatigue damage, the location of the hand hole with respect to the mast arm should be considered.

Similar attention should be paid to the orientation of the base plate. Triangular base plates inevitably result in one side of the cross-section and one anchor bolt being subjected to larger stresses. This was observed in the laboratory as the base plates were oriented so that the single bolt was in line with the applied load. However, if the base plate was rotated 90°, no bolts would be adjacent to the extreme tension fiber of the cross-section resulting in lower peak stresses at the base plate connection. In the field, the single bolt side should be located on the same side as the mast arm or 180° from the mast arm. This will ensure that when the high stress cycles occur due to natural wind gust pressures normal to the plane of the mast arm, the peak stresses will not be amplified by the presence of the single bolt adjacent to the extreme tension fiber of the cross-section.

8.4 Conclusions

The two tested in-service luminaire support structures had sufficient fatigue resistance to remain in the field despite a long service history. The critical details were subjected to a significant number of cycles at high stress ranges and fatigue cracking initiated at the corners of the hand hole in both specimens. When designing luminaire support structures it is important to consider both the fatigue resistance of the details used as well as the fatigue loads the structure will be subjected to. Typically, it is more cost effective to use improved fatigue details than to increase the structural dimensions to reduce the nominal fatigue stress ranges. Luminaire support structure orientation is a critical aspect of fatigue life because it drastically impacts the peak stress ranges in the critical details. A better understanding of the existing inventory of luminaire support structures in the state is necessary for prioritizing inspection and/or replacement of luminaire support structures.

8.5 Recommendations for Future Research

The additional research efforts that would be necessary to develop a methodology to estimate the remaining life of luminaire support structures were summarized in Chapter 6 and will not be restated here. However, before developing a remaining life estimate, it is important that a significant effort be made to database and characterize the currently in-service and newly installed luminaires in Washington. A database of cantilevered support structures in the state with important details such as type of pole-to-base plate connection, location, dimensions, thickness of hand hole stiffener, and pole orientation would help to rapidly identify types of luminaire support structures for which inspection and/or replacement is a priority.

Additional fatigue testing of other older details common in Washington is necessary. The actual fatigue resistance of specific details may vary significantly from its AASHTO classification. A sophisticated methodology for estimating life that uses an AASHTO stress life equation that may not accurately model the fatigue resistance of the specific detail may produce poor results.

Additional research should be performed to examine the flow of stresses from the bottom of the pole to the triangular base plate for both CJP welded connections and pole socket connections. Limited research exists on the behavior of triangular base plates and the behavior appears to be complex. Extensive finite element modeling of these base plates as well as quasi-static testing with a high concentration of rosettes at the base of the pole would improve understanding of the behavior. Further, parameters other than base plate thickness that impact the base plate stiffness should be investigated. The ratio of the pole diameter to the thickness of the plate and the location of anchor bolts may play roles in base plate stiffness which directly impacts stress concentration factors at the base plate connection.

.

References

American Association of State Highway and Transportation Officials. (1994). *AASHTO LRFD Bridge Design Specifications.* AASHTO.

American Association of State Highway and Transportation Officials. (1994). *Standard Specification for Structural Supports for Highway Signs, Luminaires and Traffic Signals.* Washington, D.C.: AASHTO.

American Association of State Highway and Transportation Officials. (2001). *Standard Specifications for Structural Supports for Highway Signs, Luminaires and Traffic Signals.* Washington: AASHTO.

ASCE. (2005). Minimum Design Loads for Buildings and Other Structures (ASCE 7-05). Reston, VA: American Society of Civil Engineers.

Calvert, E. A., Fouad, H. F., and Nunez, E. (1998). *NCHRP Report 411: Structural Supports for Highway Signs, Luminaires, and Traffic Signals.* Washington, D.C.: National Academy Press.

Caracoglia, Luca and Velazquez, Antonio. (2008). Experimental Comparison of the Dynamic Performance of Steel, Aluminum and Glass-Fiber-Reinforced-Polymer Light Poles. *Engineering Structures , 30* (4), 1113-1123.

Connor, R. J. et al. (2004). *Laboratory and Field Fatigue Investigation of Cantilevered Signal Support Structures in the City of Philadelphia--Final Report.* Lehigh University, Center for Advanced Technology for Large Structural Systems, Bethlehem, PA.

Connor, Robert J and Hall III, John H . (2008). Influence of Base Plate Flexibility on the Fatigue Performance of Welded Socket Connections. *Journal of Structural Engineering , 134* (6), 911-918.

Crandall, S.H and Mark, W.D. (1963). *Random Vibration of Mechanical Systems.* New York: Academic.

DelGrego, Michael and DeWolf, John T. (2003). *Field Monitoring and Evaluation for Sign Support Structures Subjected to Dynamic Loads.* JHR 03-291, University of Connecticut.

Dexter, R. J. and Ricker, M. J. (2002). *NCHRP Report 469: Fatigue Resistant Design of Cantilevered Signal, Sign, and Light Supports.* Washington, D.C.: National Academy Press.

Dexter, R. J., Kaczinski, M. R., and Van Dien, J. P. (1998). *NCHRP Report 412: Fatigue Resistant Design of Cantilevered Signal, Sign, and Light Supports.* Washington, D.C.: National Academy Press.

Dexter, R.J. and Fisher, F.W. (1997). Fatigue and Fracture-Chapter 8. (A. Tamboli, Ed.) *Steel Design Handbook LRFD Method* .

Dexter, Robert J., Hajjar, Jerome F., and Ocel, Justin M. (2006). *Fatigue-Resistant Design for Overhead Signs, Mast-Arm Signal Poles, and Lighting Standards.* Report No. MN/RC-2006-07, University of Minnesota, Minneapolis, MN.

Federal Highway Administration. (1990). *FHWA Electronic Information Survey on Sign Structure Failures.* Washington, D.C.: U.S. Department of Transportation.

Fouad, F. H. (2003). *NCHRP Report 494: Structural Support for Highway Signs, Luminaires, and Traffic Signals.* University of Alabama. Birmingham, AL: Transportation Reserach Board.

Gilani, Amir and Whittaker, Andrew. (2000). Fatigue Life Evaluation of Steel Post Structures. I: Background and Analysis. *Journal of Structural Engineering , 126* (3), 322-330.

Gilani, Amir and Whittaker, Andrew. (2000). Fatigue-Life Evaluation of Steel Post Structures. II: Experimentation. *Journal of Structural Engineering , 126* (3), 331-340.

Ginal, S. J. (2003). *Fatigue Performance of Full-Span Sign Support Structures Considering Truck-Induced Gust and Natural Wind Pressures.* MS Thesis, Marquette University, Milwaukee, WI.

Goode, Jonathan S. and van de Lindt, John W. (May/June 2007). Development of a Semiprescriptive Selection Procedure for Reliability-Based Fatigue Design of High-Mast Lighting Structural Supports. *Journal of Performance of Constructed Facilities , 21* (3), 193-206.

Iannuzzi, A., and Spinelli, P. (1987). Artificial Wind Generation and Structural Response. *Journal of Structural Engineering , 113* (12), 2382-2398.

Johns, Kevin W. and Dexter, Robert J. (May 1998). *Structures, Fatigue Testing and Failure Analysis of Aluminum Luminaire Support: Final Report.* Lehigh University, National Center for Engineering Research on Advanced Technology for Large Structural Systems, Bethlehem, PA.

Kaimal, J. (1972). Spectral Characteristics of Surface-Layer Turbulence. *Journal of the Royal Meteorological Society ,* 563-589.

Levy, R. (1996). *Structural Engineering of Microwave Antennas.* New York, NY: Institute of Electical and Electronic Engineers, Inc.

Marc Volume B: Element Library. (2008). 425-430. Santa Ana, CA: MSC Software Corporation.

Miki, C., Fisher, J., and Slutter, R. (n.d.). Fatigue Behavior of Steel Light Poles. *Fritz Engineering Laboratory Report No. 200.81.714.1, 1981 .* Lehigh, PA.

Miner, M. A. (1945). Cumulative Damage in Fatigue. *Journal of Applied Mechanics, 12 ,* A159-A164.

Palmatier, Amanda H. and Frank, Karl H. (2005). *Application of Ultrasonic Impact Treatment to In-Service Signal Mast Arms.* The University of Texas at Austin, Center for Transportation Research.

Rios, C. A. (2007). *Fatigue Performance of Multi-Sided High-Mast Lighting Towers.* M.S. Thesis, University of Texas at Austin, Graduate School, Austin, TX.

Rios, Craig Abel. (2007). *Fatigue Performance of Multi-Sided High-Mast Lighting Towers.* Master's Thesis, University of Texas at Austin.

Shinozuka, M., and Jan, C. (1972). Digital Simulation of Random Processes and Its Applications. *Journal of Sound and Vibration , 25 (1)*, 111-128.

Appendix 1 Fatigue Testing Database

		Summary of Fatigue Testing		
Project Name	*Type of Detail Tested*	*Specimen Description*	*Test Results/Conclusions*	*Recommended Detail Classificaiton*
Miki et al. (1981)	Socket Connections	-6 Equal Leg Fillet Welds -6 Unequal Lef Fillet Welds	1. Unequal leg fillet welds have higher fatigue resistance than equal leg fillet welds	-Unequal leg fillet weld performed slightly better than Category E' -Eqaul leg fillet weld performed slightly worse than Category E'
NCHRP Project 10-38	Anchor Bolts	-47 Specimens Made up of the Following 4 Bolt Types: Grade 55---1.5 in. dia.---6 UNC---Cut Grade 55---1.5 in. dia.---6 UNC---Rolled Grade 105---1.5 in. dia.---6 UNC---Cut Grade 105---1.5 in. dia.---6 UNC---Rolled	1. Bending stress in bolt do not need to be considered if bolt misalignment is less than 1:40 2. Maximum stress in anchor bolts greatly influences fatigue strength 3. At low stresses, anchor bolts with rolled threads had greater fatigue resistance than those with cut threads 4. Grade 55 and 105 bolts had the same fatigue resistance when tested to the same maximum stress	-Category E' for snug-tightened anchor bolts in finite life region -Category E for fully-tightened anchor bolts in finite life region -Category D for both snug-tightened and fully-tightened anchor bolts in infinite life region
Johns (1998)	Aluminum Luminaire Specimens with Shoe Base Socket Connection	-12 Luminaire Pole-to-Base Plate Connections Tested -6 Cantilevered Support Structures -6 Straight Support Structures -7 of the Specimens Used Transformer Bases -see Figure 2.5 and 2.6	1. 3 of 7 transformer base specimens cracked (2 at access hole and one in transformer base wall opposite the access hole 2. Cracks appeared in the weld toe of the shoe base connection	-The mean minus 2 standard deviations line for the pole-to-base plate connections plotted above the Category E line in the finite life region and below the Category E line in the infinite life region for the specimens with cracking at the weld toe -3 Specimens had cracking in the weld root and the mean minus 2 standard deviations line plots below the Category F line from the *Bridge Specification*
Gilani and Whittaker (2000b)	CJP Welded Post-to-Base Plate Connection for Typical CMS Used by Caltrans	-One Connection Tested -0.5 in. Post Wall Thickness, 2.75 in. Thick Base Plate, 4 in. Tall by 1 in. Thick Backing Ring Tack Welded to Post -Cycled at Range of 11.8 ksi about Zero Mean Stress -4 in. Wide by 6 in. Tall Conduit Hole 18 in. Above Base Plate -see Figure 2.10	1. Cracks first appeared in the conduit hole at 1 million cycles and propagated through the thickness of the post wall by 1.2 million cycles 2. Specimen failed (Type I failure mode) at 2.7 million cycles and repairs were made including a patch plate over the conduit hole cracks and testing continued 3. At 1.7 million cycles after the repair, cracks began to appear in patch plate-to-post fillet weld and Type I failure was eventually reached at 2.7 million cycles after the repair	-No recommendations were made since it is based on only one specimen, however, this performed far better than the *2001 Specifications* classification of Category E'
Gilani and Whittaker (2000b)	CJP Welded Mast Arm-to-Annular Flange Plate Typical Connection	-Three Connections Tested -0.375 in. Mast Arm Wall Thickness, 1.37 in. Thick Flange Plate -Cycled at Range of 10 ksi about Mean Stress of 9 ksi Just Above Flange	1. One specimen developed cracks in HAZ of CJP weld after 1.5 million cycles, reached Type I failure mode at 2.8 million cycles 2. The other two specimens were tested out to 4 million cycles and neither the Type I or II failure modes were	-No recommendations were made since it is based on only one specimen, however, this performed far better than the *2001 Specifications* classification of Category E'

172

Summary of Fatigue Testing				
Project Name	*Type of Detail Tested*	*Specimen Description*	*Test Results/Conclusions*	*Recommended Detail Classificaiton*
Gilani and Whittaker (2000b)	Gusset Stiffened Post-to-Base Plate Socket Connection Typically Used in CMSs by Caltrans	-One Specimen Tested -Eight 0.56 in. thick gusset stiffeners 4 in. Wide at the Base Plate by 6 in. Tall Fillet Welded to Post and 2.75 in. Thick Base Plate -Cycled at a stress range of 12.4 ksi at a Mean Stress of 13 ksi Just Above Base Plate -see Figure 2.14 for Drawing	1. Type I failure mode reached after just 800,000 cycles, however, by 60,000 cycles 2 cracks initiated in the conduit hole and propagated into post wall 2. Conduit opening caused major stress concentrations 3. Testing was continued and by 1,000,000 cycles conduit hole cracks propagated into fillet weld at socket connection 4. Gussets failed to prevent crack propagation into socket weld	-No recommendations were made since it is based on only one specimen, however, this specimen performed very poorly.
Gilani and Whittaker (2000b)	CJP Post-to-Base Plate with Reinforced Concrete Jacket	-One Specimen Tested -42 in. Outside Diameter Concrete Jacket with 16 0.86 in. Diameter with Longitudinal Bars and 0.51 in. Diameter Radial Bars at 4 in. Spacing--72 in. Tall -Tested at variable stress range as measured in post neglecting jacket -see Figure 2.15	1. Performed extremely well, reached 4,500,000 cycles with no cracking in the post 2. Measured stress ranges were 20 times less than those measured in non-retrofitted CJP welded post-to-base plate connection	-No recommendations were made since it is based on only one specimen, however, this specimen performed very well.
Chen (2003)	Steel Fillet Welded Socket Mast Arm-to-End Plate Connections	-5 Specimens Tested -4 Circular Mast Arms and 1 Octagonal Mast Arm -2 Specimens Utilized Unequal Leg Fillet Weld Design -3 Fabricated by Valmont, 1 by Union Metals, and 1 by JEM	1. In all 4 specimens with the circular cross-section, cracking initiated in the weld toe at the extreme tension fiber 2. In the one octagonal cross-section specimen, cracking initiated in the pole bends of the extreme tension fiber 3. Fatigue resistant weld did not improve fatigue life 4. Fabrication problems discovered through metallurgical analysis including lack of penetration and fusion, undercutting, and excessive grinding	-The mean of the 5 specimens plotted just above the Category E' Line

Summary of Fatigue Testing				
Project Name	*Type of Detail Tested*	*Specimen Description*	*Test Results/Conclusions*	*Recommended Detail Classificaiton*
Palmatier and Frank (2005)	Steel Mast Arm-to-End Plate Socket Connections with Varying End Plate Thicknesses	-8 Mast Arm Specimens Tested -2 Taken Out of the Field--One Underwent UIT Treatment at Mast Arm-to-Transverse End Plate Connection and End Plate-to-Pole Connection After 1 Year of Service--The Other Was Untreated and Had Been In-Service for 10 Years -6 Taken From Fabrication Yard Where Two Had UIT Treated Mast Arm-to-End Plate Connections and the other 4 were Untreated	1. UIT is an effective method of improving fatigue performance of connections 2. End plate thickness effects fatigue resistance of mast arm-to-pole connection 3. Mast arms with larger diameters can have higher stresses at the weld toe due to higher moments resulting in higher end plate deflections	-The two treated specimens performed at the Category E' level while the untreated specimens performed below the Category E' level
Azzam (2006)	Aluminum Luminaire Shoe Base Socket Connection	-19 Specimens Tested -Aluminum Alloy 6063-T4 Temper -Specimens 10 in. Diameter---0.25 in. Thick -see Figure 2.20	1. All cracks initiated at the weld toe of the shoe base to pole fillet weld 2. Some initiated at the farthest distance from neutral axis and propagated through the thickness of the weld toe 3. A couple had cracks initiate at the weld root which grew through the weld throat. 4. Curve much shallower than AASHTO S-N curves, this is thought to be due to compressive residual stresses in the shoe base connection	-CAFL for shoe base socket connection is between 3.0 and 3.5 ksi -For high cycle fatigue (approximately 700,000 to 10,000,000 cycles), data falls between Categories C and D -For low cycle fatigue (approximately 10,000 to 700,000 cycles), the data falls between Categories D and E'
Azzam (2006)	Aluminum Luminaire Through Plate Socket Connection	-10 Specimens Tested -Aluminum Alloy 6063-T4 Temper -Specimens 10 in. Diameter---0.25 in. Thick	1. Cracks developed at the weld toe in all through plate socket connections 2. In 80% of the specimens, the cracks initiated opposite the anchor bolts, not at the location farthest from neutral axis as would be expected, this is evidence of the butterfly trend	-Fatigue resistance below Category E'
Ocel, et al. (2006)	MnDOT Standard Box Connection (Octagonal Mast Arm-to-Octagonal Pole Built-up Box Connection)	-8 MnDOT Standard Box Connections: -3 Tested In-Plane -4 Tested Out-of-Plane -1 Tested at 45 Degrees (Equal Parts In-Plane and Out-of-Plane) -see Figure 2.30	1. In the 3 specimens cycled in-plane, cracking initiated at the intersection of the flange plate and the pole tube and the side plates buckled outwards 2. In the 4 specimens cycled out-of-plane and 1 specimen cycled at 45 degrees, cracking initiated in the pole wall at the connection to the side plates indicative of punching shear	-Category ET for MnDOT standard box connection subjected to in-plane loading -Category K_2 for MnDOT standard box connection subjected to out-of-plane loading -Category K_2 for MnDOT standard box connection subjected to 45 degree loading

TECHNICAL REPORT STANDARD TITLE PAGE

Summary of Fatigue Testing				
Project Name	Type of Detail Tested	Specimen Description	Test Results/Conclusions	Recommended Detail Classificaiton
Ocel, et al. (2006)	Octagonal Pole-to-Base Plate Socket Connection with 1.25 in. Thick Base Plate	-8 Pole Socket Connections: -3 Tested In-Plane -4 Tested Out-of-Plane (Cycled on Both Sides of the Connection) -1 Tested at 45 Degrees (Cycled on Both Sides of the Connection) -All specimens had 1.25 in. thick base plate, octagonal pole with 14 in. corner to corner dimension, and 0.3125 in. thick tube walls -see Figure 2.30	1. Cracking initiated in one or two of the pole bends in the extreme tension fiber in all specimens 2. Cracks either initiated in the tube side weld toe and propagated into tube wall or at the root of the socket weld and grew through the thickness of the weld	-Category K_2 for pole socket connection with 1.25 in. thick base plate
Ocel, et al. (2006)	Octagonal Pole-to-Base Plate Socket Connection with 2.5 in. Thick Base Plate	-4 Pole Socket Connections: -2.5 in. thick base plate -2 specimens had 0.3125 in. tube thickness -2 specimens had 0.1875 in. tube thickness -All specimens had 14 in. corner to corner dimension -see Figure 2.30	1. Similar cracking pattern to 1.25 in. thick base plate specimens 2. Two to three category improvement in fatigue resistance to 1.25 in. thick base plate specimens 3. Specimens were tested on both sides, however, unlike in 1.25 in. thick base plate specimens, this impacted the test results, so second side data was neglected	-Category E for pole socket connection with 0.3125 in. thick tube wall and 2.5 in. thick base plate -Category E' for pole socket connection with 0.1875 in. thick tube wall and 2.5 in. thick base plate
Ocel, et al. (2006)	Hammer Peen Retrofitted Socket Connections	-5 Hammer Peen Retrofitted Pole Socket Connections -Identical to 1.25 in. Thick Pole Socket Connections	1. Two category improvement over untreated specimens	-Category E' for hammer peen retrofitted socket connection
Ocel, et al. (2006)	Hammer Peen Repaired Socket Connections	-5 Pole Socket Connections were Repaired and the Cycle Counter was Restarted at Zero -Identical to 1.25 in. Thick Pole Socket Connections	1. One category improvement over untreated specimens (not including cycles accumulated prior to cracking and repair)	-Category ET for hammer peen repaired socket connection
Ocel, et al. (2006)	Access Hole of Integrated Transformer Base	-8 Transformer Bases -3 Cycled In-Plane -4 Cycled Out-of-Plane -1 Cycled at 45 Degrees -see Figure 2.30	1. Cracks initiated at the bottom corner of the access hole 2. Some cracks initiated in the flame cut access hole corner and propagated horizontally into the transformer base 3. Some cracks initiated in the fillet weld connecting the stiffening ring to the base plate	-Category K_2 for transformer base access hole detail

Summary of Fatigue Testing				
Project Name	*Type of Detail Tested*	*Specimen Description*	*Test Results/Conclusions*	*Recommended Detail Classificaiton*
Ocel, et al. (2006)	Triangular Gusset Stiffened Mast Arm-to-Transverse Plate Socket Connections	-4 Gusset Stiffened Socket Connections Tested on Both Sides -1.25 in. Thick Mast Arm End Plate -4 Gusset Stiffeners are 8.13 in. Tall, no other dimensions given -Octagonal Mast Arm with 11.6 in. Corner to Corner Dimension with 0.3125 in. Wall Thickness -see Figure 2.30	1. Gusset stiffeners did not prevent cracking at socket weld toe in any of the 4 specimens 2. When cracks appeared at weld toe, they were hammer peen repaired to determine fatigue resistance at gusset tip 3. Cracks initiated in gusset tip at weld toe and propagated into the pole wall 4. Two specimens had simultaneous cracking in the gusset stiffener at the weld toe at the tip and at the weld to the base plate 5. Connection performed one category better than unstiffened socket connection	-Category E for gusset tip -Category ET for gusset stiffened socket category
Ocel, et al. (2006)	CJP Welded Mast Arm-to-Transverse Plate Connections	-4 CJP Welded Connections -Tested on Both Sides Backing Bar Not Welded to End Plate -1.25 in. Thick Mast Arm End Plate -Octagonal Mast Arm with 11.6 in. Corner to Corner Dimension with 0.3125 in. Wall Thickness -see Figure 2.30	1. Cracks initiated at pole bends on extreme tension side	-Category E' for CJP welded tube-to-transverse plate connection
Ocel, et al. (2006)	CJP Welded Mast Arm-to-Mast Can Connection (Mast Arm 15 Degrees Above Horizontal)	-8 CJP Welded Mast Arm-to-Mast Can Connections with Backing Bar -3 Cycled In-Plane -4 Cycled Out-of-Plane -1 Cycled at 45 Degrees -Mast Arm Thickness is 0.3125 in with an 11.6 in. Corner to Corner Dimension -see Figure 2.30	1. Cracks initiated on the mast can side of the weld in all 8 specimens indicated punching shear 2. Connection is not in *2001 Specifications*, closest connection is a fillet welded tube-to-tube connection typically used for truss element connections in sign bridges 3. *2001 Specifications* requires that fillet welded tube-to-tube connection be checked both for cracking of the CJP weld and for cracking due to punching shear	Category K_2 for CJP welded mast arm-to-mast can connection

		Summary of Fatigue Testing		
Project Name	*Type of Detail Tested*	*Specimen Description*	*Test Results/Conclusions*	*Recommended Detail Classificaiton*
Rios (2007)	Steel HML Pole-to-Base Plate Connections	-4 Fillet Welded Socket Connections with 8 Bolt Base Plate Configuration--2 with 1.5 in. and 2 with 2.0 in. Thick Base Plate -4 Fillet Welded Socket Connections with 12 Bolt Base Plate Configuration--2 with 1.5 in. and 2 with 2.0 in. Thick Base Plate -2 Wyoming CJP Details with 8 Bolt Configuration and 2 in. Thick Base Plate -2 Fillet Welded Stool Base Plate Details with 8 Bolt Configuration and 2 in. Thick Base Plate -2 Fillet Welded Socket Connections with 8 Bolt Configuration and 3 in. Thick Base Plate -2 Texas CJP Details with 12 Bolt Configuration and 3 in. Thick Base Plate - see Figures 2.45 and 2.46	1. CJP welded specimens failed due to cracking that initiated at the weld toe and propagated about 20 in. before resistance was reduced to 10% of maximum resistance 2. Cracks in stool base initated at the toe of the cap plate-to-pole fillet weld and propagated into the pole wall	-All pole socket connections performed well below Category E' regardless of base plate thicknessand bolt configuration -Data for stool base connection plots close to Category E line -Texas CJP performed better than Wyoming CJP but utilized stiffer base plate

Appendix 2: Computation of Stress Ranges for Valmont poles

Pole Dimensions:
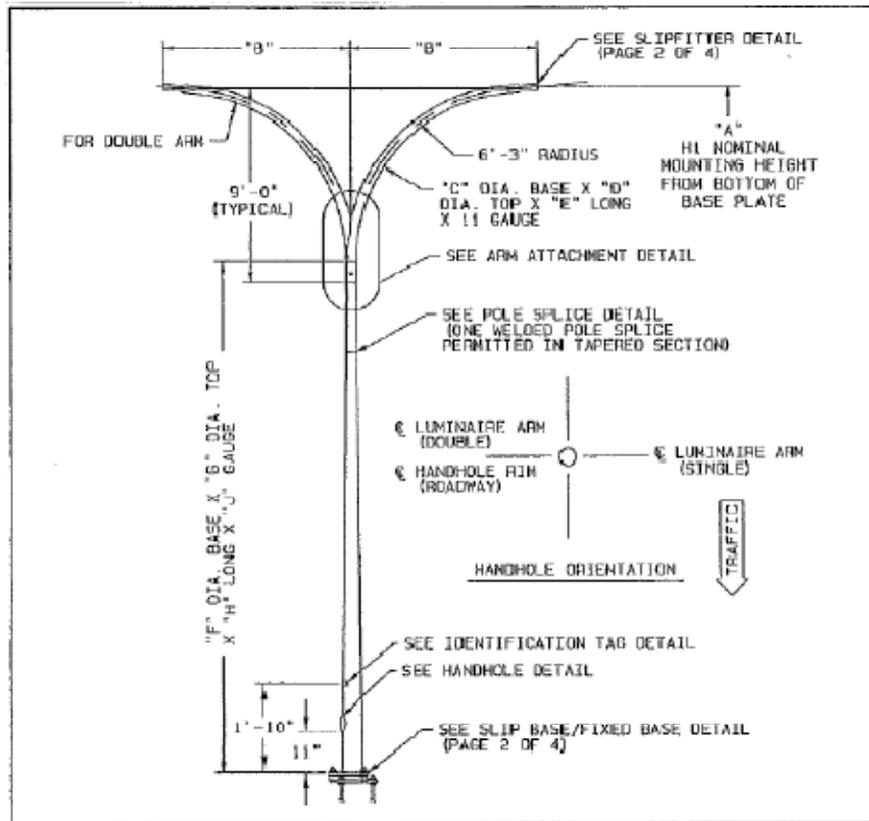
Arm Dimensions:

$A := 35 \cdot ft$ Nominal Mounting Height

$B := 6 \cdot ft$ Arm Length

$C := 5.41 \cdot in$ Base Outside Diameter

$D := 3.77 \cdot in$ Top Outside Diameter

$E := 11.666 \cdot ft$ Arm Length

$R := 6.25 \cdot ft$ Radius of Curve of Arm

$H_{arm} := 9 \cdot ft$ Height of Arm

$\theta := 85 \cdot \dfrac{\pi}{180}$ Radians in Arc

Pole Dimensions:

$F := 8.75 \cdot in$	Base Outside Diameter
$G := 4.94 \cdot in$	Top Outside Diameter
$H := 27.25 \cdot ft$	Shaft Length
$J := 0.1196 \cdot in$	Wall Thickness

Fatigue Importance Factors Assuming Fatigue Category III (AASHTO Table 11-1) and Pole and Luminaire Drag Coefficients (AASHTO Table 3-6) :

$I_{vs} := 0.31$	Importance Factor for Vortex Shedding

In accordance with AASHTO 11.7.2, vortex shedding must not be analyzed for tapered poles

$I_{nw} := 0.48$	Importance Factor for Natural Wind Gusts
$C_d := 1.10$	Wind Drag Coefficient for Cylindrical Pole and Arm
$C_{dlum} := 0.5$	Wind Drag Coefficient for Luminaire with Generally Rounded Surface
$C_{dsign} := 1.2$	Wind Drag Coefficient for Pole Mounted Sign

Unit Definitions:

$$psf := \frac{lb}{ft^2} \qquad kip := 1000 \cdot lb \qquad ksi := \frac{kip}{in^2}$$

Computation of Vortex Shedding Pressure Range:

Luminaires are observed to vibrate in the second mode. A SAP2000 analysis was performed to determine the second modal frequency and the luminaire will be analyzed for second mode vibration. Second mode vibration is characterized by large displacements at midheight and small displacements at the top of the pole. Since the column is tapered, a range of critical diameters is possible. The Ontario Bridge Code recommends that the vortex shedding induced pressure be applied over a range of diameters plus or minus 10% of the critical diameter. The structure will be analyzed for the worst case of vortex shedding at the very top of the pole and bottom of the pole. The critical diameter for the top of the pole will correspond to a diamter where the diameter at the top of the pole is 10% less than the critical diameter. The critical diameter for the bottom of the pole will correspond to a diameter where the diameter at the bottom of the pole is 10% greater than the critical diameter. In practice, it is unlikely that vortex shedding lock-in would occur in the field in a luminaire structure with a mast arm. This would only occur if the angle of attack of the wind was parallel to the plane of the luminaire structure. In this case, the structure would behave like a vertical cantilever with a concentrated mass at the top. In all other directions, the structure is non symmetric and it is unlikely vortex shedding would occur. More likely, vortex shedding lock in would occur in a luminaire structure without a mast arm. Regardless, the vortex shedding calculation will be made for the example luminaire pole with a mast arm.

$T_{n2} := 0.14608 \cdot sec$ Natural Period Corresponding to Second Out of Plane Mode Vibration

Natural Frequency Corresponding to Second Out of Plane Mode Vibration:

$f_{n2} := T_{n2}^{-1}$ $f_{n2} = 6.846 \, Hz$

Computation of Vortex Shedding Pressure Range on Bottom of Pole:

Compute Critical Diameters and Ranges:

$d_{botcrit} := \dfrac{F}{1.1}$ $d_{botcrit} = 7.955 \, in$

$d_{botmin} := 0.90 \cdot d_{botcrit}$ $d_{botmin} = 7.159 \, in$

$d_{botmax} := 1.10 \cdot d_{botcrit}$ $d_{botmax} = 8.75 \, in$

$d_{topcrit} := \dfrac{G}{0.9}$ $d_{topcrit} = 5.489 \, in$

$d_{topmin} := 0.90 d_{topcrit}$ $d_{topmin} = 4.94 \, in$

$d_{topmax} := 1.10 \cdot d_{topcrit}$ $d_{topmax} = 6.038 \, in$

Compute Critical Heights:

$taper := \dfrac{F - G}{H}$ Pole taper

$h_{botcrit} := \dfrac{0.20 \cdot d_{botcrit}}{taper}$ $h_{botcrit} = 11.379 \, ft$

$h_{topcrit} := \dfrac{0.20 \cdot d_{topcrit}}{taper}$ $h_{topcrit} = 7.852 \, ft$

Compute Critical Velocities at Which Vortex Shedding Lock-in Occurs (AASHTO 11.7.2 Eq. 11-2):

$S_n := 0.18$ Strouhal Number

$V_{botcrit} := \dfrac{f_{n2} \cdot d_{botcrit}}{S_n}$ $V_{botcrit} = 25.21 \, \dfrac{ft}{sec}$

$V_{topcrit} := \dfrac{f_{n2} \cdot d_{topcrit}}{S_n}$ $V_{topcrit} = 17.396 \, \dfrac{ft}{sec}$

Equivalent Static Vortex Shedding Pressure Range (AASHTO 11.7.2 Eq 11-4):

$\beta := 0.005$ Estimated Damping Ratio

$P_v := \dfrac{0.00118 \cdot V_{botcrit}^2 \cdot C_d \cdot I_{vs}}{}\left(\dfrac{ft}{} \right)^{-2} \cdot psf$

$$P_{bot\_vs} := \frac{\dots}{2 \cdot \beta} \cdot \left(\frac{\dots}{sec}\right)^{\dots} \cdot psf$$

$$P_{bot\_vs} = 25.573 \, psf$$

$$P_{top\_vs} := \frac{0.00118 \cdot V_{topcrit}^2 \cdot C_d \cdot L_{vs}}{2 \cdot \beta} \cdot \left(\frac{ft}{sec}\right)^{-2} \cdot psf$$

$$P_{top\_vs} = 12.176 \, psf$$

Equivalent Static Vortex Shedding Force Range:

$$F_{bot\_vs} := \frac{1}{2} \cdot P_{bot\_vs} \cdot \left(d_{botmin} + d_{botmax}\right) \cdot h_{botcrit}$$

$$F_{bot\_vs} = 192.885 \, lb$$

$$F_{top\_vs} := \frac{1}{2} \cdot P_{top\_vs} \cdot \left(d_{topmin} + d_{topmax}\right) \cdot h_{topcrit}$$

$$F_{top\_vs} = 43.73 \, lb$$

Compute Centroids of Distributed Forces:

$$z_{bot} := \frac{P_{bot\_vs} \cdot d_{botmin} \cdot h_{botcrit} \cdot \frac{h_{botcrit}}{2} + \frac{1}{2} \cdot P_{bot\_vs} \cdot \left(d_{botmax} - d_{botmin}\right) \cdot h_{botcrit} \cdot \frac{h_{botcrit}}{3}}{\frac{1}{2} \cdot P_{bot\_vs} \cdot \left(d_{botmax} + d_{botmin}\right) \cdot h_{botcrit}}$$

$$z_{bot} = 5.5 \, ft$$

$$z_{top} := \frac{P_{top\_vs} \cdot d_{topmin} \cdot h_{topcrit} \cdot \left(H - \frac{h_{topcrit}}{2}\right) + \frac{1}{2} \cdot P_{top\_vs} \cdot \left(d_{topmax} - d_{topmin}\right) \cdot h_{topcrit} \cdot \left(H - \frac{2}{3} h_{top}\right)}{\frac{1}{2} \cdot P_{top\_vs} \cdot \left(d_{topmax} + d_{topmin}\right) \cdot h_{topcrit}}$$

$$z_{top} = 23.193 \, ft$$

Compute Resulting Moments at Base:

$$M_{base\_from\_bot} := z_{bot} \cdot F_{bot\_vs} \qquad M_{base\_from\_bot} = 12.73 \, kip \cdot in$$

$$M_{base\_from\_top} := z_{top} \cdot F_{top\_vs} \qquad M_{base\_from\_top} = 12.171 \, kip \cdot in$$

Computation of Natural Wind Gust Pressure Range:

Equivalent Static Natural Wind Gust Pressure Range (AASHTO 11.7.3 Eq. 11-5):

$$P_{nw} := 5.2 \cdot C_d \cdot I_{nw} \cdot psf \qquad P_{nw} = 2.746 \, psf$$

Overlap Between Pole and Arm:

$$over := H + H_{arm} - A \qquad over = 1.25 \, ft$$

181

Outside Diameter of Pole at Bottom of Overlap:

$$OD_{bot} := F - \frac{H - over}{H} \cdot (F - G) \qquad OD_{bot} = 5.115\ in$$

Projected Area of Pole Normal to Wind Gust Up to Attachment With Arm:

$$A_{pole} := \frac{1}{2} \cdot (F + OD_{bot}) \cdot (H - over) \qquad A_{pole} = 15.02\ ft^2$$

Equivalent Static Force on Pole Due to Natural Wind Gust and Distance Above Base At Which the Force is Applied:

$$F_{pole} := P_{nw} \cdot A_{pole} \qquad F_{pole} = 41.239\ lb$$

$$z_{pole} := \frac{H - over}{3} \cdot \left(\frac{2 \cdot OD_{bot} + F}{OD_{bot} + F} \right) \qquad z_{pole} = 11.864\ ft$$

Outside Diameter of Arm at Top of Overlap:

$$OD_{begarc} := C - \frac{over}{E}(C - D) \qquad OD_{begarc} = 5.234\ in$$

Projected Area of Overlap Normal to Natural Wind Gust and Distance Above Base At Which the Force is Applied:

$$A_{ov} := \frac{1}{2} \cdot (C + OD_{begarc}) \cdot over \qquad A_{ov} = 0.554\ ft^2$$

Equivalent Static Force on Overlap Area Due to Natural Wind Gust and Distance Above Base At Which the Force is Applied:

$$F_{ov} := P_{nw} \cdot A_{ov} \qquad F_{ov} = 1.522\ lb$$

$$z_{ov} := H - over + \frac{over}{3} \cdot \left(\frac{2 OD_{begarc} + C}{OD_{begarc} + C} \right)$$

$$z_{ov} = 26.622\ ft$$

Projected Area of Arc Portion of Arm Normal to Wind Gust:

$$arclen := R \cdot \theta \qquad arclen = 9.272\ ft$$

$$OD_{endarc} := C - \frac{over + arclen}{E}(C - D) \qquad OD_{endarc} = 3.931\ in$$

$$A_{arc} := \frac{1}{2} \cdot (OD_{begarc} + OD_{endarc}) \cdot arclen \cdot 2$$

$$A_{arc} = 1.02 \times 10^3\ in^2$$

Equivalent Static Force on Arc Portion of Arm Due to Natural Wind Gust:

$$F_{arc} := P_{nw} \cdot A_{arc} \qquad F_{arc} = 19.443\ lb$$

Distance Along Arc (Where the base=0) at Which Force is Applied:

$$arccent := \frac{arclen}{3} \cdot \left(\frac{2 OD_{endarc} + OD_{begarc}}{OD_{endarc} + OD_{begarc}} \right)$$

$$\text{arccent} = 4.416 \, \text{ft}$$

Height Above Base at Which Force on Arc Portion of Arm is Applied:

$$\text{anglecent} := \frac{\text{arccent}}{R} \qquad\qquad \text{anglecent} = 0.707$$

$$z_{arc} := R \cdot \sin(\text{anglecent}) + H \qquad\qquad z_{arc} = 31.308 \, \text{ft}$$

Projected Area of Sloped Portion of Arm Normal to Wind Gust:

$$\text{slopdist} := E - \text{arclen} - \text{over} \qquad\qquad \text{slopdist} = 1.144 \, \text{ft}$$

$$A_{slop} := \frac{1}{2} \cdot \left(OD_{endarc} + D \right) \cdot \text{slopdist} \cdot 2 \qquad A_{slop} = 0.734 \, \text{ft}^2$$

Equivalent Static Force on Sloped Portion of Arm Due to Natural Wind Gust:

$$F_{slop} := P_{nw} \cdot A_{slop} \qquad\qquad F_{slop} = 2.016 \, \text{lb}$$

Distance Along Slope (Where base=0) at Which Force is Applied:

$$\text{slopcent} := \frac{\text{slopdist}}{3} \cdot \left(\frac{2 \cdot D + OD_{endarc}}{D + OD_{endarc}} \right) \qquad \text{slopcent} = 0.568 \, \text{ft}$$

Height Above Base at Which Force on Sloped Portion of Arm is Applied:

$$z_{slop} := A - (\text{slopdist} - \text{slopcent})\cos(\theta) \qquad z_{slop} = 34.95 \, \text{ft}$$

Force on Luminaire Attachment:

$$P_{nwlum} := 5.2 C_{dlum} \cdot I_{nw} \cdot \text{psf} \qquad\qquad P_{nwlum} = 1.248 \, \text{psf}$$

$$A_{lum} := 3.3 \cdot \text{ft}^2 \cdot 2$$

$$F_{lum} := P_{nwlum} \cdot A_{lum} \qquad\qquad F_{lum} = 8.237 \, \text{lb}$$

$$z_{lum} := A \qquad\qquad z_{lum} = 35 \, \text{ft}$$

Force on Sign Attachment:

$$P_{nwsign} := 5.2 C_{dsign} \cdot I_{nw} \cdot \text{psf} \qquad\qquad P_{nwsign} = 2.995 \, \text{psf}$$

$$A_{sign} := 10 \cdot \text{ft}^2$$

$$F_{sign} := P_{nwsign} \cdot A_{sign} \qquad\qquad F_{sign} = 29.952 \, \text{lb}$$

$$z_{sign} := 9.5 \, \text{ft}$$

Moments at Base Plate Due to Natural Wind Gusts for Single and Double Arm Configurations:

$$M_{nw} := F_{pole} \cdot z_{pole} + F_{ov} \cdot z_{ov} + F_{arc} \cdot z_{arc} + F_{slop} \cdot z_{slop} + F_{lum} \cdot z_{lum} + F_{sign} \cdot z_{sign}$$

$$M_{nw} = 21.381 \, \text{kip} \cdot \text{in}$$

Moment of Inertia of Pole at Base:

$$I_{polebase} := \frac{\pi}{64} \cdot \left[(F)^4 - (F - 2J)^4 \right] \qquad I_{polebase} = 30.197 \, in^4$$

Equivalent Stress Range at Base Plates Due to Natural Wind Gusts for Single and Double Arm Configurations:

$$\sigma_{nw} := \frac{M_{nw} \cdot F}{2 I_{polebase}} \qquad\qquad \sigma_{nw} = 3.098 \, ksi$$